

Understanding the mechanism of Adenovirus endosomal escape

Kirsty Sawtell

St. Hilda's College

Supervisor: Professor Kay Grünewald

Division of Structural Biology

A thesis submitted in partial fulfilment of the requirements for the degree of Doctor of Philosophy at the University of Oxford

Michaelmas Term 2020

Abstract

Adenoviruses (AdV) are non-enveloped dsDNA viruses that cause respiratory and gastrointestinal diseases and are commonly used as vaccine and gene therapy vectors. In order to replicate inside a host cell, AdV must first penetrate the endosomal membrane and gain access to the cytosol. A highly conserved amphiphilic alpha helix within AdV protein VI (pVI) has been proposed as the membrane-lytic factor that is necessary for endosomal escape. However, the precise mechanism of endosomal membrane disruption is uncertain. This investigation aimed to characterise pVI and investigate the contribution of different domains using several biophysical techniques and electron microscopy. Firstly, a purification protocol was developed for recombinant wild type pVI and two loss of function mutants. The three pVI proteins, along with a synthetic peptide composed of the suggested membrane-lytic domain of pVI, were then examined using circular dichroism and analytical ultracentrifugation in order to further understand their secondary structure and oligomeric state. The effect of pVI on liposomes was then investigated using dynamic light scattering and a dye release assay and visualised using electron cryo-microscopy (cryoEM). Finally, electron cryo-tomography (cryoET) was used to examine membrane disruption events in 3D. The activity of pVI constructs upon liposomes was observed to be highly dependent on the membrane composition, with phosphatidylethanolamine reducing the activity of pVI.

COVID-19 statement

My data collection was largely complete by the time the lockdown was brought into effect in the UK due to the COVID-19 pandemic. However, I would have liked to have examined some additional cryoEM samples, particularly for the two pVI mutants, since I had the least amount of useable data for these and already had vitrified grids prepared.

Acknowledgements

Firstly, I would like to thank my supervisor, Kay Grünewald for giving me the opportunity to join your group and for your constant support and encouragement throughout my time at Oxford. I would also like to thank Tzviya Zeev-Ben-Mordehai, Thomas Bowden and Yvonne Jones for their supervision and advice.

Thank you so much to Lindsay for your help all way through my DPhil for always pointing me the in right direction. Thank you to Suzi for your huge support with the dye release and AUC methods and to both Lindsay and Suzi for helping me put this thing together. I would also like to thank all present and past members of the Kay Group Outpost, Oxford, particularly Cathy for getting me started in STRUBI and to Vojta, Daven, Emily and Emma for the support and for all the laughs. Thanks to everyone in the Grünewald group at the CSSB, I only wish I'd had the chance to meet you all. Thanks to Pascale for her amazing introduction to cellular CLEM, even if it didn't make into this thesis. Thanks to everyone in STRUBI, the most open (literally) and lively lab I have worked in and everyone in OPIC for help with all things EM. Thank you to Harald's Group in Bordeaux for providing the starting materials for this project and for our interesting discussions about pVI.

I would like to thank my family for their continued support and encouragement, including my nephew Jasper, for giving me one more reason to submit my thesis before you arrived. Finally, I would like to thank John, who has been by my side for over ten years, and without whom I could have never made it this far.

Contents

Abstract 1

COVID-19 statement 2

Acknowledgements 3

Contents 4

List of Figures 10

List of Tables 14

Abbreviations 15

Chapter 1 Introduction 18

1.1 Cell entry of viruses 18

1.1.2 Endocytosis of non-enveloped viruses 20

1.2 Adenoviridae 23

1.2.1 AdV associated diseases 24

1.2.2 Use in vaccines and gene therapy 25

1.2.3 Capsid structure 27

1.2.4 The Adenovirus protease and capsid maturation 31

1.2.5 Replication cycle 33

1.3 Adenovirus protein VI 37

1.3.1 Domain architecture 38

1.3.2 Capsid location of protein VI 41

1.3.3 Copy number of protein VI 44

1.3.4 Amphipathic helices 47

1.3.5 Predicted mechanism of membrane rupture 50

1.3.6 Additional roles of pVI in the Adenovirus replication 53

1.4 Objectives 55

Chapter 2 Expression and purification of recombinant Adenovirus wild type pVI and mutants 59

2.1 Introduction 59

2.2 Optimisation of pVI-WT expression and purification 62

2.2.1 Preliminary experiments 62

2.2.2 Optimisation of expression 64

2.2.3 Optimisation of cell lysis and protein solubilisation 65

2.2.4 Optimisation of affinity purification 69

2.2.5 Size exclusion chromatography 74

2.3 Optimisation of pVI-L40Q expression and purification 76

2.4 Optimisation of pVI-Δ54 expression and purification 81

2.5 Summary of changes made during optimisation of pVI purification 87

2.6 Mass spectrometry analysis of pVI-WT 90

2.7 Discussion 93

2.8 Materials and methods 100

2.8.1 Proteins and plasmids 100

2.8.2 Site-directed mutagenesis. 100

2.8.3 Expression in *E. coli* and cell lysis 101

2.8.3.1 Transformation and induction 101

2.8.3.2 Cell lysis and protein solubilisation 101

2.8.4 Affinity purification 102

2.8.4.1 Affinity purification in initial experiments 102

2.8.4.2 Affinity purification in later experiments 103

2.8.5 Size-exclusion chromatography 103

2.8.6 SDS-PAGE and Western Blotting 104

2.8.7 Protein quantification and storage 105

2.8.8 Peptide mapping 106

Chapter 3 Biophysical characterisation of Adenovirus protein VI with model membranes 107

3.1 Introduction 107

3.2 Prediction of pVI structure 109

3.2.1 Prediction of pVI secondary structure 109

3.2.2 Prediction of pVI disorder 111

3.3 Analysis of pVI folding state 115

3.3.1 Analysis of pVI secondary structure using circular dichroism. 115

3.3.2 Analysis of pVI oligomeric state using analytical ultracentrifugation. 119

3.4 Analysis of pVI–membrane binding 124

3.4.1 Analysis of pVI-liposome interactions using dynamic light scattering 127

3.4.2 Exploration of membrane disruption by pVI using a 132

fluorescent dye release assay 132

3.5 Discussion 135

3.6 Materials and methods 147

3.6.1 Disorder prediction 147

3.6.2 Liposomes 148

3.6.3 Circular dichroism 149

3.6.4 Analytical ultracentrifugation 149

3.6.5 Dynamic light scattering 150

3.6.6 Liposome leakage assay..... 150

Chapter 4 Analysing the interaction of pVI with model membranes using cryoEM..... 152

4.1 Introduction..... 152

4.2 Negative stain analysis of liposomes and pVI-WT..... 155

4.3 Optimisation of cryoEM sample preparation..... 156

4.4 CryoEM of PC/cholesterol liposomes..... 160

4.4.1 Characterisation of PC/cholesterol liposomes..... 161

4.4.2 Characterisation of PC/cholesterol liposomes + pVI-WT..... 163

4.4.3 Characterisation of PC/cholesterol liposomes + pVI-L40Q..... 165

4.4.4 Morphology comparison of PC/cholesterol liposomes..... 168

4.5 Characterisation of PC/PE/Chol liposomes..... 169

4.5.1 Characterisation of PC/PE/Chol liposomes..... 170

4.5.2 Characterisation of PC/PE/Chol Liposomes + pVI-WT..... 172

4.5.3 Characterisation of PC/PE/Chol Liposomes + pVI-L40Q..... 174

4.5.4 Characterisation of PC/PE/Chol liposomes + pVI-Δ54..... 176

4.5.5 Characterisation of PC/PE/Chol Liposomes + pVI-34-54..... 178

4.6 3D observation of pVI interaction with membranes using cryoET..... 180

4.7 Discussion..... 182

4.7.1 Addition of PE reduced the membrane lytic activity of pVI-WT 187

4.7.2 Study limitations 190

4.7.3 Conclusion 192

4.8 Materials and methods 192

4.8.1 Negative stain EM 192

4.8.2 CryoEM 193

4.8.2.1 Sample preparation 193

4.8.2.2 CryoEM data collection. 194

4.8.2.3 Tomogram reconstruction and data processing 195

4.8.3 Quantification and statistical analysis. 196

Chapter 5 Discussion 198

Chapter 6 Appendix 210

6.1 Mass spectrometry analysis of pVI-WT 210

6.2 Additional examples from cryoEM analysis of liposomes and pVI constructs 211

References 222

List of Figures

1.1 Routes of virus entry into cells 19

1.2 Routes of entry into cells via endocytosis 21

1.3 HAdV-C5 capsid structure based on cryoEM studies 28

1.4 Adenovirus replication cycle 34

1.5 Predicted domains of Adenovirus pVI 39

1.6 Modelled densities of pVI within the AdV hexon 43

1.7 Helical wheel projection of Adenovirus pVI (positions 34-53) 48

1.8 Proposed model of membrane rupture by AdV pVI 52

1.9 pVI constructs used in this project 55

2.1 Preliminary purification of pVI-WT and L40Q by Wodrich et al 61

2.2 Results of small-scale affinity purification experiments using Triton X-100 lysis buffer. 63

2.3 The effect of IPTG concentration and temperature on expression levels in Rosetta (DE3) cells 64

2.4 Comparison of detergents in the solubilisation of pVI-WT 67

2.5 Comparison of 8M urea and 6M guanidine hydrochloride in the solubilisation of pVI-WT from 1L culture 68

2.6 Comparison of pVI-WT purified from 1 L of culture using different types of nickel charged Sepharose resin 71

2.7 Comparison of pVI-WT purified from 1, 2 and 4 L culture 72

2.8 Overview of changes made during optimisation of pVI-WT affinity purification 73

2.9 Size exclusion chromatography of pVI-WT from 1, 2 and 4L of culture 75

2.10 Comparison of pVI-L40Q purification from 1 L culture in urea and Triton X-100 lysis buffer 78

2.11 Size exclusion chromatography of pVI-L40Q from 1, 2 and 4L of culture 80

2.12 Results of small-scale pVI-Δ54 experiments 82

2.13 Comparison of detergents in the solubilisation of pVI-Δ54 83

2.14 Comparison of pVI-Δ54 purification from 1 L culture in urea and Triton X-100 lysis buffer 84

2.15 Size exclusion chromatography of pVI-Δ54 from 1, 2 and 4 L of culture 86

2.16 Overview of optimised expression and purification protocol for pVI-WT and mutants 88

2.17 Comparison of pVI WT protein and mutants purified with respective optimised protocols 89

2.18 Results of pVI-WT peptide mapping by LC-MS/MS 92

3.1 Comparison of pVI secondary structure prediction results 110

3.2 Prediction of disorder in pVI 115

3.3 Analysis of pVI secondary structure using circular dichroism 118

3.4 Sedimentation coefficient distribution c(s) from the analysis of interference data for pVI-WT and pVI-Δ54 samples 120

3.5 Analysis of protein-membrane interactions using dynamic light scattering 129

3.6 Analysis of protein-membrane interactions using a fluorescent dye release assay 133

3.7 Comparison of the circular dichroism spectra 136

4.1 Negative stain analysis reveals liposome damage by pVI-WT 155

4.2 Optimisation of cryoEM sample preparation improved the concentration and distribution of liposomes 158

4.3 Three main morphology types were observed in PC/cholesterol liposomes without protein 162

4.4 Two additional morphology types were observed in liposomes upon addition of pVI-WT that indicated membrane disruption 164

4.5 No evidence of liposome disruption was observed in upon addition of pVI-L40Q 167

4.6 pVI-WT but not pVI-L40Q produced open liposomes and membrane fragments and there was little difference in proportions of interfaces counted 168

4.7 PC/PE/cholesterol liposomes were very similar in appearance to liposomes without PE and did not demonstrate evidence of membrane damage 171

4.8 PC/PE/cholesterol liposomes showed evidence of membrane disruption upon addition of pVI-WT and included two new morphology classes 173

4.9 A single example of a pointed liposome was found in liposomes on addition of pVI-L40Q, but none of the other disrupted morphologies 175

4.10 A single example of an open liposome was found in liposomes on addition of pVI-Δ54, but none of the other disrupted morphologies 177

4.11 All of the morphological categories observed in pVI-WT samples were also observed for peptide 34–53 179

4.12 CryoET reveals membrane fragments and the curved membranes of open liposomes in liposomes with pVI-WT 181

4.13 pVI-WT typically induced more membrane disruption events than pVI-34-53 in PC/PE/cholesterol liposomes, with only a few examples for pVI-L40Q and pVI-Δ54 183

4.14 The presence of PE increased the number of pointed liposomes and hemifusion sites, but greatly reduced the number of open and fragmented liposomes 189

Figure 5.1 Schematic models for the mechanism of AdV pVI disruption of endosomal membranes based on the data obtained in this study.....200

5.2 PC/cholesterol liposomes damaged by pVI-WT have curved edges that are similar to those of endosomes ruptured by mutant Ad5-M1 206

6.1 Full map of detected peptides from mass spectrometry analysis of pVI-WT 210

List of Tables

1.1 Adenovirus types and associated clinical diseases 21

1.2 Domains of the AdV pVI protein 39

1.3 Physical and chemical properties of AdV5 pVI wild type and L40Q pVI N-terminal helices 49

4.1 Datasets for PC/cholesterol and PC/PE/cholesterol liposomes 197

6.1 Examples of liposome features excluded from counts 211

6.2 Additional examples of liposome features observed in liposomes without protein 213

6.3 Additional examples of liposome features observed in liposomes incubated with pVI-WT 214

6.4 Additional examples of liposome features observed in liposomes incubated with pVI-L40Q ... 218

6.5 Additional examples of liposome features observed in liposomes incubated with pVI-Δ54 219

6.6 Further examples of liposome features observed in liposomes incubated with pVI-34-53 220

Abbreviations

AdV – Adenovirus

AVP – Adenovirus Protease

AFM – Atomic Force Microscopy

ALPS – amphipathic lipid packing sensor

AH – Amphipathic helix

ARD – acute respiratory diseases

AUC – analytical ultracentrifugation

CAR – coxsackie and adenovirus receptor

CD – circular dichroism

CryoEM – electron cryo-microscopy

CryoET – electron cryo-tomography

DBP – DNA-binding protein

DLS – dynamic light scattering

EEA-1 – early endosome antigen 1

GON – Groups Of Nine hexons

GUV – giant unilamellar vesicles

GuHCl – guanidine hydrochloride

HIV – Human immunodeficiency virus

HSV – Herpes simplex virus

IDP – Intrinsically disordered protein

IDR – Intrinsically disordered region

IMAC – Immobilized Metal Affinity Chromatography

MTOC – microtubule organising centre

NLS – nuclear localisation signal

NMR – nuclear magnetic resonance

NPC – nuclear pore complex

FPLC – Fast protein liquid chromatography

PC – phosphatidylcholine

PDB – Protein Data Bank

PE – phosphatidylethanolamine

PI – phosphatidylinositol

PML-NB – promyelocytic leukaemia protein nuclear body

PS – phosphatidylserine

PSD – particle size distribution

PPH – peri-pentonal hexons

pVI – adenovirus protein VI

pVIc – C-terminus of precursor pVI

pVIn – N-terminus of precursor mature pVI

pVI-WT – wild type recombinant Adenovirus protein VI

MTOC – microtubule organizing centre

RGD – Arginylglycylaspartic

SDS-PAGE – sodium dodecyl sulphate-polyacrylamide gel electrophoresis

SRB – sulforhodamine B dye

SNR – signal-noise ratio

SUV – small unilamellar vesicles

TP – terminal protein

VV – vaccinia virus

VSV – vesicular stomatitis virus

XRC – X-ray crystallography

Chapter 1 Introduction

1.1 Cell entry of viruses

Viruses cannot self-replicate and rely on host cell machinery for reproduction. To gain access to the cytosol, viruses must either penetrate plasma membranes at the cell surface or the membranes of cell compartments, such as endosomes, after internalisation [1]. Virus entry into cells is a complex multistep process. Both enveloped and non-enveloped viruses have evolved to take advantage of a variety of fundamental processes to enter cells. The first step of viral entry is attachment to cellular receptors present on the surface of the host cell, generally proteins, carbohydrates, or lipids. Often, primary receptors stabilize the virion on the cell surface and enable the high-affinity interactions between viral proteins and secondary receptors that trigger various cellular signalling pathways and result in the next stages of internalisation [2]. Figure 1.1 illustrates two basic cell entry routes.

Enveloped viruses are able to use several routes of viral entry, including endocytosis. Common factors, such as membrane fusion mechanisms and cell surface receptors, are shared among evolutionary distant virus families [3]. Some enveloped viruses initiate fusion between the viral envelope and plasma membrane, resulting in the merging of the two membranes and release of the viral genome (Fig 1.1B, bottom panel) [1]. Three classes of viral fusogen glycoproteins have been identified, with the class I hemagglutinin of influenza virus being among the best characterised [3, 4]. At the multicellular level, several modes of virus cell-to-cell spread exist. For some viruses including human immunodeficiency virus

(HIV), vaccinia virus (VV) and herpes simplex virus (HSV), infected cells express cell surface proteins that attract nearby uninfected cells and viruses can also spread by cell-cell fusion [2, 5]. Non-enveloped viruses typically penetrate cell membranes after internalisation [6].

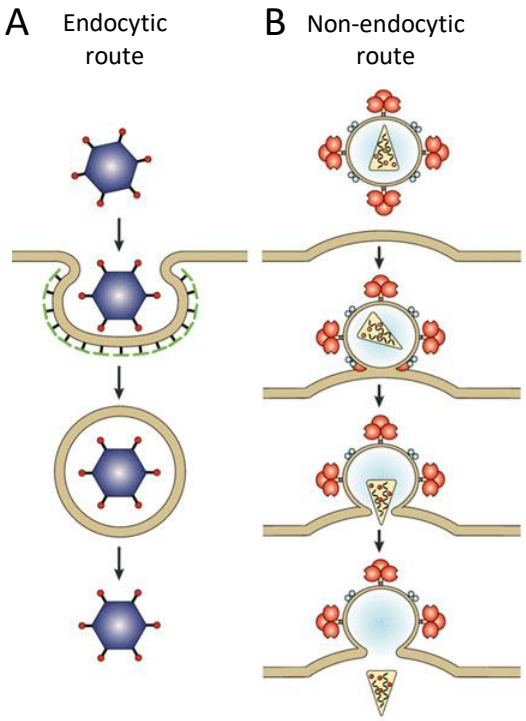


Figure 1.1 Routes of virus entry into cells.

A) An example of non-enveloped virus entry: clathrin-mediated endocytosis and penetration, as utilised by adenoviruses. B) An example of enveloped virus entry through fusion at the plasma membrane, as utilised by human immunodeficiency virus (HIV) . Membrane fusion can also occur from inside an endosome, as in the case of influenza virus. Taken from reference [7].

1.1.2 Endocytosis of non-enveloped viruses

In order to enter cells, the majority of non-enveloped viruses depend on the endocytosis pathways that are used by cells to take up molecules through the phospholipid bilayer into dynamic and biochemically specialized structures derived from the plasma membrane [3, 8]. Endocytosis is crucial for regulating cell signalling and homeostasis, and in some specialised cells, regulating neurotransmission and immune responses [9, 10]. The activation of signalling receptors on the cell surface by binding of ligands promotes downstream signalling and internalisation of external molecules [8]. Specific endocytic mechanisms include endocytosis mediated by networks of specialised proteins like caveolin and clathrin, as well as clathrin- and caveolae-independent endocytosis [9]. The major known endocytic pathways are depicted in Figure 1.2.

Phagocytosis of solid particles and pinocytosis of solutes into large vesicles is dependent on remodelling of the plasma membrane by the actin cytoskeleton [11]. Most endocytosed cargoes are delivered to the early endosome via vesicles coated with the scaffolding proteins clathrin or caveolin. Clathrin-mediated endocytosis is the best characterized endocytic pathway. Vesicles are formed through polymerization of clathrin monomers and a network of interacting adaptor proteins to form a curved clathrin coat [12]. Three self-assembling clathrin heavy and three light chains form a triskelion structure that is the assembly unit of the clathrin coat that stabilises vesicles and facilitates budding [13]. Caveolae are small membrane invaginations formed by the polymerisation of caveolin

proteins [14]. Some of the clathrin-dependant and -independent pathways also require dynamin, a large GTP-ase that mediates membrane fission, while others involve other GTPases such as CDC42, RhoA or ARF6 [11, 15]. Viruses that enter cells by caveolin and clathrin dependant pathways include adenovirus and simian virus 40 (SV40) [16].

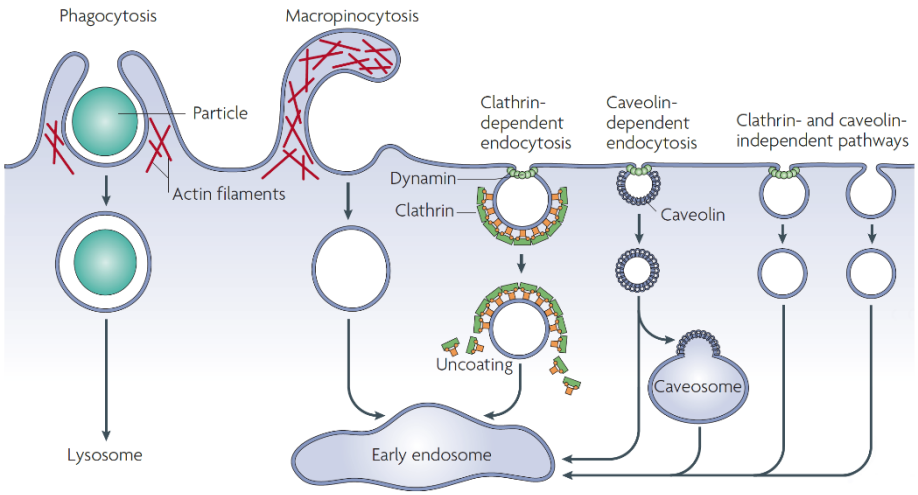


Figure 1.2 Routes of entry into cells via endocytosis.

Phagocytosis allows the uptake of large solid particles, and macropinocytosis is used for the uptake of extracellular liquid. Both of these processes are actin dependent. Smaller vesicles are formed by clathrin and caveolin-dependent endocytosis, involving the polymerisation of protein subunits to form a coated pit. Clathrin- and caveolin-independent pathways are less well defined but may involve other cellular GTPases. Adapted from reference [11].

The size and nature of cargo taken up via these mechanisms is specific to each pathway, and they are themselves regulated by cell density and other factors [17]. The first internal compartments of the endocytic pathway are early endosomes, which are acidified shortly after internalisation. Endosomes mature into late endosomes and may fuse with lysosomes

for degradation of endosomal contents. The luminal pH drops from around 6 to 4.9 during endosome maturation [8, 18]. Viruses that enter the cell through endocytosis must avoid degradation in the lysosome and hence escape the endocytic vesicle to gain access to the cytosol [1, 19]. This endosomal membrane penetration can occur at any stage of the endocytic pathway [20]. Disruption of host membranes by non-enveloped viruses can occur through several mechanistically diverse processes. Viral proteins can trigger membrane damage by mechanisms including pore or channel formation, osmolysis, or induction of membrane curvature [21]. Membrane interacting peptides have been identified in diverse viruses and are often small peptides with hydrophobic or amphipathic properties [21]. Membrane disruption by pore formation is thought to be involved in the entry of several non-enveloped viruses, such as poliovirus [22] and reovirus [23, 24]. Several viruses encode viroporins, small and usually hydrophobic viral proteins with at least one amphipathic helix that forms a transmembrane domain which oligomerises to form pores [25]. Proteins that have been identified as potential viroporins include the M2 proton channel of influenza A, HIV-1 Vpu [26], the E protein of SARS-CoV-1 [27] and HCV p7 [28, 29]. VP4 proteins of certain picornaviruses such as human rhinovirus 16 are responsible for the formation of multimeric pores [30]. On the other hand, other viral proteins are able to disrupt membranes without the formation of pores. The γ peptide of Flock house virus (FHV) contains an amphipathic α-helix which forms pentamers that integrate horizontally into the upper bilayer of the membrane, inducing disorder in the lipid core and resulting in disruption of the membrane with no indication of pore formation [31].

In human adenoviruses (HAdV), the membrane penetration process occurs within early endosomes and involves partial disassembly and the release of a membrane lytic factor from the interior of the capsid. The final step in the entry process generally involves the complete release of the viral genome from the capsid, a process known as "uncoating" [6]. After gaining access to the cytosol, viruses are then able to traffic towards the appropriate site of genome replication.

1.2 Adenoviridae

The family *Adenoviridae* comprises large (90–100 nm) non-enveloped icosahedral viruses with linear double stranded DNA genomes. Adenoviruses (AdV) have been isolated from every major vertebrate class [32] and the human AdV (HAdV) belong the genus Mastadenovirus. To date, 103 types of HAdV have been reported to the Human Adenovirus Working Group, classified into 7 species (A–G) [33, 34]. HAdV of species C, particularly HAdV-C2 and HAdV-C5 are among the most extensively studied. HAdVs have genomes of approximately 36 kb that encode 38 genes [35, 36].

AdV were first isolated in 1953 by Rowe et al. from adenoid tissue used to study poliovirus growth in human cells and were later identified as cytopathic in certain cell types [37-39]. The oncogenic potential of AdV was first observed in rodent cells infected with HAdV 12, but AdV have not been associated with cancer in humans [40]. After it was identified as an oncolytic agent, an AdV was trialled for the treatment of cervical cancer [41, 42].

Certain HAdV also became model systems for studying oncogenesis and their study has contributed to the understanding of several fundamental eukaryotic cell processes such as cellular gene expression and regulation, cell cycle control, DNA replication and RNA splicing [43-45]. HAdV is now used as a model for complex virus organization and assembly, DNA replication and virus-host interactions of non-enveloped viruses [46, 47].

1.2.1 AdV associated diseases

HAdV are associated with a wide spectrum of clinical diseases, the most common of which include mild upper respiratory tract, gastrointestinal and ocular infections [48]. Transmission usually occurs via respiratory droplets or faecal-oral transmission [43]. Table 1.1 presents the infections most commonly associated with each HAdV species.

HAdV infections are typically self-limiting or sub-clinical, but HAdVs can cause severe disease in immunocompromised individuals, the elderly and young children. An estimated 5–7% of paediatric respiratory tract infections worldwide are caused by HAdV [39, 40] and most people have serologic evidence of prior infection by the age of 10 [41]. Outbreaks of HAdV-associated acute respiratory infections occur frequently in schools, hospitals, and care facilities, and in military populations [49, 50]. Additionally, several AdV types cause veterinary disease, for example, fowl AdV outbreaks have become increasingly common in Asia since 2015 [43].

Table 1.1 Adenovirus types and associated clinical diseases.

Adapted from reference [56].

HAdV species	Type	Type of infection	Reference
A	12, 18, 31	Gastrointestinal, respiratory, urinary	[48, 49]
B	3, 7, 11, 14, 16, 21, 34, 35	Keratoconjunctivitis, gastrointestinal, respiratory, urinary	[51-53]
C	1, 2, 5, 6	Respiratory, gastrointestinal, hepatitis, urinary	[48, 49]
D	8–10, 13, 15, 17, 19, 20, 22–30, 32, 33, 36–39, 42–49	Keratoconjunctivitis, gastrointestinal	[52, 54]
E	4	Keratoconjunctivitis, respiratory	[51, 52]
F	40, 41	Gastrointestinal	[55]
G	52	Gastrointestinal	[55]

1.2.2 Use in vaccines and gene therapy

Much of the clinical interest in adenoviruses came from their wide application as vectors in vaccine delivery and in gene therapy into mammalian cells [50, 57], owing to their high genome capacity, transduction efficiency and tropism, and ease of large-scale production [46, 58, 59]. HAdV systems have been well characterised, particularly HAdV-C5, the most common cause of HAdV-associated infections [60, 61]. Adenovirus-based vectors are now widely employed as for gene and cancer therapy vectors [57, 61]. Gene therapy trials with HAdV-derived vectors in the 1990s included the transient correction of a chloride transport defect in cystic fibrosis patients using an AdV-C5 vector [62, 63]. Adenovirus based oncolytic, or tumour selective viruses, present a new strategy for cancer therapy, although

few have been approved for clinical use [64, 65]. Although gene therapy trials in animals and humans using adenoviral gene transfer were largely unsuccessful, they were found to induce innate and adaptive immune responses to the adenoviral antigens, making them attractive vaccine vectors [66].

Subunit AdV vaccine vectors have been trailed for a variety of infectious agents including malaria, tuberculosis, HIV, Ebola and Influenza [42, 66, 67]. Attenuated adenovirus type 4 and 7 vaccines have also been used to decrease the number of acute respiratory diseases (ARD) among military recruits [68]. More recently, several AdV vectors expressing the spike glycoprotein of severe acute respiratory syndrome coronavirus-2 (SARS-CoV-2), showed promising results in inducing immune responses in rhesus macaques and humans [69-72] and were subsequently approved for use in many countries. These included the Oxford-Astra Zeneca chimpanzee AdV vectored vaccine (ChAdOx1 nCoV-19) and the Ad26.COV2.S developed by Harvard Medical School in collaboration with Janssen Vaccines [73]. Further understanding of AdV host cell attachment and entry mechanisms can be applied in both inhibitor design in the treatment of clinical disease and improvement of vaccine and gene therapy vector efficiency. Therefore, there is a need to better understand the structural details of AdV capsid structure and molecular interactions with the host.

1.2.3 Capsid structure

HAdV was first visualised by electron microscopy in 1959 [74]. Structural studies of capsids and individual component proteins of several HAdV types have since contributed to the detailed understanding of many aspects of adenovirus capsid structure, assembly, and virus-host cell interactions [75]. The structure of the icosahedral HAdV-C5 capsid has been solved at high resolution (~3.2–3.8 Å) by both electron cryo-microscopy (cryoEM) [76, 77] and X-ray crystallography (XRC) [78, 79]. Mature HAdV virions have a complex icosahedral structure (pseudo T=25 icosahedral symmetry) with a diameter of 90–100 nm and a total mass of around 150 MDa. The capsid is composed of three major proteins and four minor proteins along with several non-structural proteins [78]. Fig. 1.3 illustrates the cryoEM model of the viral capsid of HAdV D26 from Yu et al. [43].

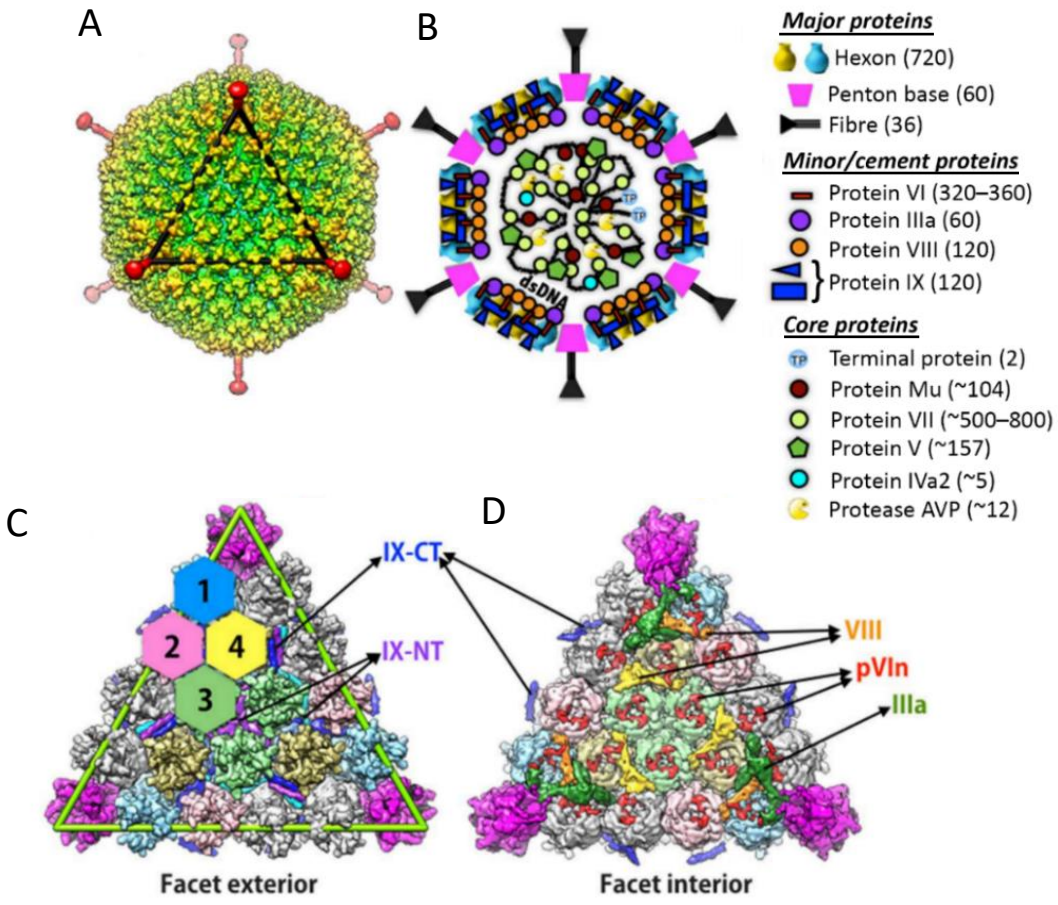


Figure 1.3 HAdV-D26 capsid structure based on cryoEM studies

(A) Colour-coded surface representation of the cryoEM reconstruction of HAdV-D26, viewed down the icosahedral threefold axis. One icosahedral facet is identified by a black triangle. (B) Schematic representation of AdV capsid showing the location and organization of the AdV capsid proteins. A list of symbols and the proteins they represent is shown on the right. The copy numbers of the capsid proteins are indicated in parentheses. (C) Exterior view of a triangular facet. Surface representations of the hexons (hexon-1 to hexon-4) are shown in four different colours (light blue, pink, green, and khaki, respectively), and the penton base is shown in magenta. The green triangle represents an icosahedral facet and is equivalent to the black triangle in (A). The hexons shown in grey belong to neighbouring facets. The locations of the N-terminal triskelions and C-terminal coiled coils (four-helical bundle; 4-HLXB) of protein IX are labelled. (D) Interior view of the facet showing the location of the minor proteins relative to each other and to the major capsid proteins. Surface representations of minor capsid proteins are labelled. Adapted from reference [77].

The major structural unit, the hexon, is a trimer of the highly conserved protein II [78]. Hexons form four structurally distinct trimeric confirmations (Fig 1.4C, H-1 to H-4) and are organised into triangular icosahedral facets of 12 units with penton bases at each of the 12 fivefold axes of symmetry. AdV capsids disassembled *in vitro* separate into a structural unit known as the Groups Of Nine hexons (GON) [80, 81]. Protein IX (pIX) cements together hexons within a GON on the exterior of the capsid and stabilises interactions between the icosahedral facets [82, 83]. The N-termini of pIX molecules form triskelion structures at the three-fold junctions of hexons, while the C-termini are arranged in tetrameric 4 helix bundles located between the GON [77, 83]. Recombinant pIX deficient viruses have reduced thermostability, indicating the importance of this protein network in capsid stability [84, 85]. Fibres protrude from each penton, composed of a trimer of protein IV arranged in a triple α-spiral fold that is noncovalently attached to the penton base, a feature which aids in the detachment of fibre during cell entry [6, 86]. Internal proteins IIIa, VI and VIII stabilize the capsid, as established by structural studies [85, 87]. The core proteins V, VII, μ, IVa2, terminal protein and the adenovirus proteinase (AVP) are associated with the viral genome [88, 89].

While HAdV is one of the most well-characterised non-enveloped viruses, until recently, two models disagreed in the location assignments of core polypeptides IIIa, VI and IX. The first model was based on moderate- to high-resolution cryoEM structures of HAdV5 and an E1/E3-deleted Ad5 [90, 91], including a 3.6 Å cryoEM structure (PDB 3IYN) [83]. The second

model was based on X-ray crystallographic studies [78, 92], some early biochemical studies [93, 94] as well as low-resolution cryoEM studies [95, 96] with the key structure being a 3.8Å XRC structure (PDB 4CWU) [86]. As improvements in EM camera technology and processing have been made, more accurate structural information has been achievable and a cryoEM structure from Dai et al. (2017) of an E1B gene-attenuated oncolytic virus containing the wild-type Ad5 capsid has replaced the older models (PDB 6B1T) [76]. This structure confirmed the assignments of proteins IIIa, VIII, and IX and crucially revealed several components within the hexon cavity for the first time: the cleaved N-termini of precursor proteins VI (pVIn) and pVII (pVIIn2) and a fragment of mature protein VI [76, 97]. These assignments will be discussed in more detail in section 1.3.2.

The protein assignments from another cryoEM study published by Yu et al. (shown in Figure 1.3) (PDB 5TX1) [77] supported the cryoEM model published by Dai et al. [76] These new models lead to the older XRC model being revised and replaced with a new model (PBD 6CGV) [79], which reassigns a density connecting peri-pentonal hexons (PPH) with hexons beneath the vertices of capsids from a pV-VI complex to pIIIa. Precise assignments of pIX chains became clearer in the newer revised crystal structure [79], in particular, a four-helix bundle assigned to the C-terminal domain of polypeptide that was previously assigned to IIIa. The newer XRC structure also identified two possible locations of pVIII, which in one location has a role in cementing the hexons underneath the vertex region along with a molecule of protein IIIa, while at a second location, pVIII connects hexons [79].

1.2.4 The Adenovirus protease and capsid maturation

Formation of infectious AdV virions requires the proteolytic processing of proteins by the 23 kDa Adenoviral protease (AVP), a cysteine protease which is highly conserved among adenoviruses [98, 99]. During maturation, AVP cleaves the precursor forms of minor coat proteins IIIa, VI, and VIII, core proteins VII along with the terminal protein μ and the packaging protein L1 52/55. AVP has an unusual mechanism of activation, as it requires two viral cofactors, viral DNA and an 11-residue peptide derived from the C-terminus of pre-protein pVI (pVIc) [98, 100]. Together, these cofactors increase the activity of AVP *in vitro* by as much as 30,000-fold [101]. During assembly, catalytically inactive AVP is bound to viral DNA but during maturation, it cleaves preprotein VI to produce pVIc. Subsequently, the AVP-pVIc complex cleaves a 33-residue peptide from the N-terminal region (pVIn; residues 1–33) resulting in mature pVI [99]. pVIc then acts as a "molecular sled" which allows AVP to slide along DNA toward other DNA-associated precursor proteins, including the precursor of pVII . The concept of the molecular sled was first identified in pVIc and is defined as a small basic molecule, such as a peptide, that binds and slides along DNA in order to translocate cargo toward specific targets [102, 103]. Mangel et al. presented a model whereby the four basic residues from residue 245–248 that form a nuclear localisation signal (NLS) in pVIc bind to phosphate groups on DNA through the formation of ion pairs [99, 102]. Sliding is not dependent on DNA sequence and is driven by thermal diffusion [104]. Molecular sled sequences have subsequently been identified in many mammalian

proteins, such as the C terminus of β-actin and NLSIII of the p53 tumour suppressor protein [104].

pVII is cleaved at two N-terminal cleavage sites, to produce the mature protein, which has a role in viral DNA import into the nucleus, as well as DNA packaging into the capsid [76, 105]. The number of AVP molecules in the capsid is estimated at between 7 and 10, but it is unknown how so few copies of the protease can perform an estimated 2000 cleavage events per virion in the highly crowded environment of the viral core [99].

The crucial role of AVP was elucidated in studies of a non-infectious temperature-sensitive mutant, Ad2ts1 [91]. The ts1 genome contains a mutation in the L3 gene that codes for AVP, resulting in a Pro137Leu substitution. AVP is not packaged into virus particles, and the precursor proteins cleaved by AVP remain in their immature forms [106, 107]. The absence of maturational proteolytic processing by AVP results in a hyper-stabilized capsid that is unable to properly disassemble and with a core of DNA and DNA-associated proteins that have not condensed and separated from the capsid as in mature AdV [108]. These mutant virions become trapped and are subsequently degraded in endolysosomes [108] or recycled out of the cell [9]. Ad2ts1 is therefore a valuable experimental system for investigation of many structural and functional aspects of AdV structure, maturation and replication [109, 110].

1.2.5 Replication cycle

An overview of the infection cycle of AdV is shown in Fig 1.4. The virus attaches to host cells via the C-terminal knob domain of the fibre protein [75]. Most HAdV species utilise the Coxsackie and Adenovirus Receptor (CAR), an integral plasma membrane protein usually sequestered in tight junctions, as a primary attachment receptor [111, 112], the exceptions being group B viruses and HAdV 26 of group D, which use CD46 and sialic acid, respectively [93, 113]. After attachment, an interaction between pentons and αvβ3/αvβ5 integrins promotes actin polymerisation and clathrin-mediated endocytosis [80, 114] or macropinocytosis [115]. This interaction is mediated by a highly conserved penton Arginylglycylaspartic acid (RGD) motif also present in cell adhesion proteins such as fibronectin [116]. Live cell microscopy studies and single virion tracking data indicate that the combination of CAR-fibre integrin-penton interactions and the resulting mechanical force results in the breakage of the weak fibre-penton connection and release of fibre from the capsid [117].

Studies on HAdV type 2 indicated that the virus traffics to early endosomes, where it was shown to colocalise with the early endosomal marker early endosome antigen 1 (EEA-1) and found less frequently in late endosomes or lysosomes [118, 119]. Further capsid disassembly takes place within the endosome, possibly enhanced by acidification. Loss of one or more penton bases results in subsequent loss of the peripentonal hexons and proteins IIIa, VI, VIII, and IX from the capsid within 15 min after internalisation [120, 121].

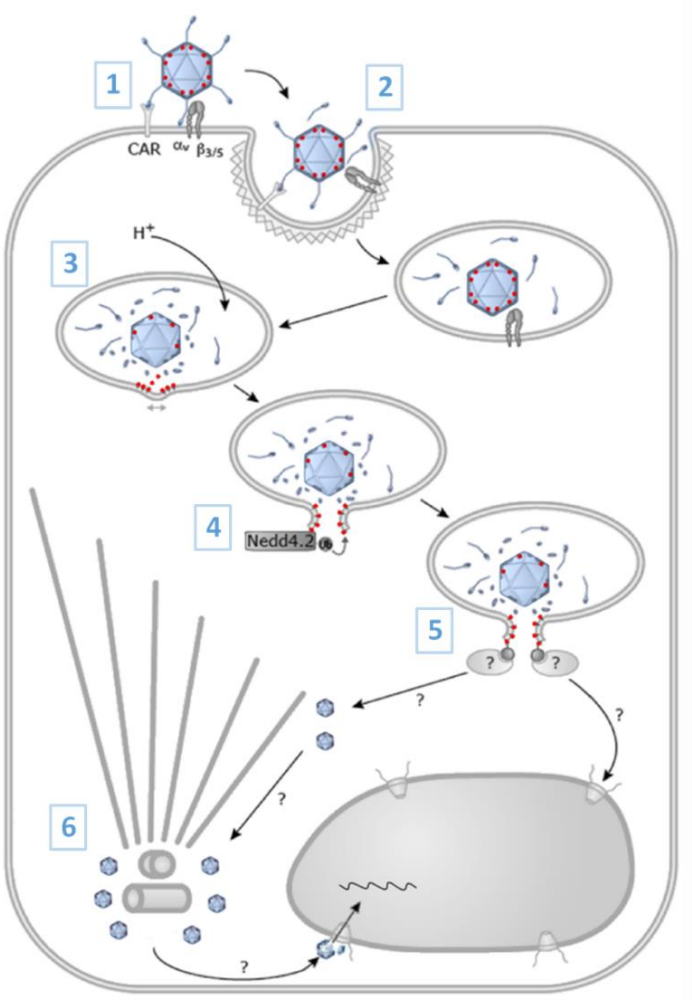


Figure 1.4 Adenovirus replication cycle.

1) attachment of fibre to CAR and interaction of penton with αvβ3/αvβ5 integrins. 2) internalization through endocytosis. 3) partial disassembly of the capsid and release of membrane lytic protein VI (red dots). 4, endosomal membrane rupture. 5) entry of capsid to the cytosol. 6) microtubule transport to the microtubule organising centre. 7) translocation through nuclear pore complex and import of the genome. Adapted from [122].

pVI is rapidly exposed after AdV entry to cells, as evidenced by antibody detection in cellular infection assays [123]. Exposure of internal capsid protein VI (pVI) results in endosomal

membrane lysis [124]. Liposome disruption experiments with purified hexon and pVI proteins revealed that hexon inhibits the membrane lytic activities of both pVI and its immature precursor, indicating that pVI must be released from the hexon cavity in order to exert its effect [125]. The structure and function of the pVI protein will be further explored in section 1.3. The process of separation from the membrane remnants that allows the capsid access to the cytosol is termed endosomal escape and occurs rapidly after internalisation [126]. The hexon then interacts with dynein motors for transport of the partially disassembled capsid along microtubules [127]. Like the majority of DNA viruses, AdV accumulate at the microtubule organising centre (MTOC) before translocation to the nucleus [123]. The effect of pH on endosomal disruption is unclear, since the interaction of pVI with membranes *in vitro* is pH-independent, but low pH is required for conformational changes in the hexon that are required for dynein recruitment [127, 128]. After exposure to the cytosol, pVI also recruits Nedd.2 ubiquitin ligases, key components of the cellular autophagic response, which results in the release of capsids from the endosomal membrane remnants [129]. This role of pVI in dissociation of the capsid from the endosomal membrane was found in a virus with a mutant pVI that stalls endosomal escape, and hence the capsid remains associated with the membrane [123].

Docking to the nuclear pore complex (NPC) requires an interaction between the nuclear localisation signal (NLS) of hexon and the nucleoporin Nup214, resulting in a final uncoating step and genome delivery to the nucleus [19, 130]. Transcription of the viral genome is

activated, and early regulatory proteins encoded by the E1A region of the genome are expressed, resulting in cell cycle deregulation and expression of another set of early genes: E1B and E2, E3 and E4. The E2 genes encode the AdV DNA polymerase (AdV Pol), DNA-binding protein (DBP) and the terminal protein precursor pTP, which acts as a DNA primer [131]. E1B, E3 and E4 encode genes that modulate the antiviral response, including prevention of the interferon response and apoptosis [132]. Viral DNA synthesis is initiated within a few hours of infection and approximately one million DNA copies are produced within 40 hours [133].

More than ten different proteins, as well as the viral genome, are required for correct assembly of an AdV infectious particle. Capsids are assembled in a highly-regulated pathway involving the viral proteins IIIa, IVa2, L1 52/55k, L4 33k and L4 22k [134]. Structural proteins are produced in the cytoplasm and must be imported into the nucleus. The C-terminus of pVI contains key nuclear import and export signals. Proteolytic cleavage of these C-terminal sequences by AVP during capsid maturation appears to trigger a functional transition in protein VI, from a role in supporting hexon nuclear import to a structural role in virus assembly. Crucially, nuclear localisation signals on proteins VI and VII facilitate transport of hexon through the NPC, aided by the recruitment of α and β importins by the C-terminal 11 residues of pVI. Assembly and packaging of viral DNA occur in a region known as the peripheral replicative zone to form non-infectious, immature capsids [135, 136]. AVP cleaves precursor versions of several capsid proteins to produce the mature capsid.

It is still unknown precisely how AdV leave the nucleus, but infectious particles are assumed to be released through autophagy-induced lysis of cells [137, 138]. Autophagy is a cellular process for targeting internalised or invading pathogens to lysosomes for degradation and processing of antigens for presentation to immune cells by major histocompatibility complexes (MHC) [139, 140]. Under certain conditions, autophagy can also trigger programmed cell death through the activation of caspases [141]. AdV-infected cells are more susceptible to lysis late in infection due to AVP cleavage of proteins involved in the cytoplasmic intermediate filament system [142]. Autophagy may have additional roles in the replication cycle, as autophagy was demonstrated to enhance AdV2 replication in airway epithelial cells [139]. Electron microscopy examination of AdVD24-infected cells also revealed excessive autophagosome formation that may result in destruction of the plasma membrane [142].

1.3 Adenovirus protein VI

The mature AdV pVI (CAP6_ADE05) possess all of the membrane lytic activity of the virion, but the mechanism of pVI endosome disruption is not fully understood [108]. The 250 amino acid precursor to pVI is cleaved by AVP, generating the mature pVI (residues 34–239) [143]. Both the precursor and mature forms of pVI have been reported to possess *in vitro* membrane lytic activity in liposome disruption assays [124]. The precise structural conformation of pVI in the context of the virus capsid and in solution is unknown. Earlier

circular dichroism (CD) spectroscopic analysis of purified pVI revealed that it contains around 25% α-helical structure, while the N-terminal domain (34–114) is around 85% α-helical and the rest predicted to be mostly disordered [124].

The N-terminal half of pVI has around 56% sequence similarity between HAdV types, highlighting the importance of this region [19, 108]. In comparison, the C-terminal half has around 18% sequence similarity, which may indicate that this section interacts with other capsid proteins in a type-specific manner [19]. Along with its role in endosomal escape, protein VI plays several other key roles in the AdV life cycle [144] , which are discussed in sections 1.2.5 and 1.3.6 of this thesis.

1.3.1 Domain architecture

Two elements of pVI have proven to be essential for endosomal rupture: the α-helical N-terminal domain and a PPxY motif, both of which are highly conserved [19, 119, 123]. Fig 1.5 illustrates the locations of the known functional motifs of pVI listed in Table 1.2. These include nuclear import and export signals and two highly conserved regions of mature pVI (48–74 and 233–239) that were determined by deletion mapping to be required for pVI interaction with hexon [145]. pVIn (residues 1–33) was also identified as an important region for controlling interactions with hexons outside of the capsid [144]. Most of pVIn was modelled within the hexon cavity in the cryoEM structure published by Dai et al. [76], shown in Fig 1.3.

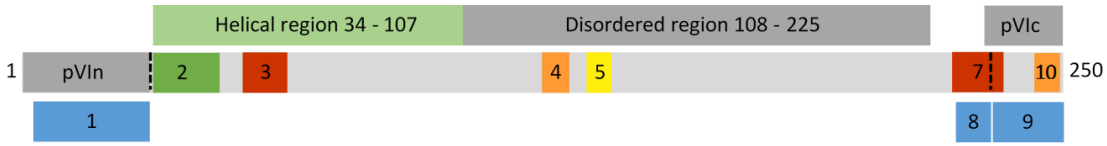


Figure 1.5 Domains and motifs of pVI.

Numbered boxes correspond to domains in Table 1.2. AVP cleavage sites (at residues 33/34 and 238/239) are indicated by dashed lines. Green, helical. Light blue, regions modelled within hexon. Dark blue, hexon interaction regions. Red, nuclear export signal. Orange, nuclear export signals. Yellow, PPxY motif.

Table 1.2 Domains and motifs of the AdV pVI protein

Adapted from the UniProt page for CAP6_ADE05 [146].

Domain #	Position	Description	Length
1	5 – 33	Interaction with hexon protein	29
2	34 – 54	Amphipathic α-helix essential for membrane lytic activity	21
3	48 – 74	Interaction with hexon protein	27
4	67 – 76	Nuclear export signal	10
5	131 – 135	Nuclear localization signal	5
6	148 – 151	PPxY motif	4
7	231 – 242	Nuclear export signal	12
8	233 – 239	Interaction with hexon protein	7
9	240 – 250	Binds to importin α/β, involved in hexon nuclear import	11
10	245 – 248	Nuclear localization signal, molecular sled.	4

PPxY motifs are consensus sequences for interaction with domains consisting of two conserved tryptophan residues (WW domains) common in many cellular proteins, including the HECT-domain E3 ubiquitin ligases of the Nedd4 family [147]. After partial capsid disassembly, Nedd4 is recruited by the the PPxY sequence between residues 147–150 of

pVI, which leads to the polyubiquitination of pVI [123, 148]. Recombinant Nedd4.2 was shown to bind directly to this motif and this is thought to have a role in translocation of capsid from the endosome to the cytoplasm, although this process is not fully understood [135].

Mutant viruses with PGAA in place of the wild type sequence (Ad5-M1) do not bind Nedd4 ligases and their pVI proteins are not ubiquitinated, which results in reduced intracellular targeting and a twenty-fold reducton in infectivity [123]. While mutation of the PPxY motif in Ad5-M1 does not affect membrane disruption, capsids are unable to fully translocate to the cytoplasm and remain associated with ruptured endosomes [123]. Experiments by Wodrich et al. found that while wild type Ad5 viruses efficiently accumulate at the MTOC, the Ad5-M1 viruses did not and were more evenly distributed throughout the cell [149]. These results suggest that the PPxY motif in pVI is also required for cytosolic trafficking of adenovirus capsids toward the MTOC [123]. Recent live-cell imaging in combination with biochemical experiments on components of the autophagosome system indicate that wild type AdV5 escapes autophagic degradation via the PPxY motif, and that parts of the autophagic response are required for endosomal escape and for efficient nuclear transport [129, 138]. PPxY motifs and similar proline-rich sequences have also been documented in proteins related to budding and release of several viruses, including the matrix proteins of the rabies and vesicular stomatitis viruses (VSV) [150, 151] and the VP40 protein of of filoviruses [152].

1.3.2 Capsid location of protein VI

Early biochemical experiments by Everitt and colleagues indicated that pVI was released from within the capsid and was found to be associated with the hexon protein [93, 153]. The interaction of cleaved pVIn with the interior of the mature hexon interaction was confirmed by hydrogen-deuterium exchange mass spectrometry-based experiments [154]. In the first cryoEM structure of Ad2, pVI was proposed to be located underneath the peripentonal hexons in intact virions, existing as a trimer of dimers [155]. This assignment was supported by the XRC structure of a chimeric Ad5 from Reddy and Nemerow [78] and cryoEM work focused on finding the defect of Ad2ts1 by Silvestry et al. [109], who identified a density within every hexon that was tentatively assigned as preprotein VI [125]. In later cryoEM structures, well-ordered densities were associated with all hexons [77, 79, 136].

Recent cryoEM and crystallographic studies have found weak, fragmented densities within the hexon cavity thought to correspond to part of pVI [83, 90, 156]. Two papers reported the assignment of different partial fragments of pVI [76, 77]. In one model, only the N-termini of pVI (pVIn), which are cleaved from the mature protein, were identified along with their binding sites in the hexon [77]. Two copies were identified in some hexons while 3 weak densities were identified in the three central hexons in a facet (Figure 1.3C, H3), indicating uneven occupancy of pVI that may explain the weak or missing density in previous models [77]. The most recently published cryoEM model by Dai et al. is presented in Figure

1.6, with the densities modelled within the hexon cavity that were assigned to fragments of pVI [76].

The structural model in Fig 1.6 presents previously unseen pVI helical motifs within the hexon cavity, including the cleaved 33-residue pVIn fragment. Ile25 and Ser31 were identified to bind a hydrophobic pocket formed from two adjacent hexon subunits [76]. The model also indicates a small central fragment of mature pVI between residue 109 and 143, close to the opening of hexon-2 [76]. A disordered segment of pVI (residues 109 to 143) crosses the opening of the cavity of each hexon (Fig 1.6, bottom). Disordered densities deeper in the hexon that could represent the rest of pVI, possibly indicating flexibility of the N-terminal region prior to disassembly [76, 77].

Due to the lack of full density modelled for pVI (Fig 1.6), it is unknown how molecules of pVI interface within the hexon cavity. The substitution of a single Cys residue (AdV-VI-G48C) within the N-terminal AH of pVI was found to result in altered capsid stability that impairs pVI release due to the formation of additional disulphide bonds between pVI molecules, suggesting that certain copies of pVI within the hexon must be in close enough proximity to form dimers [157, 158]. While no potential oligomerisation-mediating sequences have been identified in wild type pVI, these findings suggested the possibility of pVI dimer formation within the capsid or the existence of different oligomeric states of pVI depending on which of the four structurally distinct hexons was occupied [157].

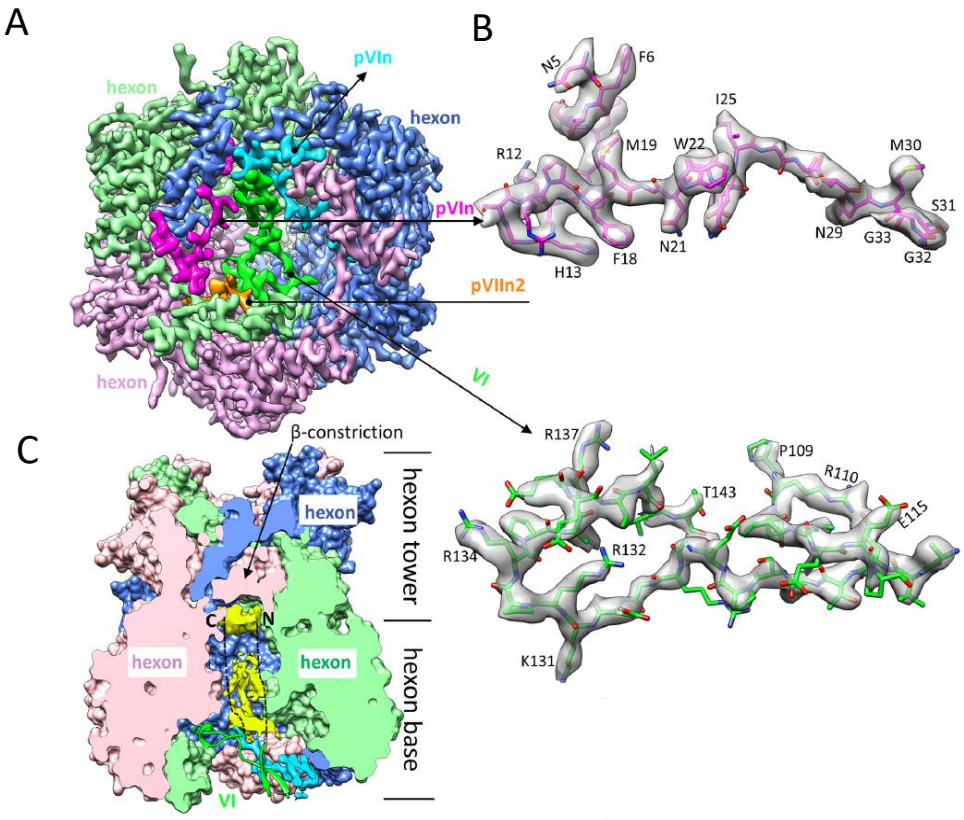


Figure 1.6 Modelled densities of pVI within the AdV hexon.

(A) Interior view of hexon H2, containing two copies of pVIn. The location of this hexon corresponds to hexon 2 in Fig 1.3C. The subunits of the hexon trimer and minor proteins are differentially coloured. Mature pVI, green. pVIn, cyan or magenta. pVIIn2, orange. (B) Atomic stick models of pVIn and VI fitted to their corresponding cryoEM densities, with some landmark residues labelled. Only one of the two equivalent copies of pVIn is shown. (C) Location of pVI and disordered densities hidden deeply in the cavity of hexon H2. The surface presentation of the hexon was calculated by use of atomic models of the hexon trimer, and one half was removed to expose the inner cavity of the hexon. Disordered densities (yellow) in the cavity were segmented from the cryoEM density map. A model of protein VI (green ribbon) crossing the opening of the cavity is also shown. The two dashed lines denote that the disordered densities are speculated to be attributable to the unmodeled N- and C-terminal regions of protein VI. Adapted from reference [76].

It is still unclear how pVI is released during disassembly and how AVP gains access to the N-terminal region of pVI, which is partially buried inside the hexon trimer [76, 159] . If the N-terminal AH is sequestered deep within the hexon as the newer models suggest, this would appear to hinder interaction of AVP during capsid maturation. Dai et al. also suggested from their model that competitive binding between pVIn and pVIIn for the three binding sites in each hexon might facilitate release of pVI during disassembly [76] This possibility has been supported by recent data from a pVII deletion mutant virus that is unable to escape the endosome due to higher occupancy of hexon bindings sites, resulting in pVI not being released [160]. The pVII competition model may also explain how pVI can have such varied functions at different stages of the AdV infectious cycle [160].

1.3.3 Copy number of protein VI

While it has been established that pVI resides within the hexon cavity in the mature wild type AdV capsid, various estimates of the capsid copy number of protein VI have been published, ranging from ~342 to 480 copies [77, 93]. Each hexon can accommodate a total of 3 copies of pVI, translating to a maximum number of 720 per capsid. However, most estimates of copy number based on structural analysis [76, 83, 125] and early biochemical studies [93, 161-163] have suggested copy numbers between 342 and 420 copies. Estimates of 340-369 are too low for one molecule of pVI to occupy each of the hexon monomers (720 copies), but too high for one pVI molecule per hexon trimer (240 copies) [86]. The estimated

pVI copy number varies between one copy per peripentonal hexon and three copies per hexon and may also differ between AdV types and depending on the treatment of viruses.

The first estimate of pVI copy number was performed by Everitt et al., who analysed disrupted Ad2 capsids and performed stoichiometric analyses of protein copy numbers using separation of extracted polypeptides on polyacrylamide gels followed by radiolabelling and scintillation counting of polypeptides [93]. The copy numbers were then estimated by dividing against the sequence of the adenovirus type 2 genome to determine the number of methionines in each polypeptide. The copy number of pVI was estimated at around 342 copies using this method [164]. Van Oostrum et al. later performed similar studies and agreed on a copy number of ~342 [161]. Further quantification of AdV5 structural proteins was performed by reversed-phase high-performance liquid chromatographic assay (RP-HPLC) and produced an estimate of ~369 pVI molecules per capsid [162]. Further mass spectrometry studies using improved quantitative proteomics were performed by Benevento et al. and found only slightly reduced copy number of pVI at ~359 [163].

Estimated copy numbers of pVI from XRC or cryo-EM studies have varied due to the lack of strong density present for mature pVI and the incorrect assignment of other minor proteins [77]. Estimates also depended on where the protein was assigned within the 3D model.

Incorrect assignment of pVI to only the peripentonal hexons resulted in low copy number estimates of ~180 [78, 154]. In the first cryoEM models of HAdV 2 [90] and 5 [125], the estimated copy numbers of pVI were similar, at around 369, both assigning the densities within the internal hexon cavities. However, the XRC model of heated virions of Ad5F35 confirmed the sequestration of pVI inside hexon cavities, but estimated the pVI copy number at ~180 based on the occupancy of pVIn-binding sites in released hexons [78]. This treatment may simulate the partially disassembled capsid and indicate that not all pVI copies are lost after uncoating within the endosome [78, 154]. Additionally, enforcing icosahedral symmetry while modelling the capsid interior may have resulted in the blurring of densities within the hexon cavities, resulting in different estimates [86]. Therefore, it seems likely that there is partial occupancy of the 720 possible binding sites for protein VI. The competitive binding of pVIn and pVIIn2 may also explain the differing estimates in copy numbers of pVI [76, 160].

It is unknown how many molecules of pVI are required for successful endosomal lysis and AdV infection. Having a higher pVI copy number could confer an advantage as it might significantly increase the chances of endosome lysis, while also potentially increasing the risk of damaging other intracellular membranes and inducing cell death. Studies of the ts1 mutant indicate that mature wild-type AdV virions release ~80% of penton base, ~25% of the hexons and ~80% of pVI from the AdV capsid up to temperatures of 45°C, while in Ad-ts1, pVI remains associated with the immature core even at ~60 °C [108, 109]. If all pVI

copies were released during disassembly and prior to endosomal escape, few if any would be available for the later transport and assembly functions. The close proximity of pVI molecules and potential oligomerisation within the hexon may explain the simultaneous release of a high percentage of this protein while leaving some copies of pVI remaining within the partially disassembled capsid [109, 143].

1.3.4 Amphipathic helices

The first N-terminal 20 residues of post-processed, mature pVI (residues 34–54 using the full protein numbering) are predicted to form an amphipathic α-helix, a common protein motif that demonstrates segregation of hydrophobic and polar residues between the two faces of the helix [108, 165]. Many amphipathic helices (AH) have been recognised in proteins with a variety of functions, including membrane curvature sensing and induction [104, 105]. Several key physicochemical properties are used to study how the sequences of an AH influence their roles in lipid membrane binding and perturbation. The hydrophobic moment is used to determine whether a predicted helical sequence exhibits hydrophobic polar faces. This together with the hydrophobicity (H) and the net charge (z) values has been instrumental for studying membrane-interfacial and pore-forming peptides [166]. AH typically have positive net charge and many are in a random coil conformation in solution but fold upon binding to lipid membrane to form an α-helix [165]. CD studies have indicated that recombinant pVI and pVI-34-114 are unfolded in the absence of lipids [19].

Membrane lytic activity is absent in an AdV deletion mutant lacking the N-terminal AH (Ad5-VI-Δ54) [108]. Random mutation of the adenovirus genome resulted in the identification of a point mutation in the N-terminal helix that *in vitro* significantly reduced membrane lytic activity, L40Q [124]. Confocal microscopy experiments demonstrated that viruses with this mutation were impaired in endosomal escape, and infectivity in cell culture was reduced tenfold. [19]. It was determined that the reduced membrane lytic activity was due to reduced insertion of the mutant protein into membranes [19]. 98% of sequenced AdV contain an aliphatic residue at position 40 (Leu 45%, Ile 30%, Val 23%), suggesting that hydrophobicity at this position is important for insertion of the helix [19]. The different physical and chemical properties of the N-terminal domain with the L40Q mutation are compared to the wild type in Figure 1.7 and Table 1.3. The N-terminal helix of pVI-L40Q has the same net charge, but a lower hydrophobic moment than the helix of the wild type. L40Q has one fewer hydrophobic residue, resulting in a less hydrophobic face.

Amphipathic helices are proposed to bind to membranes in three thermodynamic steps. The first is the formation of electrostatic interactions between negatively charged membranes and the positively charged unfolded peptide sequence. Secondly, the entropy of the hydrophobic effect drives the insertion of hydrophobic side chains between the lipid acyl-chains and water molecules are released. Finally, the coil transitions to α-helix conformation to reduce the energy penalty of exposed peptide bonds in a hydrophobic environment, which accounts for 50–60% of the free energy of binding [165, 167].

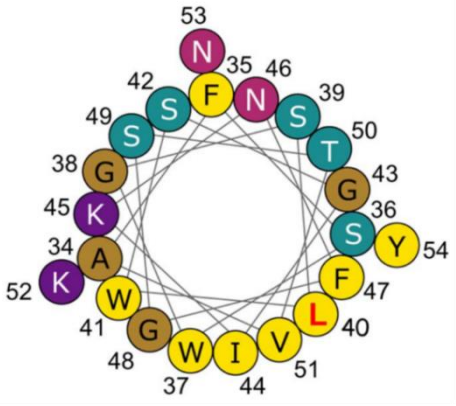


Figure 1.7 Helical wheel projection of Adenovirus pVI wild-type N-terminal helix (positions 34–54). Residue 40, mutated in the L40Q mutant, is coloured red. Colour code for amino acids: yellow, hydrophobic. Purple, basic. Green, Ser and Thr. Magenta, Asn. Brown, Ala and Gly. Figure from reference [168].

Table 1.3: Physical and chemical properties of AdV5 pVI wild type and L40Q pVI N-terminal helices.

Helical sequences were analysed using heliquest [169].

Property	**Wild type**	**L40Q mutant**
Hydrophobicity <H>	0.551	0.539
Hydrophobic moment <μH>	0.431	0.327
Net charge z	2	2
Polar residues	57.11%	61.11%
Nonpolar residues	42.86%	38.89%
Uncharged residues and GLY	Gln 1, Ser 4, Thr 1, Asn 1, Gly 3	Gln 2, Ser 4, Thr 1, Asn 1, Gly 3
Charged residues	Lys 2	Lys 2
Aromatic residues	Trp 2, Phe 2	Trp 2, Phe 2

The N-terminal domain was predicted to contain three additional amphipathic helices [124, 143]. The free energy change associated with spanning the lipid membrane interface, Δ_{Gif}, was predicted for these helices and negative values were calculated for each, suggesting that all of the helices would spontaneously associate with membranes [143]. However, the value for the first N-terminal AH was larger than that of the other three helices, indicating a greater contribution in the interaction of pVI with membranes [143].

1.3.5 Predicted mechanism of membrane rupture

Disruption of endosomal membranes allows AdV to travel toward the nucleus and avoid lysosomal sorting. The N-terminal amphipathic helix (section 1.3.4) of mature wild type pVI was identified as the membrane lytic factor of the AdV capsid [108]. The interaction is known to be pH-independent *in vitro* but it is unknown if the low pH of the endosomal compartment has any effect on pVI activity within cells [108]. The research groups of Christopher Wiethoff and Harald Wodrich performed many of the experiments that identifed the mechanism of AdV pVI [19, 108, 123, 124, 143].

Maier et al. performed fluorescent liposome leakage assays on different recombinant pVI constructs to compare their membrane-lytic activity [124]. They also used fluorescence microscopy to observe giant unilamellar vesicles (GUV) and purified wild type pVI, which resulted in fragmentation of vesicles into tubules [143]. Furthermore, Maier et al. used intrinsic tryptophan fluorescence quenching to determine the membrane insertion depth

of tryptophan residues of various mutant pVI constructs into the membrane. Shallow insertion of residues into the polar region of the bilayer expands the polar lipid headgroups most, resulting in localised positive membrane curvature, while deeper insertion causes expansion of both the lipid headgroups and hydrocarbon chains and results in less curvature generation [124]. These results suggested that the helix adopts a parallel orientation and inserts shallowly into the bilayer [124, 143] and that the L40Q mutation reduced insertion into the membrane and lowered endosomal rupture [19]. Furthermore, a peptide composed of residues 34–54 showed a greater affinity for smaller liposomes with higher curvature [152]. Maier et al. therefore proposed a model in which the hydrophobic face of the N-terminal α-helix inserts into the membrane, resulting in positive curvature induction and disruption of the lipid bilayer, illustrated in Fig 1.8 [124, 143].

The N-terminal AH fits the criteria defined by Drin et al. for identifying features of helices with sensitivity to membrane curvature, based on the amphipathic lipid packing sensor (ALPS) motif of ArfGAP1 and its homolog in yeast, Gcs1p [165]. The primary sequences of these helices all contain seven or more Ser, Thr and Gly residues on the hydrophilic face, up to three Arg, Lys and Asp residues, and have a net charge between –1 and +2 [165]. The N-terminal AH of pVI shares these properties (Table 1.3). The polar face of the helix also contains two lysine residues, a feature found have been helices that sensors membrane curvature [144].

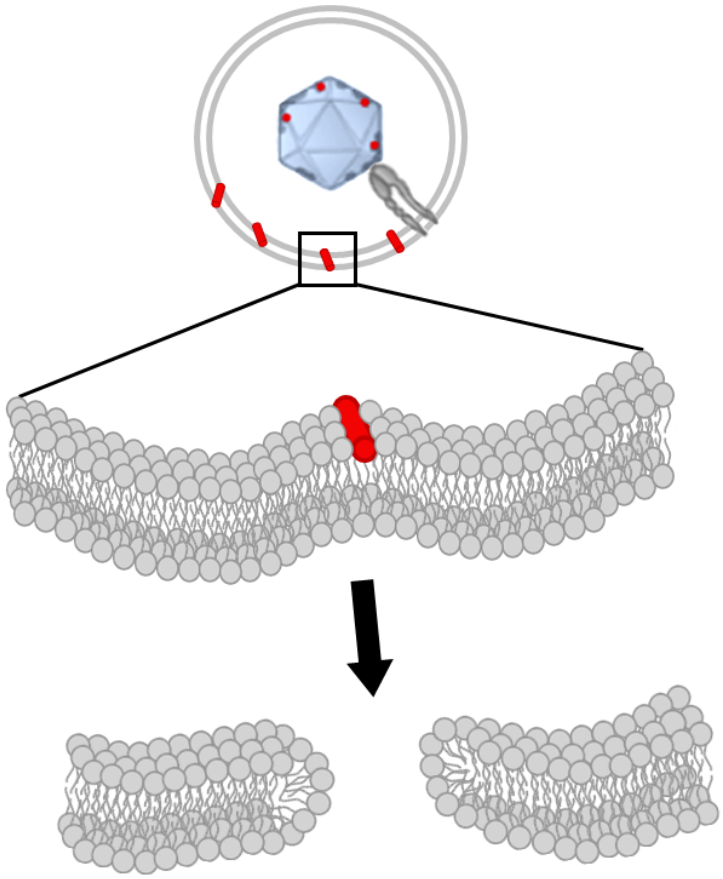


Figure 1.8 Proposed model of membrane rupture by AdV pVI.

AdV capsid (blue) partially disassembles after endocytosis to release pVI molecules (red cylinders). The N-terminal amphipathic helix of pVI is predicted to insert shallowly into the bilayer and induce curvature induction and membrane rupture, allowing the capsid to escape into the cytosol. Adapted from reference [170].

The N-terminal helix of pVI bears similarities to amphipathic helices of class I viral fusion peptides, including the presence of several glycine residues and aromatic or aliphatic residues [108]. It also bears similarities to helical motifs of proteins which induce positive membrane curvature, such as the the N-BAR (Bin, amphiphysin, Rvs) domain, found in

amphiphysin, endophilins, and a wide variety of other proteins. Several BAR domains also present an N-terminal sequence that forms an AH upon membrane binding. These domains dimerise to produce a positively charged concave surface that induces tubulation. [165, 166].

1.3.6 Additional roles of pVI in the Adenovirus replication cycle

AdV Protein VI is known to be multi-functional, and several roles have emerged aside from its most established role in endosomal escape. The role of pVIc as a substrate and cofactor for AVP during capsid maturation is covered in section 1.2.4 and the role of the PPxY motif in intracellular targeting is covered in section 1.3.1. The first N-terminal AH of pVI also has a role in capsid stability by preventing premature disassembly and loss of pentons, which ensures that the virus escapes at the appropriate time to prevent sorting into lysosomes [148]. The pVI-L40Q mutant virus is thought to have lower infectivity *in vitro* due to greater instability in the capsid which results in penton release before attachment to cells [148], further demonstrating the importance of pVI in capsid structure.

pVI has overlapping roles in promoting the initiation of early viral gene expression and in host immune response modulation through repression of Daxx, a cellular transcriptional repressor [171, 172]. Daxx associates with chromatin and a macromolecular structure called

the promyelocytic leukaemia protein nuclear body (PML-NB), involved in control of apoptosis [171]. Schreiner et al. proposed that upon entering the nucleus, the PPxY motif of pVI associates with Daxx and displaces it from PML-NBs, which prevents antiviral apoptotic processes [172]. The N-terminal AH of pVI was also identified as a PML-NB targeting domain, and contributes to intranuclear targeting of protein VI [172]. Counteracting Daxx is also necessary for the efficient initiation of AdV gene expression by activating the E1A promoter, a crucial transcriptional AdV early protein E1B-55K, a multifunctional regulator of cell-cycle-independent Ad5 replication [171]. Gene expression of other DNA viruses, such as human papillomavirus (HPV), human cytomegalovirus (HCMV) and herpes simplex virus (HSV-1) is also repressed via the PML-NBs, suggesting a role in antiviral defence [173-175].

Finally, pVI contains both nuclear import and export signals in its C-terminus (Fig 1.5), which enable it to shuttle between the cytoplasm and nucleus [123]. Structural proteins such as the hexon are produced in the cytoplasm and must be transported to the nucleus for capsid assembly [176]. pVI forms a complex with hexon in the cytoplasm and then recruits importins α and β to promote translocation through the NPC [123]. Wodrich et al. reported the conversion of pVI from an adapter for transport of proteins to the nucleus to a structural component of the capsid during assembly [176]. AVP was found to remove C-terminal transport signals from pVI, which increases pVI affinity for hexon and switches the functionality of pVI from supporting hexon import to a structural role in virus assembly [82].

1.4 Objectives

While membrane curvature is understood to have an important role in pVI function, the mechanism of membrane perturbation by mature AdV protein VI is not fully understood. The objective of this project was to explore the nature of interactions between highly purified pVI and model membranes using various complimentary techniques. The other recognised functions of pVI, explored in section 1.3.6, are not within the scope of this thesis. The following constructs will be used and are illustrated in Figure 1.9. Constructs 1–3 contain an N-terminal polyhisitidine tag for affinity purification.

1. pVI-WT
2. pVI-L40Q, which has a point mutation in the N-terminal AH.
3. pVI-Δ54, which lacks the whole N-terminal AH sequence.
4. pVI-34-54, a peptide corresponding to pVI amino acids 34-54, comprising the entire N-terminal AH, as described in [168]. Sequence: acetyl-AFSWGSLWSGIKNFGSTVKNYG-amide.

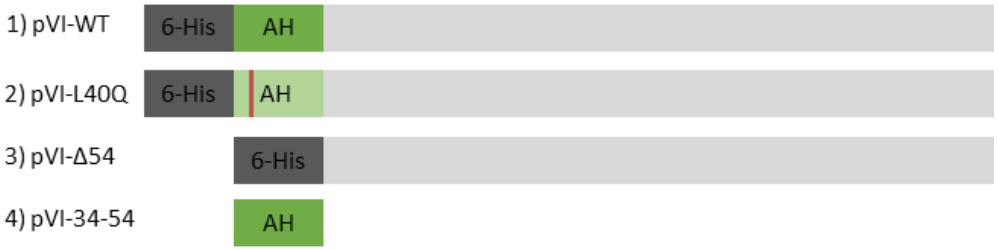


Figure 1.9 pVI constructs used in this project.

6-His, polyhistidine tag. AH, N-terminal amphipathic helix. Red bar, approximate location of the L40Q mutation.

The project was focused on three areas:

1. Expression and purification of recombinant pVI-WT and mutants.

Purification protocols exist for recombinant pVI, but previous studies have only obtained small amounts of protein and the preparations used to characterise pVI showed remnants of other co-purified proteins. Therefore, an optimised protocol for purification of wild type pVI (pVI-WT) is required in order to study its properties unambiguously. This protocol can then be adapted for purification of the two recombinant mutant pVI constructs. Any differences in the behaviour of the mutant proteins compared to the wild type may provide further details about their characteristics. Disordered proteins are generally challenging to work with, so the largely unstructured nature of pVI will have to be considered in handling samples. pVI-WT is also lytic to membranes, which poses an additional technical challenge for optimisation of expression protocols. Initial protein samples and plasmids coding for the various constructs were provided by the group of Harald Wodrich at the University of Bordeaux.

2. Biophysical characterisation of pVI with and without model membranes.

Secondary structure and disorder predictions have been published, but will be performed using the updated versions of several servers. While some circular dichroism (CD) has been performed to characterise the secondary structure of pVI-WT and pVI-L40Q, little is known about the oligomeric state of pVI, and this can be examined using analytical ultracentrifugation (AUC).

Interactions of the constructs with membranes will be explored using unilamellear liposomes, artificial spherical vesicle structures formed of single lipid bilayers enclosing an aqueous volume [177]. Liposomes are widely used as vehicles for drug delivery and as model membranes, which has provided insights into the physiology and biochemistry of plasma membranes and the membranes of different biological compartments [178]. Using unilamellar liposomes allows the straightforward identification and quantification of interaction events as compared to the crowded environment of the cytosol.

The nature of pVI interactions in a minimal *in vitro* system will be explored using dynamic light scattering and an indirect assay to assess the ability of the recombinant pVI constructs to facilitate membrane disruption by monitoring the release of an entrapped fluorescent dye (SulfoB) from liposomes. The combined data from these experiments will provide further insights into pVI-membrane interactions.

3. Observation of the interaction of pVI with membranes using cryoEM and tomography.

The interaction between pVI and membranes has not been studied using cryoEM. While recombinant pVI itself will not be visible in cryoEM due to its small size (~25kDa), it is possible to observe the effect of the protein on lipid membranes. CryoEM and electron cryo-tomography (cryoET) will be employed to visualise the nature of membrane attack to gain further, more specific, insights into the mechanism of pVI. CryoEM will enable the

quantitative analysis of pVI-membrane interactions captured in projection images. These events can be categorised by the type of membrane morphology observed, such as liposome distortions or formation of openings and membrane fragments. The types of interactions exhibited by pVI-WT and the mutant constructs can then be compared to identify morphological classes unique to, or more common with, particular constructs.

Details from previous experiments provide a basis for the types of interactions that may be found. Maier et al. reported from fluorescence data that pVI-WT tubulates membranes of GUVs, while pVI-34-54 displays membrane effects without tubulation [113, 126]. CryoEM is able to visualise the same interactions with greater resolution. CryoET will enable individual liposome disruption events to be captured in three-dimension. Together, these experiments will provide further molecular details of pVI-membrane interactions. This information could then be applied to the enhancement or attenuation of cell entry of HAdV vectors and provide a better basis for engineering of artificial cell delivery vehicles [113].

Chapter 2 Expression and purification of recombinant Adenovirus wild type pVI and mutants

2.1 Introduction

The objective of this project was to characterise pVI and investigate the mechanism of membrane disruption. In order to conduct these experiments, an efficient over-expression and purification method needed to be developed for wild type pVI and the mutant pVI constructs pVI-L40Q, which has a single point mutation, and the truncation mutant pVI-54. Earlier, Harald Wodrich's group at the University of Bordeaux had started to develop a protocol for expression and purification of recombinant pVI-WT using a pet15b vector in *Escherichia coli* BL21 (DE3) using IPTG-induced T7 promoter-driven expression [1]. The construct contains a 6-His tag at the N-terminus (Fig 1.7).

Plasmids encoding pVI-WT and the mutant pVI-Δ54 were provided by the Wodrich group, along with a small amount of the recombinant pVI-WT and pVI-L40Q proteins purified according to a protocol developed by Ruben Martinez [122]. pVI-WT was found by Martinez to be toxic to bacterial cells, as observed by monitoring the optical density (OD) at 600 nm, which stops increasing after 1 hour of induction followed by reduction in OD [122]. Therefore, Martinez et al. expressed protein for only 45 minutes in high-density cultures (>OD 0.8 at 600 nm), and complemented their growth media at the time of induction by addition of NaCl to a final concentration of 150 mM to balance osmotic pressures and limit

the lysis of bacteria [122]. In their hands, pVI-Δ54 did not appear to have the same toxicity as pVI-WT in *E. coli* (Harald Wodrich, personal communication), but the effect of pVI-L40Q was unknown. They released protein from harvested cells by detergent lysis combined with sonication, followed by affinity purification and further separation from contaminants using size-exclusion chromatography (SEC).

Purified pVI-WT samples provided by Wodrich et al., prepared in reducing sample buffer, contained two bands of approximately 32 (Fig 2.1, top black arrowhead) and 28 kDa (bottom black arrowhead) on a SDS-PAGE gel, higher than the theoretical weight of 24.8kDa, along with several additional bands (Fig 2.1A), which was consistent with previous observations by their group [122]. The pVI-L40Q sample contained one main band (Fig 2.1, yellow arrowhead) of ~28 kDa along with several contaminant bands.

Although these protein preparations were previously used for preliminary in vitro experiments with model membranes [124, 143], supply of these was limited to less than 200 µl. More importantly, the presence of contaminant proteins precludes interpretation of many experiments, as observed effects cannot be linked to a specific protein. Therefore, it was necessary to obtain preparations of wild-type and mutant pVI proteins with greater yield and with improved purity.

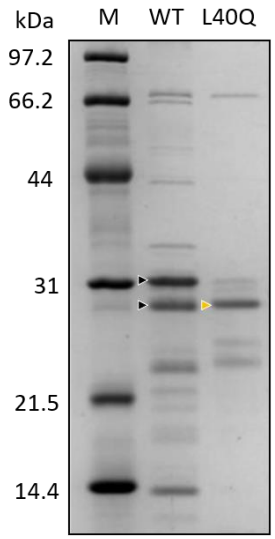


Figure 2.1 Preliminary purification of pVI-WT and L40Q by Wodrich et al.

(A) Coomassie stained 12% SDS-PAGE gel of pVI proteins. M, low molecular weight marker. pVI-WT at approx. 0.35mg/ml. Black arrowhead, pVI-WT upper and lower bands of interest. pVI-L40Q at approx. 0.25 mg/ml. Yellow arrowhead, pVI-L40Q band of interest.

The cause of the lower band in the doublet is unclear and could be the result of protein degradation by bacterial proteases. The possibility of translation interruption due to lack of certain codons in *E. coli* was ruled out by Martinez by comparing expression of the BL21 (DE3) and Rosetta (DE3) strains. This Rosetta strain is a derivative of BL21 that co-expresses genes encoding tRNAs rarely used in *E. coli* to enhance eukaryotic protein expression. Rosetta has been found to improve the yield and purity of some expressed recombinant proteins [179]. Yield of pVI-WT was similar between the two strains, but this Rosetta strain was used in further experiments [122].

Several approaches were used to optimise expression and purification of WT pVI and its mutants for biophysical characterisation and analysis using electron microscopy techniques. These approaches are described and discussed in this chapter. The toxicity of pVI-WT in *E. coli* and the inherently disordered nature of pVI-WT posed a challenge for further purification. In particular the C-terminal portion may be prone to proteolytic degradation. This can be reduced by including protease inhibitors after induction of protein expression.

2.2 Optimisation of pVI-WT expression and purification

2.2.1 Preliminary experiments

Preliminary expression and affinity purification experiments were carried out according to the protocol received from Wodrich et al. with small cell volumes (0.5–1 L) induced with 1 mM IPTG for 45 minutes. Cells were pelleted, resuspended, and lysed in 20 mM phosphate, 150 mM NaCl purification buffer with Tween-20 and lysozyme. Released protein was bound to cobalt charged Sepharose chromatography resin and eluted with imidazole. The fractions collected from the affinity purification of 0.5 L of culture were analysed using SDS-PAGE (Fig 2.2A, top panel) and Western blot analysis using an anti-His antibody (bottom panel).

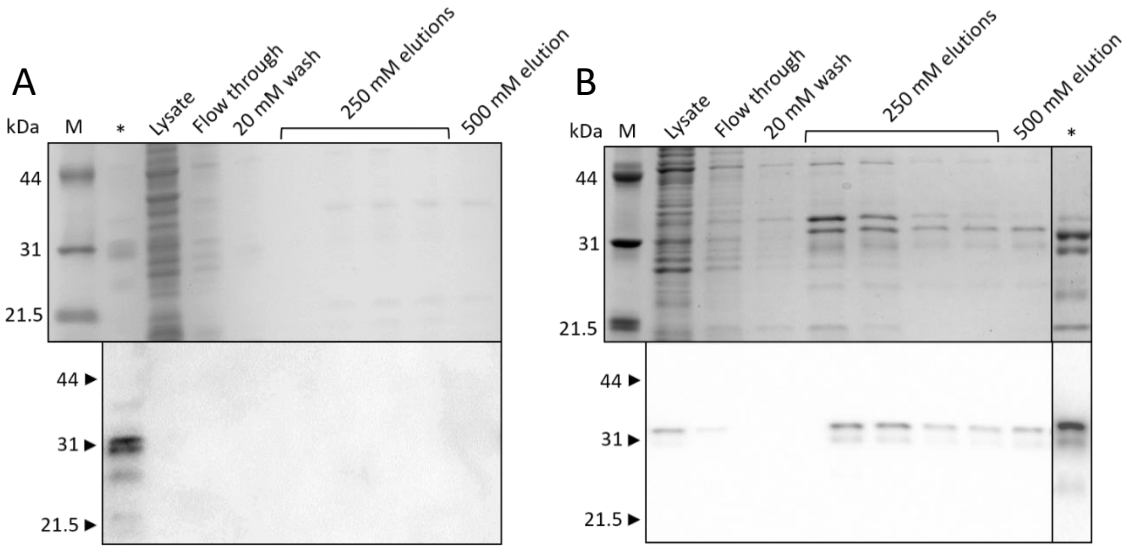


Figure 2.2. Results of small-scale affinity purification experiments using Triton X-100 lysis buffer.

(A) 0.5L culture. (B) 1L culture. Washes and elutions were carried out with PBS + concentration of imidazole stated in labels. Top panels, Coomassie stained 15% SDS-PAGE gels. Bottom panels, Western Blot with anti-His antibody. Asterisks, reference pVI-WT from Wodrich et al. M, low molecular weight marker.

The results showed that early small-scale experiments of 0.5 L of culture yielded no protein (Fig 2.2A). After a fresh transformation of the pVI constructs into Rosetta cells, 1 L of culture yielded some pVI-WT, but less than expected compared to the protein provided by Wodrich et al., as judged by visual inspection of SDS-PAGE gels. The apparent molecular weight of the newly expressed protein was similar to that of the protein from Wodrich et al., but additional bands of varying sizes were observed in Fig 2.2B, particularly in the first protein elutions. The yield of protein from 1L of bacterial culture (0.2–0.5 mg/ml) was unsatisfactory and Western blotting revealed that some of the pVI protein did not bind cobalt-charged

resin and was present in the flow-through from the column (Fig 2.2B). Therefore, it was necessary to optimise expression conditions for pVI-WT.

2.2.2 Optimisation of expression

Various factors were explored in order to increase the amount of pVI-WT expression in Rosetta (DE3) cells, including the post-induction temperature, length of the induction period and final concentration of IPTG. Western blots of whole cell fractions expressed under different conditions are compared in Fig 2.3.

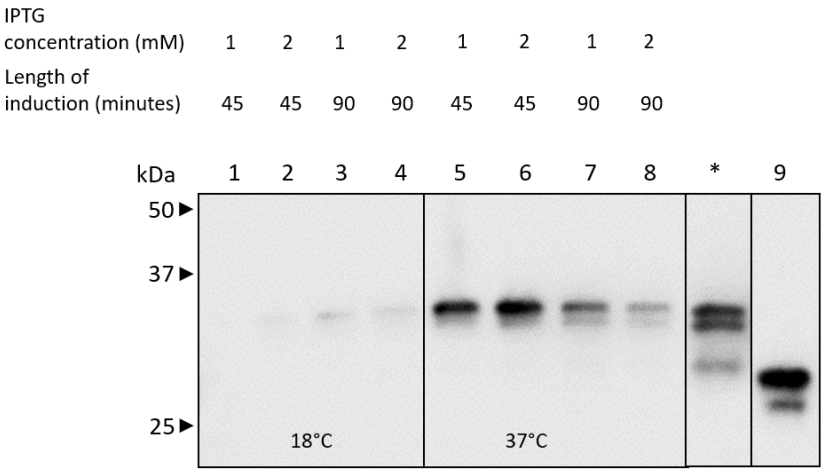


Figure 2.3 The effect of IPTG concentration and temperature on expression levels of pVI-WT in Rosetta (DE3) cells.

Western Blot of whole cell extracts with anti-His antibody. Asterisk, reference pVI-WT from Wodrich et al. Lane 9, His-tagged Herpes simplex virus protein UL34 (positive control). Protein markers based on Dual colour standards.

Considerably more protein was expressed when cells were incubated post-induction at 37°C than 18°C (Fig 2.3). As well as increasing activity of the bacterial polymerase, protein expression at higher temperature may reduce aggregation of the expressed pVI protein. While two protein bands reacted with the anti-His antibody in all samples at 37°C, extending the expression period past 45 minutes resulted in reduced intensity of the upper band (Lanes 7 and 8), suggesting increased degradation of pVI-WT. Doubling the IPTG concentration to 2 mM (Lane 6) resulted in an increase of protein in the upper band. The optimal conditions found for pVI-WT expression were 2mM IPTG for induction and a 45-minute expression period. These conditions were used subsequently for pVI-WT experiments.

2.2.3 Optimisation of cell lysis and protein solubilisation

The previously observed toxic effect of pVI on *E. coli* cells is attributed to the N-terminal amphipathic helix (AH) of pVI. This helix interacts with membranes *in vitro* in a way that is not yet fully understood, but the protein could remain associated with fragments of membrane. Therefore, approaches used for purification of integral membrane proteins were considered, including the use of detergents, which can be used to solubilise lipid bilayers and incorporate proteins in detergent micelles. Methods of detergent removal from protein samples vary depending on the molecular weight of the detergent, and these must also be taken into consideration.

The protocol prepared by Wodrich et al. utilised BugBuster protein extraction reagent (Novagen), a mixture of detergent and proprietary lysis reagents that were not explicitly stated by the manufacturer. Therefore, we aimed to produce a protocol with more control over the reagents used. The base purification buffer for early experiments was 20 mM phosphate, but this was changed to 20 mM Tris due to the tendency of phosphate to precipitate with negative stain. A higher salt concentration (300 mM) was used to reduce the potential for protein aggregation. After incubation with the purification buffer containing detergent, cells were sonicated and centrifuged to separate un-lysed cells and cellular debris. The cleared lysate was then applied to Sepharose Co^{2+} resin for immobilized metal affinity chromatography (IMAC).

The solubilisation of protein released from cells was an important factor in optimisation of the purification protocol. A small-scale purification experiment was set up to screen different detergents for their potential to release pVI-WT from membranes and increase final yield. A 1 L culture was split into 5 aliquots and each was lysed in buffer containing lysozyme and one detergent at a concentration approximately 10 times the critical micelle concentration (CMC). One aliquot was lysed using only lysozyme as a control. Detergents were chosen from different categories: non-ionic (Triton X-100 and Tween-20), and zwitterionic (CHAPS and Empigen BB). Lysates were then applied to Cobalt-bound affinity purification resin and protein eluted as in previous experiments. The results are shown in Fig 2.4.

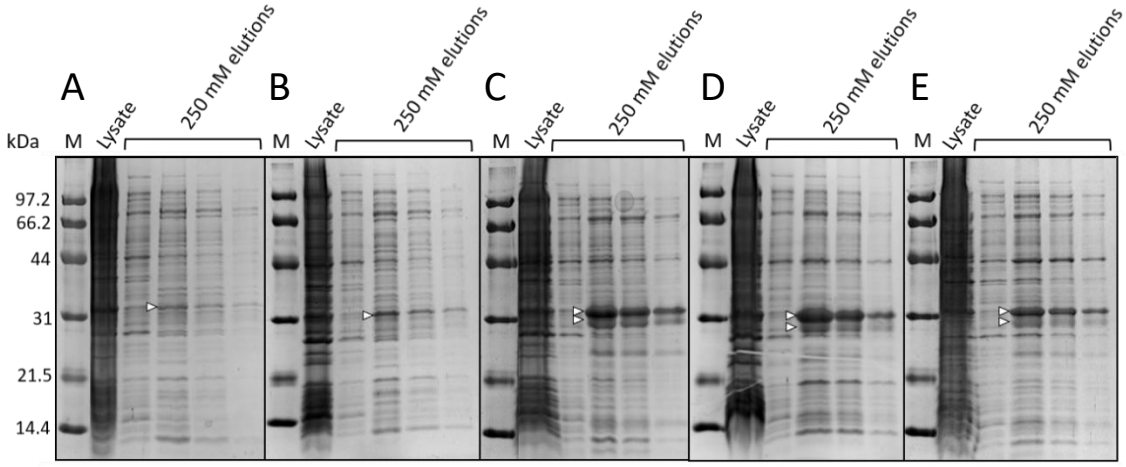


Figure 2.4 Comparison of detergents in the solubilisation of pVI-WT.

SDS-PAGE of samples lysed in buffer containing lysozyme and different detergents. Protein was eluted from Co^{2+} Sepharose resin and run on 15% SDS-PAGE gels. (A) No detergent. (B) Tween-20. (C) Triton X-100. (D) CHAPS. (E) Empigen BB. M, low molecular weight marker. Arrowhead, bands of interest.

All purifications resulted in a large number of contaminant bands. Very little protein was purified without detergent (Fig 2.4A) or with Tween-20 (Fig 2.4B). Empigen BB (Fig 2.4E) enabled considerably more pVI-WT to be purified, but of the four detergents tested, lysis in Triton X-100 and CHAPS buffer (Fig 2.4 D and E, respectively) produced larger pVI-WT yields. The yields and levels of contamination were similar with Triton X-100 and CHAPS.

Next, the ability of urea and guanidine hydrochloride (GuHCl), reagents that promote protein unfolding, to solubilise pVI were compared (Fig 2.5). Since the presence of GuHCl causes SDS to precipitate, it is necessary to remove GuHCl from protein samples prior to

SDS-PAGE analysis, and this was carried out by diluting samples followed by alcohol precipitation.

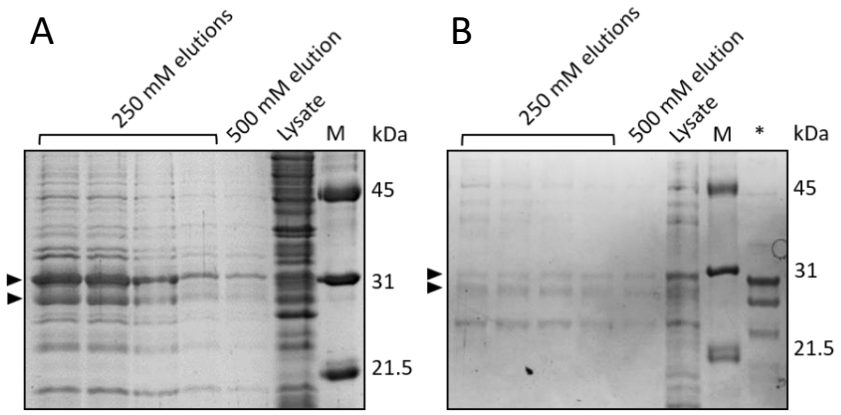


Figure 2.5. Comparison of 8M urea and 6M guanidine hydrochloride in the solubilisation of pVI-WT from 1 L culture.

Samples were purified from 1 L of Rosetta (DE3) cells using Co^{2+} Sepharose resin and protein eluted from resin using imidazole. (A) 8 M urea. (B) 6 M guanidine hydrochloride. M, low molecular weight marker.

Asterisk, pVI-WT provided by Wodrich et al. Arrowheads, bands of interest.

Using a high concentration of urea resulted in the greatest amount of protein binding to resin (Fig 2.5A). Use of GuHCl produced a lower concentration of protein in total cell lysate and eluted fractions than Tween-20 or urea (Fig.2.5C), although this may have been due to loss of protein during precipitation. Therefore, 8M urea was used in subsequent experiments, as it makes the most pVI-WT available for purification. It is also important to note that urea solutions decompose to form ammonium cyanate, which reacts readily with various protein functional groups [180], therefore urea solutions are prepared within an hour of use and affinity purification is performed within 24 hours.

2.2.4 Optimisation of affinity purification

A wide range of materials are available commercially for affinity purification of proteins, including IMAC chromatography media charged with divalent metal ions that can selectively bind soluble Histidine-tagged proteins. Early experiments were carried out using cobalt-charged resin, as this was previously used by Wodrich et al. [122]. Resin is available suspended in ethanol for gravity-flow purification or pre-packed into 1 or 5ml columns for use with FPLC purification systems. The latter provides precise control of imidazole gradients and visualisation of the eluted protein.

Cell lysate is applied to resin to allow protein to bind. A low concentration of imidazole in the lysis buffer (20 mM) helps to prevent nonspecific binding of endogenous proteins that have histidine clusters. Resin is then washed with a higher imidazole concentration buffer to remove unbound proteins, followed by a step gradient of imidazole concentration. A range of imidazole concentrations was tested to find the optimal concentrations for binding and elution of protein. The majority of His-tagged protein eluted between 200–400 mM, therefore multiple 250 mM elutions were used for subsequent protein purifications. Alternatively, protein bound to IMAC columns can be eluted using a linear or step imidazole gradient. Buffer exchange during the wash step should permit denatured protein to refold while bound to resin.

Major considerations in the affinity purification of pVI-WT were the choice of chromatography resin and the type of metal ion bound to the resin, as His-tagged proteins can have different affinities to these ions. Two of the more commonly used metal cations in protein purification are cobalt and nickel. The yield and purity of purified protein depend on the binding capacity and specificity of the resin, respectively. Nickel generally provides greater capacity for His-tagged proteins, while cobalt has a greater specificity [181]. Other important considerations are chemical stability of the resin, buffer conditions and method for separation of proteins from resin [182]. In further experiments using 1L of culture, pVI-WT expressing cells were incubated and sonicated in 8M urea buffer and the filtered lysates loaded on various types of Sepharose agar resin charged with nickel (Fig 2.6). The binding of pVI-WT to Sepharose resin was compared with binding to Sepharose Excel resin (both GE Healthcare), to which nickel ions are more strongly bound and intended for use in samples containing EDTA or other chelating agents. Protein eluted from pre-packed columns containing 1 ml Sepharose Excel resin was also compared.

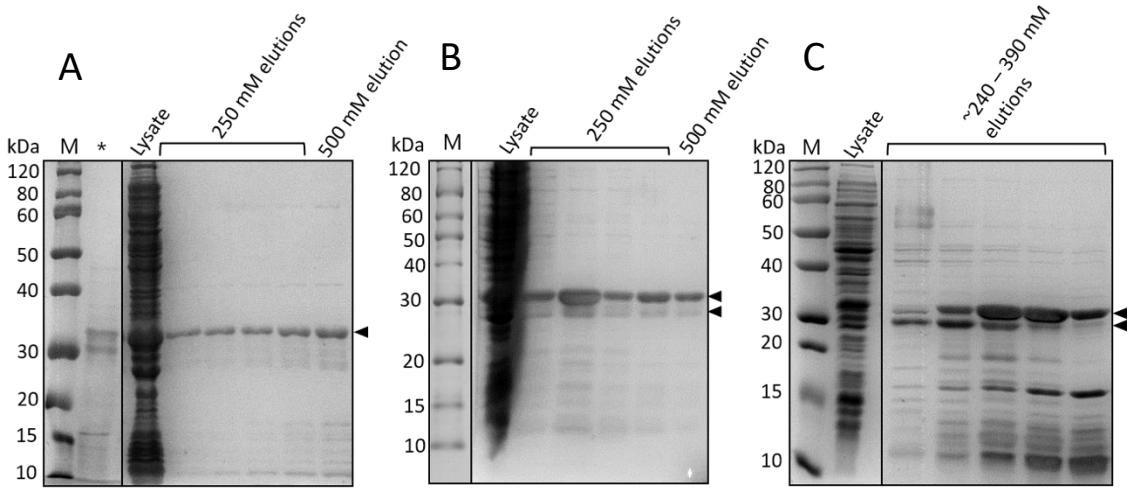


Figure 2.6 Comparison of pVI-WT purified from 1 L of culture using different types of nickel charged Sepharose resin.

All cell pellets were lysed in purification buffer with 8 M urea buffer. Protein was eluted from resin using gravity-flow step elution (A) and (B) or a 1 M imidazole gradient applied to resin packed into 1 ml columns on an AKTA Purifier (C). (A) 1ml Ni2+ Sepharose resin, gravity flow. Protein eluted with 250 mM or 500 mM imidazole (500 µl fractions). (B) 1ml Ni2+ Sepharose Excel resin, gravity flow. Protein eluted with 250 mM or 500 mM imidazole (500 µl volume). (C) 1ml Ni2+ Sepharose Excel HisTrap column. Protein eluted with a 30 ml 1 M imidazole gradient and fraction volumes of 300 µl; concentration of imidazole in respective fractions is indicated. Asterisks, reference pVI-WT received from Wodrich et al. M, Benchmark protein standards. Arrowhead, bands of interest.

While less pVI-WT bound to nickel resin (Fig 2.6A) than cobalt resin (Fig 2.5A) in 8 M urea buffer, fewer contaminants bound in the former. Sepharose Excel resin used in gravity flow purification (Fig 2.6B) appears to bind more His-tagged protein than the standard Sepharose resin (Fig 2.6A). The number of contaminant bands varied between cell extracts. While the prepacked Sepharose Excel column (Fig 2.6C) bound more pVI-WT, it also bound more contaminant or degraded protein of ~15 kDa or below. Sepharose Excel columns were used in subsequent experiments for scaling up expression since the yield was higher and

contaminant bands could be removed using size exclusion chromatography. Purification of pVI-WT from culture volumes of 2 and 4 L was performed using 1 ml HisTrap Excel affinity columns (Fig 2.7).

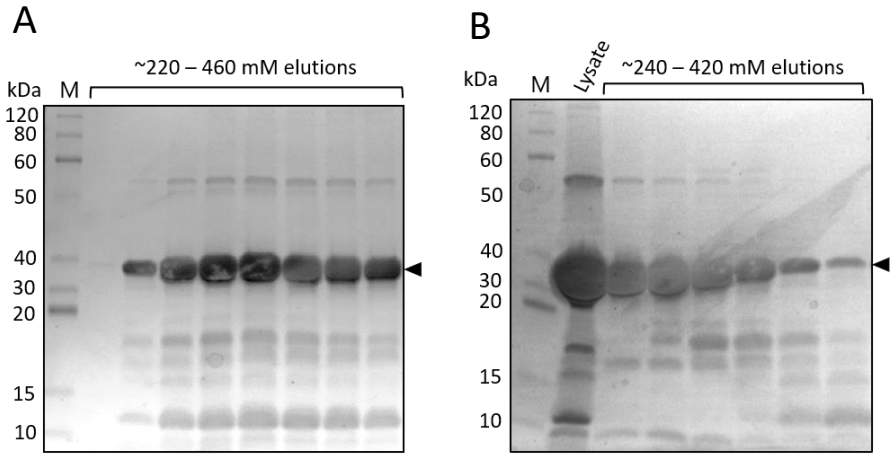


Figure 2.7 Comparison of pVI-WT purified from 2 and 4 L of culture.

Cell pellets were lysed in purification buffer with 8 M urea buffer. Protein was eluted from resin using a 30 ml 1 M imidazole gradient (effective concentration range indicated) applied to resin packed into 1 ml Ni2+ Sepharose Excel columns on an AKTA purifier. (A) 2 L of culture. (B) 4 L of culture. Asterisks, reference pVI-WT received from Wodrich et al.; M, Benchmark protein standards. Arrowheads, bands of interest.

The increase of culture volume from 2 (Fig 2.7A) to 4 L (Fig 2.7B) resulted in an increase in pVI-WT purified, but not an increase in contaminant bands. In this case, the number of contaminant bands was slightly lower in Fig 2.7B, but this was highly variable between biological replicates. Figure 2.8 summarises the conditions checked in optimising pVI-WT

affinity purification and demonstrates the changes that made the most difference in the purity and yield.

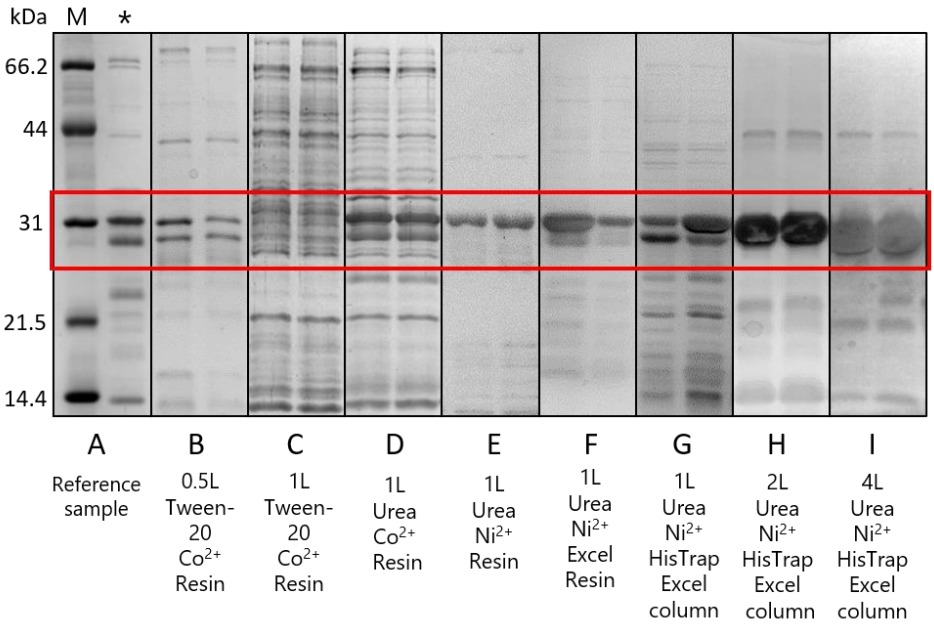


Figure 2.8 Overview of changes made during optimisation of pVI-WT affinity purification.

SDS-PAGE gels of pVI-WT samples from affinity purification. Red box indicates the bands of interest. Sample in A, pVI-WT sample provided by Wodrich et al. In panels B - I, two lanes from each sample are shown, representing the most concentrated fractions or the peak of each trace. M, low molecular weight marker.

Using urea to solubilise protein released by sonication of cells increased the amount of protein recovered, as seen in Fig 2.8D compared to Fig 2.8B. Switching from cobalt-charged resin to nickel increased the purity of eluted protein, which can be seen by comparing Fig 2.8D and E. Switching to Sepharose Excel resin (Fig 2.8G compared to F) increased the protein yield, as did use of pre-packed columns, although there was also an increase in

contaminant protein. Further yield increases resulted from scaling expression cultures up to 2 L (Fig 2.8H) and 4L (Fig 2.8I).

2.2.5 Size exclusion chromatography

Size exclusion chromatography (SEC) is a widely used technique that allows the separation of proteins by their hydrodynamic radius. SEC columns consist of a matrix of spherical beads with pores of a specific size distribution that determine whether molecules of a certain size can enter pores or flow through the matrix unimpeded. Fractions from the preceding affinity purification peak with the greatest concentration of protein were concentrated to volumes below 500 µl and filtered through 0.2 µm PVDF membrane syringe filters. Protein samples were injected onto a Superdex 75 10/300 column equilibrated with purification buffer on an AKTA purifier system. Initially, this was carried out at room temperature, but the number of contaminant bands were reduced when both affinity purification and SEC were carried out at 4 °C. pVI-WT can be separated from other bands in affinity-purified samples. Protein fractions with the least contaminant protein were achieved from 1–4 L of Rosetta culture after affinity purification and SEC (Fig 2.9).

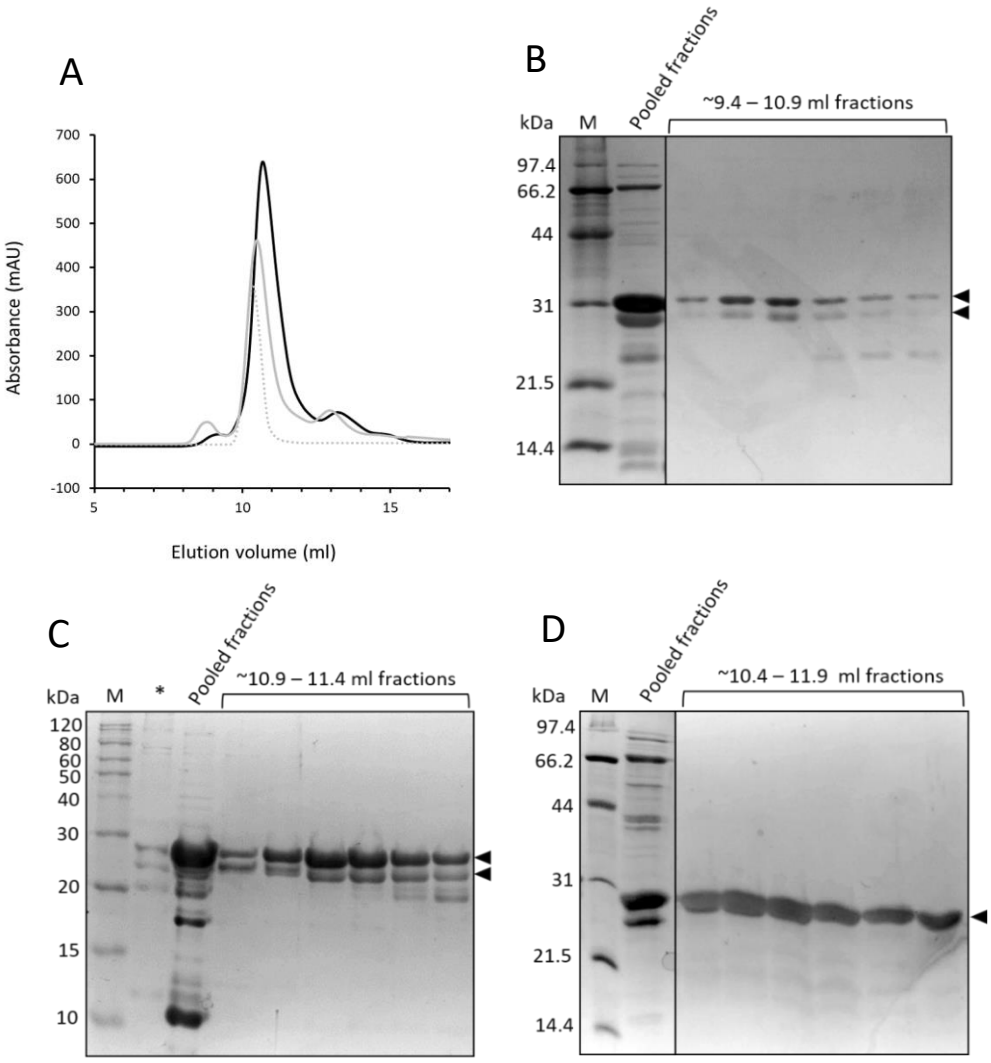


Figure 2.9 Size exclusion chromatography of pVI-WT from 1, 2 and 4L of culture.

Protein purified from 1 and 2 L of Rosetta (DE3) culture using 8 M urea lysis buffer and a 1 ml HisTrap column was further purified by SEC. Arrowheads, bands of interest. (A) SEC Traces of pVI-WT run on a Superdex 75 30/100 column. Dotted grey line, 1L. Solid grey, 2L culture. Solid black line, 4L culture. (B) SDS-PAGE gel of 1 L pVI-WT. M, Low Molecular Weight standard. (C) SDS-PAGE gel of 2 L pVI-WT. M, Benchmark protein standard. (D) SDS-PAGE gel of 4 L pVI-WT. M, Low Molecular Weight standard. Pooled fractions, fractions from the peak of affinity purification, pooled and injected into SEC column.

Using size exclusion to purify pVI-WT following affinity purification 2 L of Rosetta (DE3) culture resulted in highly pure protein that was suitable for downstream applications, while scaling up to 4 L of cultures resulted in a similar yield of pVI-WT but also some faint contaminant bands. The concentration of protein in the first three eluted fractions in Fig 2.9B was 0.09, 0.35 and 0.45 mg/ml, in Fig 2.9C the concentrations were 0.92, 2.06 and 3.72 mg/ml, and in Fig 2.9D, the concentrations in the first two fractions were 3.1 and 3.5 mg/ml. Fig 2.9 also demonstrates the variability between pVI-WT SEC fractions prepared in the same way, with doublet bands in Fig 2.9B and C and single bands in Fig 2.9D. The appearance of the single bands could be attributed to lower exposure to proteolytic enzymes or differences in handling.

Optimisation of pVI-WT expression and purification resulted in high concentrations of protein available for downstream applications. The optimised purification protocol for pVI-WT was next applied to pVI-L40Q.

2.3 Optimisation of pVI-L40Q expression and purification

After the effectiveness of solubilising pVI-WT using 8 M urea was established, small-scale experiments were carried out to find the optimal conditions for purification of the mutant protein pVI-L40Q. These results also enabled the comparison of the expression behaviour of the mutant to the wild type. pVI-L40Q contains a point mutation in the first N-terminal helix that results in 11-fold lower infectivity of the virus and a considerable increase in the

amount of virus required for endosomal rupture in cells, as well as attenuated ability to rupture liposomes *in vitro* [19]. Although pVI-L40Q preparations provided by Wodrich et al. contained fewer contaminant proteins than the pVI-WT samples (Fig 2.1), increasing the yield of pVI-L40Q was required for biophysical characterisation.

The toxicity to *E. coli* cells was not previously known, but since pVI-L40Q has a similar amino acid sequence to pVI-WT, it was expected to have a similar effect during expression. The optimised lysis and purification protocol for pVI-WT was applied to 1 L of pVI-L40Q culture in order to compare expression to the wild type. A longer expression period and solubilisation with Triton X-100 were also explored to determine the optimal set of conditions for expression and cell lysis. Cells were induced for 45 minutes or 3 hours and sonicated in urea or Triton buffers and the results shown in Fig 2.10. Affinity purification and SEC were then carried out according to the same protocol as pVI-WT.

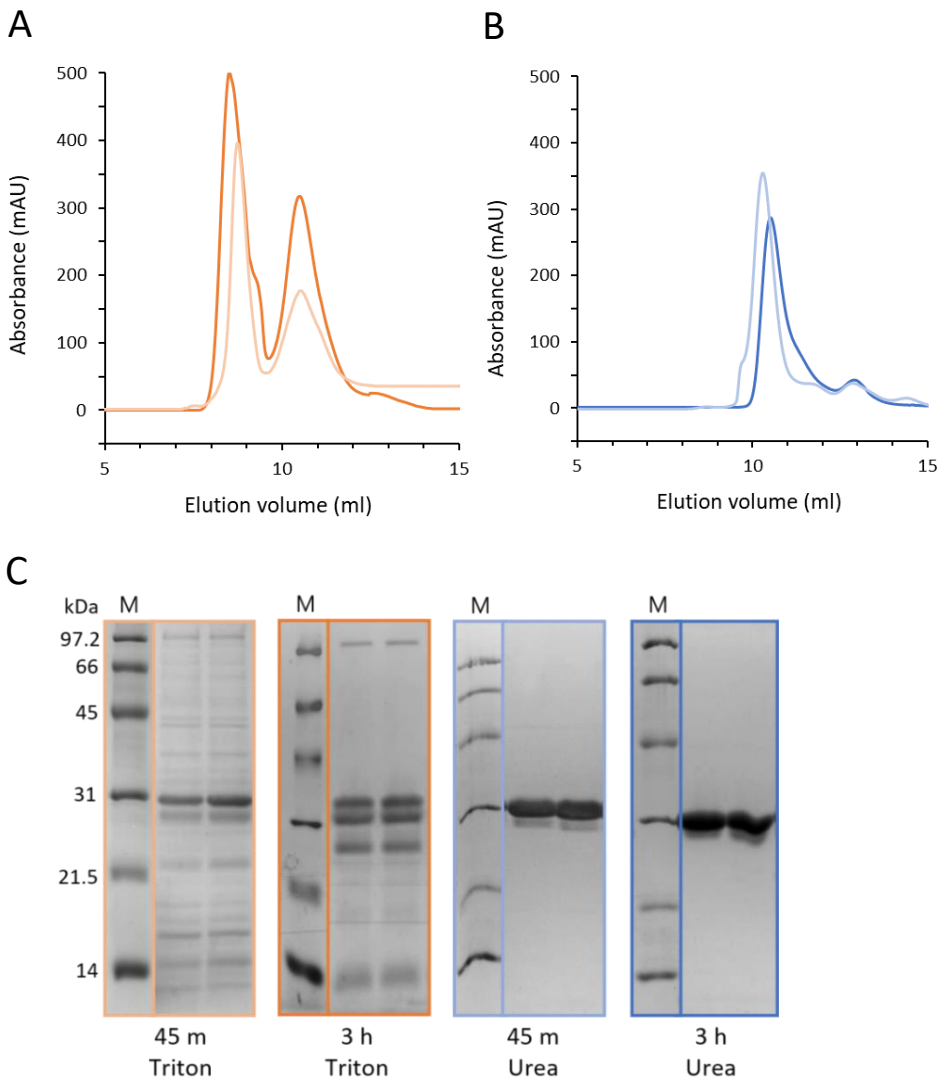


Fig 2.10 Comparison of pVI-L40Q purification from 1 L culture in urea and Triton X-100 lysis buffer.

(A) and (B) SEC Trace of pVI-L40Q samples run on a Superdex 75 30/100 column. Samples correspond to traces in (C). (A) Light orange, 45-minute induction and Triton X-100/lysozyme buffer. Dark orange, 3-hour induction and Triton X-100/lysozyme buffer. (B) Light blue, 45-minute induction and 8M urea buffer. Dark blue, 3-hour induction and 8M urea buffer. (C) SDS-PAGE gel of pVI-L40Q samples. Two lanes from each sample are shown, representing the peak of each trace.

Lysing cells in the Triton buffer resulted two elution peaks at approximately 9 and 10.5 ml (Fig 2.10A), whereas a main SEC elution peak at 10.5 ml was observed with urea (Fig 2.10B). Additional protein bands were also observed in both of the Triton samples, and there were many more contaminant bands seen in the protein expressed for 45 minutes and purified in Triton (Fig 2.10C). The difference in yield between the samples produced using urea were not as distinct as with pVI-WT in this experiment, but the total absorbance was higher and therefore the same expression and lysis conditions used for pVI-WT were applied to future pVI-L40Q experiments. It was also possible to scale up L40Q production in 1–4 L of Rosetta culture, using the same expression and purification conditions, as shown in Fig.2.11.

Although there was an increase in protein yield with increasing culture volume, as expected, the 1 L preparation of pVI-L40Q (2.11B) contained fewer contaminant bands than the 2 and 4 L preparations. The additional bands of 50–60 kDa in the 2 L sample (Fig 2.11C), may also correspond to the small peak at ~8.5 ml in Fig 2.11A. Although there was variability in number of contaminant band between samples, the 2 and 4 L of pVI-L40Q cultures produced greater protein yields than the reference material from Wodrich et al.

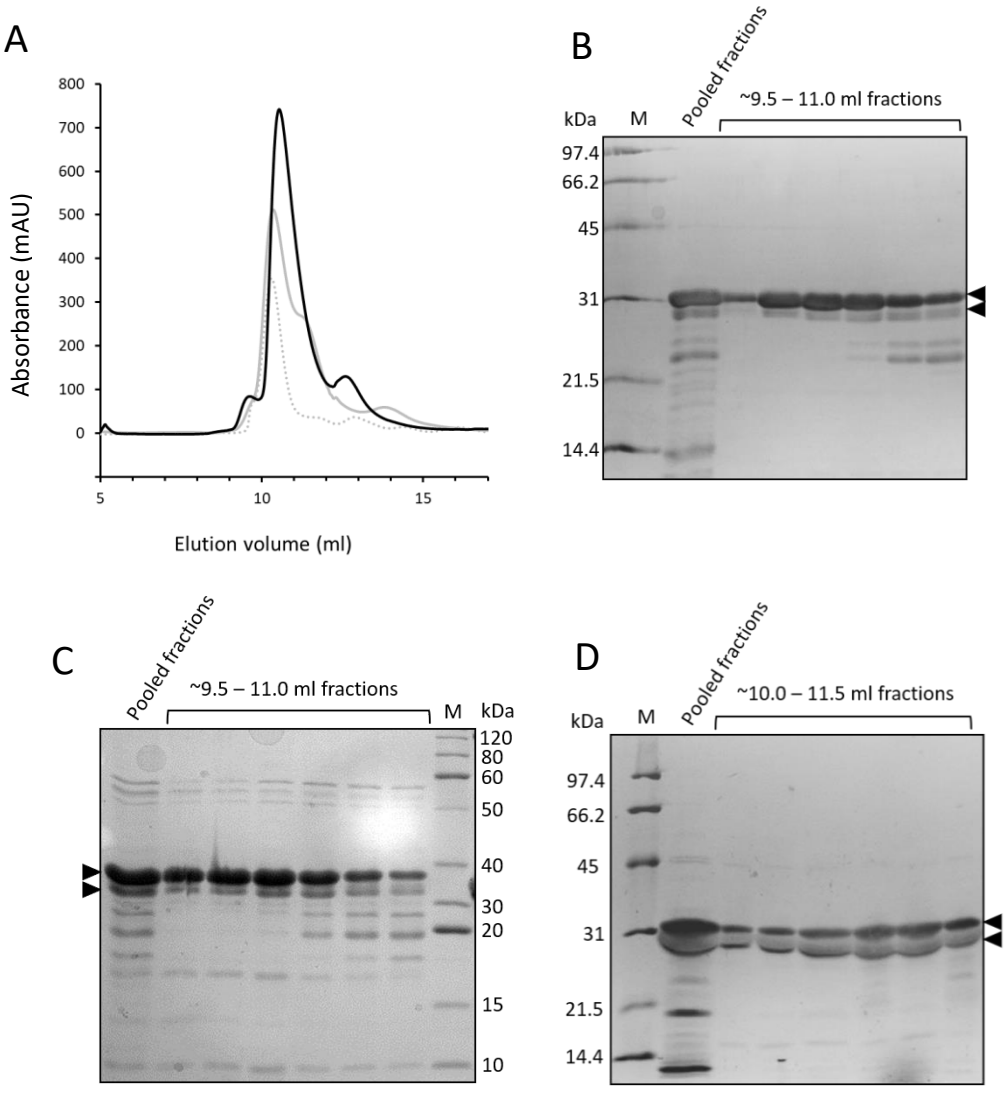


Figure 2.11 Size exclusion chromatography of pVI-L40Q from 1, 2 and 4L of culture.

(A) SEC traces of protein purified from 1, 2 and 4L of Rosetta (DE3) induced for 45minutes with urea lysis buffer. Dotted light grey line, 1 L (B). Solid light grey, 2 L culture (C). Black, 4 L culture (D). (B) SDS-PAGE gel of samples from 1 L culture. M, Low molecular weight marker. (C) SDS-PAGE gel of samples from 2 L culture. M, BenchMark His-tagged marker. (D) SDS-PAGE gel of samples from 4 L culture. M, Low molecular weight marker. A, eluted fractions from affinity purification applied to column. Arrowheads, bands of interest. Pooled fractions, fractions from the peak of affinity purification, pooled and injected into SEC column.

2.4 Optimisation of pVI-Δ54 expression and purification

Recombinant pVI-Δ54 lacks the N-terminal AH that is known to disrupt membranes, making it a valuable tool for exploring the function of this particular protein sequence and its effect on membranes. Purified pVI-Δ54 was not available from collaborators. Expression of pVI-Δ54 does not appear to lyse bacterial cells during expression, as the optical density of the bacterial culture after induction does not decrease (Harald Wodrich, personal communication). A small-scale expression test of pVI-Δ54 was carried out using Tween-20 and Co^{2+} IMAC resin and the protein purified by SEC, as with the other pVI proteins (Fig 2.12). The use of the InVision His-Tag stain allows visualisation of His-tagged protein bands without the additional steps required for Western Blotting. The stain consists of a fluorescent dye conjugated to a Ni^{2+} nitrilotriacetic acid (NTA) complex which binds to the polyhisitidine domain of His-tagged proteins [9].

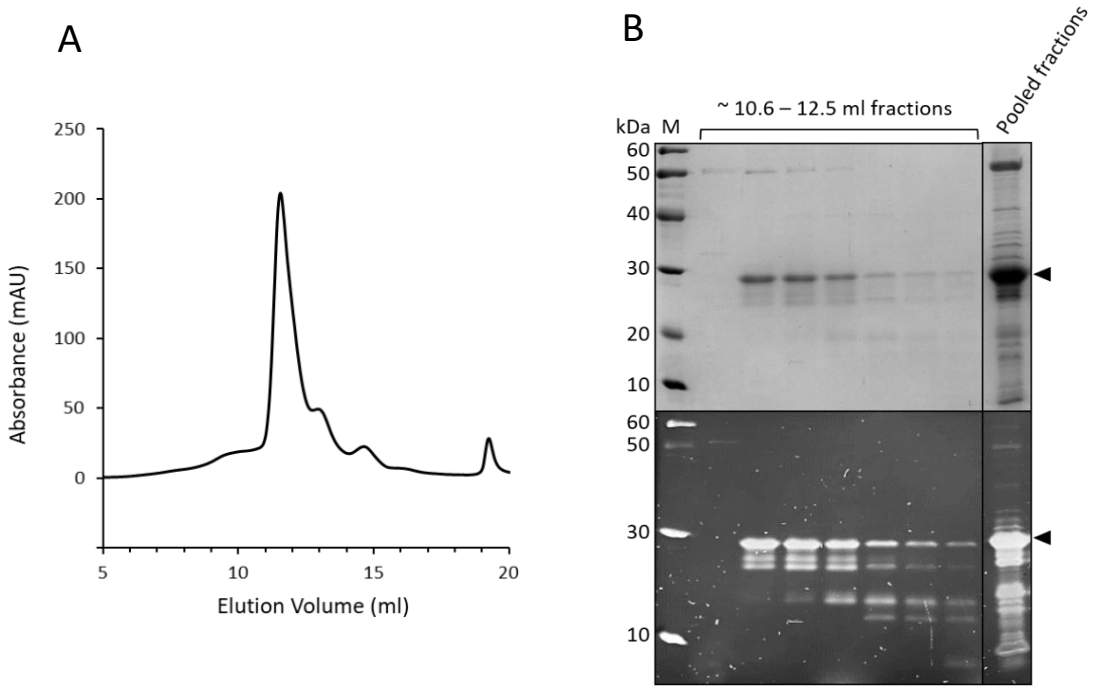


Figure 2.12 Results of small-scale pVI-Δ54 experiments.

pVI-Δ54 was expressed in 0.5L Rosetta (DE3) cells for 3 hours. Cells were lysed with Tween-20 and the protein purified using Sepharose Ni2+ resin, as with WT-pVI in Fig 2.3. (A) SEC Trace of pVI-Δ54 run on a Superdex 75 30/100 column. (B) SDS-PAGE (top panel) and with InVision His-Tag In-Gel Stain (bottom panel). M, BenchMark His-tagged marker. A, eluted fractions from affinity purification applied to column. Pooled fractions, fractions from the peak of affinity purification, pooled and injected into SEC column.

A band of approx. 28 kDa and three smaller molecular weight bands below the main protein band are visible in Fig 2.12. Use of the InVision stain in Fig 2.12B demonstrates that the lower molecular weight bands below the main band were also His-tagged and therefore likely the result of degradation at the C-terminus. The stain also allows the visualisation of faint bands, such as the one of ~20 kDa in lanes 1 and 2 which are less visible through

Coomassie staining only. In order to optimise solubilisation of pVI-Δ54 after lysis of cells through sonication, the same four detergents applied to pVI-WT samples were also tested with pVI-Δ54 (Fig 2.13).

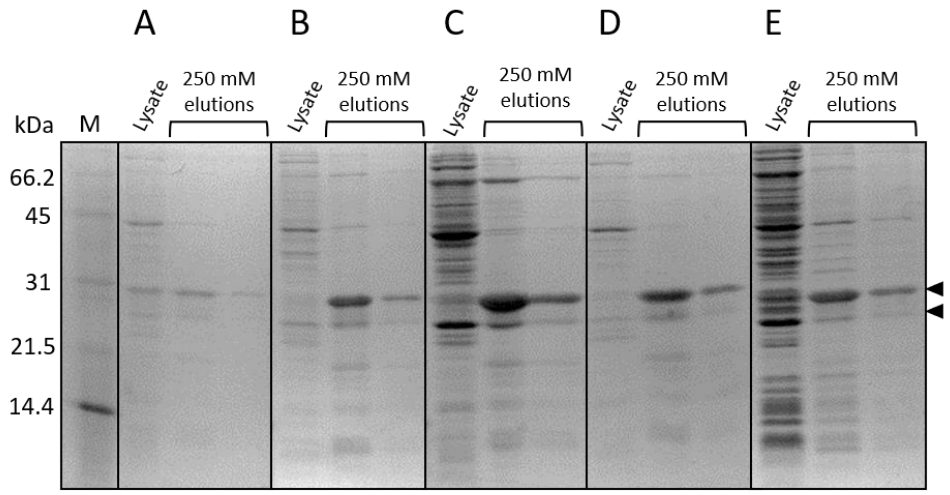


Figure 2.13 Comparison of pVI-Δ54 purification from 1 L culture using different detergents.

SDS-PAGE of samples lysed in buffer containing lysozyme and different detergents. Protein was eluted from Co^{2+} Sepharose resin and run on 15% SDS-PAGE gel stained with Instant Blue Coomassie stain. (A) No detergent, (B) Tween-20, (C) Triton X-100, (D) CHAPS, (E) Empigen BB. M, low molecular weight marker. Lanes 1–3, protein eluted with 250 mM imidazole.

The number of bands and size of the main protein band varied between cell samples lysed in the presence of the different detergents. Use of Triton X-100 (Fig 2.13C) resulted in the highest yield of the upper protein band (upper arrowhead) with a lower number of contaminant bands than were seen with CHAPS (Fig 2.13 D) or Empigen BB (Fig 2.13E). Therefore, Triton X-100 was also used for the next experiment in which use of detergent to

solubilise protein release from cells by sonication was compared to use of 8 M urea (Fig 2.14), which produced the optimal yield of pVI-WT and pVI-L40Q.

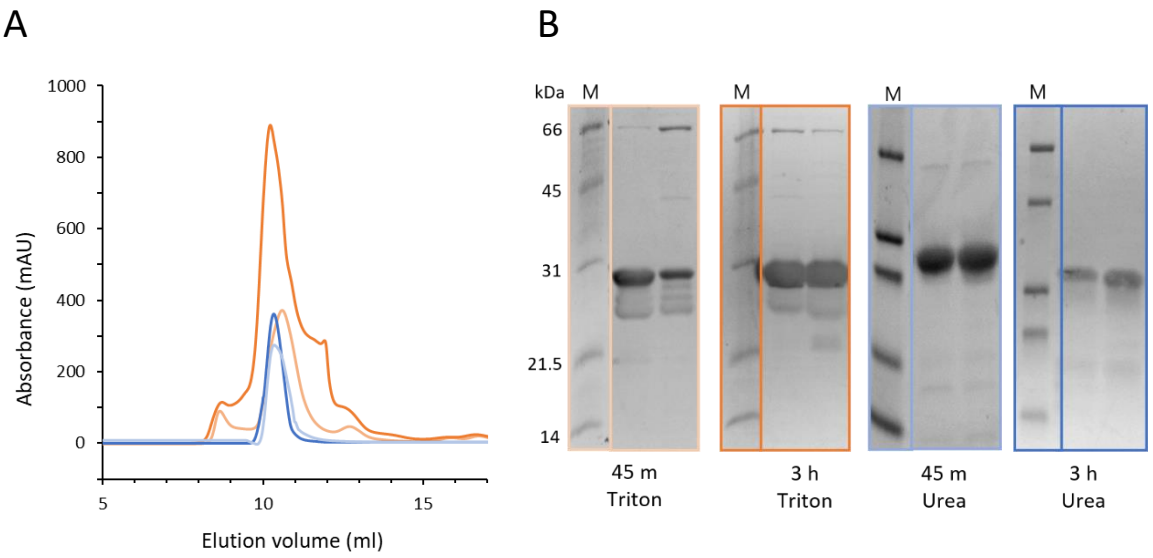


Figure 2.14 Comparison of 1 L pVI-Δ54 purification in urea and Triton X-100 lysis buffer.

Protein was purified using 1 ml HisTrap Excel columns, fractions were pooled and loaded onto a Superdex 75 10/300 column. (A) SEC Traces of pVI-Δ54 samples from 1 L Rosetta cultures. The traces corresponds to samples shown in (B). Light orange, 45-minute induction and Triton X-100 buffer. Dark orange, 3-hour induction and Triton X-100 buffer. Light blue, 45-minute induction and 8M urea buffer. Dark blue, 3-hour induction and 8M urea buffer. (B) SDS-PAGE gel of pVI-Δ54 samples. Two lanes are shown, representing fractions from the peak of each trace.

A 3-hour expression period and use of Triton buffer during purification substantially increased the protein yield (Fig 2.14, dark orange border). Use of urea did not increase the amount of protein recovered, in contrast with purifications of pVI-WT and pVI-L40Q. However, the larger protein band of approx. 70 kDa was reduced or absent in samples

purified in urea. Several bands were observed beneath the main peaks in each of the samples, indicating degraded protein and more of these were observed directly below the main protein band for the Triton X-100 samples. Further expression experiments with larger volumes of pVI-Δ54 culture were carried out using a 3-hour expression period and Triton X-100 to solubilise protein during purification. The results of SEC of larger cultures are shown in Fig 2.15.

Scaling up of pVI-Δ54 expression resulted in a proportional increase in both the target protein bands and contaminant or degraded protein bands. In particular, the 4 L pVI-Δ54 purification resulted in a large amount of contamination, due to protein overloading (Fig 2.15A, black line). Bands of ~70 kDa were observed in purified protein from 2 L and 4 L cultures (Fig 2.15C and D), which might represent dimers reformed after elution. Lighter bands of ~90 kDa are also visible in all samples, which might represent reformed trimers. 1 L of culture was sufficient for experiments described in the following chapters.

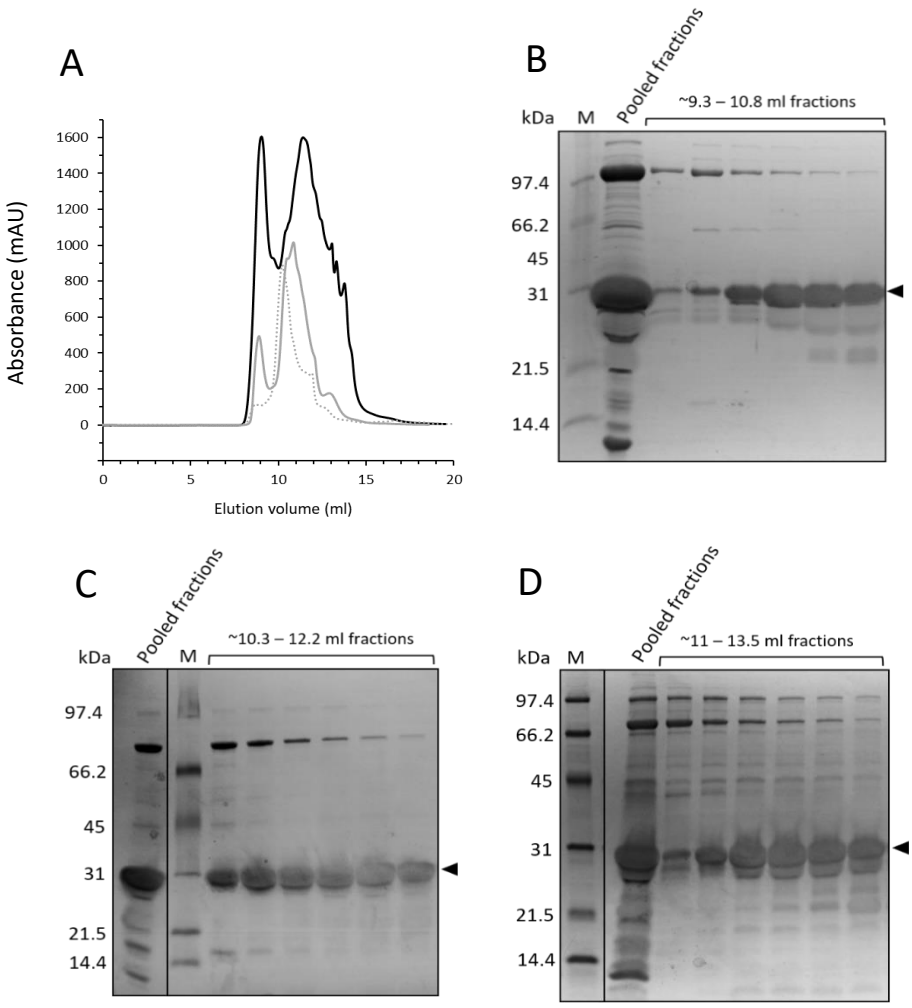


Figure 2.15 Size exclusion chromatography of pVI-Δ54 from 1, 2 and 4 L of culture.

(A) SEC traces of protein purified from 1, 2 and 4 L of Rosetta (DE3) induced for 3 hours and purified with Triton X-100 lysis buffer. Dotted grey, 1L culture from Fig 2.14 (B, second panel). Solid grey, 2 L culture. Black (overloaded), 4 L culture. (B) SDS-PAGE gel of samples from 1 L culture. M, Low molecular weight standard. (C) SDS-PAGE gel of samples from 2 L culture. M, Low molecular weight standard. (C) SDS-PAGE gel of samples from 4 L culture. M, Low molecular weight standard. Pooled fractions, fractions from the peak of affinity purification, pooled and injected into SEC column.

2.5 Summary of changes made during optimisation of pVI purification

pVI-WT and the two mutant pVI constructs were purified to a much higher concentration and purity than the samples originally provided by our collaborators (Fig 2.1), and this required several changes to be made to the original protocol. Figure 2.16 summarises the optimised protocol for recombinant His- tagged pVI constructs. The biggest changes from the original protocol were the change of protein solubilizing agent, 8M urea in the case of pVI-WT and pVI-L40Q, or Triton X-100 for pVI-Δ54 in place of Tween-20, and using His Trap Excel columns for affinity purification. Using a longer induction period increased the yield of pVI-Δ54. The appearance of each construct purified under optimal conditions is compared using SDS-PAGE analysis in Figure 2.17.

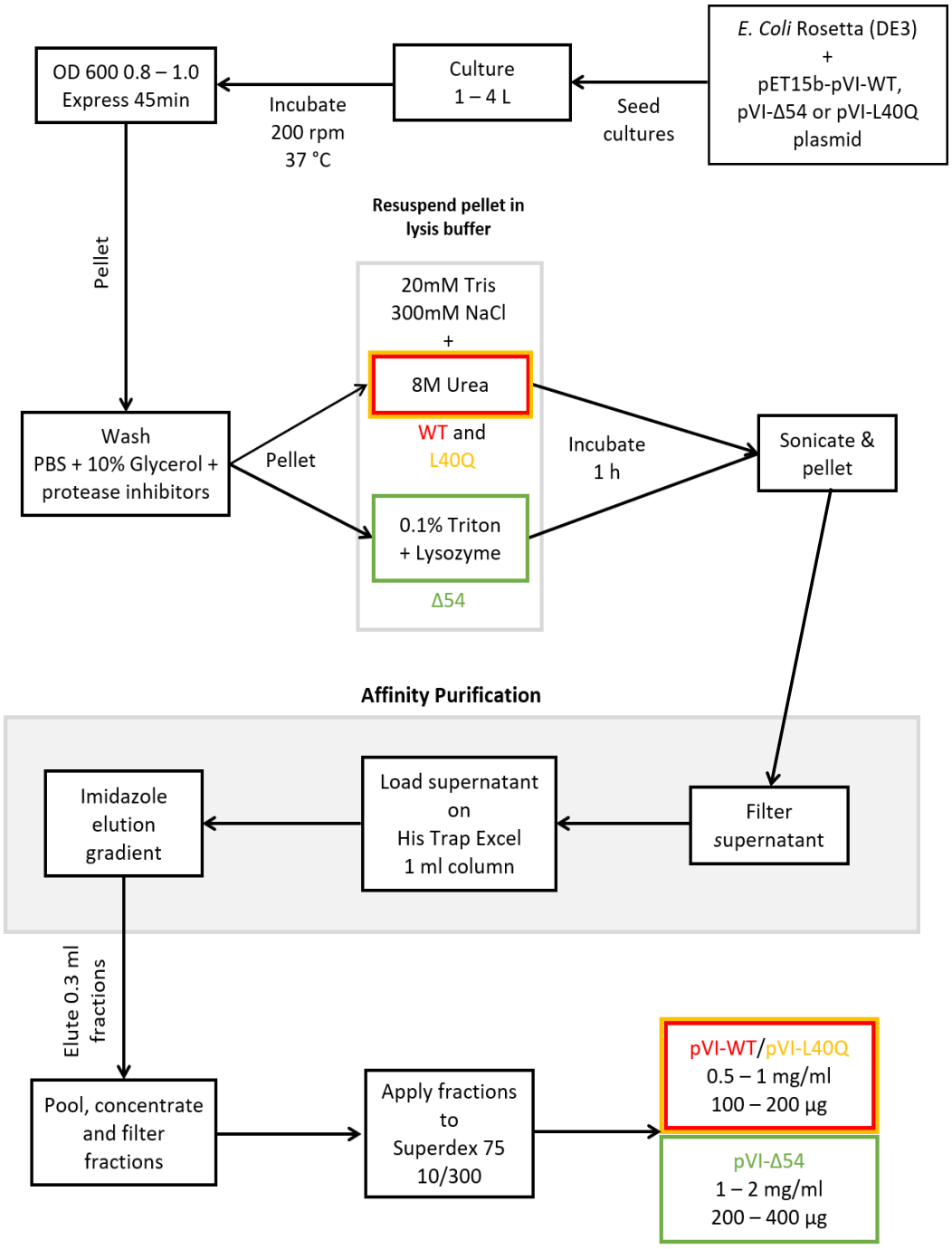


Figure 2.16 Overview of optimised expression and purification protocol for pVI-WT and mutants

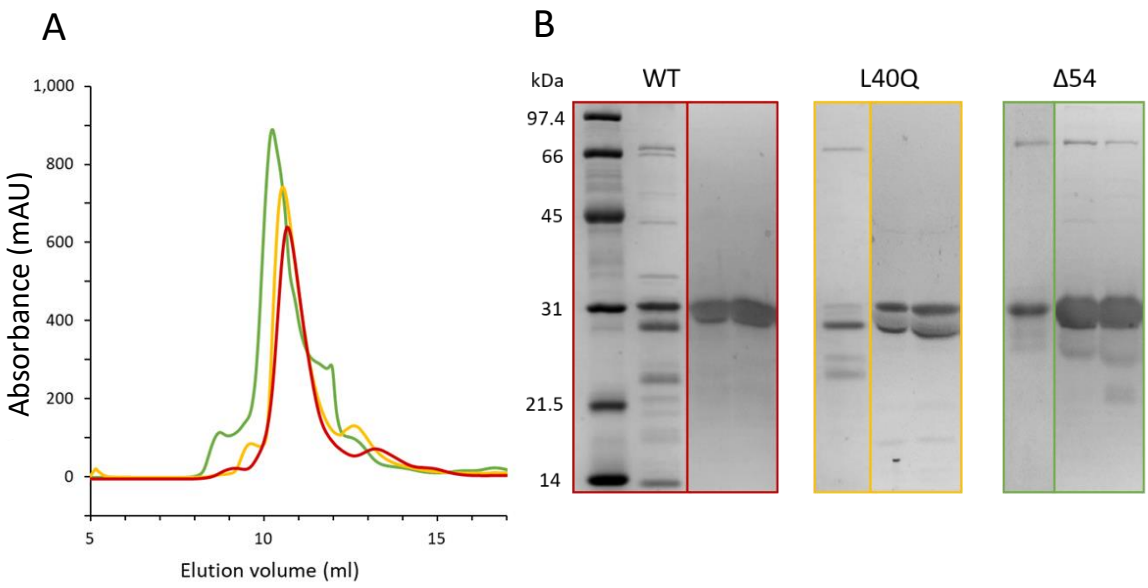


Figure 2.17 Comparison of pVI WT protein and mutants purified with respective optimised protocols.

(A) SEC Trace of pVI samples run on a Superdex 75 30/100 column. Traces correspond to samples in (B). Red, from 4 L pVI-WT culture with 45-minute induction and 8M urea buffer. Yellow, from 4 L pVI-L40Q culture with 45-minute induction and 8M urea buffer. Green, from 1 L pVI-Δ54 3-hour culture with induction and Triton X-100 buffer. (B) SDS-PAGE gels of pVI samples. Left panels taken from Figs 2.1 and 2.12 represent samples received from Wodrich et al. (WT and L40Q) and an early expression test of pVI-Δ54, respectively. Right panels were produced using optimised protocols. Two lanes from each optimised sample are shown, representing the peak of each trace.

Improvements were made in the purity of pVI-WT and pVI-L40Q purified from 4 L of Rosetta (DE3) using 8 M urea, including the removal of the bands at ~66 kDa. The peaks of the pVI-WT and pVI-L40Q traces were similar in height and contained similar levels of contamination. The yield of pVI-Δ54 was greatly increased by lengthening the expression period to 3 hours and was greater than the yield of pVI-WT or pVI-L40Q despite the use of

only a quarter of the culture volume. However, more contamination was also present in the pVI-54 samples.

These changes made to the preliminary protocol resulted in protein that was more suitable for structural biology techniques and cryoEM analysis of protein-liposome interactions. Although the yield of pVI-WT from 1 L of culture was lower than that of the mutants, Fig 2.9 demonstrates that pVI-WT expression can be scaled up without a corresponding increase in contaminant proteins. Protein samples can be concentrated using Amicon centrifugal filter devices, although concentrating will also increase the concentration of contaminant proteins. No visual evidence of aggregation was seen in any of the protein samples up to 2 mg/ml.

2.6 Mass spectrometry analysis of pVI-WT

More information was sought regarding the identity of the two protein bands that separate during reducing SDS-PAGE of pVI-WT. This was done to confirm if this result was due to proteolytic cleavage of the C-terminal portion, which was suspected as the bands typically both reacted to anti-His antibodies and the tag was on the N-terminus. The size difference of the bands was estimated to be 2–4 kDa by visual comparison with molecular weight ladders. The two bands were excised from gels and digested with trypsin. The resulting peptides were analysed using liquid chromatography-mass spectrometry (LC-MS/MS), a technique commonly used in identification of protein sequences. The peptide mass

fingerprints were compared to a database of known protein sequences. Digestion of upper and lower bands with trypsin resulted in 90 peptides found either in the upper or lower band, or both. Aside from five peptides matching *E. coli* protein sequences that were detected at low intensity, all peptides matched with Adenovirus pVI-WT. Figure 2.18 shows the coverage of peptides detected compared to the full sequence.

Peptides were detected in the excised upper band (blue bars) throughout the protein sequence up to residue 225 of 231, although no peptides were detected in a large segment from residue 187 to 217, likely due to the high frequency of protease cleavage sites there. No peptides covering the N-terminal AH were detected, although many peptides were detected in the following predicted helical region extending to residue 101. The most C-terminal peptide detected in both top and bottom bands (grey bars) covered residues 174–187. pVI-WT cleavage at residue 187 would result in a protein fragment with an approximate molecular weight of 20 kD, consistent with the estimated size of the bottom band based on its appearance on SDS-PAGE gels. 10 peptides were detected in the upper band in the region after residue 147 residues that were not detected in the lower band, and the intensity of the six peptides detected after residue 147 decreased hundredfold, indicating that the region after this position is much more unstable. Some of the predicted cleavage sites after residue 147 had very low cleavage probabilities: R155 (0.0001%) and R197 (0.0001%) while K184 and R214 still had 37.4% and 29.9%, respectively and other predicted cleavage sites in this region had probabilities above 84%.

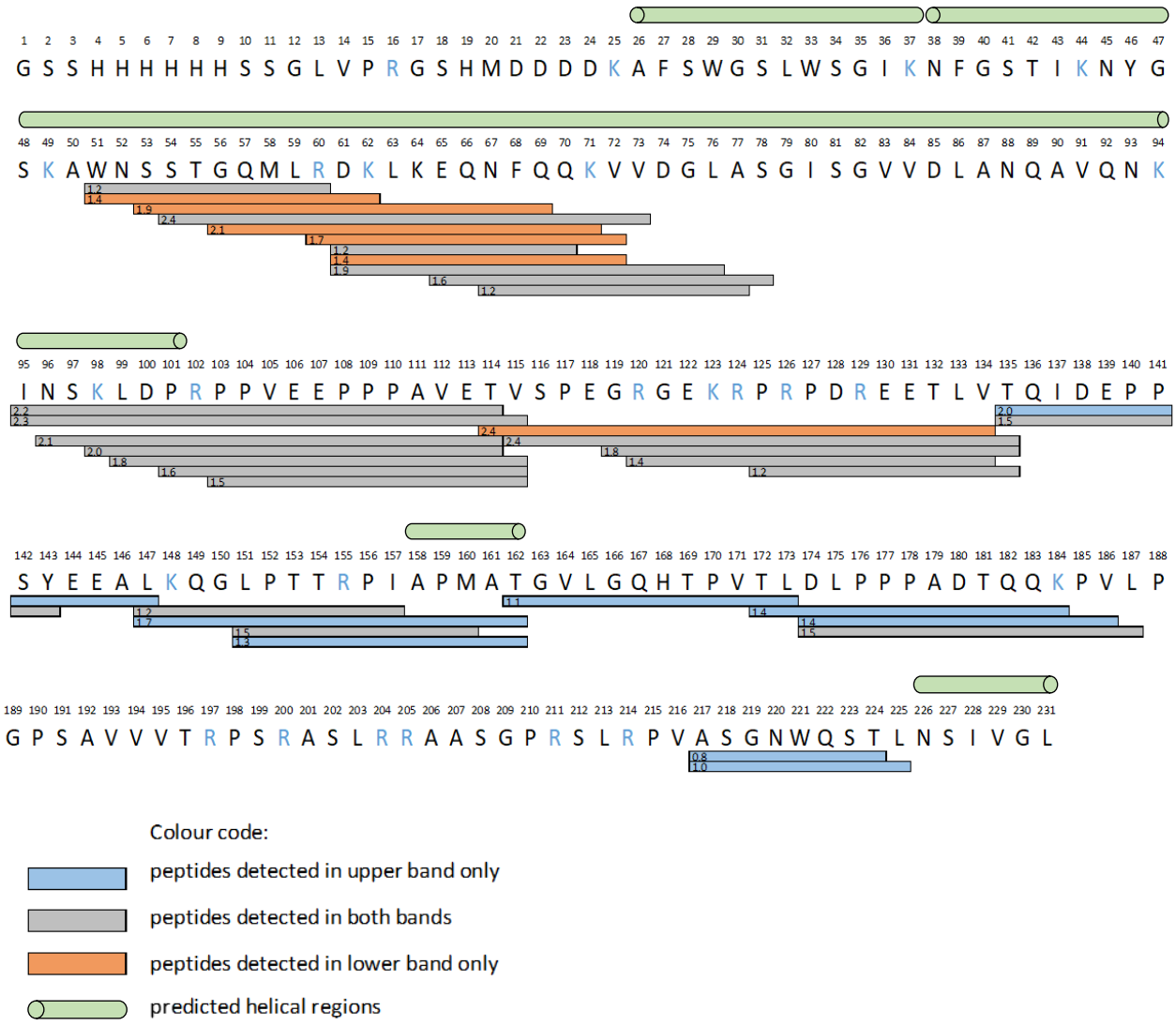


Figure 2.18 Results of pVI-WT peptide mapping by LC-MS/MS

Only the longest peptides cleaved at each residue are shown. Detected peptides are depicted as colour coded bands. Molecular weight of peptides is shown in each band. Predicted enzyme digestion sites (Lys and Arg residues) are highlighted in blue. Full map can be found in appendix.

2.7 Discussion

The work of the Wodrich group produced recombinant His-tagged pVI-WT and pVI-L40Q. However, these preparations contained contaminant proteins and were not of a suitable concentration for downstream applications requiring pure concentrated protein, such as cryoEM. Therefore, an optimised protocol was developed for pVI-WT and the mutant pVI-L40Q. The main changes to the protocol were the use of nickel bound affinity purification resin instead of copper and using 8 M urea instead of a detergent in the lysis stage. This protocol was then adapted for pVI-Δ54 and a higher yield of this mutant was achieved with a longer expression period and lysis in buffer containing Triton X-100. Overall, considerable improvements were made in the yield and purity of all pVI protein preparations. In the case of pVI-WT, the yield was increased from 0.2–0.5 mg/ml of protein with many contaminants from 1 L culture to up to 1mg/ml much cleaner protein from 4 L of culture.

While the temperature during expression was maintained from the preliminary protocol, doubling the IPTG concentration at induction of pVI-WT to 2 mM produced an increase in protein yield (Fig 2.3). These parameters were then maintained for subsequent purification experiments for all three constructs. The optimal expression period was explored for each protein and it was found that expressing pVI-WT and L40Q for longer than 45 minutes resulted in the appearance of protein bands below the target bands, likely due to more extensive exposure to proteolytic enzymes. The first N-terminal AH is responsible for endosomal rupture and also results in lysis of *E. coli* cells during recombinant pVI-WT

expression. This is also the case for pVI-L40Q, which contains a point mutation in the N-terminal helix which abrogates infectivity in mammalian cells. Due to the similar behaviour of pVI-L40Q compared to pVI-WT during expression and purification (as evidenced by the visual comparison of SEC traces in Figure 2.19) and the significant amounts of contaminants detected in pVI-L40Q samples purified with detergent (Fig 2.10C), it is likely that L40Q also interacts with membranes. In contrast, it was determined that a higher yield of pVI-Δ54 was achievable through extending the expression time to 3 hours (Fig 2.14), due to the lack of the N-terminal AH resulting in much lower toxicity to *E. coli* cells.

The next major consideration when optimising the purification protocol was the lysis of cells and release of protein. Sonication of cells resulted in a decrease in viscosity of lysates produced using lysozyme and detergents due to physical breakdown of cell walls and shearing of cellular DNA. Lower viscosity ensured that cellular material pelleted, which made filtration easier, prevented affinity resin from becoming blocked and enabled higher recovery of proteins. Optimising solubilisation of the protein constructs after cell lysis also required a change to the protocol. In the absence of solubilising agents, it was likely that pVI-WT remained bound to bacterial membranes and reduced the protein available for binding to IMAC resin. Several detergents with varying properties were tested and compared (Fig 2.4), along with urea and GuHCl (Fig.2.5A and B). Urea appeared to disrupt the structures of pVI-WT and pVI-L40Q enough that any associated lipids were released.

Urea and GuHCl possess similar chemical structures and both denature proteins by weakening hydrophobic bonds within native protein conformations [183]. Studies suggest that urea destabilizes proteins by forming hydrogen bonds to exposed amide groups on the protein backbone that are stronger than the amide-amide hydrogen bonds within the folded secondary structure [183, 184]. While GuHCl is thought to be more efficient than urea at protein denaturation per mole [180, 185], GuHCl disrupts β-sheets more efficiently than α-helices [186], which may account for it being less efficient at solubilising pVI-WT. However, the lower protein yield after use of GuHCl may also be due to protein loss during GuHCl removal by protein precipitation. The expression of pVI-Δ54 was also tested with several detergents (Fig 2.13) and urea (Fig 2.14), but optimal yields of pVI-Δ54 were obtained by lysing cells in buffer containing Triton X-100 rather than urea. Removing the membrane-interacting N-terminal AH from pVI-Δ54 eliminated the requirement for urea in the lysis buffer. It is not clear why yield of pVI-Δ54 was higher in Triton X-100 buffer, but since the expressed protein was already mostly free of membrane, urea binding to protein may have reduced binding to IMAC resin, resulting in lower yield.

The next major change was the choice of metal ion bound to affinity purification resin. Nickel-charged resin bound more of the target protein and reduced the number of contaminant bands (Fig 2.6). This result was somewhat surprising, since nickel generally has a higher binding capacity for His-tagged proteins, while cobalt has a higher binding specificity [6]. The improvement in yield with nickel-bound resin was in contrast to the

results of experiments by Ruben Martinez, who found that pVI-WT optimally bound cobalt-charged resin [122]. The use of Sepharose Excel resin further increased yield, albeit with an increase in contaminant proteins (Fig 2.7). This difference may be explained by the differing strength of the cation binding to resin. Using pre-packed columns allowed more control of flow rate through resin and visualisation of protein elution, allowing further optimisation of the imidazole gradient.

Size exclusion chromatography (SEC) was then used to separate contaminants from pVI constructs, but the final purity of samples varied considerably. It was found that higher cell density and protein concentration from larger cultures generally resulted in additional protein contamination, which is particularly obvious in Fig 2.15D of pVI-Δ54 expressed in 4 L of culture, which contains many additional contaminant bands. Since pVI-Δ54 does not lyse cells and protein is expressed for longer, the amount of protease and time exposed could potentially have increased. Therefore, when higher numbers of cells are present, more protease inhibitors should be added. The amount of protein applied to the SEC column would have been more appropriate for a SEC column with larger bed size, which would have better resolved the expected protein peak. At higher protein concentration, the target protein and contaminants may also aggregate, which can hinder protein progress though the column and result in protein eluting later than expected. Aggregates move more quickly through a gel filtration column and therefore elute earlier, reducing the protein in the expected peak.

While the N-terminus of pVI contains several predicted alpha helices, the C-terminal half of pVI is predicted to be mostly disordered [124]. The disordered structure of the C-terminal section of pVI may explain the apparently higher molecular weight on SDS-PAGE gels than the theoretical weight of 24.8 kDa. Intrinsically disordered proteins (IDP) have been reported to display aberrant mobility in SDS-PAGE [187, 188] attributed to their high net charge and hydrophobicity [189], properties shared by pVI-WT. pVI-Δ54 runs smaller than the other proteins, at approximately 28 kDa, due to the missing 20 residues of the first N-terminal helix but still appears larger on SDS-PAGE gels due to the intact disordered C-terminus.

The appearance of pVI-WT and pVI-L40Q on SDS-PAGE gels also varied after both affinity purification and SEC. In some cases, single bands were present while in most others, the samples separated into a doublet. Use of Western blot to visualise His-tagged pVI-WT (Fig 2.2) revealed that both bands in the doublets contained the N-terminal His tag. Additional lower MW bands that were also His-tagged were also identified in pVI-WT samples and in pVI-Δ54 visualised using a HisTag stain to (Fig 2.12). These additional bands likely correspond to pVI protein truncated at the C-terminus. Peptide mapping of pVI-WT fragments cleaved using trypsin and identified using mass spectrometry (Fig 2.18) revealed many potential cleavage sites that could be vulnerable to digestion by cellular proteases, especially in the C-terminal portion. This analysis indicated that the lower protein band observed in SDS-PAGE of pVI-WT only produced peptides up to residue 147, indicating

cleavage after this residue. Longer induction periods result in more material in the lower bands for both pVI-WT and pVI-L40Q, indicating that more degradation is taking place due to higher exposure to bacterial proteases, although these enzymes will not be active at all of the same sites in each protein preparation.

Some of the larger MW bands observed in SDS-PAGE gels of SEC-purified pVI-L40Q (e.g. Fig 2.10B and 2.11C) and pVI-Δ54 (Triton samples in Fig 2.14 and 2L and 4L samples in Fig 2.15) may correspond to peaks on the SEC traces that eluted earlier to the main protein peaks, or show the intrinsic property of the protein to oligomerize after purification. These bands of ~50 kDa (L40Q), 50–55 kDa and ~70 kDa (Δ54) correspond to the approximate MW of a putative dimer or trimer reformed after elution, respectively. Affinity-purified pVI-WT samples also contain bands of 44–65 kDa (Fig 2.6C and 2.7A and B), potentially corresponding to dimers or trimers, but SEC was largely successful at separating these proteins. These bands were more prevalent in samples purified in the presence of urea, which may have prevented aggregation or oligomerisation.

The process of optimising conditions for expression and purification of pVI-WT required many changes, but this resulted in the availability of protein of much higher concentration and purity that was suitable for further biophysical characterisation. Developing the revised protocol for pVI-WT expression also revealed the behaviour of the mutant proteins pVI-Δ54 and pVI-L40Q during expression and purification in comparison to the wild type, which may

possibly inform purification for other similarly disordered and or membrane-interacting proteins.

However, the final yields may still not be concentrated enough for techniques such as Nuclear magnetic resonance (NMR) spectroscopy and potentially X-ray crystallography. SEC still results in very little pure protein as sometimes only one fraction (0.3 ml) is free of contamination. While fractions can be pooled and re-run, there is still a considerable loss of protein at each stage of purification. Improvements in yield could be made by improving solubility of proteins, by changing affinity and solubility tags and further optimising purification conditions. Moving the His-tag to the C-terminus of pVI may also reduce cleavage of the unstructured region, which may reduce the number of contaminant bands below 25kDa. However, this approach could be complicated by protease digestion at the N-terminus potentially removing the His-tag, making these products unavailable for purification. It is not known what effect removing the tag from the N-terminus will have on this region, in particular the first AH, although Wodrich et al. demonstrated that the tag does not affect *in vitro* pVI-WT membrane lytic activity (personal communication, Harald Wodrich). Use of an alternative plasmid vector may be another solution for increasing protein yield. While recombinant proteins encoded on pET vectors can represent up to 50% of the total cell protein after induction [190], this high protein expression can slow bacterial growth. Furthermore, expression can be leaky and expression of a toxic protein such as pVI-WT before the optimal cell density has been achieved could reduce the final yield [191].

However, leaky expression in the pVI expression system was not explored here, so this possibility was not confirmed. pET vectors are also limited to *E. coli* strains with the DE3 cassette. Alternative choices include pBAD vectors under the control of the Ara promoter, which have lower background expression levels [192]. Expressing the pVI constructs in a mammalian cell system has not been explored in this project but may be another way to improve pVI yield.

2.8 Materials and methods

2.8.1 Proteins and plasmids

Proteins pVI-WT and pVI-L40Q were provided by Harald Wodrich (University of Bordeaux). Plasmids pET15b-VI-WT and pET15b-VI-Δ54 with an N-terminal 6-His tag and an Ampicillin resistance gene were also provided by Harald Wodrich.

2.8.2 Site-directed mutagenesis.

pET15b-VI-WT was mutated to produce the plasmid for the L40Q point mutant protein using the following primers (Integrated DNA Technologies) and Phusion high fidelity polymerase (NEB).

5’- GCT GGG GCT CGC AGT GGA GCG GCA T -3’

5’- ATG CCG CTC CAG TGC GAG CCC CAG C -3’

Mutated DNA was transformed into Turbo Competent *E. coli* cells (NEB) for amplification and purified DNA prepared using a Plasmid Miniprep kit (Qiagen).

2.8.3 Expression in *E. coli* and cell lysis

2.8.3.1 Transformation and induction

Plasmids were transformed into Rosetta (DE3) cells (which contain a plasmid with chloramphenicol resistance) and plated on LB agar with 100 ng/µl ampicillin and 35 ng/µl chloramphenicol. Single colonies were inoculated into 5ml LB plus antibiotics and grown at 37°C, 200 rpm for 4–6 hours, these cultures were then used to inoculate 250 ml overnight cultures. 2 L flasks with 500 ml LB plus antibiotics were inoculated with 15 ml overnight culture and incubated at 37°C, 200 rpm. Once they had reached OD600 of 0.8–1.0, cultures were supplemented with 300mM NaCl and induced with 2 mM IPTG. Induced cultures were incubated for a further 45 minutes (pVI-WT and L40Q unless stated in text) or 3 hours (Δ54), before being pelleted at 3,000 x g at 4°C. Pellets were re-suspended in ice cold PBS with 10% glycerol and 1 mM PMSF and re-pelleted. Cell pellets were either flash-frozen in liquid nitrogen or the lysis protocol was continued.

2.8.3.2 Cell lysis and protein solubilisation

Cells were lysed with 30 ml buffer/litre of pelleted culture. Unless stated in text, detergent lysis buffer contained 20 mM Tris, 300 mM NaCL, 0.1% Triton X-100 and 1 mM lysozyme,

1 mM DNase, 10 mM MgCl2, 1 mM PMSF and cOmplete mini protease inhibitor cocktail (Roche). Urea lysis buffer was identical except detergent was replaced with 8 M urea. Lysate was agitated at 4 °C for 30 minutes before being placed in ice and sonicated using a VCX 750 ultrasonic processor (Sonics and Material inc.) with 13 mm probe set at 36% amplitude in cycles of 5 seconds on, 10 seconds off for 10 minutes. Lysate was centrifuged at 20,000 x g for 30 minutes before filtering to 0.45 µm.

Detergents used in the small-scale purification experiment in Fig 2.4 were used according to the following concentrations: (B) Triton X-100, 0.1%w/v. (C) Tween-20, 0.1%w/v. (D) CHAPS, 40 mM. (E) Empigen BB 30%, 20 mM.

2.8.4 Affinity purification

2.8.4.1 Affinity purification in initial experiments (sections 2.2.1– 2.2.2)

0.5ml Sepharose-6 Fast Flow resin (GE Life Sciences) was washed with MilliQ water (MQ), and then incubated with 0.1M cobalt (II) or nickel (II) sulphate for 30 minutes with frequent agitation. Resin was washed with 10 volumes of MQ water to remove unbound metal.

Co^{2+} or Ni^{2+} charged resin was equilibrated with 10 volumes of purification buffer (20 mM phosphate, 300 mM NaCL). Filtered lysate was incubated with resin for one hour before

being poured into empty gravity flow columns. Resin was washed with purification buffer plus 20 mM imidazole and protease inhibitors. Bound protein was eluted in 4 x 0.5 ml fractions of purification buffer plus 250 mM imidazole and protease inhibitors.

2.8.4.2 Affinity purification in later experiments (section 2.2.3 onward)

HisTrap Excel 1ml columns (GE healthcare) were washed with MQ water and equilibrated with purification buffer: 20 mM Tris, 300 mM NaCl with 1 mM PMSF. Supernatant was loaded at a rate of 1 ml/min, then washed with ~10 column volumes purification buffer. Proteins were eluted with an imidazole gradient of 0–1 M over 30 ml at 0.5 ml/min on an AKTA purifier, with 0.5 ml fractions collected. Fractions containing the peak protein were analysed by SDS PAGE.

2.8.5 Size-exclusion chromatography

To separate pVI from major contaminants, elution fractions containing the highest protein concentration were pooled, concentrated to ~250 µl in 0.5 ml or 14 ml 10K centrifugation units (Amicon) and filtered through 0.2 µm 0.5 ml centrifugation units (Millipore). The concentrated protein fraction was loaded on a Superdex 75 10/30 size exclusion column (GE Healthcare) equilibrated with PB. Protein was eluted in 0.3 ml fractions. Proteins from the different peaks were then compared by SDS-PAGE and Western Blotting.

2.8.6 SDS-PAGE and Western Blotting

Eluted protein fractions from affinity purification or SEC were analysed by SDS-PAGE using hand-made 15% acrylamide gels or Bio-Rad Tricine Any-kD precast gels. 10µl of each protein sample was mixed with 20µl gel running buffer and boiled at 95°C for 5 min before being applied to gels. Separated protein was visualised by adding Instant Blue Coomassie total protein stain (Expedeon) or InVision™ His-tag In-gel Stain (Thermo Fisher). InVision was used according to manufacturer protocol. Briefly, after electrophoresis, gels were fixed for 1 hour at RT in 50% ethanol, 10% acetic acid in MQ water. Gel was washed twice in MQ water and incubated in stain solution for 1 hour at RT. Gel was then washed in 20mM phosphate buffer before imaging at 560–590 nm. Protein markers used were low molecular weight standards (Bio-Rad) and BenchMark His-tagged marker (Thermo Fisher).

Western Blotting was carried out onto nitrocellulose membranes using a Trans-Blot SD Semi-Dry transfer cell (Bio-Rad). Antibody detection was carried out using the Penta·His HRP Conjugate Kit (Qiagen) according to manufacturer's protocol. Protein markers used were Precision Plus Dual colour standards (Bio-Rad) and BenchMark His-tagged marker (Thermo Fisher)

2.8.7 Protein quantification and storage

Protein concentration was measured in mg/ml at 280 nm using a NanoDrop 1000 Spectrophotometer using estimated molecular weight and extinction coefficient for each construct. Protein concentration was then estimated based on a BSA standard curve scaled to the extinction coefficient of BSA (43,824M^{-1} cm^{-1}). The properties of each of the constructs are given below:

Construct	Estimated Mw (kDa)	Extinction coefficient (M-1 cm^{-1})
6-His-pVI-WT	24.85	24980
6-His-pVI-L40Q	24.86	24980
6-His-pVI-Δ54	22.46	12490
pVI-34-54	2.46	12490

The concentration of protein fractions was carried out using Vivaspin 0.5 ml concentrators 10,000 MWCO PES (Sartorius). Protein fractions were supplemented with 10% w/v glycerol and flash-frozen in liquid nitrogen.

Protein aliquots were thawed as needed and dialysed in 20mM Tris, 300mM NaCl to eliminate glycerol in buffer using Slide-A-Lyzer 10K MINI Dialysis Devices (Thermo Fisher). Samples were centrifuged at 20,000xg for 20 minutes prior to use.

2.8.8 Peptide mapping

Predicted trypsin cut sites and cutting probability were predicted using the Expasy PeptideCutter tool [193]. Digestion and LC-MS/MS were carried out by the Advanced Proteomics Facility, Department of Biochemistry, University of Oxford.

Chapter 3 Biophysical characterisation of Adenovirus protein VI with model membranes

3.1 Introduction

Once a purification protocol for pVI-WT and the two mutant constructs had been established, the next objective was to further biophysically characterise the resulting proteins, crucially necessary for understanding the function of pVI. In this chapter, several biophysical techniques were employed to produce a more detailed overview of pVI structure and membrane lytic function. A combination of prediction software, circular dichroism and analytical ultracentrifugation was used to characterise the structure of the pVI protein generated from the purification protocols in Chapter 2, followed by dynamic light scattering and liposome lysis assays to test protein activity. In addition to structural characterisation, the pVI constructs were also incubated with liposomes to determine their effects on membranes and further understand the mechanism of pVI membrane disruption. The role of individual domains within pVI was investigated by comparing the effect of the wild type and mutant proteins.

The N-terminal 20 residues of the mature pVI protein (34-54) after cleavage by AVP are predicted to form an amphipathic α-helix (AH), which has been identified as the membrane lytic factor, while the rest of the protein is predicted to be largely unstructured [108, 124]. While circular dichroism (CD) spectroscopy has been carried out on pVI-WT and pVI-L40Q

[19], the secondary structure of the truncation mutant pVI-Δ54 is not known, but it is assumed to have less α-helical contact due to the lack of the first N-terminal AH. As these earlier studies were performed using protein of significantly lower purity than achieved here (Chapter 2), the biophysical characterisation experiments were repeated and extended.

The exact location of pVI within the hexon of the AdV capsid is still unknown and little is known about the oligomeric state of pVI (Chapters 1.3.2 and 1.3.3). After endocytosis, pVI is assumed to be released from the capsid into the endosome where it can perform its lytic function [108]. The current model of pVI endosomal lysis is through shallow insertion of the N-terminal AH, resulting in induction of positive membrane curvature and fragmentation of membranes [108, 124, 143]. The *in vitro* experiments that contributed to our current understanding of the interaction of pVI with model membranes included fluorescent microscopy of cells, [119] fluorescent dye release assays [19, 124, 143] and intrinsic tryptophan fluorescence quenching experiments to determine membrane penetration of pVI-WT and pVI-L40Q [19, 143].

Functional dye release assays carried out by Maier et al. and Moyer et al. contributed to the current model of membrane rupture by Ad pVI [19, 124, 143]. In an experiment using liposomes composed of POPC and POPS, wild type pVI and the peptide pVI-34-54, corresponding to the first N-terminal helix, caused a dose dependent release of SRB from

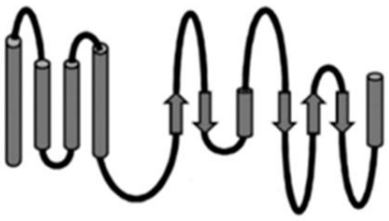
liposomes [10]. pVI-Δ54 membrane-induced SRB release was considerably lower than the wild type, requiring a much higher concentration to reach the same amount of dye release [10]. However, these experiments were performed using simple lipid mixtures that lacked cholesterol. Therefore, cholesterol was included in the liposomes used in this study to provide a more native model of the endosomal membrane.

3.2 Prediction of pVI structure

3.2.1 Prediction of pVI secondary structure

The precise structural conformation of pVI in the context of the virus capsid and in its mature released form are unknown. The N-terminal portion of pVI (residues 34–54) was predicted by Maier et al. to form an AH and three further helices using the PSIPRED structural analysis programme [124, 194]. However, the software has been updated several times since, and while the first two predicted helices predicted by PSIPRED 4.0 remain similar, only one longer helix is now predicted between residues 75–105 (Figure 3.1B). The secondary structure predictions in Figure 3.1B are mostly consistent with the previous prediction that the C-terminal domain of the mature protein, extending from residues 108–225, is mostly or entirely disordered with some predicting a mixture of α-helical and β structure [124, 157].

A



B

```
                31--------41--------51--------61--------71--------81--------91--------101-------111-------121-------131-------141
Sequence:       AFSWGSLWSGIKNFGSTVKNYGSKAWNSSTGQMLRDKLKEQNFQQKVVDGLASGISGVVDLANQAVQNKINSKLDPRPPVEEPPPAVETVSPEGRGEKRPRPDREETLV
PSIPRED*:       CCCCCHHHHHHHHHHHHCCCCCCCCCCHHHHHHHHHHCCCHHHHHHHHCCCCCHHHHHHHHHHHHHHHHCCCCCCCCCCCCCCCCCCCCBBBBCCCCCCBBBBB
PSIPRED 4.0:    CCCCCHHHHHHHHHHHHHHHCCCCCCCHHHHHHHHHHHHCCHHHHHHHHHHHHHHHHHHHHHHHHHHHHCCCCCCCCCCCCCCCCCCCCCCCCCCCCCCCCCCC
RaptorX SS3:    CCCCCHHHHHHHHHHHHHHHCCCCCCCCHHHHHHHHHHHHCCHHHHHHHHHHHHHHHHHHHHHHHHHHHHCCCCCCCCCCCCCCCCCCCCCCCCCCCCCCCCCCC
Jnet:           CCCCCCHHHHHHHHHHHHHHCCCCCCCCHHHHHHHHCCCCCHHHHHHHHHHHHHHHHHHHHHHHHHHHHHCCCCCCCCCCCCCCCCCCCCCCCCCCCCCCCCCCC
Jpred4:         CCCCCCHHHHHHHHHHHHHHCCCCCCCCHHHHHHHHHCCCHHHHHHHHHHHHHHHHHHHHHHHHHHHHHHCCCCCCCCCCCCCCCCCCCCCCCCCCCCCCCCCCC
Predprot:       CCCCCCHHHHHHHCHHHHHCCCCCCCCCHHHHHHHHCCCCCCHHHHHHHHHHCHHHHHHHHHHHHHHHHHCCCCCCCCCCCCCCCCCCCCCCCCCCCCCCCCCCC
Phyre2:         CCCCHHHHHHHHHHHHHHHHHHHHHHHHHHHHHHHHHHHHHHHHHHHHHHHHHHHHHHHHHHHHHHHHHHHHHHHHHHHHHHHHCCCCCCCCCHHHHCCCCCCCCCCCCCHHHCC
SSPro8:         CCCSHHHHTCHCHHHHHHHHTCSCTCHHHHHHHHHHHHTTCHHHCHHHHHHHHHHHHHHHHHHHHHHHHHHCCCCCCCCCCCCCCCCCCCCCCCCCCCCCCBBBBBB

                31--------41--------51--------61--------71--------81--------91--------101-------111-------121-------131-------141

-------151-------161-------171-------181-------191-------201-------211-------221-------231-------
TQIDEPPSYEEALKQGLPTTRPIAPMATGVLGQHTPVTLDLPPPADTQQKPVLPGPTAVVVTRPSRASLRRAASGPRSLRPVASGNWQSTLNSIVGL
BCCCCCCCCCCCCCCCCCCCCCHHHHHCCCCBBBBBCCCCCCCCCCCCCCCCCCCCBBBBCCCCCCBBBBBCCCCCCCCCCCCCCCCCCHHHHHH :
CCCCCCCCHHHHHCCCCCCCCCCCCCCCCCCC
```

Figure 3.1 Predicted pVI secondary structure and conservation results

(A) Ribbon diagram from reference [124], PSIPRED* secondary structure prediction made in 2005 from [108]. (B) Comparison of predicted secondary structure elements from several prediction servers. H (red), helical residues. B (blue), Beta sheet residues. References for prediction servers, PSIPRED 4.0 [195], RaptorX [196] Jnet [197], Jpred4 [198], Predprot [199], Phyre2 [200], SSPro8 [201]. (C) Sequence alignments of mature pVI protein from multiple AdV types. (i) Conservation of residues. Purple, high conservation. Green, low conservation. Only alignment positions with no gaps are coloured. (ii) Hydrophobicity of residues. Red, hydrophobic. Blue, hydrophilic. Alignment schematics were created using the NCBI Multiple Sequence Alignment Viewer, Version 1.19.1 from 30 human and simian AdV sequences aligned using NCBI Standard Protein BLAST.

Fig 3.1Ci demonstrates that pVI proteins from human and simian AdV are highly conserved, with most of the variation found in the C-terminal half of the proteins, in agreement with the literature [108]. The entire ~110 residue N-terminal portion is the best conserved, indicating its importance to the function of pVI. Fig 3.1Cii indicates that pVI is weakly hydrophobic overall.

3.2.2 Prediction of pVI disorder

Intrinsically disordered proteins (IDPs) are characterised by the lack of a stable, well-defined tertiary structure under physiological conditions. The C-terminal region of pVI has similarities to IDPs, including a low proportion of bulky hydrophobic residues and high number of charged residues [202, 203]. IDPs and intrinsically disordered regions (IDR) within proteins are thought to exist in a dynamic and flexible conformation and can become structured upon binding to their specific biological targets, including lipid membranes or

other proteins [2, 3]. IDPs are highly represented in eukaryotic proteins and around 30% of eukaryotic proteins contain IDRs larger than >50 residues [204]. Nuclear magnetic resonance (NMR) spectroscopy is the major experimental method for the characterization of disordered proteins, but CD spectroscopy and biochemical studies of proteolytic susceptibility can also provide important information [202, 205]. Disordered regions are inherently sensitive to proteolysis due to residues being exposed to the solvent and not protected within a folded core [205, 206]. The C-terminus of pVI-WT appears to be particularly sensitive to protease degradation, as confirmed by mass spectroscopy analysis of the two bands typically obtained through SDS-PAGE analysis of pVI-WT (Figure 2.18).

A large portion of mature pVI in the region from around residue 107 to 225 is predicted to be unstructured, and is less conserved than the N-terminal portion (Fig 3.1Ci). A number of programs are available for the prediction of unstructured regions from amino acid sequences of proteins. The Predictors of Natural Disordered Regions (PONDR), utilise a neural network with various polypeptide sequence characteristics as training sets to predict disorder tendency in proteins [207]. Constant improvements are made to these software packages and the various versions of PONDR are distinguished by their training sets and machine learning models. PONDR VL-XT uses three neural networks based on X-ray crystallography and NMR studies [208].

The IUPred server provides an alternative algorithm for predicting disordered regions in polypeptide sequences by estimating pairwise energy interactions between residues, based on the hypothesis that the primary sequence of IDPs does not allow favourable interactions to form [209, 210]. Both PONDR and IUpred calculate a score of disorder tendency for each residue between the value of 0 and 1, with predicted scores above 0.5 indicating disorder [210]. The predicted disorder of mature pVI-WT and the two mutant proteins were run using these two programmes and the prediction profiles are presented in Fig 3.2.

The first ~20 residues of the mature pVI sequence (aa 34–54), which correspond to the membrane lytic AH, have an intrinsic disorder score below 0.5 in both the PONDR VL-XT (Fig 3.1B) and IUpred (Fig 3.1C) prediction profiles, indicating that the sequence is ordered. This is consistent with the outputs of secondary structure prediction programmes presented in Figure 3.1 and with the analysis of Maier et al. [124]. The various secondary prediction software servers returned different predictions for helices within the first 107 residues, but most predicted residues 38–51 as helical. In the PONDR disorder profile (Fig 3.1B), this sequence has the lowest score of any part of the sequence, of less than 0.1. The PONDR prediction also indicates a less structured section between residues ~54–65, which corresponds to a gap between helices in most of the outputs in Fig 3.1. The rest of the sequences are predicted as disordered, which is also in line with previous predictions.

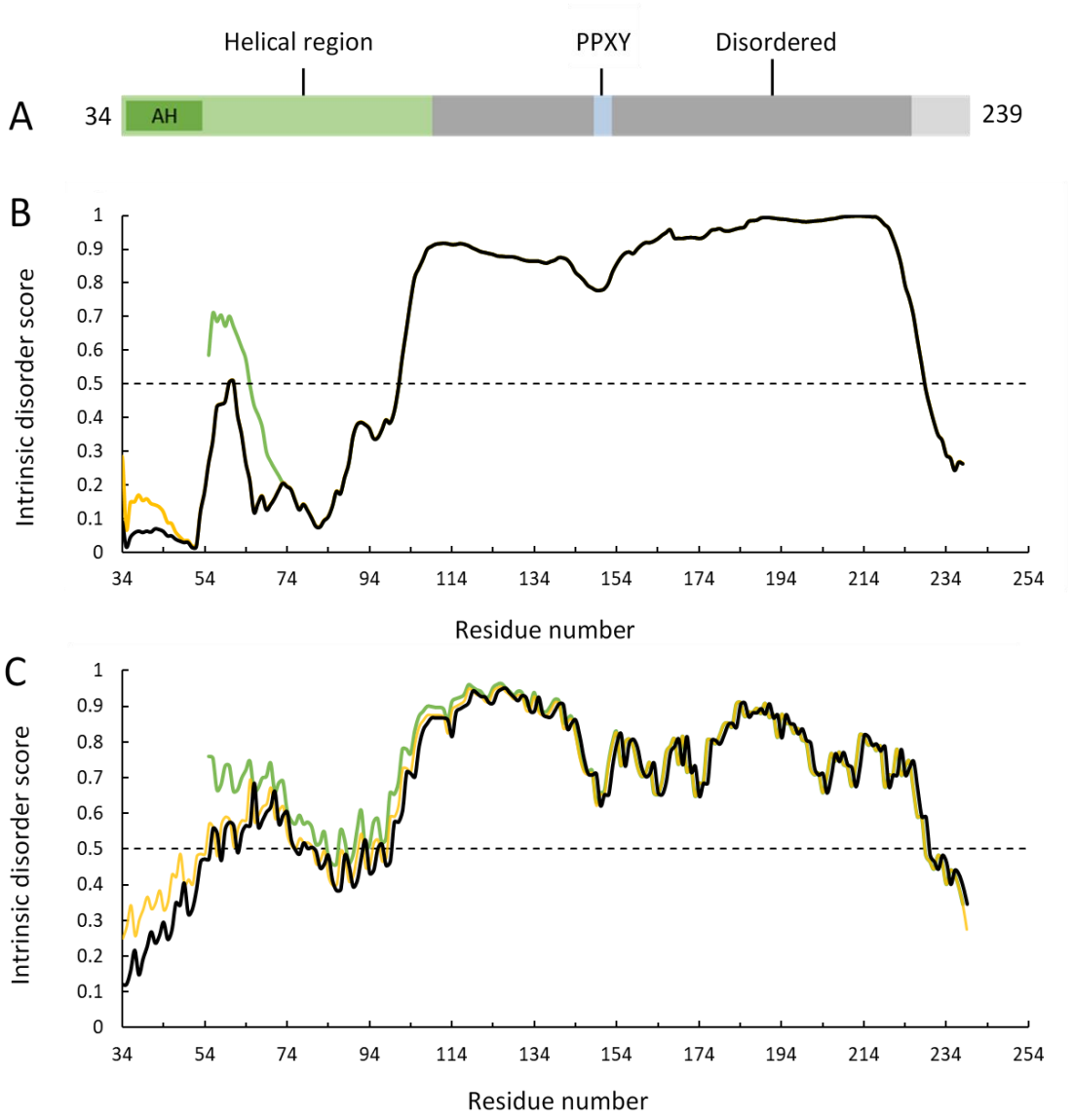


Figure 3.2 Disorder prediction profiles of pVI-WT and mutants.

(A) Predicted domains of pVI. NTH, N-terminal helix. (B and C) Structural disorder predication profiles for mature pVI-WT (black), pVI-L40Q (yellow) and pVI-Δ54 (green). (B) PONDR VL-XT prediction (C) UIpred2A prediction.

The predicted disorder score for pVI-L40Q is higher in both profiles up to residue ~52, after which it is very close or identical to that of pVI-WT. The small (<0.3) spikes in the PONDR profile of pI-L40Q at the N-terminus may correspond to disruption of the N-terminal AH by the point mutation. Both profiles predict more disorder in the N-terminus of pVI-Δ54, which is consistent with the lack of the first N-terminal helix. The final ~10 residues were predicted to be ordered, which corresponds with several functional motifs found at the C-terminus. The rest of the protein has a high predicted disorder score in both profiles, which also agrees with the secondary structure predictions. Previous studies of pVI focused on the role of secondary structure elements, and the role of disorder in protein function has been examined more closely in the literature since those studies [211, 212]. Therefore, the work in this chapter also aimed to consider the potential role of disorder in pVI function.

3.3 Analysis of pVI folding state

3.3.1 Analysis of pVI secondary structure using circular dichroism.

Circular dichroism (CD) spectroscopy was used to evaluate the folding state of purified recombinant pVI-WT and mutants. CD spectroscopy is an important technique for the determination of folding properties and presence of secondary structure elements of proteins in solution [213]. CD is the difference in absorbance of left-handed and right-handed circularly polarized light by optically active chiral groups in a molecule [214]. While

CD spectroscopy does not reveal the secondary structure of specific residues, the advantages of the method include relatively fast data collection and analysis and the low sample concentration required [214].

CD is measured as a function of wavelength. The far-UV CD of a protein (180 to 260 nm) originates primarily from its peptide bonds and is used to determine secondary structure [215]. CD is measured as millidegrees ellipticity and can be converted to mean residue molar ellipticity upon correction for protein concentration. α-helices have strong negative signals around 208 and 222 nm, and a positive signal at 195 nm, while β-sheet structures have negative signals around 218 nm and positive signals at 190 nm [216, 217]. Random coil structures have very low ellipticity above 210 nm and negative peaks near 195 nm [214, 218]. Proteins with mixed secondary structure content will result in a combination of these elements [219]. pVI-WT and L40Q have been previously been analysed using CD by Moyer et al, whose data demonstrated elements of alpha helical motifs in pVI-WT, with negative peaks at 208 and 222 nm for, but not for pVI-L40Q [19]. pVI-Δ54 has not previously been analysed using CD but based on structural predictions and functional analysis of the construct from the literature [124, 143], it was expected that α-helical structure would be weaker or absent. CD spectra for independent protein preparations of pVI-WT, pVI-L40Q, pVI-Δ54 and peptide 34-54 were acquired and are shown in Figure 3.3.

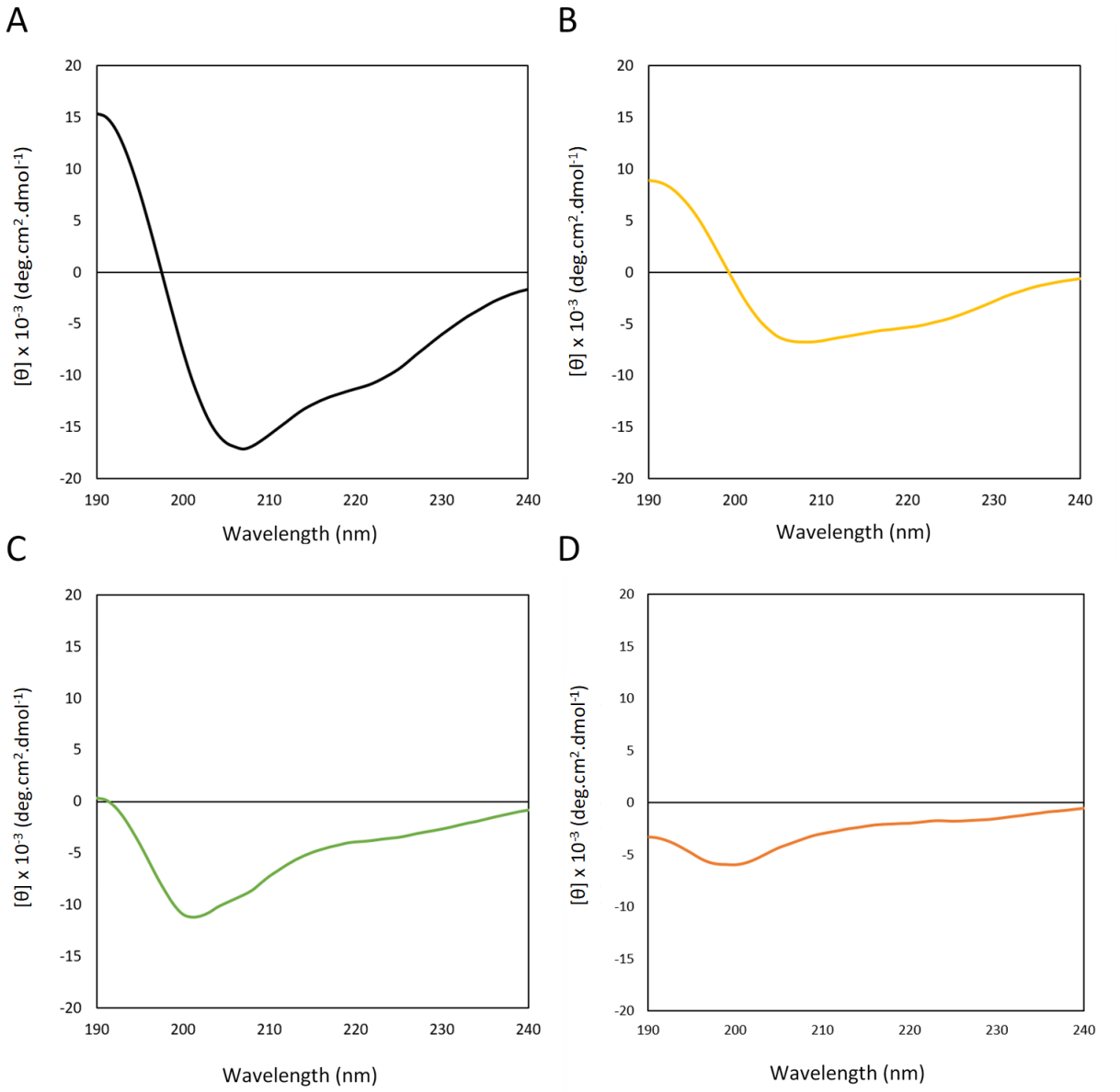


Figure 3.3 Analysis of pVI secondary structure using Circular Dichroism.

The representative CD spectra of purified pVI-WT (A), VI-L40Q (B), pVI-Δ54 (C) and pVI- 34-54 (D) are presented as mean residue molar ellipticity as a function of wavelength between 190 and 240nm. Spectra are averages of 9 scans.

All of the proteins had an apparent mixture of secondary structure elements. A strong negative peak at approximately 208 nm is present in the pVI-WT spectrum (Fig 3.3A), similar to those indicative of α-helices. However, the peak at 222 nm is much weaker than a typical α-helical structure and is closer to 195 mm, as expected for the random coil configuration. Therefore, the pVI-WT sample most likely had a mixture of α-helical and random coiled structure. The spectrum acquired for pVI-L40Q had weaker positive and negative peaks than pVI-WT that suggested a mixture of β-sheet and α-helical elements (Fig 3.3 B). The lower helical content may correspond to the alteration of the N-terminal helix. The truncation mutant pVI-Δ54 (Fig 3.3C) lacks a positive peak at the lower wavelengths for α-helical elements; there is a small negative shoulder at 208 nm, consistent with some helicity, but the spectrum is also negative at 195 nm, where the peak would be expected for random coil conformations.

All CD measurements performed in this study were collected in 20 mM NaCl buffer, which may reduce the ability of proteins to fold. Data collection was not possible at NaCl concentrations above 20 mM since chloride ions increase the absorbance of solutions in the 190-200 nm range, resulting in noisy data in this region [215]. The CD data presented by Murayama et al. for the peptide [168] and Moyer et al. for pVI-WT and pVI-L40Q [19] were collected in 150 mM buffer, and the spectra for pVI-WT and pVI-L40Q in Fig 3.3. indicate more random coil conformation compared to samples analysed by Maier et al. [19], possibly due to not refolding after urea was removed during affinity purification.

3.3.2 Analysis of pVI oligomeric state using analytical ultracentrifugation.

To investigate the oligomeric state of pVI, analytical ultracentrifugation (AUC) experiments were performed. AUC is used to determine molar mass and oligomeric state in solution, as it allows the properties of proteins to be studied in their native state under biologically relevant conditions, requiring no label or chemical modification [220, 221]. Sedimentation velocity (SV) describes the rate of a protein's migration in the centrifugal field [222]. In sedimentation velocity experiments, the sedimentation coefficient 's' and the diffusion coefficient 'D' can be determined, and from these parameters the Molar Mass 'M' can be calculated via the Svedberg equation. Two samples of pVI-WT and one sample of pVI-Δ54 were assayed using sedimentation velocity analysis. The data were analysed using the c(s) continuous distribution model and sedimentation profiles are shown in Figure 3.4.

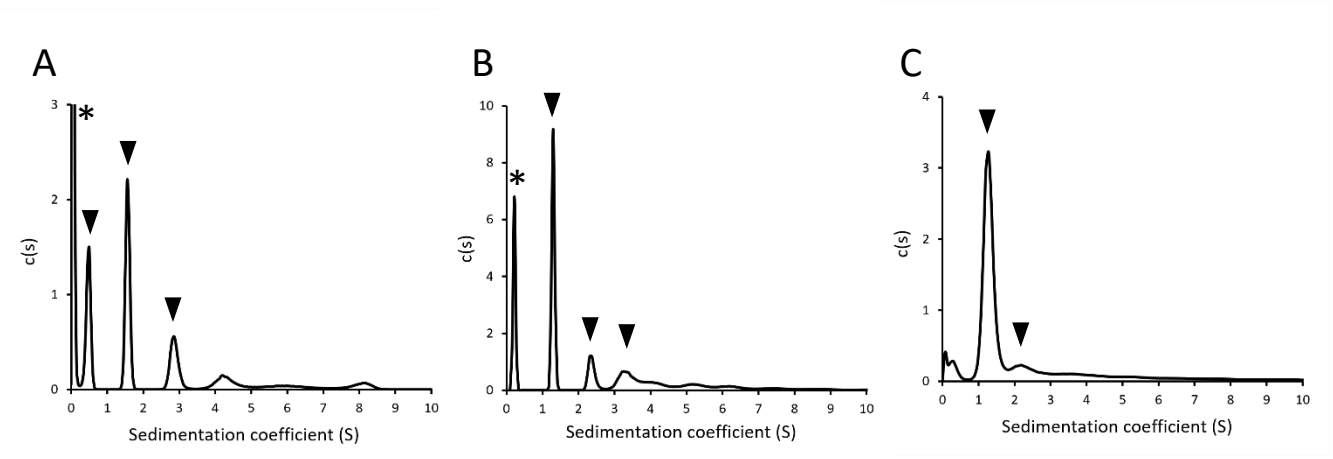


Figure 3.4 Sedimentation coefficient distribution c(s) from the analysis of interference data for pVI-WT and pVI-Δ54 samples.

Proteins purified according to the protocol described in Chapter 2. A) pVI-WT at 0.7 mg/ml. B) pVI-WT at 1 mg/ml C) pVI-Δ54 at 0.7 mg/ml. Arrowheads, main peaks. Asterisks, low Mw contaminant peaks.

The continuous distributions for the two pVI-WT samples have similar profiles with 4 clear peaks (Fig 3.4 A and B). The peaks for the 0.7 mg/ml pVI-WT sample (Fig 3.4 A) had sedimentation coefficients of 0.6, 1.6, 3 and 4.7 S. These peaks represented 21.9, 39, 17.5 and 5.3 % of total sedimenting material, respectively. In the 1 mg/ml sample (Fig 3.4 B), the same pattern of peaks had values of 0.2, 1.3, 2.4 and 3.7 S. These peaks represented 20, 34, 10 and 22% of total sedimenting material, respectively. It was noted that despite the similar profiles, the sedimentation coefficients did not closely match, with the 0.7 mg/ml sample (Figure 3.4A) having larger values for all peaks. The 0.7 mg/ml sample contained an apparent large peak of rapidly sedimenting species at 0 S. This type of peak is frequently obtained as an artefact introduced by convection near the meniscus or by sample reference buffer mismatch. However, this peak resulted in the overestimation of the sedimentation

coefficient values for the subsequent peaks. The difference in s value could also be explained by the dependence of sedimentation coefficient on concentration, as molecules in a more concentrated sample experience more interference from other molecules, resulting in a smaller s values [220]. This factor is referred to as sc and the effect is also more pronounced in disordered states, further indicating that pVI-WT is disordered [223]

The non-linear regression tool in SEDFIT [224] was used to find the best-fit frictional coefficient (f/f0). The best-fit f/f0 for the 0.7 mg/ml sample pVI-WT was 1.46 and for the 1 mg/ml sample was 2.29. The behaviour of pVI-WT during purification and the results of disorder prediction (section 3.2.1) and CD analysis (section 3.3.1) would indicate that it is unlikely this protein has the well folded globular structure indicated by the f/f0 value of 1.46, and instead the f/f0 of 2.29 more realistically describes the likely disordered nature of pVI-WT. The lower f/f0 of the 0.7 mg/ml sample results in larger apparent s values for all peaks than those seen for the 1 mg/ml sample, where this artefact peak is absent. This interpretation of the SV results is further supported by the estimated molecular weights generated for each of the sedimentation peaks in both samples.

For the 0.7 mg/ml sample (Fig 3.4 A) with the best-fit f/f0 1.49, the molecular weights for the 4 main peaks are 2.2, 16.2, 40.1 and 73.2 kDa. For the 1 mg/ml sample (Fig 3.4 B) with the best-fit f/f0 2.29, the same profiles of peaks are estimated to be 1.7, 24, 59.5 and 101 kDa. The monomer peak for the 0.7 mg/ml pVI-WT sample (Figure 3.4A) had a calculated

Mw from C(s,ff0) analysis very close to the predicted and apparent weight (24.8 kDa), and this peak comprised ~40% of the total sedimenting material. Peaks 3 and 4 were also much closer to the weight of a theoretical dimer and trimer, respectively, with ~18% of the sedimenting material in the dimer peak and 5% for the putative trimer peak. In the 1 mg/ml sample, the calculated Mw of the main sample peak (Fig 3.4 B, first arrow) had a predicted weight of 24 kDa that comprised ~34% of sedimenting material, while the next peaks comprised 10 and 22% of the total material. As pVI constructs are prone to degradation from the C-terminus (Chapter 2), these smallest molecular weight species (Fig 3.4 A and B, indicated by the asterisks) may represent small degradation products present in both samples.

To investigate whether the N-terminal AH, essential for membrane lysis activity, was involved in possible oligomerisation of pVI, the same experiment was carried out with the 0.7 mg/ml pVI-Δ54 sample (Fig 3.4 C). The continuous distribution modelled a dominant peak for pVI-Δ54 (indicated by the arrowhead) at 1.3 S comprising 60% of all sedimenting material and with an estimated molecular weight of 22.4 kDa, in excellent agreement with the predicted and apparent molecular weight (22.4 kDa). As with the pVI-WT samples, there are higher molecular weight species, but they contribute much less material than those identified in the pVI-WT distribution. The peak at 2.6 S comprises ~10% of the sedimenting material and is estimated to be 56.9 kDa with 3% material contained in a possible trimer peak at 3.3 S corresponding to a weight of 92.8 kDa. These masses are also in close

agreement with the 1 mg/ml sample of pVI-WT. Reassuringly the best-fit frictional ratio for pVI-Δ54 was 2.21, close to the 1 mg/ml pVI-WT sample. Given that these two constructs are largely similar in composition with the mutant missing only 20aa, the agreement in frictional coefficients suggests a similar, largely disordered protein structure in both.

Overall, the evidence from all three samples suggests that pVI-WT and pVI-Δ54 are predominately monomer in solution. Both pVI-WT samples have species of 2–3 times the mass of the monomer which may represent dimers or trimers. Peaks with even larger S values, which contribute less material than the other peaks overall, could be caused by higher order oligomers. The increased presence of higher Mw species of 1 % (40.1 kDa) and 5% (73.2 k Da) in the 0.7 mg/ml sample and 10% (59.5 kDa) and 22% (101 kDa) in the 1 mg/ml sample, might simply be due to better detection of these species. Alternatively, these may represent aggregated protein due to the higher concentration. Interestingly, in the pVI-Δ54 sample (Fig 3.4 C) the monomer peak was substantially higher (at 60%) than for the pVI-WT samples. There was markedly lower contribution from higher Mw peaks (at 9 and 3%), indicating less oligomerisation or aggregation by the truncated mutant. The sedimentation distribution suggests that the mutant sample was more homogenous than the pVI-WT samples, although this may relate to the behaviour of pVI-Δ54 during purification and the difference in the lysis buffers used.

It is not known whether pVI oligomers have the same lytic activity as monomers, or any at all. However, the presence of species that matched the expected size of oligomers for both pVI-WT and pVI-Δ54 from sedimentation velocity analysis (Fig 3.4) suggests that domains other than the N-terminal AH of the protein, possibly the other predicted helices, could contribute to oligomer formation or stability of oligomers. The sedimentation coefficient distribution profiles of both pVI-WT samples also contained small Mw species of approximately 2–5 kDa. These small Mw species in the sedimentation analysis may represent C-terminal degradation that was the likely cause two main protein bands observed on SDS-PAGE gels throughout Chapter 2.The percentage of total mass of these species was similar for both pVI-WT samples, at approximately 20%. For the pVI-Δ54 sample, the contribution of the lower Mw material in peak 1 was less than that seen in the WT samples, potentially indicating lower amount of degradation of the C-terminus. However, it is more likely that these smaller species represent experimental artefacts rather than contaminants.

3.4 Analysis of pVI–membrane binding

Having investigated the secondary structure and oligomeric state of pVI, the constructs purified according to the optimised protocol were applied to model membranes to investigate their membrane disruptive activity. Liposomes are closed spherical vesicles consisting of one (unilamellar) or more (multilamellar) phospholipid bilayers that self-

assemble from water-insoluble phospholipids when mixed with water. Lipid composition determines the properties of liposome preparations, such as surface charge and fluidity of the bilayer [225]. Small unilamellar vesicles (SUV) typically have diameters of 20–100 nm, while large unilamellar vesicles (LUV) can be 200 nm or larger. Multilamellar vesicles (MLV) are formed of several concentric bilayers and are generally larger in size. MLV typically form through hydration of layers of dried lipids and can be broken down through cycles of freezing and thawing or sonication. Extrusion through a membrane with a defined pore size results in a liposome preparation with a desired size distribution. Several methods can be used to determine SUV size, including size exclusion chromatography (SEC), light scattering, ultracentrifugation, and electron microscopy [226]. These techniques can also be used to investigate protein-lipid interactions through changes in size distribution or morphology.

The membrane-disrupting activities of recombinant pVI-WT and mutants were explored using two complimentary methods, dynamic light scattering (DLS) and liposome leakage assays. In order to investigate the interaction of pVI with membranes, simple liposomes composed of 40% PC, 30% Phosphatidylethanolamine (PE) and 30% cholesterol were generated and sized by extruding through a 100 nm filter membrane, then analysed alone or after incubation with protein or peptide. Wiethoff et al. demonstrated that purified pVI alone is sufficient to rupture liposomes composed of PC, PE and PS [97]. They found that membrane lytic activity was not affected by presence of the N-terminal 6-His-tags in their

experimental system, and therefore the protein can be used without tag removal (Harald Wodrich, personal communication). Cholesterol and PE were included in the lipid mixture to increase biological relevance of the liposomes compared to the POPC/POPS or POPC/POPS/POPE mixtures used in previous studies [19, 124, 143]. Cholesterol has important roles in membrane fluidity and stability, owing to its structure that alters acyl chain packing [227, 228], and *in vivo* cellular experiments have shown that cholesterol is necessary for AdV internalisation and endosomal escape [229]. The plasma membrane is estimated to contain between 25 and 50 mol% cholesterol and around 15 mol% PE [230]. The proportion of cholesterol is lower in late endosomes but the proportion in early endosomes is not well defined [227, 230].

The shape of individual lipids is determined by their head group and hydrophobic tail sizes, and these properties affect the propensity of these lipids to assemble into lipid bilayers, as well as the curvature of the bilayer. The smaller head group of PE gives it a conical shape that can promote negative membrane curvature [227, 231] and increase the rigidity of membranes [228]. As DLS measures the size distribution of the particles in solution, stable interaction of pVI-WT and mutants with liposomes will be revealed as change in size of the particles, either as a decrease in size if liposomes are fragmented or an increase if liposomes aggregate. Building on from this, the liposome leakage assay is an indirect measurement of dye concentration that measures the ability of these proteins to disrupt membranes.

3.4.1 Analysis of pVI-liposome interactions using dynamic light scattering

DLS was used as a preliminary screen for pVI-membrane interaction, as it enables analysis of the sizes of particles in solution. The pattern of light scattered by particles in solution will fluctuate over time due to changes in the interference patterns between neighbouring particles as a result of Brownian motion [232]. From these measurements, the particle size and size distribution can be calculated. DLS can be used to study interactions between macromolecules and aggregation in solutions [12]. Measurements are rapid and non-destructive and the technique requires relatively small sample volumes [233]. DLS can complement data from other analytical methods, such as SEC, mass spectrometry and analytical ultracentrifugation [226]. DLS has not previously been used to study the interaction of pVI-WT with liposomes. The technique can provide accurate information about the range of liposome sizes in a sample and is therefore useful for assessing the influence of pVI on liposomes.

The DLS results shown here are presented as an intensity distribution of particle sizes weighted according to the scattering intensity of each particle fraction, which is proportional to the square of the molecular weight [234]. The hydrodynamic diameter (D_h), the mean particle size, is that of a hypothetical sphere with the same diffusion behaviour as the particle under examination and is calculated from the translational diffusion coefficient. Polydispersity index (PDI) is used as a measure of the range of molecular weight

distribution within a samples. PDI values below 0.5 indicate a relatively homogenous sample, whereas greater values indicate heterogeneity of molecular weight. Each of the three recombinant constructs and peptide were mixed with PC/PE/chol liposomes and DLS was used to measure D_h. The particle size distribution of each sample is shown in Figure 3.5.

The z-average (mean size) D_h values of pVI-WT pVI-L40Q, pVI-Δ54 and pVI-34-54 measured alone (dotted lines) were 9.26, 10.00, 8.77 and 7.8 nm, respectively. The peak D_h for liposomes measured alone (grey line, all panels) is broad and extends from approximately 80 nm to 500 nm but had a PDI value of 0.058 (Fig 3.4 A–C) or 0.071 (Fig 3.5 D), indicating relatively homogeneous samples. The liposomes alone had an average D_h of 138.69 nm (Fig 3.5 A–C) or 126.32 nm (Fig 3.5 D). Buffer measured alone had a D_h value of 3.63 nm.

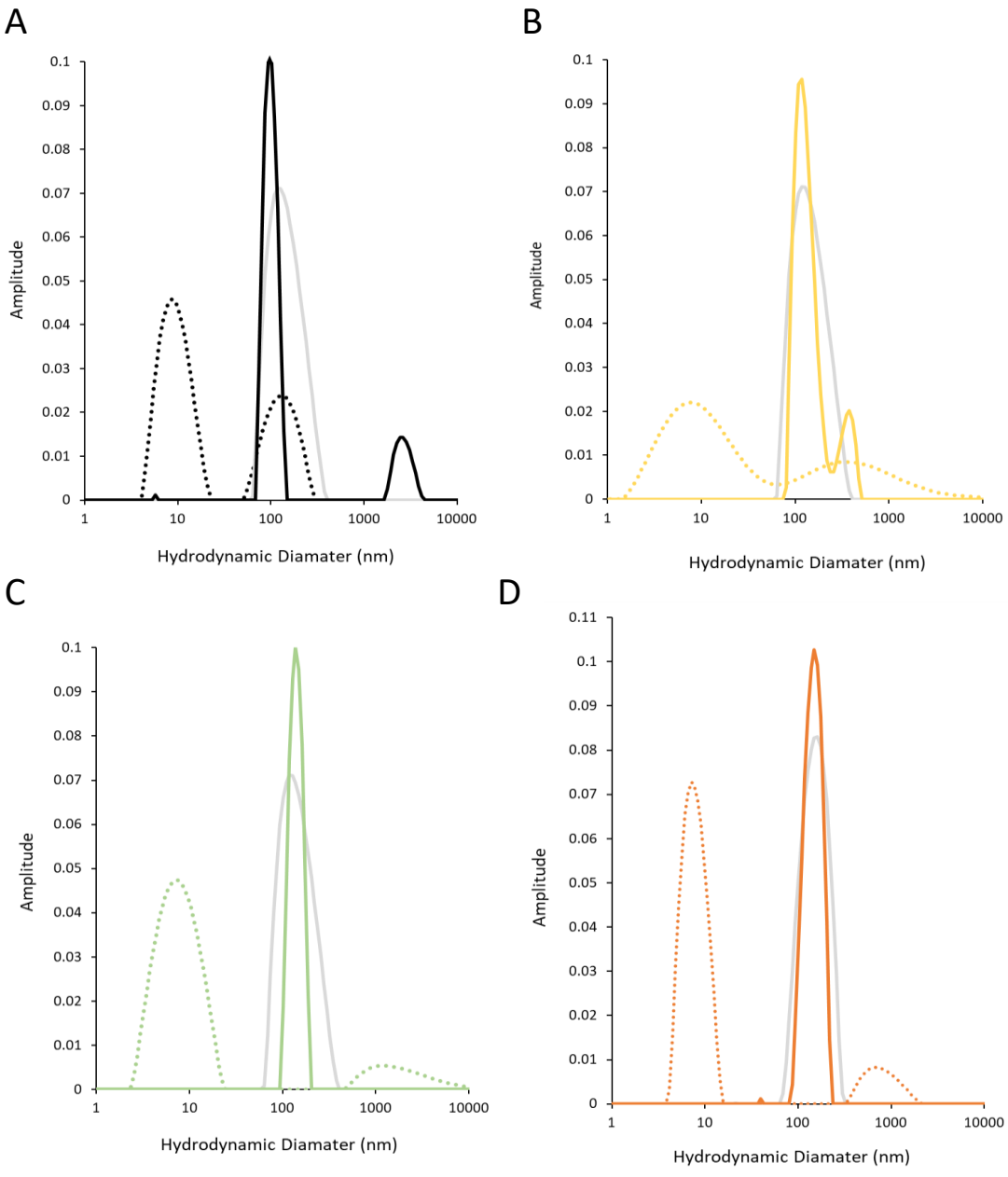


Figure 3.5 Analysis of protein-membrane interactions using Dynamic Light Scattering.

DLS particle size distributions of 1.5 µM 40% PC, 30%PE, 30% cholesterol liposomes mixed with 20 µM pVI-WT (A), 20 µM pVI-L40Q (B), 24 µM pVI-Δ54 (C) and 200 µM pVI-34-54 (D) incubated with 100 nm diameter liposomes. Dotted lines, protein measured alone at ~20 µM and peptide at 200 µM. Grey lines, liposomes without protein at ~1.5 µM.

When pVI-WT is incubated with liposomes (Fig 3.5A), a separate peak of approximately 2000–6000 nm is present, resulting in an increased average D_h value of 142.13 nm and PDI of 0.562. In the pVI-L40Q sample (Fig 3.5B), an additional peak of ~4000–6000 nm is present, the D_h increased to 140.61 nm and the PDI to 0.078. The average D_h of liposomes incubated with pVI-Δ54 (Fig 3.5C) was 137.36, the PDI was 0.252, and there was no larger diameter peak. The average D_h value of liposomes incubated with pVI-34-54 (Fig 3.5D) was 133.85 nm and the PDI was 0.595. A very small peak at around 60 nm is also present in the peptide sample. Such peaks can also be the result of signal from the buffer component in the sample [235].

The size of the main liposome peak of ~100 nm narrows when any of the pVI constructs are added to liposomes, indicating a more heterogenous size distribution within the sample. This effect is most pronounced for pVI-WT and pVI-Δ54 and much less pronounced for the peptide. It is not clear why the liposome distribution is more heterogenous in the presence of the pVI constructs, but this could be an effect of their association with membranes. The binding of protein to the liposome membranes would be expected to change the intensity of light scattering altering the signal detected, which may explain the narrowing of the peaks. As all constructs alter the size distribution profile, it is evident that all four constructs interacted with the liposomes in some way. pVI sticking to the liposome surfaces helping to define them better.

There is no indication of liposome lysis, which would be expected to result in a reduction in amplitude of the main peaks, instead the amplitude increases. The PDI of liposomes incubated with all of the constructs increases, but with pVI-WT and the peptide, it rises above 0.5, indicating a more heterogenous sample. However, the narrowing of the peak indicates less heterogeneity. The high PDI agrees with the size distribution profile for liposomes incubted with pVI-WT, but not for peptide, which demonstrated less change to the main peak than the recombinant pVI proteins and no additional large diameter peak. On the other hand, liposomes incubated with pVI-L40Q have a very low PDI despite the additional peak of 4000–6000 nm.

The additional high diameter peaks present in the liposome samples with pVI-WT and pVI-L40Q are not present in the distribution of pVI-WT collected alone and may indicate the aggregation of intact or disrupted liposomes as a result of association with protein. The size distribution profiles for liposomes with pV-WT and pVI- L40Q are similar, but the PSI for the pVI-L40Q samples is much lower, indicating that the larger sized aggregate peak for PVI-WT has more impact on the PDI and results in a more heterogenous sample. The very small peaks between 8 and 50 nm present with WT and peptide possibly represent fragmented membranes of very small diameter. While the membrane interacting activity of the peptide in both DLS and dye release assays was low, the changes in peak diameter reveal some differences in interaction between liposomes and the constructs that reflect their function.

3.4.2 Exploration of membrane disruption by pVI using a fluorescent dye release assay

pVI-WT has been found to cause membrane damage in vitro, and this property can be explored using dye-filled liposomes to assess the percentage of dye released due to membrane rupture. The fluorescent dye sulforhodamine B (SRB) self-quenches at around 10 mM [236]. As fluorescent dye leaks from the liposomes it becomes diluted and therefore dequenched, and an increase in fluorescence is seen. After addition of protein, buffer, or Triton X-100 detergent (control), the fluorescence of 100 nm diameter liposomes loaded with SRB were monitored for 90 minutes. Simple liposomes composed of PC and cholesterol were initially used while developing the experimental protocol for the dye release assay, but these liposomes were harder to handle and tended to dequench more quickly in the absence of protein. Therefore, PE was added both for ease of use and so that liposomes closer resembled biological membranes. Figure 3.6 compares the percentage dye release by liposomes incubated with each construct over a range of concentrations.

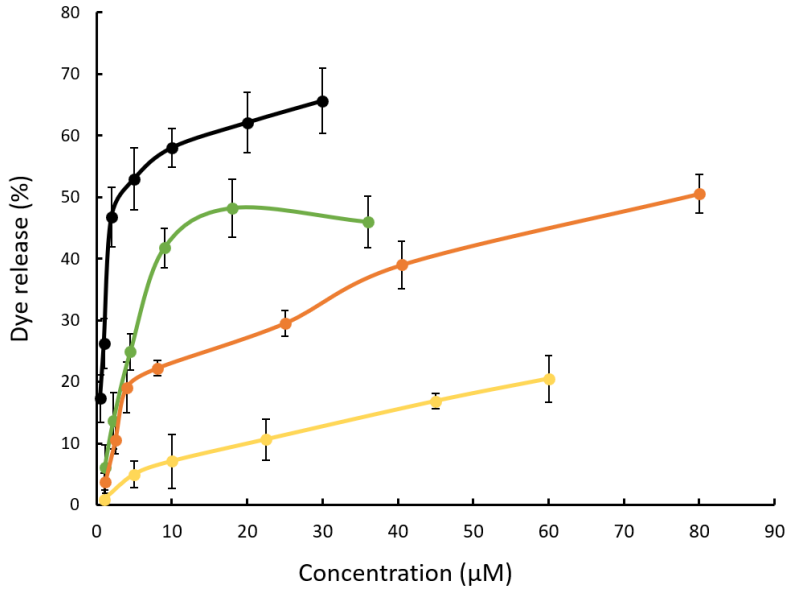


Figure 3.6 Analysis of protein-membrane interactions using a fluorescent dye release assay.

pVI-WT (black), pVI-Δ54 (green), pVI-L40Q (yellow) pVI 34-54 peptide (orange). Error bars represent the standard deviation of each measurement.

The percentage of dye release increased with protein concentration for all pVI constructs. pVI-WT demonstrated more membrane lytic activity than any of the other pVI constructs, with maximum observed dye release of 65.0 % at 30 µM. Surprisingly, pVI-Δ54 produced the next highest dye release of 48.5 % at 18 µM, although the percentage dye release dropped slightly to 45.9 % upon doubling the protein concentration. The peptide produced 50.6 % dye release at 80 µM, a much higher concentration than required for pVI-WT or pVI-Δ54. pVI-L40Q produced the lowest percentage of dye release at its highest concentration, at 20.5 % at 60 µM, double the concentration required to elicit maximum dye release for

pVI-WT. pVI-WT caused the highest rate of increase in fluorescence, followed by peptide and pVI-Δ54 with pVI-L40Q having the lowest rate.

Results of previous *in vitro* functional assays using 75% POPC and 25% POPS liposomes found that pVI-L40Q was more effective at releasing dye than pVI-Δ54, and that in order for pVI-Δ54 to elicit the same percentage of dye release as pVI-WT, it had to be used at ~200 times the concentration [19, 124]. Therefore, the degree of membrane lytic activity seen for pVI-Δ54 in Figure 3.6 was unexpected, since this construct demonstrated less activity than pVI-WT and pVI-L40Q in previous publications [19, 124]. Based on previous SulfoB release assays and microscopic examination of large vesicles, the low activity of the peptide in dye release experiments was also unexpected [124, 143].

Recombinant pVI-WT and peptide proteins used in this experiment produced lower levels of dye release compared to previous experiments. Even at more than double the concentration of pVI-WT, the peptide was unable to elicit the same degree of dye release reported by Maier et al. [124] The differences in membrane composition used in these experiments may explain the lower membrane disrupting activity observed here, since the properties of PC/PE/cholesterol liposomes differ substantially from POPC/POPS liposomes. The percentage of PE used in the experiments reported here was higher, which may explain why much higher concentrations of protein were required to produce a similar percentage of dye release. Additionally, cholesterol has a role in membrane rigidity [237], and more

energy is required to bend membranes with a higher percentage of cholesterol [238-240]. These properties may explain why higher concentrations of pVI-WT were required to see a similar percentage dye release as in previous experiments where cholesterol was not used [19, 124]. However, the differences in membrane composition between these sets of experiments, particularly the inclusion of cholesterol in my experiment, mean that it may not be appropriate to compare them. Maier et al. performed further dye release experiments to determine whether pVI induces positive or negative membrane curvature by using PE and lysophosphatidylcholine (lysoPC), which has a preference to adopt positive curvature. They found that PE inhibited pVI membrane lytic activity [124].

3.5 Discussion

Several complementary biophysical techniques were used to characterise the recombinant pVI proteins purified according to the protocol developed in Chapter 2 and the peptide composed of residues 34–54 of the mature protein. pVI is predicted to contain several functional regions including an N-terminal amphipathic helix [124]. The rest of the protein is mostly disordered and shares several features commonly found in found in intrinsically disordered proteins [189, 241]. However, the oligomeric state and precise nature of the interaction of pVI with membranes is not well understood, and the aim of this chapter was to answer some of the remaining questions about pVI structure and how it relates to membrane interaction. AUC analysis of pVI-WT and pVI-Δ54 samples (Fig 3.4) suggested

that neither adopt an ordered, globular structure in solution, in agreement with disorder predictions (Fig 3.1). Based on the existing literature, pVI-WT was expected to possess the most secondary structure and membrane-lytic activity, in comparison to the two mutants. The peptide was expected to lack secondary structure but exhibit similar or higher membrane lytic activity than pVI-WT [124]. CD analysis revealed that all of the pVI constructs exhibited mixed secondary structure characteristics, and the resulting spectra are compared in Fig 3.7.

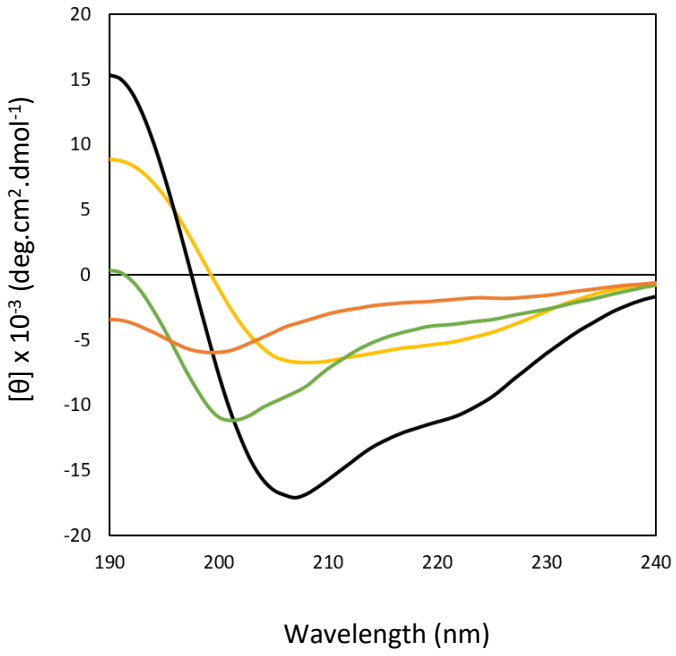


Figure 3.7 Comparison of the Circular Dichroism spectra.

The representative CD spectra for each construct from Figure 3.3 are compared. Black, pVI-WT. Yellow, pVI-L40Q. Green, pVI- Δ54. Orange, peptide pVI-34-54.

The results of the CD analysis are in agreement with the secondary structure predictions (Fig 3.1) and disorder predictions (Fig 3.2), since pVI-WT demonstrated the strongest α-helical structure and pVI-L40Q demonstrated less apparent helical character, consistent with the higher disorder score in the N-terminal 20 residues. These findings are also consistent with the CD analysis performed by Moyer et al. who found less helical structure present in pVI-L40Q than pVI-WT [19]. The CD spectrum for pVI-Δ54 indicates a much weaker α-helical element in a predominantly randomly coiled structure, which was also consistent with the higher disorder predicted in its N-terminus due to having one fewer helix. CD analysis of the pVI-Δ114 mutant, corresponding to the N-terminal 80 residues of mature pVI (residues 34–114) found greater helical content than pVI-WT [124], further suggesting that it is the C-terminal portion of recombinant pVI-WT which contributes the randomly coiled elements observed in the CD spectrum in Fig 3.7. The spectrum from peptide 34–54 corresponding to the first helix of pVI-WT is not folded, which is consistent with the CD analysis previously performed for this peptide [168].

While little was previously reported about the oligomeric state of pVI, it was expected that some higher order species might be present based on studies of disassembled wild type virus capsids [242] and size-exclusion chromatography studies of protein purified from AdV capsids [58] that indicated that pVI forms dimers. The oligomeric state of pVI within the mature AdV capsid is also not known. There are three potential pVI binding sites within each hexon cavity, but the copy number of pVI is disputed due to lack of strong density present

for mature pVI in capsid structures and ambiguous assignment of other minor proteins [10-13]. Due to potential partial occupancy of these sites and apparent flexibility, it has not been possible to model the entire protein and therefore potential homo-oligomeric interactions within the capsid cannot be examined [54-56].

Each of the pVI-WT and pVI-Δ54 samples analysed by AUC contained species that may represent dimers and trimers based on the molecular weight calculated from their sedimentation coefficient. This suggests that the N-terminal alpha helix is not solely responsible for oligomerisation, and that other domains within pVI may be involved. However, the monomer peak of pVI-Δ54 was substantially higher than for the pVI-WT samples and there was also lower contribution from higher Mw peaks, indicating less oligomerisation or aggregation. It is not known whether oligomerisation affects the membrane-lytic function of pVI and while this analysis suggests that a large proportion of both pVI-WT and pVI-Δ54 are monomeric and presumably active, AUC cannot be used to conclusively determine whether any oligomers detected are active. The higher proportion of monomeric material observed for pVI-Δ54 than for pVI-WT in the AUC analysis might partially explain why the activity of pVI-Δ54 in the dye release assay was higher than expected. It is also possible that pVI-Δ54 may fold differently due to the lack of the N-terminal AH. Due to the hydrophobicity of the N-terminal region (Fig 3.1C), the folding of pVI may be driven by the energetic need to bury these residues. As the CD spectrum of pVI-

Δ54 indicates weaker structure than pVI-WT, the former may require membrane lipids to form additional secondary structure.

The data collected in this study suggest a mixed oligomerisation state that agrees with the lack of a definite copy number within the capsid, unequal occupancy of the hexon cavity [76] and dimerization of pVI purified from virus capsids observed previously [242]. Some proteins exist in solution in one folding confirmation, whereas others have been observed as homogenous mixtures in different folding states [203, 243]. This flexibility also extends to the oligomerisation state of some proteins [244]. The oligomeric interface of pVI is also unknown and due to the number of functions of pVI (section 1.3.6), there may be different oligomerisation states and interfaces at different stages of the replication cycle. It is possible that pVI adopts a range of folding states and a range of interactions in different contexts and this flexibility may have a role in enabling pVI to carry out a variety of functions at different stages of the viral cycle. AUC was not performed on pVI-L40Q, although based on the presence of species corresponding to the Mw of oligomers in the pVI-WT and pVI-Δ54 samples, it would be expected that similar species would be found in L40Q samples. Further information about the role of the N-terminal AH in oligomerisation could be obtained from analysing pVI-L40Q and peptide pVI-34-54. Additionally, the concentration at which any of the pVI constructs oligomerise is also not known, so further experiments could be performed over a range of concentrations.

The dynamic light scattering analysis presented in Figure 3.5 demonstrates that all of the constructs had some influence on liposome size distribution, most notably through the narrowing of peaks that was likely due to binding of protein to liposomes altering the pattern of light scattering in the samples. Both pVI-WT and pVI-L40Q produced additional peaks of higher diameter, possibly indicating some liposome aggregation when exposed to pVI-WT or pVI-L40Q. As expected, pVI-Δ54 exhibited little activity against liposomes measured using DLS, since there was no larger aggregate peak as seen with pVI-WT and pVI-L40Q. DLS analysis indicated less of an effect on liposomes by peptide but revealed a low diameter peak, possibly indicating fragmentation of liposomes.

The range of influence of the recombinant proteins on size distribution of liposomes measured using DLS (Fig 3.6) agrees somewhat with CD results shown in Fig 3.3, in which pVI-WT had the most apparent secondary structure, followed by pVI-L40Q and pVI-Δ54. The size distribution of liposomes + pVI-WT agrees with the CD result for pVI-WT. pVI-Δ54 had less secondary structure and produced less of an effect on liposome size. pVI-34-54 had no evident secondary structure and produced only a slight change in liposome size distribution. Furthermore, changes suggesting decrease of liposome size and liposome rupture, such as peaks in the lower size range, were not observed. However, the DLS experiments were carried out with only one set of concentrations for each construct. More data from experiments with a greater range of concentrations and lipid: protein ratios would be needed to further explore the effect of pVI on the size distribution of liposomes.

Earlier membrane interaction studies using GUVs and liposome dye release assays indicated that pVI-WT and the peptide disrupted membranes more than the mutants pVI-L40Q and pVI-Δ54, and that membrane activity was dose dependent for all pVI constructs [124, 143]. A SulfoB release assay was used here to assess the activity of recombinant pVI-WT on 40% PC, 30% PE and 30% cholesterol liposomes with purer protein preparations. A dose dependent effect was also observed here, and pVI-WT produced the greatest amount of dye release. pVI-L40Q was the least active construct tested in the dye release assay, which reflects the data from a similar experiment performed by Moyer et al., where ~10 times the concentration of pVI-L40Q was required to cause the same percentage of SulfoB release as pVI-WT [19]. Maier et al. found that the maximum dye release by pVI-L40Q was ~60% at 120 nm concentration, whereas in the present study, pVI-L40Q could only release ~22% of dye at 60 µM [124].

However, it was expected that pVI-Δ54 would exhibit less activity in the dye release assay than all of the other constructs, based on similar experiments performed previously [19, 124]. The activity of pVI-Δ54 in the dye release assay (Figure 3.6) was much higher than expected based on the literature and the DLS assays (Fig 3.5), and this mutant induced more liposome leakage than pVI-L40Q. It can be concluded that breaking the N-terminal AH through the loss of Lysine 40 in the hydrophobic face of the helix greatly reduces liposome disruptive activity far more than removing it entirely. This observation confirms the importance of the first N-terminal helix. It is possible that lack of the first helix in pVI-Δ54

entirely frees up one or more of the additional predicted α-helices (Fig 3.1) to associate with membranes, whereas disrupting the first helix, as with pV-L40Q, greatly reduces its ability to disrupt membranes. Experiments using liposomes suggested some cooperativity between the N-terminal AH and putative helices within residues 54–114 of mature pVI, since pVI-WT was able to induce highly curved membrane tubules while the helix alone was sufficient to lyse membranes with no evidence of curved tubules [143]. Maier et al. suggested the possibility of residues 34–114 stabilising the highly curved structures induced by pVI [143]. There is also a possibility of pVI-Δ54 behaving in a completely different manner that does not require the formation of another amphipathic helix. For example, some antimicrobial peptides such as dermaseptin S [245] disrupt membranes through a "carpet" mechanism in which proteins cover the membrane and disintegration occurs when a concentration threshold is reached [246, 247]. This mechanism does not require insertion of peptides into the hydrophobic core of the membrane and can involve protein monomers or some degree of oligomerisation [246, 247]. The drop in fluorescence at the highest measured concentration of pVI-Δ54 (Fig 3.6) could be due to the saturation of liposome surfaces with protein inhibiting membrane-lytic activity.

For some IDPs, structure is gained upon interaction with the target molecule, whereas disorder is critical to function for others. Folding coupled to binding has been demonstrated for many eukaryotic proteins, where disordered proteins adopt ordered structure only upon binding to their targets [243, 248]. Additionally, many amphipathic helices previously

described are unfolded in ionic buffer and in the absence of binding partners [166]. CD spectroscopy analysis has shown that peptide pVI-34-54 gains helical structure upon interaction with DOPC/DOPS liposomes [168], but it is not yet clear if there are any such changes for pVI-WT or the two mutants. The L40Q mutation is thought to prevent the N-terminal AH from fully inserting into the membrane bilayer and inducing positive curvature stress [19]. If additional helical segments in pVI-Δ54 are able to fold in the presence of lipids, this may explain the higher percentage of dye release compared to pVI-Δ54. These helical segments may be prevented from folding in pVI-L40Q due to the reduced folding of the N-terminal helix, but these hypotheses have not been tested. In order to further explore the possibility of one of the other predicted helices in pVI-Δ54 folding and inducing membrane damage, CD experiments would need to be performed with protein and liposomes mixed together to examine differences in helical content.

Dye release assays performed by Maier et al. [124] and Moyer et al. [19] using POPC/POPS liposomes were the basis of my experiments. Based on comparison of the results obtained in the present study to previous experiments, the activity of pVI constructs upon liposomes is highly dependent on the membrane composition, with negative curvature promoting lipids such as PE reducing the activity of all pVI constructs [19, 124, 143]. The higher proportion of dye release elicited by pVI-WT indicates that it was able to overcome the effect of PE, while pVI-L40Q was less able. Cholesterol is an important component of plasma and endosomal membranes and is required for several processes during the AdV life cycle

[229, 249, 250]. Therefore, the results of previous dye release assays that excluded cholesterol from membranes are less representative of the membranes faced by pVI within endosomes. The charge of the lipid headgroups may also contribute to the differences in pVI activity between the current study and previous experiment. Phosphatidylserine (PS) headgroups carry a negative charge, in contrast to the zwitterionic headgroups of PC and PE. The positively charged Lys residues at the boundary between the potential hydrophobic and hydrophilic faces of the predicted N-terminal AH would be expected to enhance the interaction with negatively charged lipids [168, 227]. Therefore, the addition of PS may have increased the membrane-lytic activity of pVI-WT in comparison to pVI-WT with the PC/PE/cholesterol liposomes. Overall, my experiments are more likely to be of significance due to the membranes more closely mimicking the composition of biological membranes. However, analysing the effect of the pVI constructs on a variety of liposome compositions through CD and assays of protein-membrane interactions will be required to fully understand the contribution of different lipids on the function of pVI.

The peptide pVI-34-54 was expected to cause a higher release of dye than pVI-Δ54, as this pattern was observed by Maier et al. in experiments with POPC/POPS liposomes [124]. In contrast, around four times the concentration of peptide than pVI-Δ54 was required to induce ~50% dye release. However, the higher activity of the peptide in the dye release assays reported by Maier et al. may also be because the peptide they used possessed an additional C-terminal tetralysine tag designed to enhance aqueous solubility [124]. The

predicted charge of the peptide with this additional tag was +5 which possibly increased the peptide's activity against liposomes, compared to the charge of +2 for the peptide used in this experiment.

The optimised purification protocol developed in Chapter 2 utilises urea to solubilise pVI-WT and pVI-L40Q due to their association with *E. coli* membranes. Less pVI-Δ54 remains associated with membranes and Triton X-100 is sufficient to disrupt interactions between *E. coli* membranes and protein. All recombinant proteins used in the previously reported dye release experiments were purified using detergent. Therefore, the results for pVI-WT and pVI-L40Q used in these studies may not be a true representation of the membrane-disruptive potential of these constructs. On the other hand, the proteins should have been able to properly re-fold even after the removal of urea and pVI-WT was demonstrated to be active. Triton may also limit the re-folding of pVI-Δ54, although the effect would not be expected to be as strong. It is therefore possible that pVI-Δ54 purified using detergent retains more membrane association activity than pVI-L40Q. Any such differences in folding may provide part of the explanation for the higher percentage of dye release seen with this mutant (Fig 3.6). In order to fully explore this possibility, it would be necessary to perform experiments with all of the pVI constructs purified with both urea and detergent. It would also be interesting to assess whether the secondary structure content and oligomerisation state differs between samples purified in urea buffers vs. Triton buffer.

Taken together, the results of structural and functional analyses of the pVI wild type and mutants pVI-Δ54 and pVI-L40Q indicate that secondary structure does not fully correlate to membrane disruptive activity. As expected, pVI-WT contained the most helical content and was the most active construct examined with liposomes. However, the activity of the other constructs is not as clearly linked to structure. It was expected that structural content found in CD analysis would correspond to activity in dye release assays, but pVI-L40Q was less active than pVI-Δ54 despite demonstrating more helical content. This unexpected result may be explained by oligomerisation reducing the amount of free monomeric protein, or the formation of helical motifs in pVI-Δ54 only in the presence of lipids, although further experiments are needed to explore this possibility. AUC analysis suggests a mixed oligomerisation state that is not dependent on the N-terminal AH. Based on the activity of pVI-Δ54 and the peptide in this study, the N-terminal helix appears to be sufficient for, but not required for membrane rupture.

In order to gain a more complete picture of the relationship between helical content of the pVI constructs and membrane lytic activity, we will need to compare the CD spectra of the pVI constructs alone and with liposomes to examine any change in secondary structure content. Far UV data collection could provide further details about the globular state of pVI constructs, although this technique requires a much larger volume and concentration of protein. Comparing other known pVI constructs using the techniques described in this chapter may provide a more complete picture of the contribution of different elements of

pVI structure. Maier et al. [124] used CD and SRB release assays to compare the structure and activity of the truncation mutant pVI-Δ114 and found much more pronounced α-helical folding present and a similar amount of dye release as the wild type. Similar experiments using peptides representing the other predicted helices of the N-terminal 114 residues could also clarify the role of this region. It is also important to note that some of the assays used here were carried out at a lower temperature and higher pH than the pVI protein would be facing within the endosome, which may affect the efficiency of the reaction with membranes, and therefore the effect of the temperature and pH on the activity of pVI should also be explored.

3.6 Materials and methods

3.6.1 Disorder prediction

PONDR VL-XT prediction [208, 251] and IUpred2A [252, 253] long disorder prediction were run on 20th June 2020.

For the following mature (excluding the 33 N-terminal residues):, untagged protein sequences

AFSWGSLWSGIKNFGSTVKNYGSKAWNSSTGQMLRDKLKEQNFQQKVVDGLASGISGVVDLANQA
VQNKINSKLDPRPPVEEPPPAVETVSPEGRGEKRPRPDREETLVTQIDEPPSYEEALKQGLPTTRPIAPM
ATGVLGQHTPVTLDLPPPADTQQKPVLPGPTAVVVTRPSRASLRRAASGPRSLRPVASGNWQSTLNSI
VGL (pVI-WT),

AFSWGSQWSGIKNFGSTVKNYGSKAWNSSTGQMLRDKLKEQNFQQKVVDGLASGISGVVDLANQA
VQNKINSKLDPRPPVEEPPPAVETVSPEGRGEKRPRPDREETLVTQIDEPPSYEEALKQGLPTTRPIAPM
ATGVLGQHTPVTLDLPPPADTQQKPVLPGPTAVVVTRPSRASLRRAASGPRSLRPVASGNWQSTLNSI
VGL (pVI-L40) and
SKAWNSSTGQMLRDKLKEQNFQQKVVDGLASGISGVVDLANQAVQNKINSKLDPRPPVEEPPPAVE
TVSPEGRGEKRPRPDREETLVTQIDEPPSYEEALKQGLPTTRPIAPMATGVLGQHTPVTLDLPPPADTQ
QKPVLPGPTAVVVTRPSRASLRRAASGPRSLRPVASGNWQSTLNSIVGL (pVI-Δ54).

3.6.2 Liposomes

Cholesterol, Phosphatidylcholine (PC) and Phosphatidylethanolamine (PE) were purchased from Avanti Polar Lipids. Lipids provided as lyophilised powders were dissolved in chloroform to a final concentration of 20 mg/ml.

Liposomes were prepared by mixing of PC and cholesterol at a molar ratio of 70:30 or PC, PE and cholesterol at 40:30:30 in chloroform at 4 mg/ml total. The lipid mixture was dried to a thin film in a glass vial by evaporation under a stream of argon, then placed under vacuum for at least 1 hour. The lipid film was hydrated in assay buffer (25 mM Hepes, 150 mM NaCl, pH 7.4) at 37°C and subjected to five cycles of freeze-thawing using liquid nitrogen. Liposomes were sized by extrusion, where the hydrated liposome mixture was passaged 21 times through a 1µm or 100nm Nuclepore® Track- Etched Membrane (Whatman) using a mini-extruder (Avanti Polar Lipids) preheated to 40°C.

3.6.3 Circular dichroism

Circular dichroism (CD) spectroscopy was performed on a Jasco J-815 spectropolarimeter with a 450 W Xe lamp. Purified proteins were diluted to 2–4 µM in 20 mM Tris, 10 mM NaCl buffer (pH 7.4) and filtered through 0.2 µm PVDF syringe filters to remove any aggregates. Samples were analysed in a 0.1 cm path-length quartz cuvette and spectra were collected at room temperature in triplicate from 190 to 250 nm in 0.2 nm increments. Spectra were analysed for secondary structure content, corrected for protein concentration, using the CAPITO CD analysis and plotting tool provided by the NMR Platform at the University of Jena [254].

3.6.4 Analytical ultracentrifugation

Sedimentation velocity experiments were performed using a Beckman Optima XL-I analytical ultracentrifuge equipped with absorbance and interference optics. Double sector 3 mm centrepieces were used with protein samples at 1 mg/ml or 0.7 mg/ml in 20 mM Tris, 150 mM NaCl buffer (pH 7.4). Both interference and absorbance (A280) measurements were collected. Experiments were performed at 20°C, taking sample distribution scans every 6 minutes. Interference data were analysed using SEDFIT software using the c(s) method of interpretation to generate sample distributions in s (sedimentation coefficient) assuming a partial specific volume of 0.73. Non-linear regression was used to find the best-fit frictional coefficient and the integration tool was used to determine the contributions of

each peak to the total sedimenting species. Accuracy in M requires prior knowledge of the partial specific volume (v-bar) of the sedimenting species. As there is no structural information on which to determine v-bar for pVI, the approximate value for proteins, 0.73 ml/g, is used.

3.6.5 Dynamic light scattering

PC/PE/cholesterol liposomes were prepared at 2 mg/ml as in section 3.6.2. Ca. 20 µM of each the three recombinant proteins and ~200 µM pVI-34-54 were mixed with ~1.6 mM PC/PE/cholesterol liposomes (0.1 nm diameter) for one hour at 37°C in 20 mM Tris, 150 mM NaCl (pH 7.4). Quartz Uni cuvettes were loaded with 9 µl samples of liposome-protein mixtures, liposomes alone or buffer and analysed using the Uncle system (Unchained Labs). Buffer was used to check background absorbance before measurements. 4 acquisitions of 5 seconds each at 660 nm were carried out at 37°C.

3.6.6 Liposome leakage assay

2 mg total lipids were mixed at a molar ratio PC/PE/cholesterol (40:30:30) were dried according to section 3.6.2. The film was hydrated in 1 ml 50 mM sulforhodamine B (SRB), 10 mM HEPES, 150 mM NaCl (pH 7.4) and liposomes were incubated for 1 hour at 37°C followed by five freeze-thaw cycles using liquid nitrogen. Hydrated liposomes were then extruded as in section 3.6.2. SRB-entrapped liposomes were separated from free dye using

Sephadex G-25 PD-10 desalting columns (GE Healthcare) pre-equilibrated with buffer. 1 ml of liposome sample was loaded onto columns, followed by 2 ml of buffer, and eluted by loading 2 ml of buffer. The liposome mixture was then run through another clean G-25 column to yield liposomes at ~0.5 mg/ml.

The liposome leakage assay was carried out in 96-well plates in triplicate. Liposomes were diluted to 0.05 mg/ml assay buffer, and 50 µl of liposomes were added to wells (~80 µM per well). 50 µl of protein was prepared by diluting in assay buffer to the final concentration indicated in Figure 3.6. pVI-34-54 was solubilised using DMSO, and the baseline buffer for peptide was adjusted to contain the same concentration of DMSO after peptide dilution. Protein or peptide was added, and readings begun as quickly as possible (within 60 seconds).

Fluorescence was recorded every 10 sec for 90 minutes using an Agilent Stratagene Mx3005 Real-Time PCR machine operated at 37°C. Triton X-100 at a final concentration of 3% was used as a complete lysis control. The percentage of SRB released was calculated using the formula % SulfoB released = 100 × [Fmeas − F0)/(Ftx − F0)], where Fmeas is the maximum fluorescence intensity measured, F0 is fluorescence intensity in absence of protein, and Ftx is the fluorescence intensity in the presence of 3% Triton.

Chapter 4 Analysing the interaction of pVI with model membranes using cryoEM

4.1 Introduction

The final objective of this project was to use electron microscopy (EM) to characterise the interactions of pVI with model membranes. Wiethoff et al. previously observed fragmentation and reduction in size of negatively-stained liposomes incubated with recombinant pVI-WT compared to liposomes alone [108], but these results have not since been replicated and cryoEM has not been performed to probe this interaction in a more native state.

After endocytosis of AdV, the capsid partially disassembles and pVI is released, which then causes permeabilisation of the endosomal membrane [108]. The exact composition of the early endosome is not well characterised, but it is thought to be similar to the plasma membrane, which contains 25–50% cholesterol and smaller proportions of various phospholipids, including phosphatidylcholine (PC), phosphatidylethanolamine (PE), phosphatidylinositol (PI) and phosphatidylserine (PS) [230, 255]. Two liposome compositions were used in this study, the first a simple PC and cholesterol mixture at a 70:30 mol ratio; in the second, PE was additionally introduced to mimic the endosomal membrane more closely. In comparing the morphology of liposomes in the presence of four pVI constructs, we aimed to contribute to our understanding of the mechanism of pVI

disruption of membranes and towards assignment of particular effects to different domains of the protein.

Transmission electron microscopy is an important tool for examining the structure of biological constructs [256-258]. Several preparation methods for electron microscopy are used depending on the type of sample and imaging requirements [259, 260]. In negative stain microscopy, samples are adsorbed onto EM grids and covered with electron-dense heavy metal salts, such as uranyl acetate. Contrast is produced by the difference in stain deposition between the background and protruding protein surfaces and the internal protein surfaces, which retain less stain [260, 261]. Negative stain sample preparation is rapid but can result in sample distortion due to dehydration and precipitation of salts on grids that form crystals and other artefacts.

In cryoEM, biological samples are added to grids covered with a thin perforated carbon film, blotted to remove excess sample, and then frozen rapidly into a thin layer of vitreous (non-crystalline) ice and imaged at liquid nitrogen temperatures [262, 263]. Vitrification preserves the fragile biological structures in a fully hydrated state as compared to negative staining of biological samples, so ultrastructural details are less altered and samples are preserved in a state that is as close to native as possible [260, 263]. However, contrast is lower than with negatively stained samples, as it is derived only from the difference in electron scattering between the atoms of the structures and the surrounding water. It is

therefore necessary to under-focus the image to improve the contrast [259, 264]. Some extensive reviews on the theory and development of cryoEM be found in the literature, including references [265-268].

CryoEM is the only imaging method at present that offers the ability to resolve membrane leaflets in the near-native conditions required for understanding the interaction of pVI with membranes [269]. At approximately 25 kDa, monomeric recombinant pVI is too small to be identified by eye in cryoEM projection images. Here, cryoEM will be used to collect snapshots of liposome morphology and compare the phenotype to liposomes samples exposed to pVI constructs. Comparing the liposome morphology in the presence of pVI proteins and peptide will contribute to our understanding of the mechanism of pVI disruption of membranes and potentially allow assignment of particular effects to different domains of the protein.

Electron cryo-tomography (cryoET) will be then used to capture further details of membrane interactions with pVI, which will enable a more thorough examination of any damaged or distorted membranes. The advantage of cryoET over 2D projection images is that it enables single objects to be observed in 3D, eliminating the need to average multiple examples to form a 3D structure [270-272]. CryoET is therefore well suited for examining pleiomorphic or heterogeneous samples, such as liposomes.

4.2 Negative stain analysis of liposomes and pVI-WT

Negative stain EM was first used to assess the liposome size distribution and morphology of 100 nm PC/cholesterol liposomes in order to optimise sample preparation (Fig 4.1A). Next, 0.5 mg/ml pVI-WT provided by Wodrich et al. was added to 2 mg/ml PC/cholesterol liposomes to determine the impact of protein on the morphology of liposomes (Fig 4.1B).

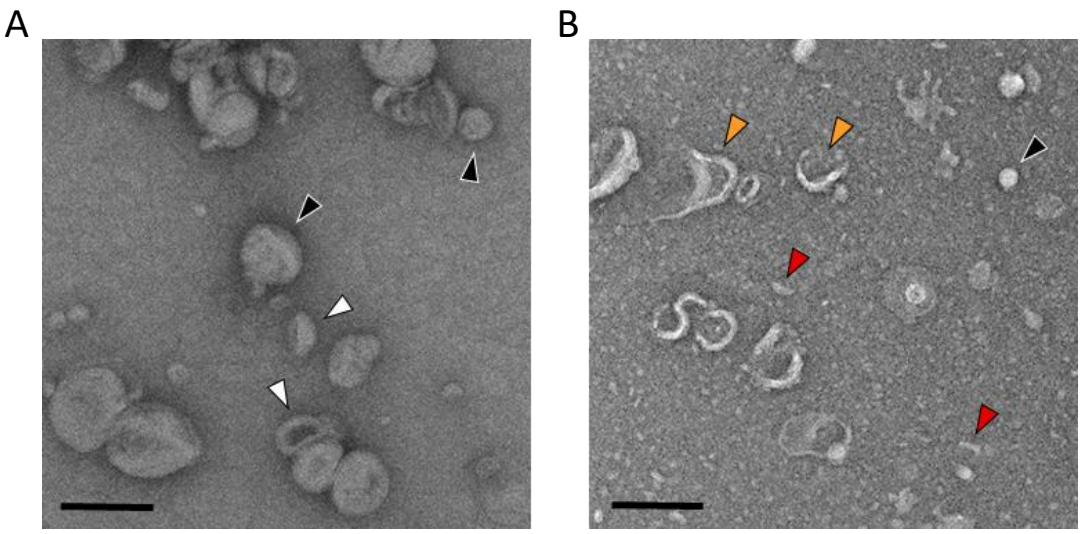


Figure 4.1 Negative stain electron microscopy reveals liposome disruption by pVI-WT.

(A) 2 mg/ml PC/cholesterol control liposomes stained with uranyl acetate. Some liposomes appeared roughly spherical (black arrowheads), while some liposomes were flattened (white arrowheads). (B) 2 mg/ml PC/cholesterol liposomes + 0.5 mg/ml pVI-WT stained with uranyl acetate showing ruptured and fragmented liposomes. Orange arrowheads, ruptured liposomes. Red arrowheads, membrane fragments. Scale bars, 200nm

In the negative control sample (Fig 4.1A), liposome diameters ranged between ~20 and 200nm and were heterogenous in shape, but all liposomes were intact. Liposomes also

clumped together in several places. When pVI-WT is added to the liposomes (Figure 4.1B), the larger liposomes appear to have ruptured, while only small liposomes of ~20 nm remain intact. Some membrane fragments are visible and grainy material is present in the background, possibly caused by small fragments of membrane. These differences indicate that the pVI-WT preparation has a disruptive effect on liposomes when compared to liposomes without protein.

4.3 Optimisation of cryoEM sample preparation

While negative stain EM is often used to inform parameters for cryoEM sample preparation, the conditions used are not always directly transferable. In negative stain microscopy, continuous carbon sample grids are used, whereas cryoEM often uses support films with holes, such that samples are suspended in vitreous ice to minimise background. Several parameters need to be optimised in order produce the ideal ice thickness (<100 nm for the liposomes used here) and distribution of liposomes across holes to facilitate viewing of individual vesicles [273]. These include the type of grid, sample concentration and vitrification methods.

Grids are usually treated prior to addition of samples by glow-discharging to give grids surface charge, which renders the material hydrophilic and aids in the even distribution of aqueous solution over the surface [274, 275]. Sample support grids are produced by different manufacturers with varying types and arrangements of holes and distances

between holes and are selected based on particle size and type. Blotting of excess liquid prior to vitrification removes some sample, so it is necessary to optimise sample concentration and blotting for the respective type of grid. C-Flat grids were initially used in this study but found to be more prone to breakage than Quantifoil grids with similar hole size and spacing. Therefore, Quantifoil grids, which have thicker carbon coating, were used for subsequent experiments.

Concentration was an important factor for this project since preparations that are too dense impede identification of the membranes of individual liposomes. The conditions used for negative stain (Figure 4.1) were applied to preparation of liposomes on holey carbon EM grids and imaged using cryoEM to assess whether the concentration and distribution of liposomes across the grid were appropriate. Figure 4.2 demonstrates the improved distribution of liposomes arising from several changes that were made to the preparation of cryoEM samples.

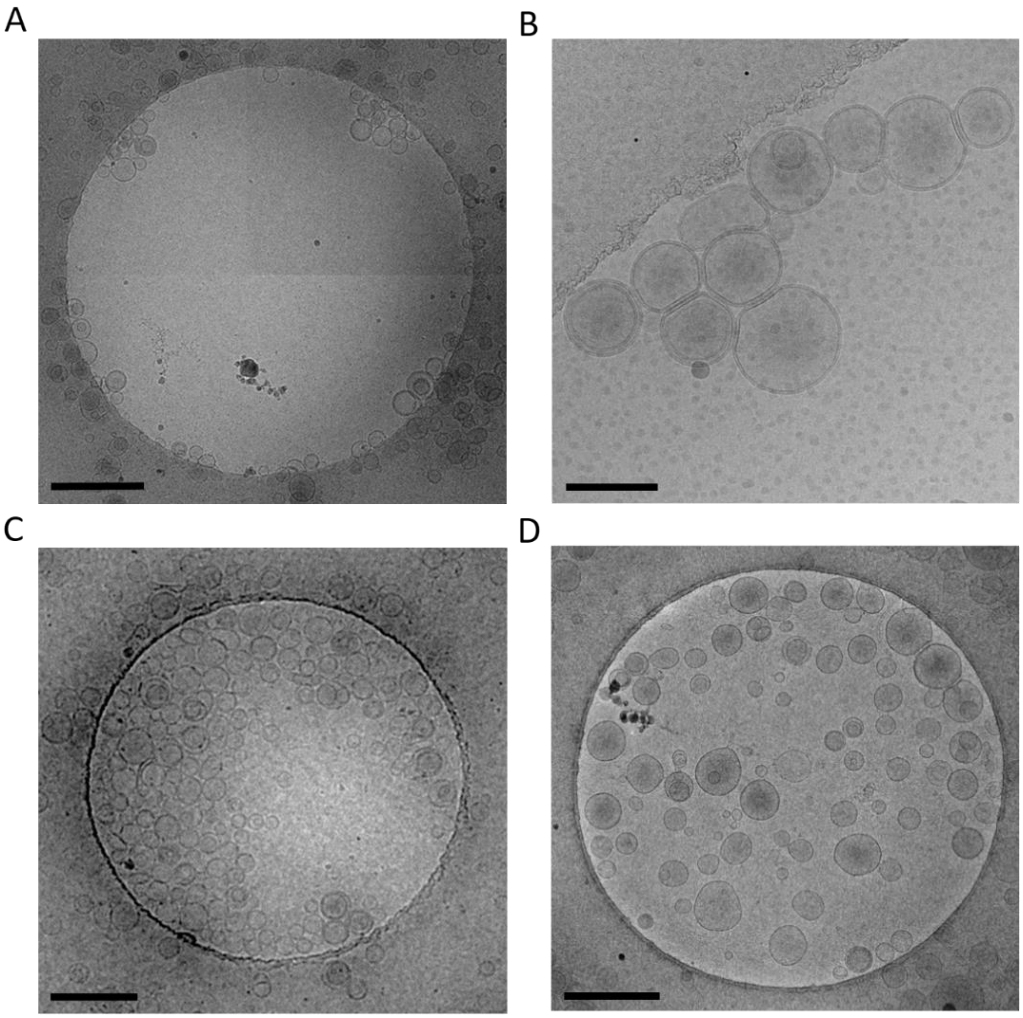


Figure 4.2 Optimisation of cryoEM sample preparation improved the concentration and distribution of liposomes.

(A) Grid hole with sparse liposome distribution. 2 mg/ml liposomes vitrified using a manual plunger (3.5 second blot time). Appearance of quadrants is due to improper gain reference prior to imaging. Liposome size distribution: ~50–100 nm. Scale bar, 500 nm. (B) Liposomes clumped at edge of hole. 2 mg/ml liposomes vitrified using a manual plunger (3 second blot time). Speckled appearance of is due to surface contamination of ice. Liposome size distribution: ~30–120 nm. Scale bar, 100 nm. (C) Grid hole with high liposome concentration. 4 mg/ml liposomes vitrified using a manual plunger (3 second blot time). Liposome size distribution: ~50–200. Scale bar, 500 nm. (D) Grid hole with ideal liposome distribution. 2 mg/ml PC/cholesterol liposomes prepared using manual plunging (3s blot time) on a graphene oxide coated grid. Liposome size distribution: ~20–250nm. Scale bar, 500 nm.

The liposomes in Fig 4.2A and B are clustered around the edges of holes, which in some samples was observed to result in liposome damage. Therefore, the aim of optimisation was to reduce the number of liposomes clustered near the edges of holes while increasing the concentration in the centre in order to maximise the number of liposomes in each field of view. Next, a higher liposome concentration was explored. Liposomes were prepared at 4 mg/ml (Fig 4.2C) using the same plunging parameters as in Fig 4.2B to assess whether concentration influenced distribution within ice. In Figure 4.2C, while liposomes are not clustered only around the edges of holes, 4 mg/ml is too high a concentration to discern individual membranes. To encourage more even distribution of the liposomes over the grid, a thin layer of graphene oxide was applied to grids to provide a layer of support that was less electron-dense than the holey carbon film (Fig 4.2D). Graphene oxide application improves the distribution of liposomes across the hole, including the centre. However, the liposomes in Fig 4.2D also have a larger size distribution, at between 20–250 nm, indicating that extrusion of liposomes through filter membranes did not produce liposomes of consistent sizes.

Initially, vitrification of grids by manual plunging was used to prepare grids, but samples were later prepared using a Vitrobot, which allows finer control of humidity, blot force and improved the consistency of liposome distribution. Ice thickness was also improved, and grid breakage reduced, which increased the number of suitable areas for imaging across the grids. It was found that a 3 second blot time was optimal using both manual plunging and

the Vitrobot. The liposomes prepared with graphene oxide coated grids at 2 mg/ml in Fig 4.2D are of a more suitable density so that as many liposomes as possible are included in a field of view without clustering.

4.4 CryoEM of PC/cholesterol liposomes

As with the negative stain imaging (section 4.2), projection images of vitrified liposomes were first collected to characterise their morphology in the absence of protein and to examine whether the process of sample preparation disrupted liposomes. Next, pVI-WT or pVI-L40Q purified according to the protocol described in Chapter 2 were mixed with liposomes and incubated before applying the mixture to sample grids. Several liposome to protein ratios were examined in order to find a suitable concentration range, but this was limited by the low concentration of many purified protein preparations and the relatively high liposome concentration required to ensure a suitable number in each field of view. 0.5 mg/ml protein was used with 2 mg/ml liposomes for all subsequent experiments.

The morphology of individual liposomes was classified according to their shape and features. The number of liposomes in each morphological class was counted for each projection image. All counted data are recorded in table 4.1 of methods section 4.8.3 and additional examples of each type of liposome feature are presented in appendix section 6.2. The morphological differences of liposomes with and without protein were compared to identify changes that occur as a result of pVI addition.

4.4.1 Characterisation of PC/cholesterol liposomes

Typical cryoEM projection images from liposome samples without protein are shown in Fig 4.3A. Several types of liposome morphologies were excluded from the count (Fig 4.3A, indicated by red crosses). Multi-laminar liposomes appearing to contain many concentric layers were not counted, since it was not clear whether pVI was able to rupture multiple membrane layers. Liposomes containing smaller liposomes were counted if the layers were separated, as these external layers would be accessible to protein and only the outer layer was counted. Liposomes outside of the grid holes and liposomes overlapping the edges of holes were also not counted, as the clustered carbon at the edges were found to deform and rupture some membranes in previous samples.

All liposomes observed in these samples were intact. A large proportion of liposomes were unilaminar and circular (Fig 4.3Bi), and these were classified as “intact circular” liposomes. This class included fully circular liposomes, including liposomes containing smaller ones (Fig 4.3Bi, in the top panel, only the outer liposome is counted) and liposomes slightly squashed by neighbouring liposomes but still mostly circular (Fig 4.3Bi, bottom panel). Liposomes that are distorted outside of a circular shape are counted as “distorted intact liposomes” (Fig 4.4Bii), some of which were still rounded (Bii, top panel) while others were compressed out of a circular shape by several neighbouring liposomes (Fig 4.3Bii, bottom panel). 39.2% and 39.7% of liposomes were categorised as intact circular and intact distorted, respectively.

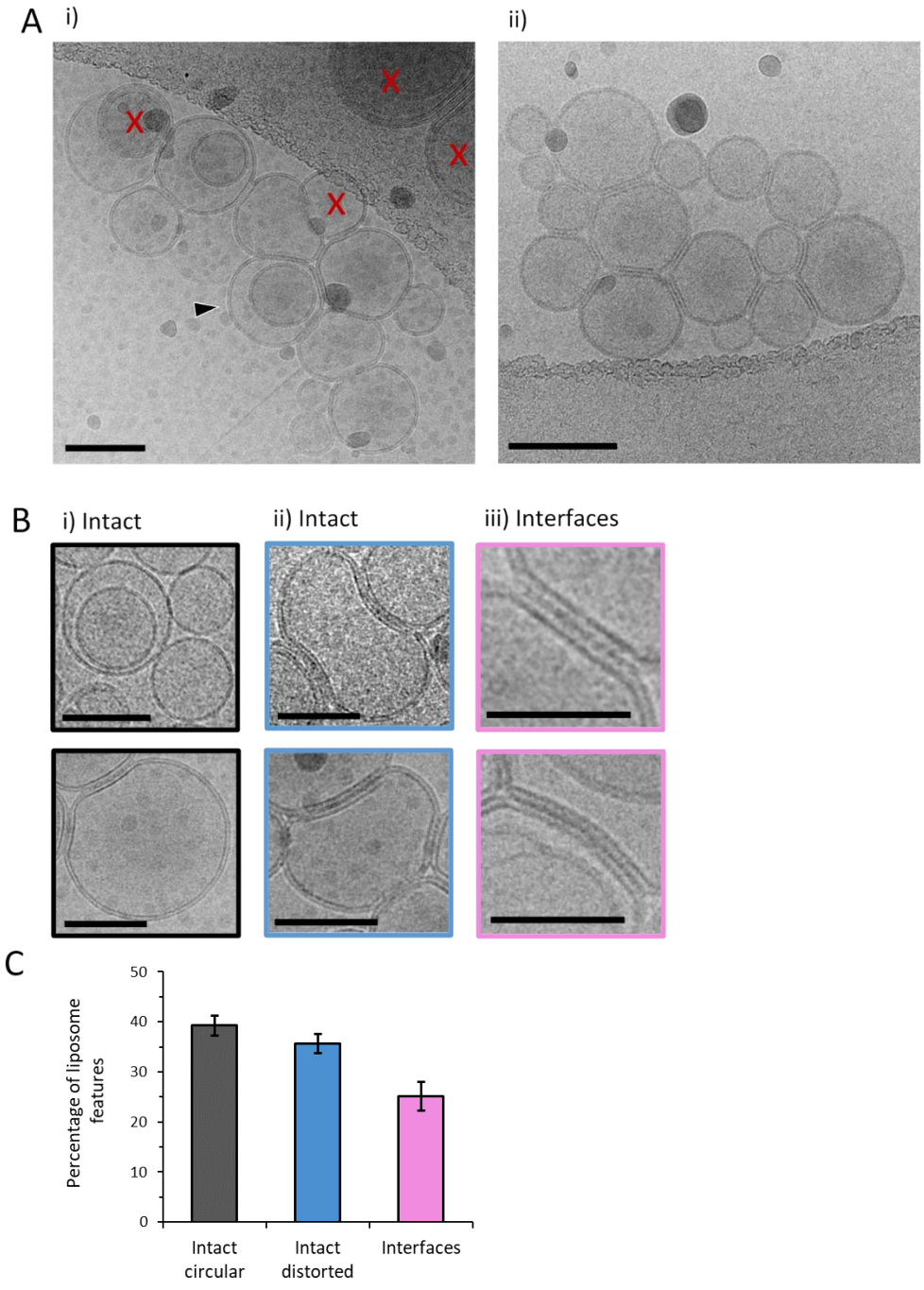


Figure 4.3 Three main morphology types were observed in PC/cholesterol liposomes without protein.
No evidence of membrane disruption was observed. (A) Example cryoEM projection images of liposomes. Red crosses, liposomes excluded from count. Black arrowhead, concentric liposome where only the outer liposome was counted. Scale bars, 100 nm. (B) Isolated examples of liposome feature classes. Scale bars, 50 nm. Estimated liposome diameter range was 30–210 nm (C) Chart of percentages of each liposome feature class. Error bars represent the standard error calculated from the total instances of each class counted and total features counted.

In areas of high liposome density, many liposomes were connected by straight (Fig 4.3Biii, top panel) or curved (Biii, bottom panel) interfaces where there was clear definition between membranes. These were counted since it was not clear whether these were an artefact of the blotting process. Multiple interfaces could be counted per liposome. Liposomes with such interfaces made up 25.1% of the total count of liposome features. Overall, all liposomes observed in the negative control samples were classified as intact, and the morphology classes provided a baseline with which to compare liposomes incubated with pVI constructs.

4.4.2 Characterisation of PC/cholesterol liposomes + pVI-WT

The three classes of liposome features counted in the liposome only samples were also the most prevalent classes in samples incubated with pVI-WT (Fig 4.4). 22.3% and 36.6% of liposomes were counted as intact circular and intact distorted, respectively. Intact circular liposomes (Fig 4.4Bi) and intact distorted liposomes (Fig 4.4Bii) appeared similar to those in the negative control samples (Fig 4.3), with a few examples of elongated liposomes (Fig 4.4Ai, white arrowhead). 28.4% of liposome features counted were categorised as interfaces between liposomes (Fig 4.3Biii), which appeared identical to those found in PC/chol liposome only samples. Many areas were observed were no damage had taken place, such as in Fig 4.4Ai, compared to areas with several instances of membrane disruption, as seen in Fig 4.4Aii.

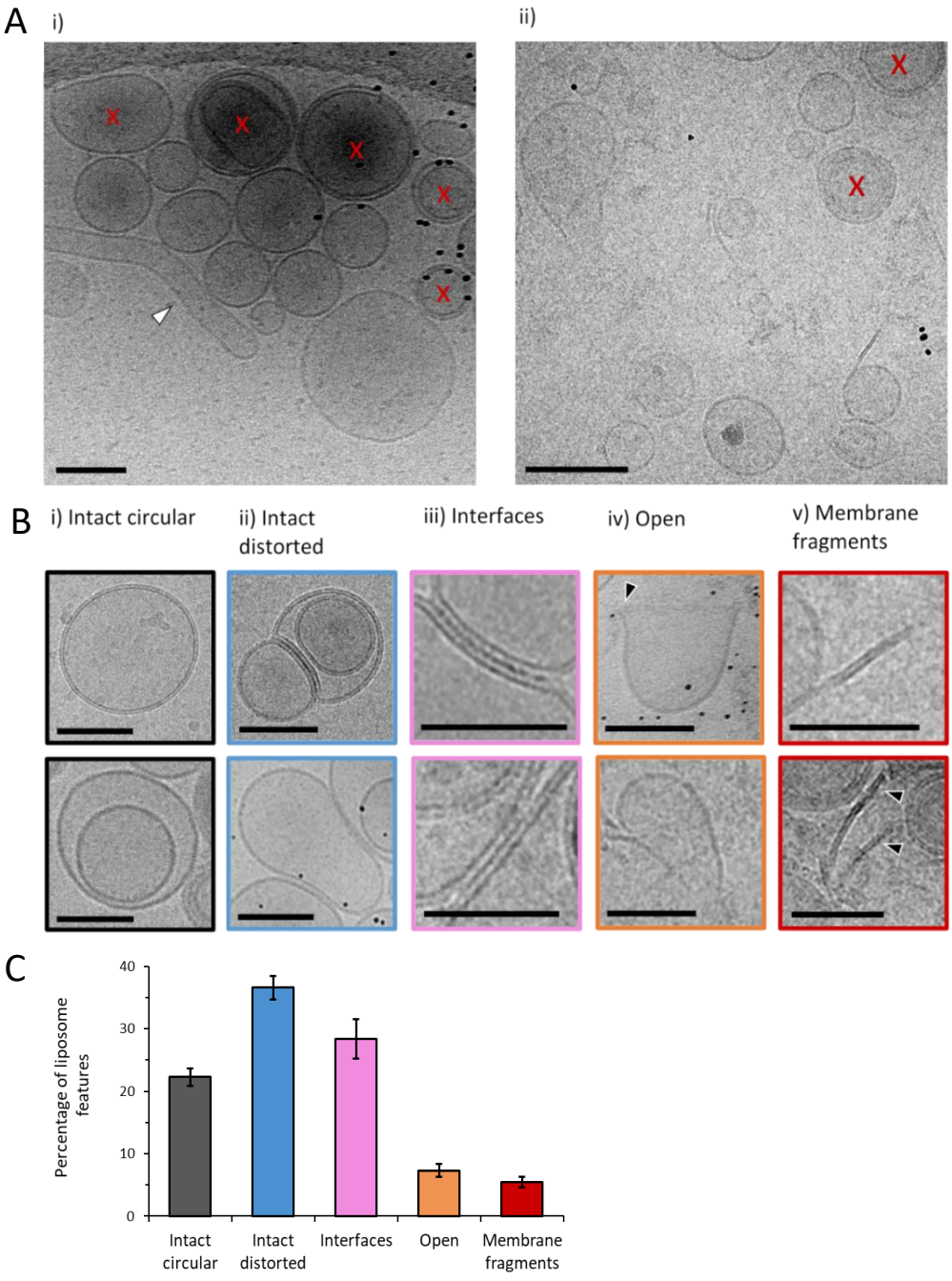


Figure 4.4 Two additional morphology types were observed in liposomes upon addition of pVI-WT that indicated membrane disruption.

(A) Example cryoEM projection images of liposomes treated with pVI-WT. Red crosses; liposomes excluded from count. Scale bars, 100 nm (B) Isolated examples of liposome feature classes. Black arrowheads, representative examples of membrane fragments. Scale bars, 50 nm. Estimated liposome diameter range was 20–290 nm. (C) Chart of percentages of each liposome feature class. Error bars represent the standard error calculated from the total instances of each class counted and total features counted.

The classes were expanded to include two types of membrane disruption events only observed when pVI-WT was incubated with liposomes: open liposomes and membrane fragments. In addition to the two intact liposome classes, liposomes with membrane discontinuities were counted as open liposomes (Fig 4.4Biv), with openings ranging in size from ~20 to 100 nm. 7.3% of total liposomes counted were open. The free edges of some of these open liposomes (Fig 4.4Biv, arrowhead) appeared to be curved away from the opening. However, the most striking evidence of membrane damage caused by pVI-WT were broken fragments of liposomes where both membrane layers could be discerned, counted as "membrane fragments" (Fig 4.4Bv). Many membrane fragments were clustered together; the frame in Fig 4.4Bv contains two fragments (arrowheads). 5.4% of counted liposome features were membrane fragments. In summary, two new liposome classes that indicated membrane damage were observed when liposomes were incubated with pVI that were not found in negative control samples and the proportion of intact liposomes was lower than in negative controls.

4.4.3 Characterisation of PC/cholesterol liposomes + pVI L40Q

Next, PC/cholesterol liposomes were incubated with recombinant pVI-L40Q purified according to the protocol described in Chapter 2. The pVI-L40Q protein contains a point mutation within the N-terminal amphipathic helix (AH) that results in impaired endosomal

escape and a 10-fold reduction in *in vitro* membrane lytic activity [19]. pVI-L40Q was therefore not expected to disrupt liposomes in the same manner seen with pVI-WT.

The same three liposome morphology classes were found as in the negative control samples (Fig 4.3). 30.7% and 41.3% of liposome features were counted as intact circular and distorted liposomes, respectively. 28% of liposome features were counted as interfaces, which were also similar in appearance to those from the other PC/cholesterol liposome samples. Intact circular liposomes observed in these images included liposomes containing multiple smaller liposomes (Fig 4.5Bi, top panel) and multi-laminar liposomes with separated membranes (Fig 4.5Bi, bottom panel), and both types were counted as "intact circular" liposomes. Unlike pVI-WT, pVI-L40Q did not produce any examples of disrupted liposomes; all liposomes counted were intact.

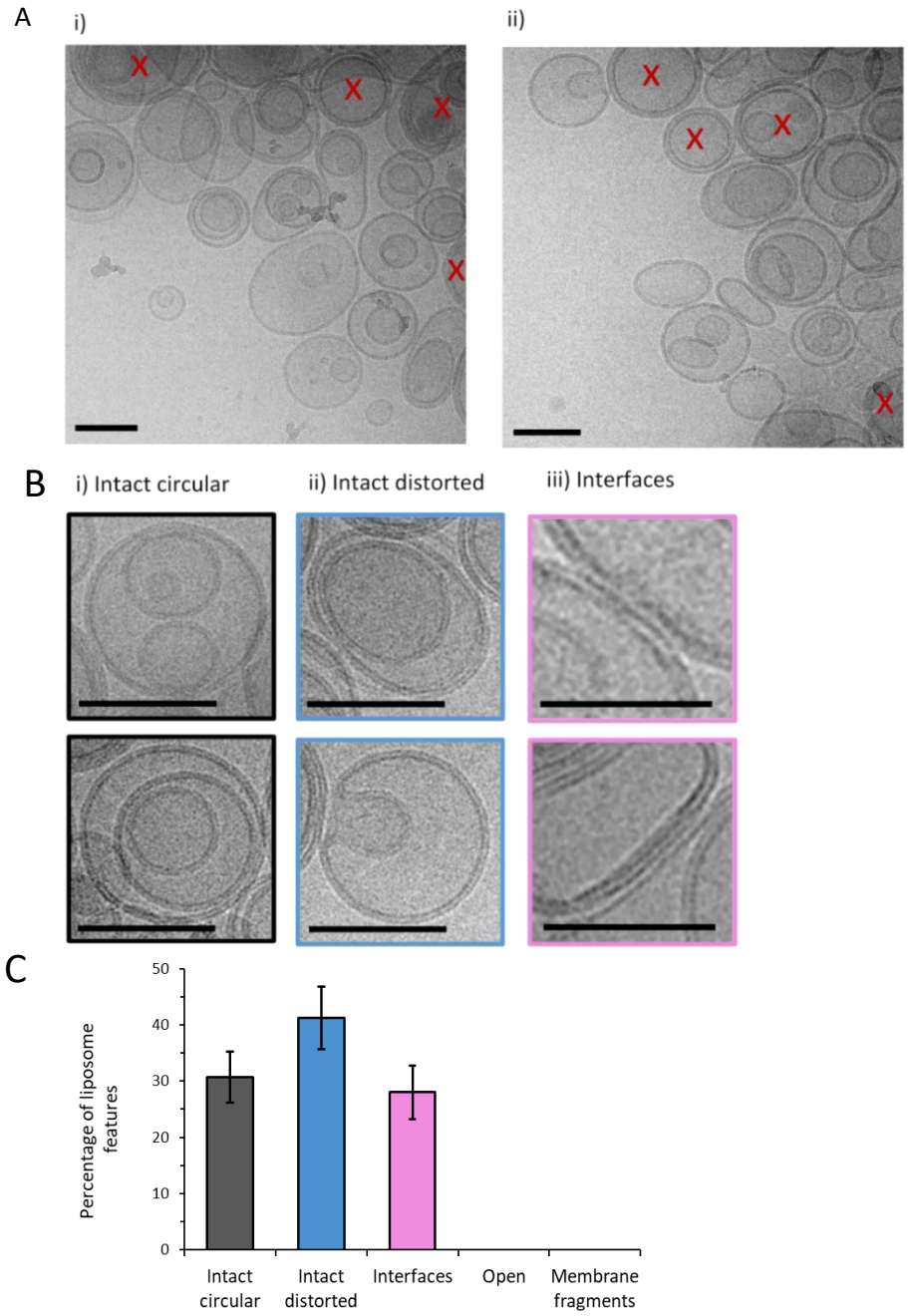


Figure 4.5 No evidence of liposome disruption was observed upon addition of pVI-L40Q to PC/cholesterol liposomes.

(A) Example cryoEM projection images of liposomes after addition of pVI-L40Q. Red crosses, liposomes excluded from count. Scale bars: 100 nm. (B) Isolated examples of liposome feature classes. Scale bars: 50 nm. Estimated liposome diameter range was 20–320 nm. (C) Chart of percentages of each liposome feature class. Error bars represent the standard error calculated from the total instances of each class counted and total features counted.

4.4.4 Morphology comparison of PC/cholesterol liposomes

The proportion of each of the liposome feature classes counted for the two recombinant proteins and negative control are compared in Fig 4.6.

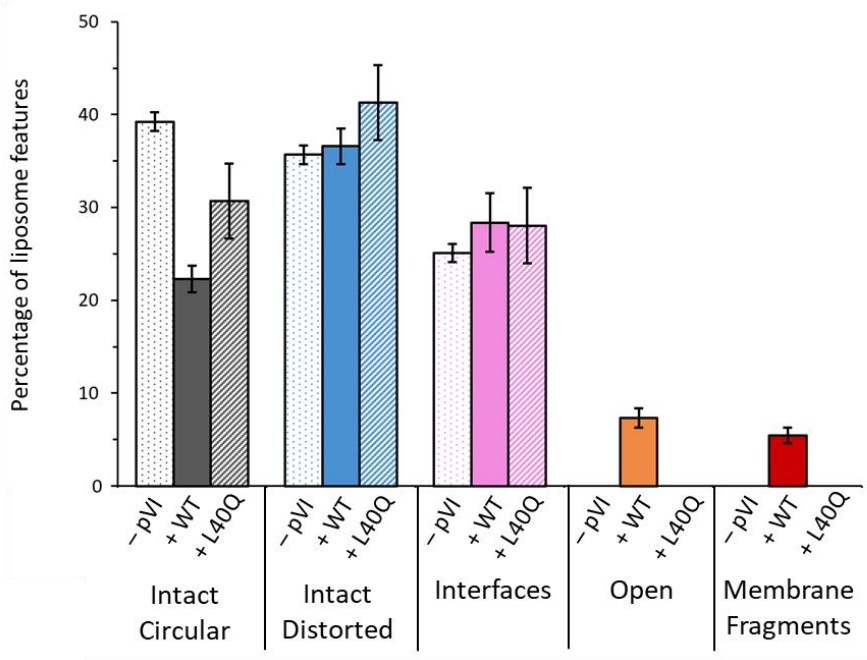


Figure 4.6 pVI-WT but not pVI-L40Q produced open liposomes and membrane fragments and there was little difference in proportions of interfaces counted.

Open and fragment categories were not observed in negative control (–pVI) or pVI-40Q samples. Error bars represent the standard error calculated from the total instances of each class counted and total features counted. Total counts of liposome features were 1243, 1301 and 187 for liposomes only, liposomes + pVI-WT and liposomes + pVI-L40Q, respectively.

Liposome samples incubated with pVI-WT contained substantially fewer intact circular liposomes than the liposome only samples, while the number of distorted liposomes was within error of the liposome only control. In the liposomes incubated with pVI-L40Q, the

proportion of intact circular liposomes agreed within error with the liposome only samples, but the number of intact disordered liposomes was higher. The proportion of interfaces observed for the negative control, pVI-WT and pVI-L40Q datasets was 25.1, 28.5 and 28.0%, respectively and agreed within error for the three datasets. The similar proportion of interfaces indicate that this morphology was not the result of protein interaction with membranes and therefore not of biological interest. These interfaces were likely the result of liposomes being pushed together during the blotting procedure, as the proportion seems related to the local liposome concentration.

Addition of pVI-WT reduced the number of intact PC/cholesterol liposomes and resulted in the appearance of two new morphologies, open liposomes and membrane fragments. This is evidence that pVI-WT causes liposome disruption. These classes were not observed in the liposomes incubated with pVI-L40Q, indicating that this mutant cannot disrupt these membranes in the same manner as pVI-WT.

4.5 Characterisation of PC/PE/Chol liposomes

Phosphatidylethanolamine (PE) was next included in the liposome mixture in order to more accurately model the endosomal membrane that pVI would be exposed to during the viral life cycle. pVI-WT and pVI-L40Q, used in section 4.4.1, plus two additional pVI constructs, pVI-Δ54 and pVI-34-54 were applied to PC/PE/cholesterol liposomes. In addition to the categories counted for PC/cholesterol liposomes, several other types of liposome features

were observed. Membrane interfaces similar to those found in PC/cholesterol liposomes were also observed, but comparison of characterised liposome samples (Fig 4.6) suggested that interfaces were unrelated to the biological activity of pVI, this category was not shown in the analysis for PC/PE/cholesterol samples.

4.5.1 Characterisation of PC/PE/Chol liposomes

Liposomes were more evenly distributed within ice than the PC/cholesterol samples with or without pVI proteins, and therefore fewer liposomes were found crowded and there were more examples of fully circular intact liposomes. 80% of PC/PE/cholesterol liposomes were classified as intact circular and 20% were distorted but intact. The liposomes included within these classes were similar in appearance to PC/cholesterol liposomes assigned to the same classes. The distorted intact (Fig 4.7Bii) class contained fewer liposomes that were pressed against other liposomes than in the PC/cholesterol liposomes (Fig 4.3). In summary, only intact liposome classes and no membrane disruption was observed in PC/PE/cholesterol samples.

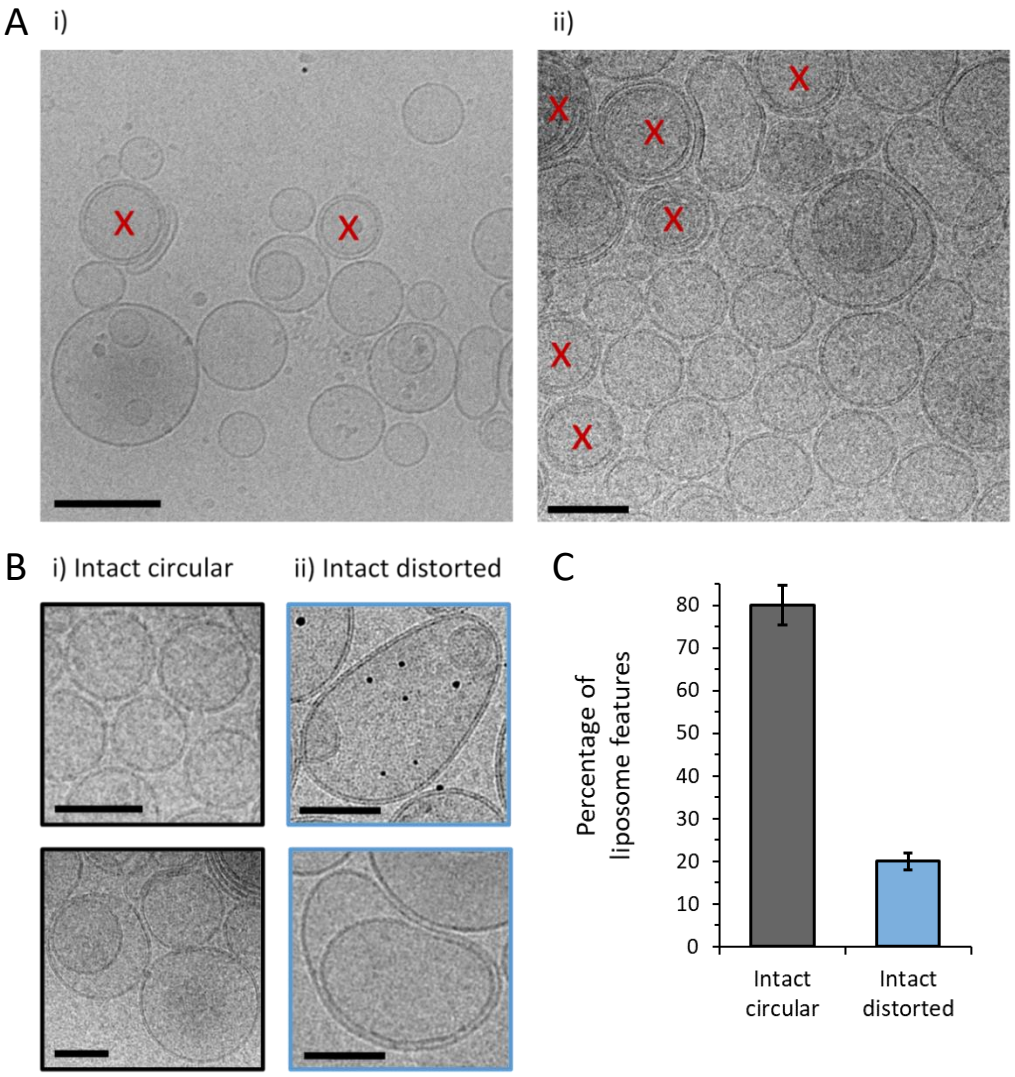


Figure 4.7 PC/PE/cholesterol liposomes were very similar in appearance to liposomes without PE and no membrane damage was evident.

(A) Example cryoEM projection images of liposomes. Red crosses, liposomes excluded from count. Scale bars: 100 nm. (B) Examples of liposomes feature classes. Scale bars: 50 nm. Estimated liposome diameter range was 30–260 nm. (C) Chart of percentages of each class of liposome features. Error bars represent the standard error calculated from the total instances of each class counted and total features counted.

4.5.2 Characterisation of PC/PE/Chol Liposomes + pVI-WT

In PC/PE/cholesterol liposomes incubated with pVI-WT, 46.5% of liposomes observed were classified as intact circular and 44.1% as intact distorted. These samples also featured open liposomes and membrane fragments, along with two additional morphology categories as compared to PC/cholesterol liposomes + pVI-WT (Fig 4.5): “pointed liposomes” (Fig 4.8Bi) and “hemifusion sites” (Fig 4.8Bii). Pointed liposomes and hemifusion sites comprised 3.6% and 0.6% of counted liposome features, respectively.

Some liposomes were pinched at one point to form a teardrop shape (Figure 4.8Ai), but without a gap in the membrane, as seen with open liposomes, that were classified as “pointed liposomes”. Other liposomes formed a single narrow contact site of <20 nm with neighbouring liposomes. A very small proportion of these sites were of less than ~10 nm and the outer layer of the membrane leaflets appear blurred, while the inner leaflets remain distinct (Fig 4.8Bii). These liposome features were assigned to a new category, “hemifusion” sites, since they resemble the intermediate stage in formation of a membrane fusion pore, an essential and distinct stage in the canonical membrane fusion process [276]. 0.6% of all liposome features observed were classified as hemifusion sites.

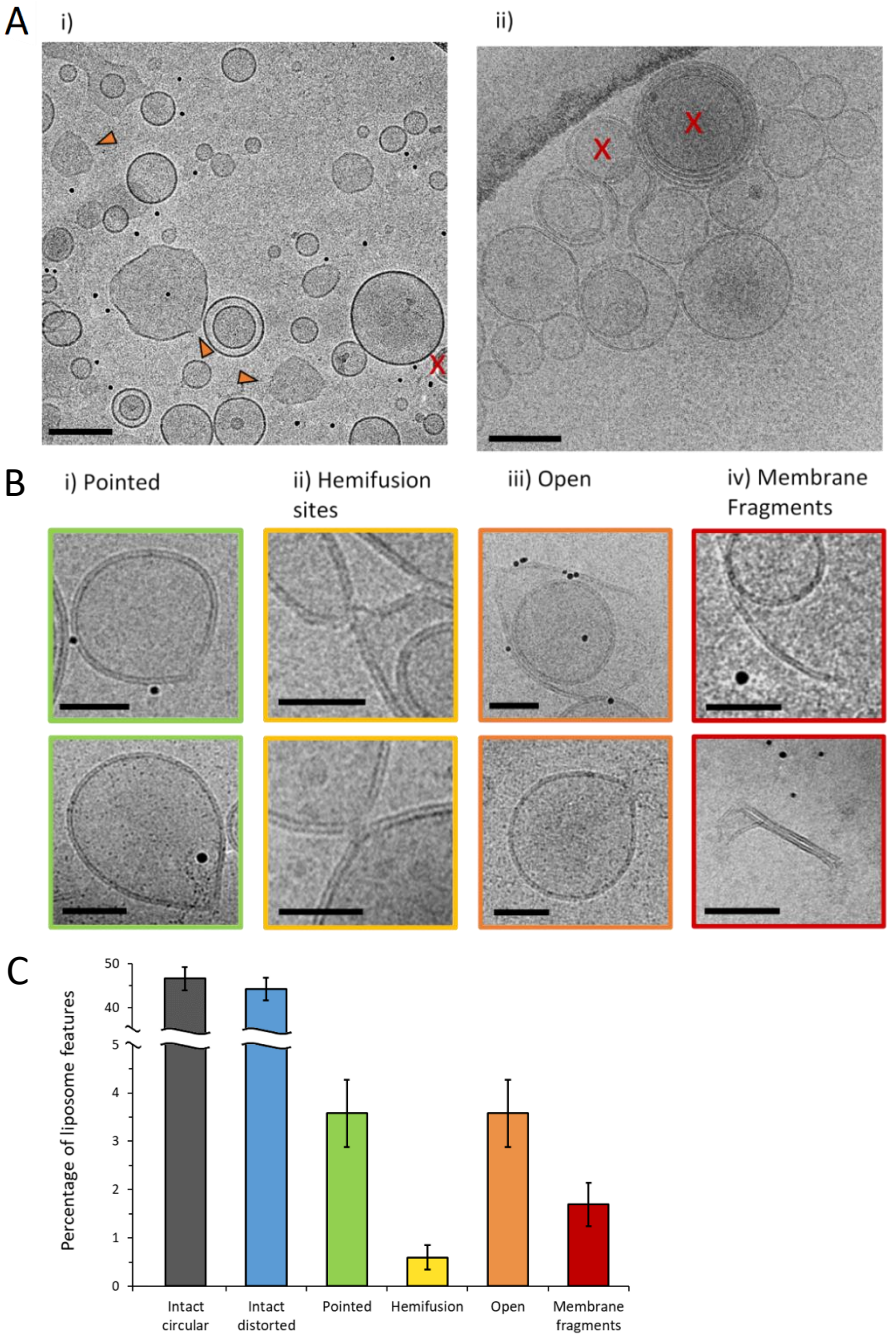


Figure 4.8 PC/PE/cholesterol liposomes showed evidence of membrane disruption upon addition of pVI-WT and included two new morphology classes.

(A) Example cryoEM projection images of liposomes with PE after addition of pVI-WT. Red crosses, liposomes excluded from count. Orange arrowheads, representative open liposomes with indistinct membranes. Scale bars, 100 nm. (B) Examples of liposome morphological classes. Scale bars, 50 nm. Estimated liposome diameter range was 20–250 nm. (C) Chart of percentages of each class of liposome features. Error bars represent the standard error calculated from the total instances of each class counted and total features counted.

In addition to the novel classes described above, the open liposome and membrane fragment classes observed in PC/cholesterol liposomes with pVI-WT were also observed. 3.6% of all liposome features observed were classified as open liposomes, with opening sizes ranging from <20 nm to >100 nm. Several open liposomes are shown in the overview in Fig 4.8Ai, including several liposomes with less distinct membranes where discontinuities were still visible (orange arrowheads). Examples of a liposome with a large (>50 nm) opening (Fig 4.8Biii, top panel) and a liposome with a very narrow (<10 nm) opening (Fig 4.8Biii, bottom panel) are given. These openings (Fig 4.8Biii) are distinguished from the pointed liposomes observed (Figure 4.8Bi) by the size of the opening. 1.7% of events observed were classified as membrane fragments, some consisting of single membrane bilayers (Fig 4.8Biv, top panel) and others of two membrane bilayers stacked on top of another (Fig 4.8Biv, bottom panel). In summary, two new morphological classes were observed that were not seen in negative control as well as the two membrane damage classes.

4.5.3 Characterisation of PC/PE/Chol Liposomes + pVI-L40Q

Compared to PC/PE/cholesterol liposomes with pVI-WT, liposomes incubated with pVI-L40Q were more homogenous in size and shape, with liposomes ranging between 20–200 nm. Fewer distorted liposomes were found overall. 75.9% of the total observed liposome features were classified as intact circular and 24.0% as intact distorted. A single example of a pointed liposome was observed (Fig 4.9Bi), making up 0.1% of the total observed

liposomes. No examples of the membrane damage classes, open liposomes or membrane fragments were observed, and all liposomes were intact.

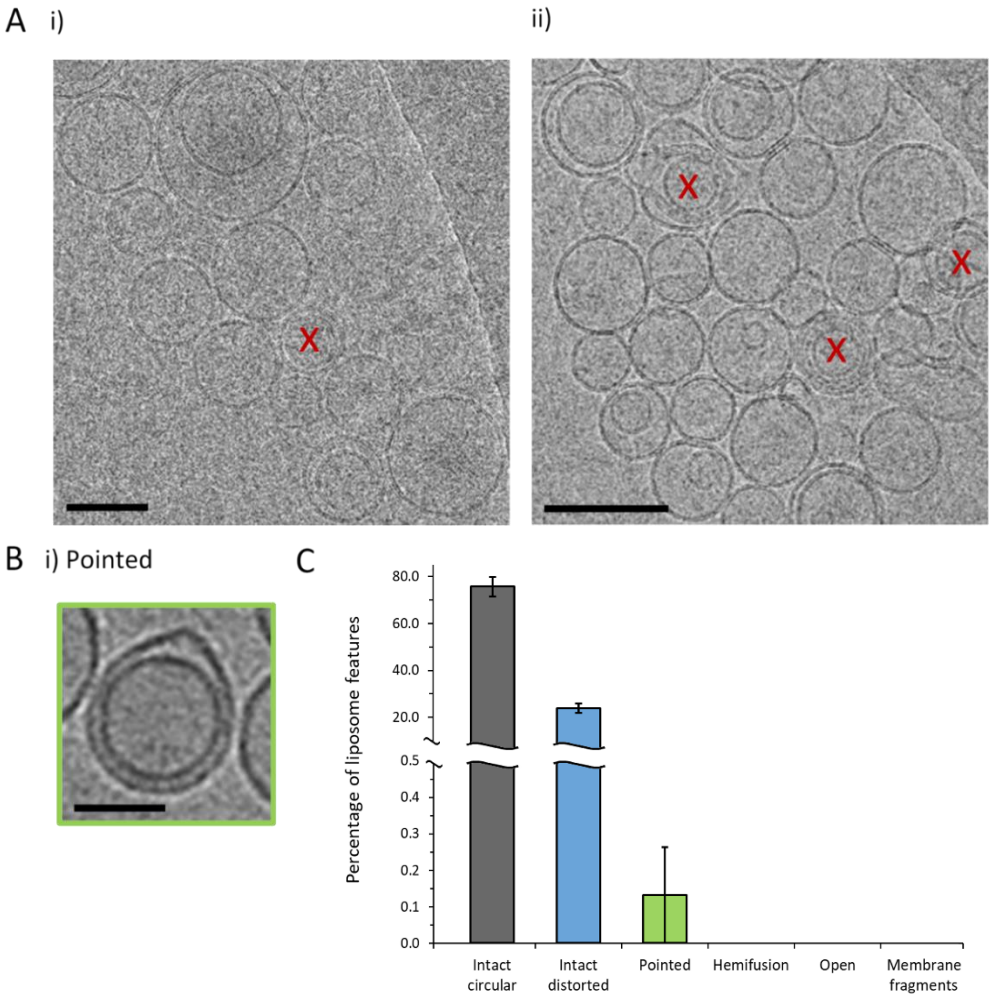


Figure 4.9 A single example of a pointed liposome was found in PC/PE/cholesterol liposomes on addition of pVI-L40Q, but none of the other disrupted morphologies.

(A) Example cryoEM projection images of PC/PE/cholesterol liposomes after addition of pVI-L40Q. Red crosses, liposomes excluded from count. Scale bars: 100 nm. (B) Examples of liposomes morphological classes. Scale bars: 50 nm. Estimated liposome diameter range was 30–280 nm. (C) Chart of percentages of each class of liposome features. Error bars represent the standard error calculated from the total instances of each class counted and total features counted.

4.5.4 Characterisation of PC/PE/Chol liposomes + pVI-Δ54

Due to the lack of the N-terminal helix, liposomes incubated with purified pVI-Δ54 were not expected to show a large amount of membrane disruption. As with negative control samples, the vast majority of liposomes were intact. Of the liposomes observed, 54.2% and 45.7% were classified as intact circular and intact distorted, respectively.

A single open liposome was counted (Fig 4.10B), making up 0.2% of the total observed liposome features. No pointed liposomes, hemifusion sites or membrane fragments were observed. In this sample, there was a higher liposome density and poor contrast due to bad ice quality, resulting from sample preparation or sample handling during transfer. These images underwent further filtering to improve contrast, and hence the image quality may have resulted in less reliable characterisation. In summary, 99.8% of observed liposomes were intact with only one example of a disrupted liposome.

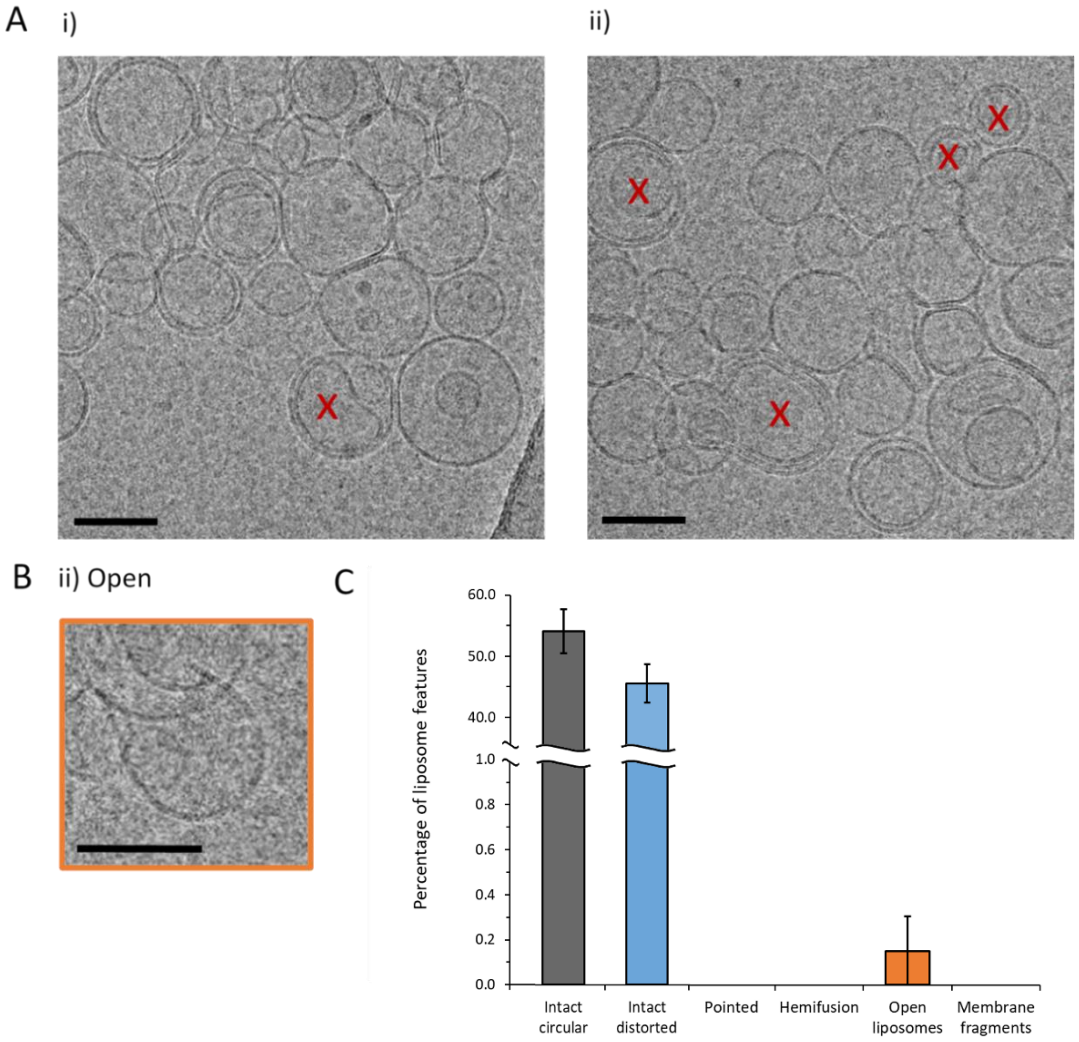


Figure 4.10 A single example of an open liposome was found in liposomes on addition of pVI-Δ54, but none of the other disrupted morphologies.

(A) Example cryoEM projection images of PC/PE/cholesterol liposomes after addition of pVI-Δ54. Red crosses, liposomes excluded from count. Scale bars, 100 nm. The mottled appearance of the ice is due to surface contamination. (B) Examples of liposomes morphological classes. Scale bars, 50 nm. Estimated liposome diameter range was 30–280 nm. (C) Chart of percentages of each class of liposome features. Error bars represent the standard error calculated from the total instances of each class counted and total features counted.

4.5.5 Characterisation of PC/PE/Chol Liposomes + pVI-34-54

In addition to the three pVI proteins, the peptide comprising the first 20 residues of pVI was incubated with liposomes. Similar to liposomes incubated with pVI-WT, all of the morphological classes were observed in liposomes incubated with pVI-34-54 (Fig 4.11). 33.5% of liposome features observed were classified as intact circular and 60.6% as intact distorted. 2.6% of liposome features observed were classified as pointed liposomes (Fig 4.11Bi) and 0.8% as hemifusion events (Fig 4.11Bii), their appearance similar to those of liposomes incubated with pVI-WT. 2.4% of liposomes were open (Fig 4.11Biii, openings indicated by the arrowheads) with opening sizes ranging from ~20–80 nm. Only 2 membrane fragments were found (Fig4.11Biv), both of which were laying alongside intact liposomes (arrowheads), making up 0.2% of the total observed events.

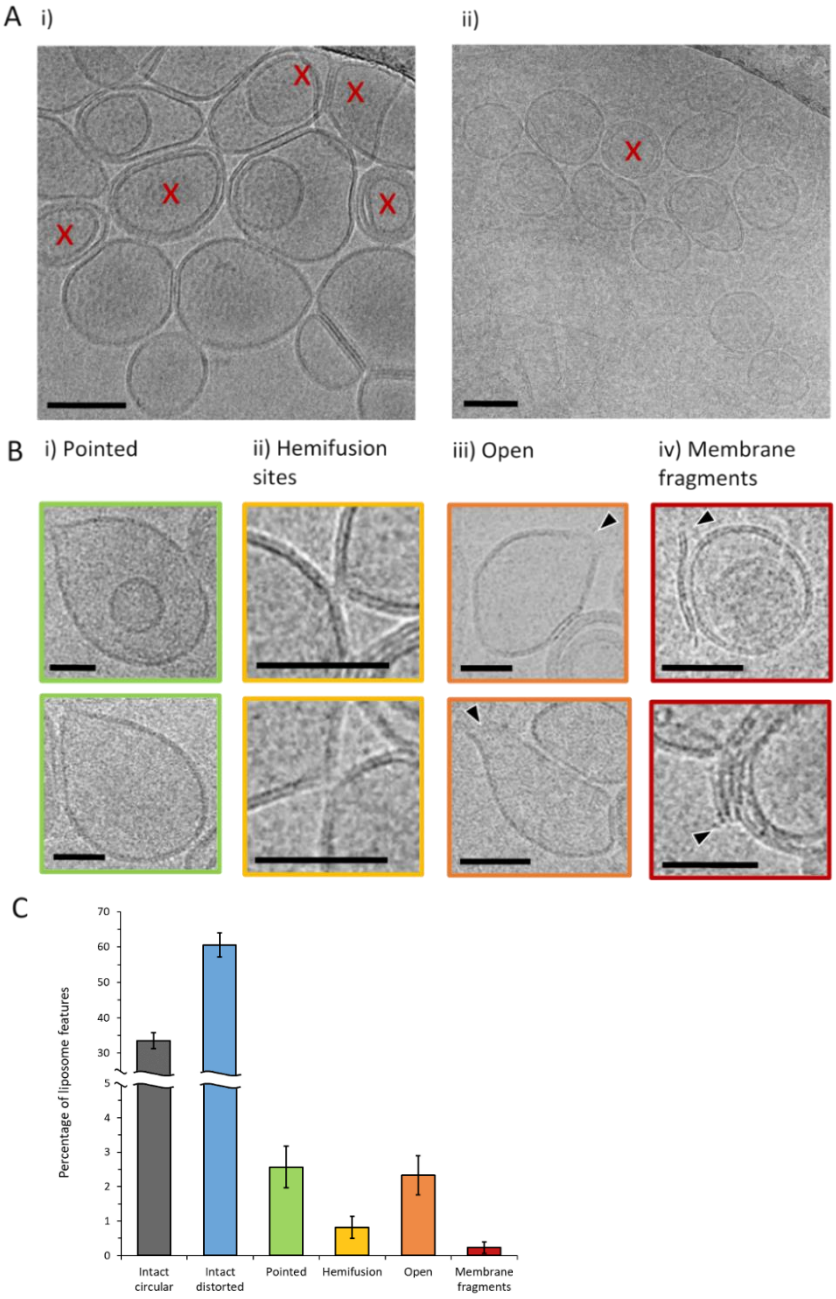


Figure 4.11 All of the morphological categories observed in pVI-WT samples were also observed for peptide pVI-34-54.

(A) Example cryoEM projection images of PC/PE/cholesterol liposomes after addition of pVI-34-54. Red crosses, liposomes excluded from count. Scale bars, 100 nm. (B) Examples of liposomes morphological classes. Arrowheads, openings of liposomes and membrane fragments. Scale bars, 50 nm. Estimated liposome diameter range was 30–250 nm. (C) Chart of percentages of each class of liposome features. Error bars represent the standard error calculated from the total instances of each class counted and total features counted.

4.6 3D observation of pVI interaction with membranes using cryoET

While projection images provide 2D spatial information which allows for rapid characterisation of a large number of liposomes, some aspects of liposome morphology, such as the dimensions of membrane openings or free membranes created by pVI can be best investigated in 3D. CryoET was used to produce 3D maps of groups of liposomes incubated with pVI-WT in order to capture membrane rupture events (Fig 4.12 A), and then compared to liposomes without protein (Fig 4.12 B). Fig 4.12 shows slices from the tomograms.

Two intact circular liposomes, one open liposome and several membrane fragments are visible in Fig 4.12Ai, while Fig 4.12Aii shows slices of a tomogram with a cluster of 5 intact circular liposomes, a small pointed liposome and one open liposome. The ends of the open liposome appear to roll outwards in the second and third panels. By contrast, the liposomes analysed without protein (Fig 4.12B) contained no evidence of membrane damage. The 20 intact liposomes in Fig 4.12B are mainly circular and only one was slightly distorted. 3D analysis of liposomes enabled confirmation that the liposomes in the negative control samples were not disrupted and that only liposomes incubated with pVI-WT exhibited membrane damage resembling the morphological classes previously identified: membrane openings and fragments.

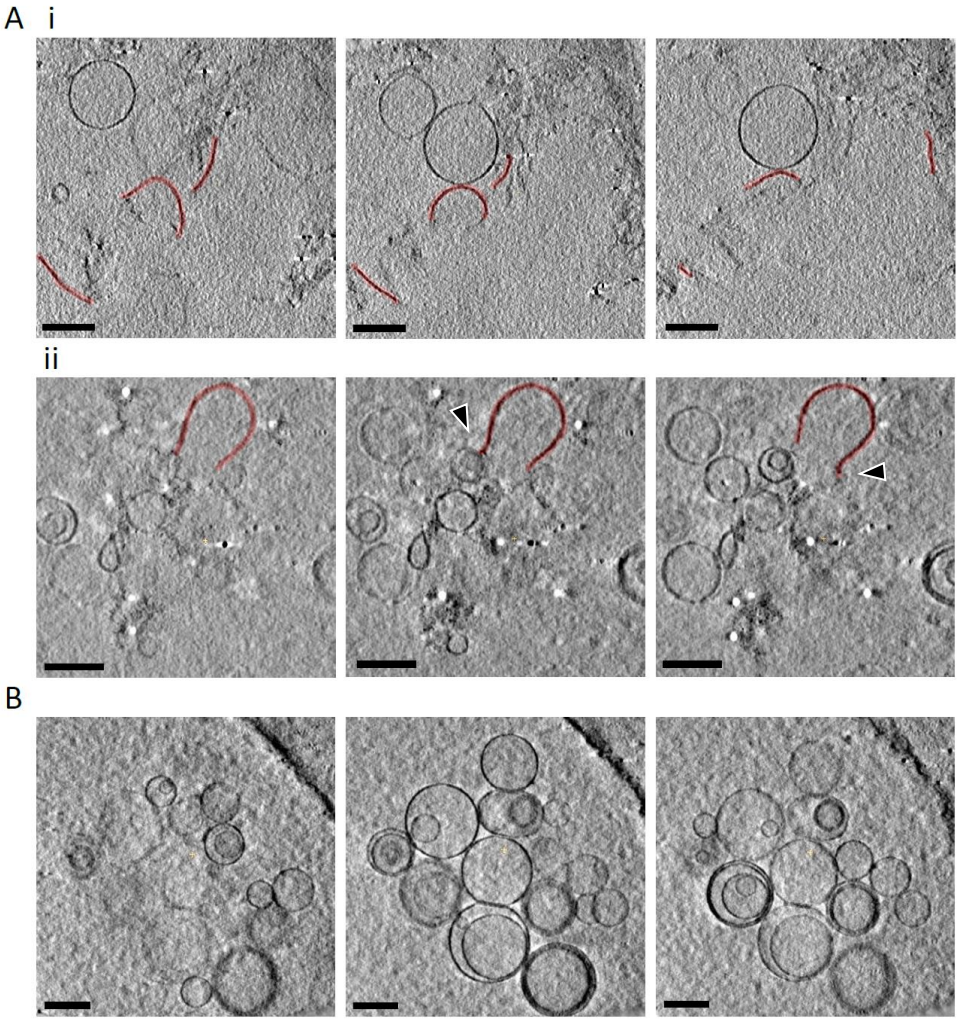


Figure 4.12 CryoET reveals membrane fragments and the curved membranes of open liposomes in liposomes with pVI-WT.

Sequential slices of ~23nm thickness through two tomograms of PC/cholesterol liposomes with pVI-WT (A) and 1 tomogram without (B). Representative membrane fragment examples and open liposomes are highlighted in red. Curved edges of open liposomes are indicated by black arrowheads. Scale bars, 100 nm.

4.7 Discussion

Four pVI constructs were examined for their ability to disrupt liposomes: recombinant wild type pVI, a loss of function mutant with a single nucleotide change in the N-terminal helix responsible for membrane rupture (pVI-L40Q), a truncation mutant lacking the entire N-terminal helix (pVI-Δ54) and a peptide corresponding to the N-terminal helix (pVI-34-54). Each construct was added to liposomes and the resultant morphological classes were compared to reveal their effect on membranes. At a liposome: protein ratio of 4:1, the majority of liposomes were intact, whether pVI proteins were present or not. The percentage of intact liposomes in the negative control, pVI-WT, pVI L40Q, pVI-Δ54 and pVI-34-54 datasets were 100%, 90.5%, 99.87%, 99.85%, 94.05%, respectively. The total counts for the two intact liposome categories (intact circular and intact distorted) and four disrupted categories (pointed, hemifusion, open and membrane fragments) were then combined to enable comparison between the samples, as shown in Fig 4.13A.

Intact distorted liposomes were observed in all samples, and therefore these were regarded as the result of sample preparation rather than an effect of the pVI constructs. Many liposomes were squashed by neighbouring liposomes in areas of local sample crowding, likely due to the force created by sample blotting pushing liposomes together. In contrast, elongated liposomes did not appear to be affected by neighbouring liposomes and were likely created during extrusion through nitrocellulose membranes.

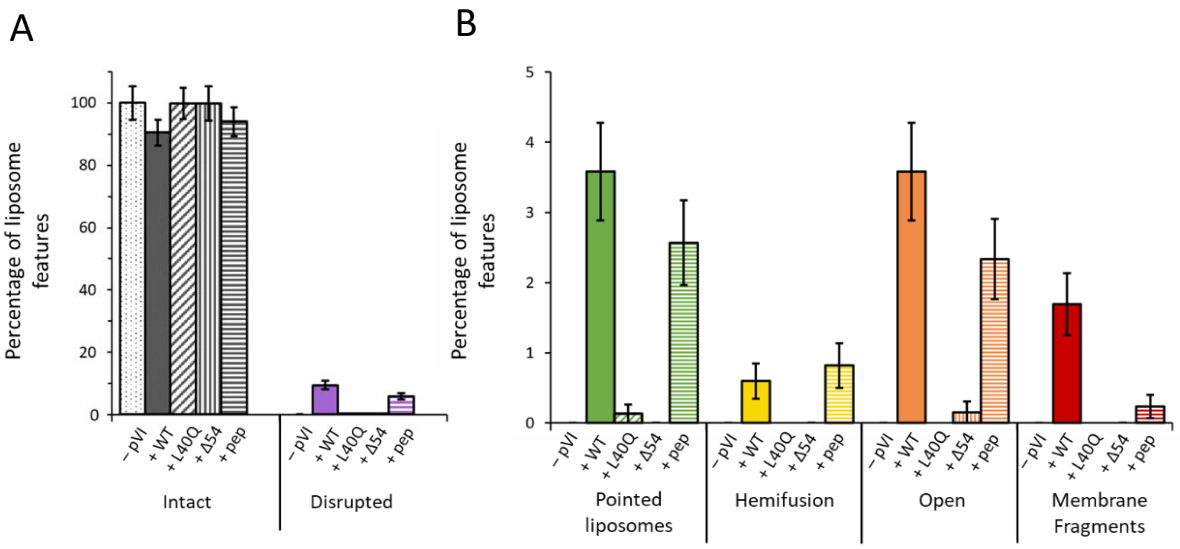


Figure 4.13 pVI-WT typically induced more membrane disruption events than pVI-34-54 in PC/PE/cholesterol liposomes, with only a few examples for pVI-L40Q and pVI-Δ54.

(A) Comparison of combined intact (intact circular and intact distorted) and disrupted liposome morphology classes (pointed, hemifusion, open and membrane fragments) for each pVI construct. (B) Comparison of the individual disrupted liposome morphology classes for each pVI construct. Error bars represent the standard error calculated from the total instances of each class counted and total features counted.

For negative control liposomes at 2 mg/ml, there were no disrupted liposomes. For liposomes and proteins mixed at a 4:1 ratio, overall proportions of disrupted liposomes was 9.50% for pVI-WT, 0.13% pVI L40Q, 0.15% for pVI-Δ54 and 5.95% for pVI-34-54. Only pVI-WT and pVI-34-54 were found to induce membrane damage that resulted in open liposomes and membrane fragments. Therefore, the differences between the two intact liposome categories is less important than the disrupted categories when examining the effects of pVI constructs on liposomes. Both loss of function mutants pVI-L40Q and pVI-Δ54

did not create very much liposome disruption. The liposome samples incubated with the loss-of-function mutant pVI-L40Q only produced one example of a pointed membrane (Fig. 4.9), while the truncation mutant pVI-Δ54 only produced one open liposome. This was consistent with previous studies which found these constructs had much lower membrane-disruptive activity *in vitro* compared to pVI-WT [19, 124].

The observation of pointed liposomes raises the question of the mechanism of pVI. Previous studies had concluded that pVI-WT does not induce size-selective pores in liposome membranes since both SulfoB and 70 kDa FITC-dextran, which have hydrodynamic radii of 6 and 100 Å (~0.6 and 10 nm) respectively, were released from liposomes with equal efficiency [124, 277]. Furthermore, very small pores would not be sufficient to allow the escape of the partially disassembled ~100 nm viral capsid. These pointed liposomes may represent a single site of membrane disruption as a precursor to larger membrane openings. In this case, the lower proportion of pointed liposomes found in the presence of pVI-34-54 may indicate the lower efficiency of the peptide in inducing membrane curvature leading to membrane disruption, suggesting the importance of the rest of the N-terminal helical region of pVI.

The interfaces between liposomes described in section 4.4 were found in all samples and were likely the result of liposome crowding and were not included in the analysis of PC/PE/cholesterol samples since there was no meaningful difference compared to

liposomes without protein (Figure 4.6). A very small number of “hemifusion sites”, where membranes appeared to merge their outer bilayer leaflets, were observed only in pVI-WT and peptide pVI-34-54 samples. The fact that hemifusion sites were only present with constructs containing the non-mutant N-terminal AH may suggest that they are the result of this helix interacting with membranes. However, no evidence has previously been found of adenovirus inducing membrane fusion. Instead, it is more likely that these sites represent a transient contact point between liposome regions that were both locally disrupted by action of the protein or peptide. Hemifusion sites also somewhat resemble later stages of membrane separation via fission, the process by which membrane-bound cellular compartments split into two discrete bodies, although there is no evidence in the literature of AdV pVI inducing membrane fission. Due to the very small number of these features observed, hemifusion sites are not likely to represent an important stage in membrane disruption by pVI.

The appearance of open liposomes was very heterogenous, ranging from liposomes that appeared very similar to pointed liposomes but with a visible opening of >10 nm, to liposomes with large openings encompassing the full diameter of the liposome or larger. These may possibly represent different stages of membrane rupture. Membrane fragmentation as a result of positive curvature formation is thought to be the mechanism responsible for endosome permeabilisation by pVI-WT [124], but fewer fragments were

observed than open liposomes, indicating that complete fragmentation of liposome membranes occurred less frequently.

Membrane fragments were found almost exclusively in pVI-WT samples. This was surprising, since pVI-34-54 was reported to exhibit higher membrane lytic activity than pVI-WT in dye release assays at similar concentrations [124]. However, the peptide used in the study by Maier et al. contained an additional C-terminal tetralysine tag added to enhance aqueous solubility, which may have increased the membrane-lytic activity of this peptide, while the peptide used in this study contained no additional tag. While no evidence of aggregation was observed in the pVI-34-54 samples examined in this study, lower solubility may have reduced local peptide concentration in the areas imaged and reduced its activity in comparison to both recombinant pVI-WT and the tetralysine-tagged peptide used by Maier et al [124]. Many of the fragments observed in projection images were clustered together near intact or ruptured liposomes. The only two examples of membrane fragments found in pVI-34-54 samples were closely associated with intact liposomes, which could be the result of them being unable to separate from other membranes or due to the higher liposome density in these samples.

4.7.1 Addition of PE reduced the membrane lytic activity of pVI-WT

After examining the interaction of simple PC/cholesterol liposomes with pVI-WT and pVI-L40Q, PE was added to the liposome mixture to produce a more complex model system that was closer to the composition of the endosomal membrane. The appearance of intact liposomes within each of the morphological classes was similar between the two liposome compositions, but two additional liposome morphology classes were observed in PC/PE/cholesterol liposomes incubated with pVI-WT and pVI-34-54, pointed liposomes and hemifusion sites. These new liposome features raised the question of whether those classes were present in the non-PE containing liposomes and had been missed. The PC/cholesterol datasets were examined for these classes and in pVI-WT samples, 1.2% of liposomes that were previously classified as intact distorted (Figure 4.8C) were reclassified as pointed liposomes. No hemifusion sites were found and reclassified in any of the PC/cholesterol samples. The two liposome types incubated with pVI-WT were then compared (Fig 4.15).

Overall, 19.9% of events in PC/cholesterol liposomes exposed to pVI-WT were categorized as membrane disruption events, compared to 9.8% for PC/PE/cholesterol liposomes. PE has a preference to adopt positively curved membranes [227, 278]. In liposomes containing PE, fewer open liposomes and fragments were found, which suggests that PE within the membranes reduced liposome disruption by pVI. This result is consistent with previous studies performed by Maier et al., where pVI-WT was found to cause membrane lysis and

that increasing concentration of PE reduced membrane lytic activity of pVI in *in vitro* dye release assays [124]. The results of Chapter 3 were consistent with this observation, as less dye release was observed from PE-containing liposomes exposed to pVI-WT (Fig 3.5) compared to liposomes without PE in experiments performed by Maier et al. [124]. However, a higher percentage of pointed liposomes was found in PE-containing liposomes, possibly due to the PE preventing formation or expansion of openings. Some of the exposed membrane edges observed by cryoEM were positively curved outward (Fig. 4.5Biv) and cryoET enabled 3D examination of one such opening (Fig. 4.12Aii). While several liposomes with curved edges were found in PC/chol liposomes, only one such open example was found in PC/PE/chol liposomes + pVI-WT, which is also consistent with the possibility of PE reducing curvature generation.

Putative hemifusion sites were found only in PC/PE/chol liposomes incubated with pVI-WT and pVI-34-54. Biophysical studies have shown that higher PE concentrations promoted greater fusion efficiency of proteoliposomes [279] and promoted formation of a hemifusion intermediate structure during membrane fusion of osteoclasts *in vitro* [280]. The presence of PE may have caused membranes disrupted by pVI-WT and the peptide to begin the process of fusion, but it is more likely also that these sites are membrane disruption intermediates that resemble hemifusion stalks. It would be useful to examine hemifusion sites in 3D using cryoET in order to further characterise them. However, as only 0.6% and

0.8% of liposome features were classified as hemifusion sites in pVI-WT and pVI-34-54 samples, respectively, these events would be very difficult to find within samples.

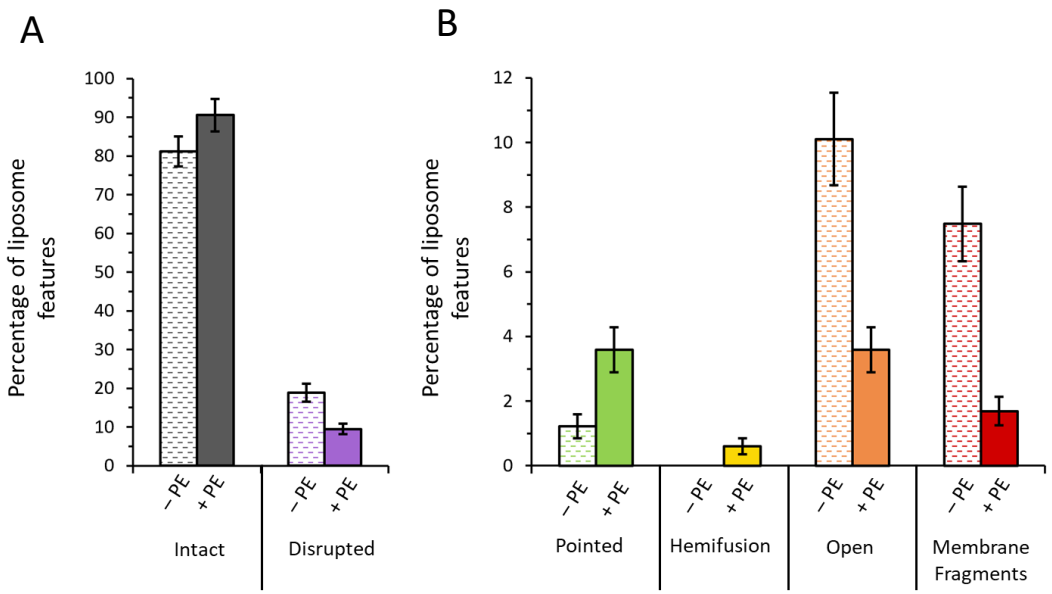


Figure 4.14 Liposomes containing PE exhibited fewer disrupted liposomes upon addition of pVI-WT.
(A) Comparison of intact (intact circular and intact distorted) and disrupted (pointed, hemifusion, open and membrane fragments) liposome morphology classes in the two liposome mixtures incubated with pVI-WT. (B) Comparison of the disrupted liposome morphology classes in the two liposome mixtures incubated with pVI-WT. Dashed line bars, PC/cholesterol liposomes + pVI-WT. Solid colour bars, PC/cholesterol liposomes + pVI-WT. Error bars represent the standard error calculated from the total instances of each class counted and total features counted.

The relative infrequency of membrane fragments and open membranes in pVI-WT and pVI-34-54 samples may be related to the function of the wild-type protein. Higher membrane lytic activity would be disadvantageous for the virus, since pVI has additional roles later in the viral replication cycle (as discussed in section 1.3.6) requiring the remaining pVI to be

released close to the nucleus where further capsid disassembly takes place. An excess of active pVI would also risk damaging the membranes of other organelles after endosomal escape, potentially resulting in premature cell death and the triggering of an immune response. It is not known whether all pVI particles remain associated with membranes after endosomal lysis, but cellular imaging studies revealed that at least some pVI appears to remain associated with gal3-positive membrane remnants after Ad5 endosomal escape [119].

4.7.2 Study limitations

This data has several limitations due to the sample preparation and data collection methods. Firstly, the counting method used was subjective and, in many cases, it was difficult to assign particular liposomes to certain classes. Despite optimisation of grid preparation, many liposome membranes were obscured. Fewer membrane disruption events were found than expected in pVI-WT and peptide samples as compared to the high percentage of dye released from liposomes in membrane rupture assays discussed in section 3.4 and in pVI dye release studies by Maier et al. [124, 143] and Moyer et al. [19]. However, this is due to the high sensitivity of the technique and low number of grid areas that can be screened compared to bulk measurement techniques such as dye release assays. This possibility may explain the disparity between the high activity of pVI-Δ54 in the dye release assay (Fig 3.6) compared to the low proportion of membrane disruption events

observed using cryo-EM. Due to the limited protein available, it is possible that the protein concentration used was not within the most active range of pVI, and a larger range of liposome to protein ratios should be explored in the future.

The formation of stable SUVs with a homogenous size distribution is challenging. Both PC/cholesterol and PC/PE/cholesterol liposomes were heterogenous with a wide range of sizes and different degrees of curvature. pVI may not be able to lyse larger liposomes with lower degree of curvature as efficiently, as suggested by SulfoB leakage assays where pVI-WT showed higher affinity to 50 nm LUVs than to 200 nm LUVs [168]. However, despite the high number of passes through membrane pores of 100 nm diameter, it is not possible to completely exclude larger liposomes from the sample. Despite the range of estimates sizes, variations in liposome diameter were not considered an important factor in the analysis.

The liposomes used in this study also lacked several of the lipids also found in endosomal membranes which may contribute to different curvature and charge properties, such as phosphatidylinositol (PI) and phosphatidylserine (PS). A lipid mixture that was closer to plasma membrane composition composed of 35% Cholesterol, 25% PC, 15% PE, 15% sphingomyelin (SM), 10% PS and 5% PI, was also examined using cryoEM, but these liposomes clumped together more readily than PC/PE/cholesterol liposomes. It may not therefore be feasible to use a more complex liposome composition for these experiments.

4.7.3 Conclusion

Liposomes composed of PC/cholesterol or PC/PE/cholesterol examined alone exhibited none of the four identified morphological categories that indicated membrane disruption. At a liposome: protein ratio of 4:1, pVI-WT was better able to damage liposomes than the peptide pVI-34-54 and to form membrane discontinuities such as open liposomes and membrane fragments. These differences between the proportions of morphology types induced by pVI-WT and the peptide suggest that other domains within pVI, such as the other predicted AH, have a role in membrane interactions. The loss of function mutants pVI-L40Q, with its altered N-terminal AH, and pVI-Δ54, which is missing the AH altogether, do not produce the membrane disruption classes. The presence of PE in liposome membranes may have reduced the number of membrane disruption events by inhibiting positive membrane curvature formation. The larger number of pointed liposomes in PE-containing liposomes may indicate that pVI-WT and the peptide are able to distort but not fragment liposomes as efficiently in the presence of PE.

4.8 Materials and methods

4.8.1 Negative stain EM

PC/cholesterol liposomes were prepared as in section 3.6 at a concentration of 2 mg/ml. 0.5 mg/ml pVI-WT and 2 mg/ml liposomes were prepared with equal volumes, mixed, and then incubated at 37°C for 30 minutes. Formvar 300-mesh EM grids (Agar scientific) were

prepared by glow-discharging using a Harrick Plasma cleaner on the high setting for 20 seconds.

4 µl of the liposome-protein mixture was pipetted onto a grid and incubated at RT for 1 minute. 5 µl of 2% pre-mixed uranyl acetate solution was added to grids and incubated at RT for 1 minute. Excess stain was wicked away with filter paper and drop of Milli-Q water was applied. Wicking was repeated and the grids allowed to air dry at room temperature.

Negative stain electron microscopy was performed at 120 keV on a Tecnai Spirit electron microscope (FEI) with an Eagle CCD camera (FEI). Images were recorded at a nominal magnification of 42,000x with a defocus of -1 µm and a pixel size of 0.27 nm.

4.8.2 CryoEM

4.8.2.1 Sample preparation

PC and cholesterol were mixed in the molar ratio 70:30 or PC, PE and cholesterol in the ratio 40:30:30 and liposomes were prepared as in section 3.4. Liposomes alone were prepared at 1–4 mg/ml. For experiments with pVI constructs, protein or peptide were prepared at 0.5 mg/ml and liposomes at 2 mg/ml in equal volumes, which were mixed and incubated at 37°C for 30 minutes.

C-Flat (Protochips) or Quantifoil EM grids covered with a carbon film of 2 µm holes with 1 µm spacing (2/1) were plasma cleaned (Harrick Plasma) for 60–90 seconds on high. Graphene oxide was diluted 1:20 in water and pelleted at 300 *x g* for 30 s. 4 µl of the graphene was pipetted from the top of the tube and allowed to adsorb onto the grid for a few minutes before blotting. A drop of water was applied, and blotting was repeated. Grids were allowed to dry at room temperature.

4 µl of liposome or liposome/protein mixture were pipetted onto the grid and 0.7 µl of 6 or 10 nm fiducial gold (Aurion) were added. Grids were blotted with Whatmann No. 1 filter paper from the back for 2–3 seconds and plunge-frozen into a liquid ethane/propane mixture [281]. Alternatively, grids were frozen using a Vitrobot (ThermoFisher Scientific) at 4°C and 100% humidity using blot force between -15 and -20 and blotting times of 2.5–3 seconds. Grids were transferred to liquid nitrogen for storage before data collection.

4.8.2.2 CryoEM data collection.

Defoci between 2 and 3 µm underfocus were used to record tilt series and projection images. CryoEM data was recorded on either a Tecnai T12 equipped with an Eagle CCD (FEI) camera, a Tecnai F30, equipped with a K2 direct electron detectors and Bio-Quantum energy filters (Gatan) or a Glacios microscope (FEI, Thermofisher), with a Falcon 3EC Detector. Projection images were taken at nominal magnifications of 7,200x to 77,000x, producing a final pixel size of 0.36 to 1.25 nm. Tomographic data was collected with

SerialEM [282] with pixel sizes of 0.228 nm at the specimen level and the energy-selecting slit set to 20 eV.

Tilt series were collected on a Tecnai F30 microscope using bidirectional acquisition covering an angular range from -30° to + 48° with 3° tilt increments for Fig 4.12 Ai, and -39° to +45° for Fig 4.12Aii and B. The total electron dose for the tilt series was kept between 60 and 80 electrons/$Å^2$. Images were collected in counting mode at an exposure rate of between 1.74 and 2.3 electrons/pix/sec. Defoci between 2 and 3 µm underfocus were used to record tilt series and projection images.

4.8.2.3 Tomogram reconstruction and data processing

Tomographic reconstructions were calculated with weighted back-projection in IMOD [283], using 10 nm gold fiducial markers to build a seed model and align stacks. Contrast transfer function (CTF) correction was performed in IMOD. Tomograms were reconstructed from CTF-corrected, aligned stacks using weighted back-projection in IMOD. Tomograms were binned by factor 4. Averaging of slices of tomograms for better visualisation was done using 3dmod.

4.8.3 Quantification and statistical analysis.

PC/cholesterol liposomes were sized with 100 nm filters and imaged with or without pVI-WT and pVI-L40Q. Morphology of individual liposomes was counted according to 5 categories: “intact circular”, “intact distorted”, “interfaces” between liposomes, “open liposomes” and “membrane fragments”. Numbers of each class were counted over the entire dataset for each construct or negative control. The error in counting statistics was estimated as the standard deviation of the Poisson distribution, which is the square root of the number of counts. This error was translated into percentages for display in bar charts using standard error propagation methods.

PC/PE/cholesterol liposomes sized to 100 nm were examined as in section 4.8.3.1, with the addition of two classes: “pointed liposomes” and “hemifusion sites”. While “interfaces” were counted for PC/PE/cholesterol liposomes, this category is not included in this set of analysis. The final datasets for counting of liposome features is presented in Table 4.1. Liposome sizes were measured using FIJI based on measuring the largest and smallest liposomes in at least 10% of projection images.

Table 4.1 Datasets for PC/cholesterol and PC/PE/cholesterol liposomes.

Dataset	Total liposomes counted	Number of projection images	Average liposomes per projection image	Approximate liposome size distribution (nm)
PC/chol no protein	1012	54	22.7	30–220
PC/PE/chol no protein	670	37	28.6	30–260
PC/chol + pVI-WT	989	80	11	20–290
PC/PE/chol + pVI-WT	1005	37	19.3	20–250
PC/chol + pVI-L40Q	147	6	23	20–320
PC/PE/chol + pVI-L40Q	762	35	18.6	30–280
PC/PE/chol + pVI-Δ54	659	24	28	30–280
PC/PE/chol + pVI-34-54	857	70	13.5	30–250

Chapter 5 Discussion

In order to characterise pVI and investigate its effect on membranes, I required a homogenous preparation devoid of contamination and protein degradation products. While the optimised purification protocol described in Chapter 2 improved greatly upon the result from previous protocols, the quality of the resulting protein fractions was still somewhat variable. The established protocol provided sufficient pure protein for the techniques used to characterise the proteins in chapters 3 and 4. Nuclear magnetic resonance (NMR) could be used to reveal more information about the structural conformation of pVI proteins and to examine particular structural regions of pVI in association with different lipids. However, if pVI proteins are to be analysed by techniques such as X- NMR in the future, the current protein yield of pVI-WT or pVI-L40Q from 4 L of *E. coli* culture and pVI-Δ54 from 1 L of culture would not be sufficient.

pVI is a difficult system to purify and study since it is likely to remain associated with bacterial membranes. Therefore, detergents or other agents are required to solubilise the protein during cell lysis. Denaturation of pVI using urea in the lysis buffer proved to be helpful for constructs where the N-terminal amphipathic helix (AH) is present, such as in pVI-WT (Section 2.2.3) and pVI-L40Q (Section 2.3), whereas detergents are sufficient for purifying pVI-Δ54, which is lacking the first helix and is therefore more soluble. However, exploring other purification approaches that do not require such a harsh purification method would be advantageous so that the constructs can be treated identically in all

experiments. pVI is also prone to degradation by bacterial proteases. Although protease inhibitors were used at all stages of the purification protocol, the amount of degraded protein might be reduced further by changing the location of the purification tag to the C-terminus and the solubility of the proteins might be improved by altering the purification tag, for example, by using a streptavidin tag in place of a His-tag. Overall, while the quality of protein preparations was improved from the starting point, additional improvements in yield and potentially also purity would be highly beneficial for our deeper understanding the structure and function of pVI.

In Chapter 3, the pVI constructs were examined using various biophysical methods to explore aspects of pVI structure and function. Circular dichroism (CD) confirmed that pVI-WT contains the strongest evidence of helical structural elements (Figure 3.3). The analytical ultracentrifugation (AUC) experiments (Figure 3.4) provided some evidence of dimerisation and trimerisation of pVI-WT and pVI-Δ54, indicating that the first N-terminal AH may be involved in, but not be essential for, oligomerisation and that other domains within pVI are possibly involved. While this is in agreement with the previous assignment of multiple pVI copies within the hexon cavities of available cryoEM structures, the oligomerisation state of pVI alone still remains uncertain. NMR and extended AUC experiments with pVI-L40Q and a range of protein concentrations would be required to further explore the oligomerisation state of pVI.

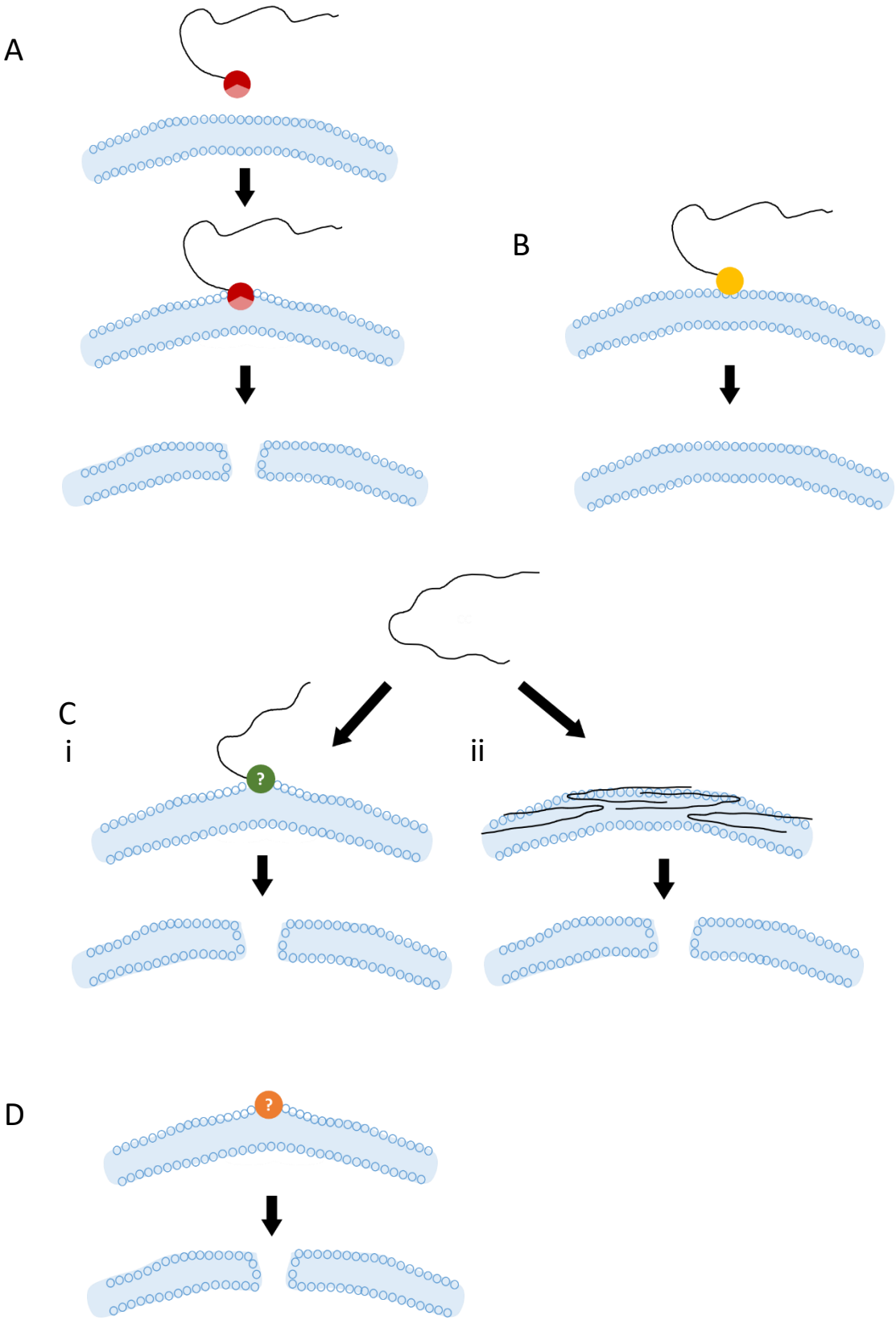

A
B
C
i
ii
?
D
?

Figure 5.1 Schematic models for the mechanism of AdV pVI disruption of endosomal membranes based on the data obtained in this study.

(A) The first N-terminal AH (amphipathic helix) of pVI-WT is predicted to insert into the membrane, resulting in membrane curvature induction and membrane lysis [124]. Top panel shows the first N-terminal AH (red circle) with the hydrophobic region (pink segment) and the unstructured remaining protein (black line). The second panel shows the insertion of the AH, followed by induction of membrane fragmentation. (B) The altered N-terminal AH of pVI-L40Q (Yellow circle) cannot insert into the membrane as deeply as the WT protein, therefore there is a ~10-fold attenuation in infectivity and in vitro liposome lysis [19]. In this instance, no membrane disruption takes place (lower panel). (C) Two potential mechanisms for the truncated pVI-Δ54 membrane disruption are proposed, represented as an unfolded protein (black line) (i) Folding coupled to binding. Residues from the remaining predicted helical region 55–107 may gain helical structure and insert into the membrane, resulting in some endosomal lysis. Top panel shows the potential AH, the insertion depth of which is not known (green circle with question mark) inserting into the membrane. Bottom panel, membrane fragmentation. (ii) Alternatively, proteins may disrupt membranes through a saturated surface binding ("carpet") mechanism. This may also be a possible mechanism for pVI-WT but is not shown in (A) for clarity. (D) The isolated N-terminal 33 residues of the wild-type protein, pVI-34-54 (orange circle) are able to insert into the membrane, but less efficiently than the full WT protein. The insertion depth of the AH formed by the peptide is also unknown (question mark).

I also demonstrated through a fluorescent dye release assay (Fig 3.6) that recombinant pVI-WT purified according to the optimised protocol was functional with liposome membranes, and this assay was used to investigate the contributions of the different domains of pVI in membrane lysis through comparison of activity of the other pVI constructs. The importance of the first N-terminal AH of pVI-WT has been established by several studies [19, 124, 143]. Our data support the suggested mechanism of this domain being responsible for membrane disruption, as illustrated in Fig 5.1A, the recombinant pVI-L40Q protein has a broken first AH and demonstrated much lower *in vitro* membrane lytic activity (Fig 5.1B). In addition to

the first AH, the N-terminal domain is predicted to contain three additional amphipathic helices that are predicted to spontaneously associate with membranes, albeit at a lower magnitude than the first helix [124, 143]. The peptide pVI-34-54 was previously demonstrated to gain helical structure upon binding to lipids [168], and is expected to behave in a similar manner to pVI-WT (Fig 5.1D). The higher activity of pVI-WT with liposomes compared to peptide pVI-34-54 in membrane interaction assays and in cryoEM projection images suggests that while the intact first AH is required for membrane binding and is sufficient for membrane disruption, other helices of pVI may be involved in membrane binding or positioning of the first helix. In order to further explore any potential complementation effect between the N-terminal helices, pVI-Δ54 and pVI-34-54 could be mixed, and the structural content and membrane-disruptive activity of this complex examined. Additional experiments with the 3 other helices alone or in combination with the first helix could be used to determine the individual contribution of each helix.

Use of CD spectroscopy in combination with fluorescent dye release assays suggested that the presence of secondary structure does not necessarily correlate with increased membrane lytic function, since pVI-L40Q contained more helical structure than pVI-Δ54, but the latter unexpectedly caused a higher percentage of dye release. CD data collected in the presence of lipids might reveal that pVI-Δ54 gains structure in the presence of liposomes, similar to pVI-34-54 [168], which may account for the higher dye permeability in liposomes exposed to pVI-Δ54 but not pVI-L40Q. An alternative mechanism, such as the saturated surface binding or “carpet” model, may also be responsible for the high activity

of pVI-Δ54 in the dye release assay (Fig 3.6), although it does not explain the lack of membrane disruption as observed by cryo-EM. These two possible models of pVI-Δ54 membrane disruption are illustrated in Fig 5.2C. However, these hypotheses remains to be tested. Examination of the protein structure by CD in the presence of liposomes could be complicated by additional light scattering and might only work at very specific concentration ranges or curvatures that might themselves limit the experiments. Instead, NMR might be better suited for studying the structural interaction of pVI proteins and membranes and lipids. Biolayer interferometry could also be used to explore interactions between proteins and model membranes to complement other techniques. The diverse roles of pVI in the AdV replication cycle suggest that it may have a dynamic secondary or tertiary structural conformation and that certain regions may gain structure when associating with different binding partners, for example, whether it is associated with hexon or facing the endosomal membrane.

CryoEM characterisation of the pVI construct with PC/PE/cholesterol liposomes (section 4.5), found no evidence of membrane disruption in either pVI-L40Q or pV-Δ54, in contrast to the relatively high activity of pVI-Δ54 suggested by the dye release assay. It is possible that dye release measures a different type of membrane activity if, for example, some of the pVI constructs produced small openings that render membranes transiently permeable to dye but were not visible using cryoEM. Luisoni et al. suggested that early pVI interactions with membranes involve the formation of small lesions that AdV capsids cannot pass through, although these experiments involved penetration of the plasma membrane rather

than the endosomal membrane [284]. If pVI-Δ54 can induce small lesions but not large openings and membrane fragmentation, this would explain both the dye release result and lack of damaged observed using cryoEM, since it was not possible to resolve structures as small as 0.6 Å, the approximate diameter of sulfoB molecules [124].

Designing a model endosomal membrane and producing stable synthetic liposomes for examining pVI constructs is challenging. The comparison between the two types of liposomes examined using cryoEM (Fig 4.14) demonstrates that the choice of lipid composition is an important consideration when designing a model membrane system for pVI, since some morphological classes were only present in liposomes containing PE. Addition of PE reduced the membrane damage by pVI-WT compared to liposomes without PE, which was consistent with the observations of Maier et al. that PE reduced dye release from liposomes by pVI-WT [124]. However, comparison of liposome composition was not carried out in this study using dye release assays and this could be combined with future cryoEM observation of liposomes. Based on the results from Chapter 4 and previous dye release experiments, it would be expected for pVI-WT to release dye from PC/cholesterol liposomes at lower protein concentrations [124]. The properties of the individual lipids, such as charge and propensity to adopt positive or negative curvature, greatly affect the activity of proteins, and not all components present in the endosomal membrane have been tested. Future experiments that could build upon the findings of this study include extending the experiments to compare the role of other lipids in the interaction of pVI with

liposomes. Furthermore, the lipid to protein ratio was kept consistent for most experiments, other than the dye release assay, and exploring different protein to liposome concentration ratios may help clarify the minimum number of pVI molecules required for infection. The effect of pH on pVI-membrane interactions was also not explored in this study and was kept constant at pH 7.4. While Wodrich et al. [108] found that the action of pVI-WT on model membranes was pH-independent *in vitro*, early endosomes have an internal pH of ~6.0–6.5 [285]. Therefore, the effect of pH on the activity of pVI with membranes should be explored.

A further consideration in assessing the biological relevance of the liposome model system to the role of pVI within cellular endosomes is that the protein used in this study faced the positively curved membranes of the outside of liposomes, whereas pVI within endosomes faces negative membrane curvature and is thought to induce positive curvature to rupture membranes [124]. However, pVI-WT did successfully induce some membrane damage to positively curved membranes from the outside of liposomes in my experiments. Furthermore, some of the exposed membrane edges observed by cryoEM and cryoET appeared to be positively curved outward. These curved membranes resemble the membranes of endosomes ruptured by the mutant AdV-M1 with a defect in the PPxY motif caused by a point mutation (covered in section 1.3.1) observed *in situ* by cryoET (Schellenberger et al., unpublished data), as compared in Fig 5.2. While several liposomes with curved edges were found in PC/chol liposomes with pVI-WT, only one such open example was found in PC/PE/chol liposomes, which is consistent with the property of PE in

negative curvature induction. These similarities indicate that a comparable membrane disruption process occurs both in endosomal escape within cells and *in vitro* with liposomes and purified pVI, despite the difference in curvature, suggesting that liposomes are adequate as a model.

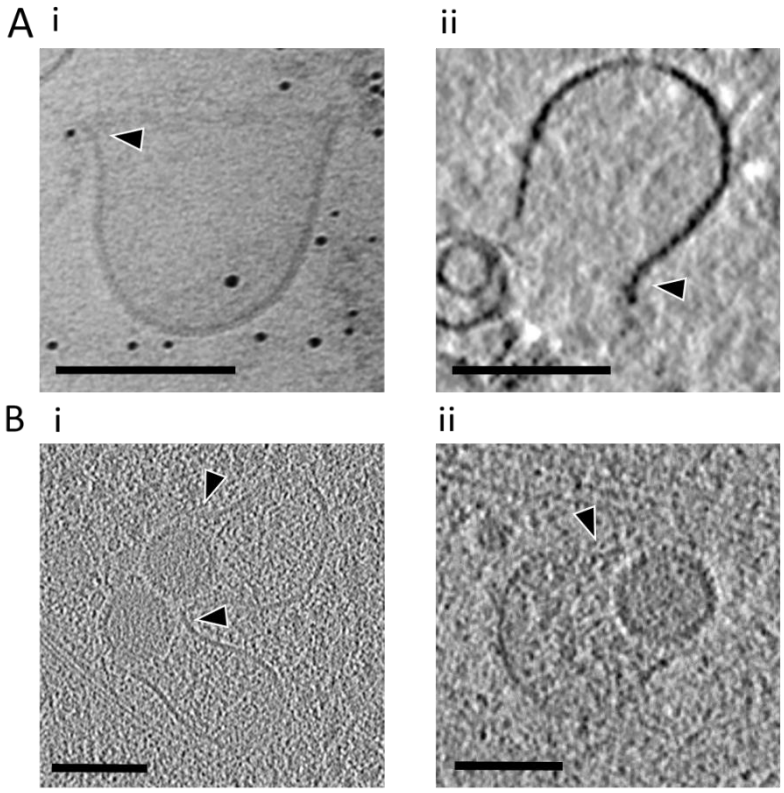


Fig 5.2 PC/cholesterol liposomes damaged by pVI-WT have curved edges that are similar to those of endosomes ruptured by Ad5-M1.

The Ad5-M1 mutant can rupture endosomal membranes but not translocate to the cytosol. (A) An example projection imaged an open liposome after incubation with pVI-WT (from Fig. 4.4). (B) An example tomogram slice of an open liposome after incubation with pVI-WT (from Fig. 4.12). (C) and (D) Example tomogram slices of endosomes ruptured by Ad5-M1 taken by Pascale Schellenberger. Examples of curled membranes are indicated by black arrows. Scale bars, 100 nm.

The quantification system used to classify different liposome morphology types using cryoEM (Chapter 4) allowed comparisons to be made between the activity of the different pVI constructs. However, the low number of membrane disruption features observed in Chapter 4 raise the question of how to image events that are rare in liposomes and even more difficult to locate within cells. Correlated light and electron microscopy (CLEM) allows areas of interest in the cell to be located using light microscopy (LM) with fluorescently labelled proteins prior to imaging the same samples at much higher resolution using cryoEM. Light microscopy of vitrified specimens (cryoLM) can also be used to pre-screen grids for damage or contamination. Furthermore, impractical searches for very rare and transient events of interest can be avoided.

A CLEM imaging pipeline was previously developed to capture important steps in the AdV replication cycle *in situ*. The system is based on a human cell line stably expressing galectin-3 (gal-3) fused to a fluorophore as a cellular marker of membrane damage [286]. When the membranes of endosomes are ruptured, galactose-containing N-linked glycans are exposed, to which the cytosolic galactose-binding lectin gal-3 binds. Gal-3 recruitment to ruptured membranes was shown to coincide with pVI release from capsids, after which virions separate from gal3, leaving pVI behind [119]. When endosomal membranes are ruptured, bright red spots and green Alexa488 labelled viruses are clearly distinguishable from the red background fluorescence of cells. The cryoCLEM workflow uses other two types of fluorescent markers, electron-dense single-channel 100 nm blue microspheres for correlation of areas of interest in LM and EM images, and 500 nm 4-colour Tetraspeck

microspheres used to monitor and correct the shifts between the fluorescence channels. LM imaging is performed on grids at cryogenic temperatures using the cryostage2, a second generation sample stage designed in the group of Wolfgang Baumeister at the Max Planck Institute for Biochemistry [287]. A protocol to enable correlative microscopy with a localisation precision of ~50 nm for events of interest was described by Schellenberger et al. [286]. A commercial cryo CLEM system has since been developed by Leica Microsystems, along with software that enables simplified correlation of samples. Further development of an optimised working pipeline for AdV imaging *in situ* is still ongoing. Thicker areas of the cell have recently become accessible through cryoEM in combination with focused ion beam milling. This allows more of these hard-to-locate events to be captured in cellular regions too thick to be imaged directly by cryoET [288]. Developing integrated workflows with these rapidly evolving technologies has enormous potential for deepening our understanding of specific cellular events that have previously been difficult to study.

The combination of the amphipathic helical and intrinsically disordered regions of AdV pVI makes it a challenging but fascinating construct to study. The data presented in this thesis confirms the importance of the intact N-terminal alpha helix in pVI activity against membranes and in pVI self-association, but also suggest a role for other regions of pVI, since the N-terminal peptide alone is less efficient at inducing membrane damage. The disordered nature of the c-terminal half of pVI and the possibility of several oligomerisation states may play a role in the numerous functions of pVI in the AdV replication cycle. Experiments using liposomes containing cholesterol and PE as model membranes also

suggest that the mechanism of pVI membrane disruption is highly dependent on individual lipid properties, and future work with more sophisticated membrane models will help to elucidate this characteristic of pVI further.

Chapter 6 Appendix

6.1 Mass spectrometry analysis of pVI-WT

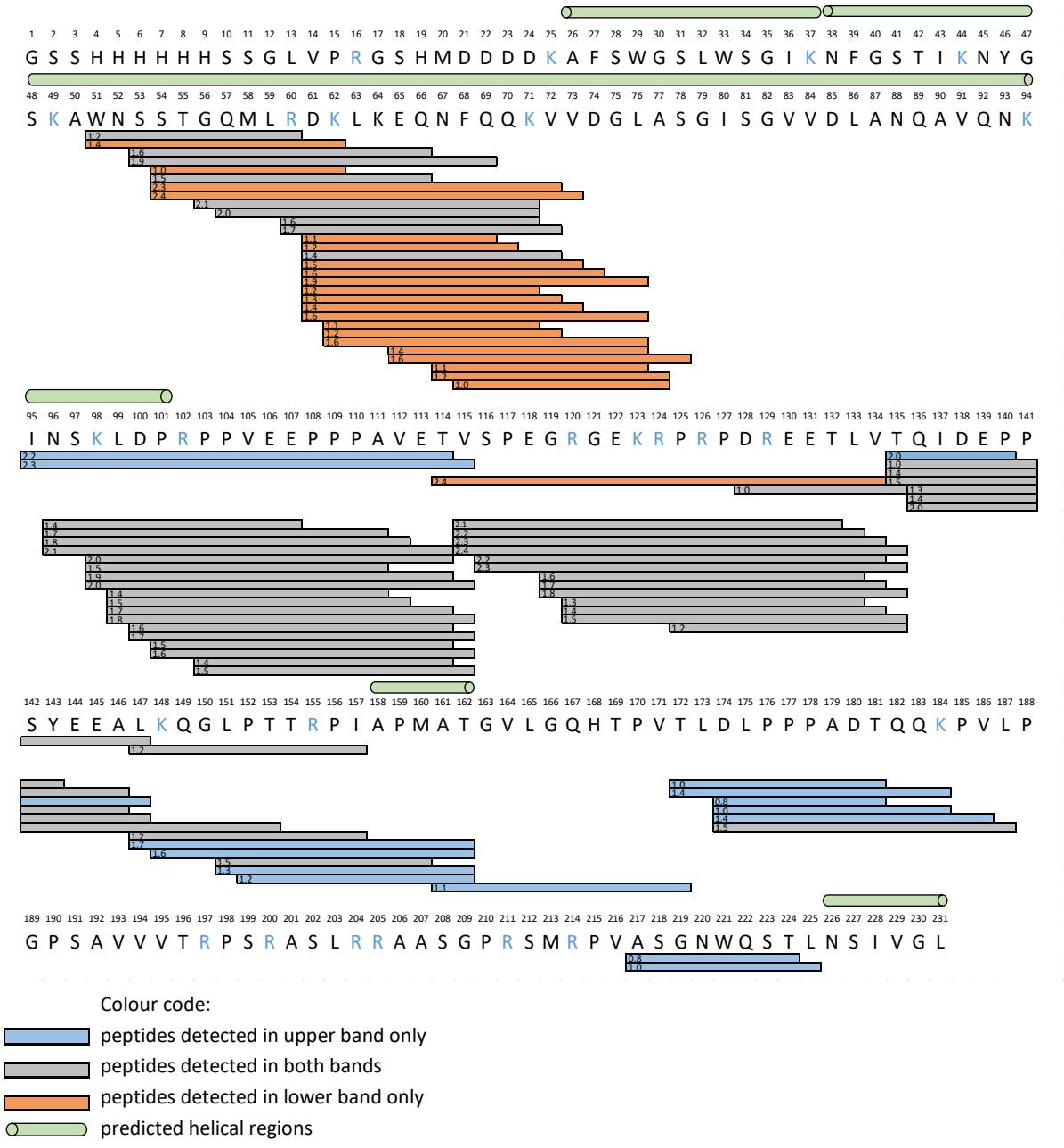
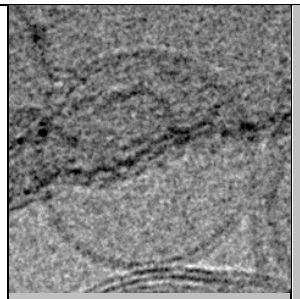
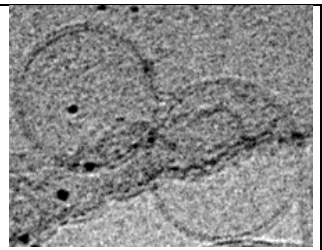
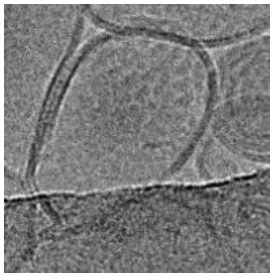
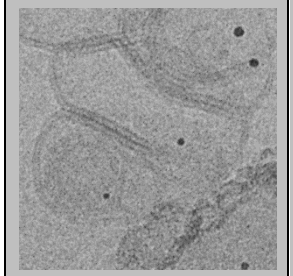
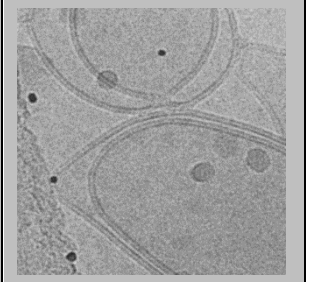
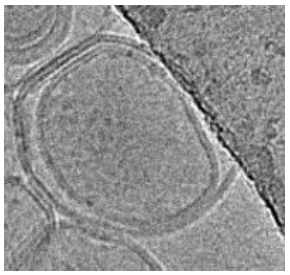
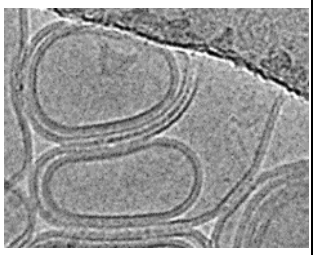
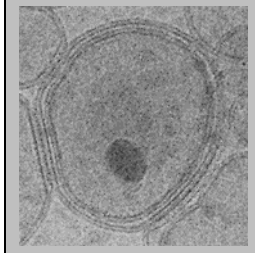
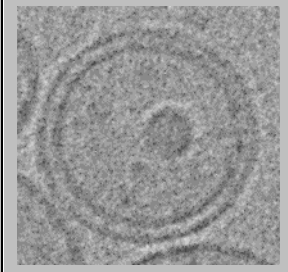
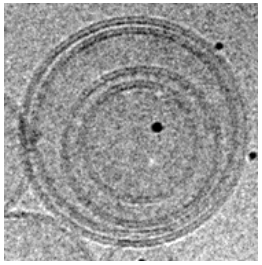
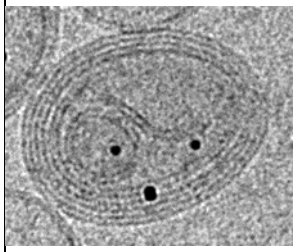
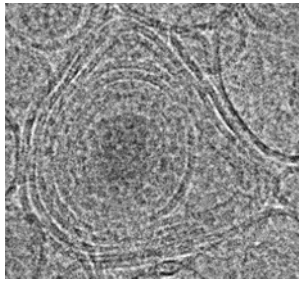


Figure 6.1 Full map of detected peptides from mass spectrometry analysis of pVI-WT
Detected peptides are depicted as colour coded bands. Molecular weight of peptides is shown in each band. Predicted enzyme digestion sites (Lys and Arg residues) are highlighted in blue.

6.2 Additional examples from cryoEM analysis of liposomes and pVI constructs

Table 6.1 Examples of liposome features excluded from counts.

PC/cholesterol (grey background) and PC/PE/cholesterol liposomes (white background).

Overlapping carbon at edge of hole					
Distorted by or interacting with carbon at edge of hole					
Multi-laminar liposomes. two or more membranes not separated					

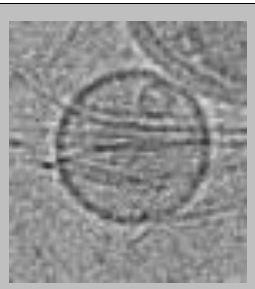
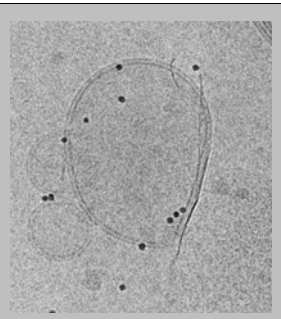
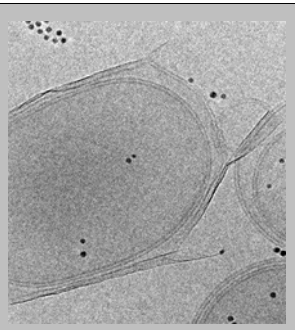
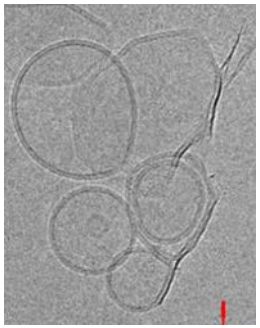
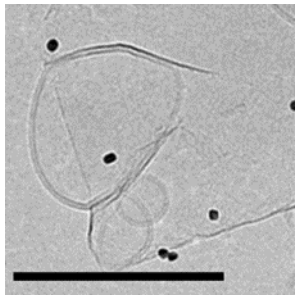
Close to folded graphene that distorts or damages liposomes					

Table 6.2 Further examples of liposome features observed in liposomes without protein.

PC/cholesterol (grey background) and PC/PE/cholesterol liposomes (white background).

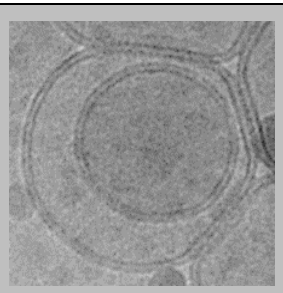
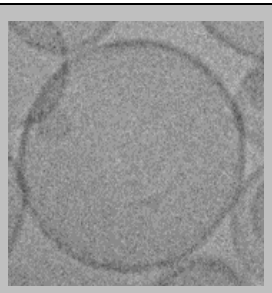
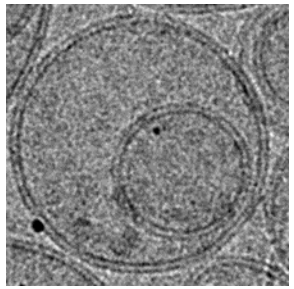
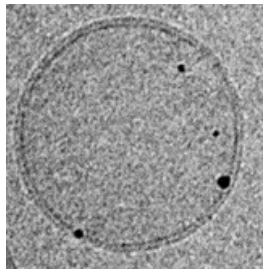
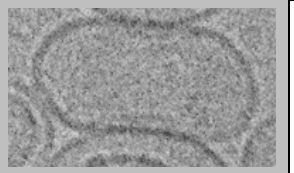
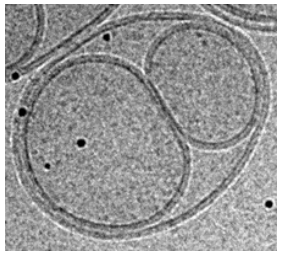
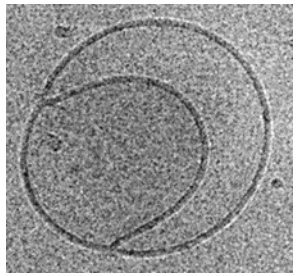
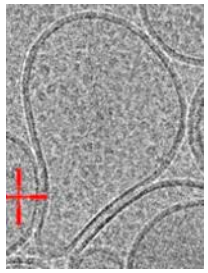
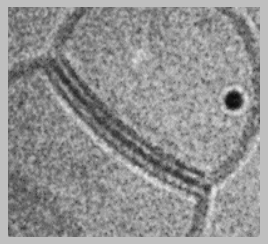
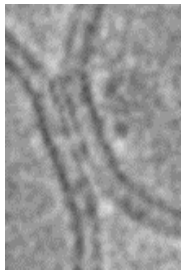
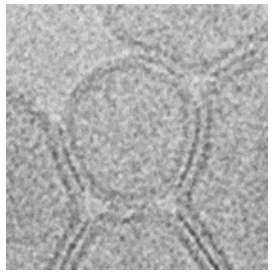
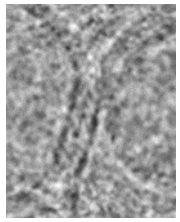
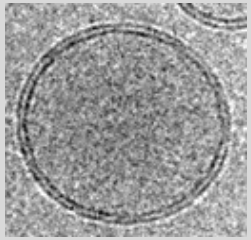
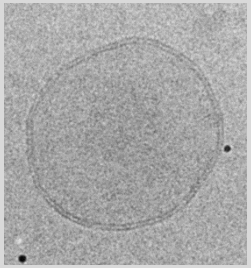
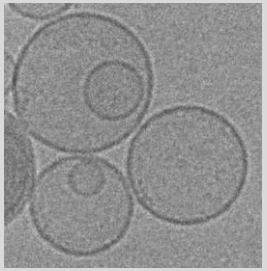
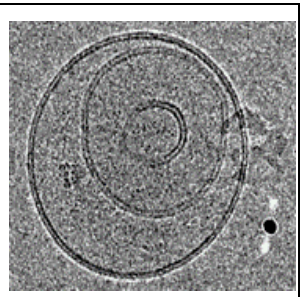
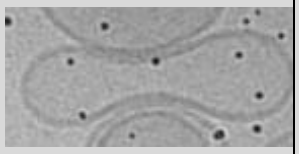
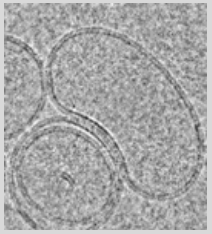
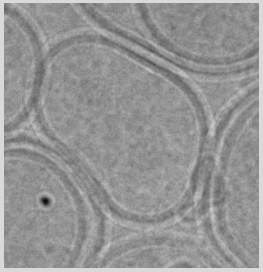
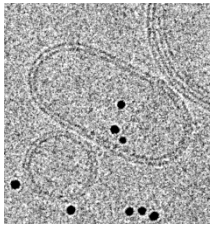
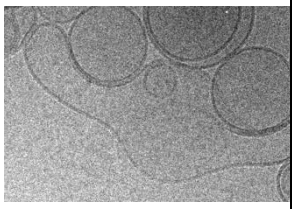
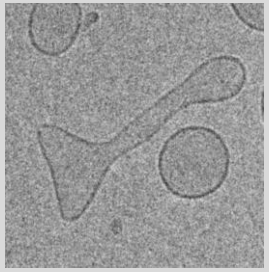
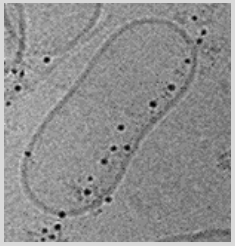
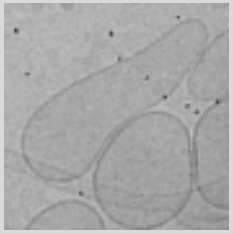
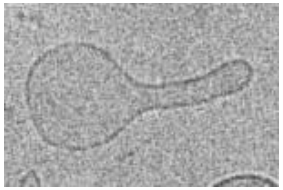
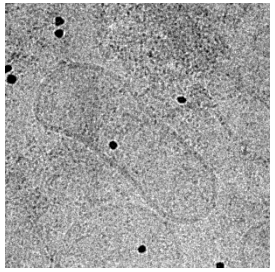
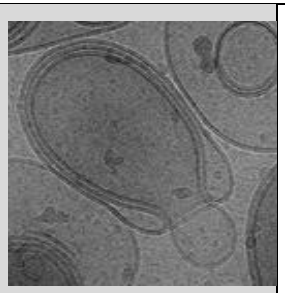
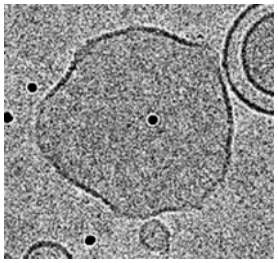
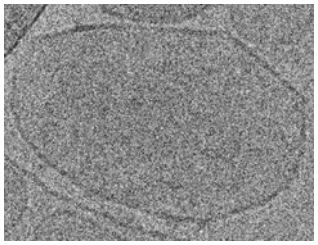
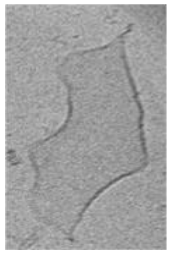
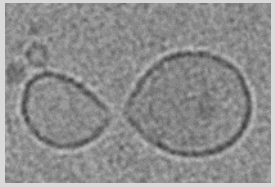
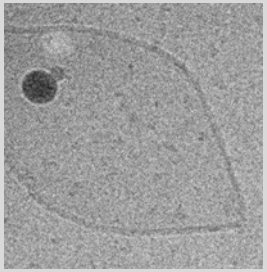
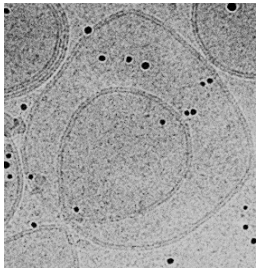
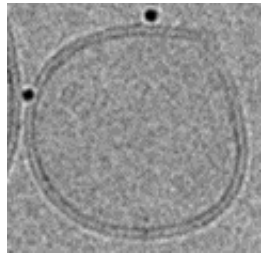
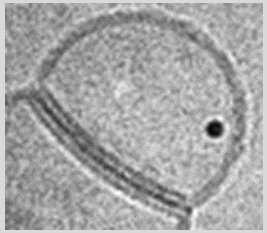
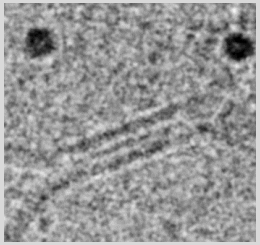
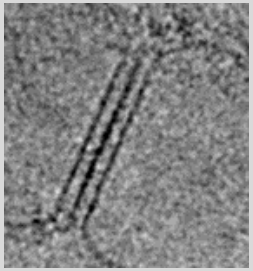
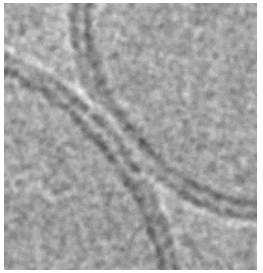
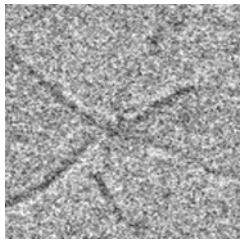
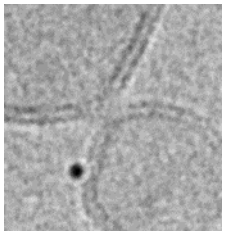
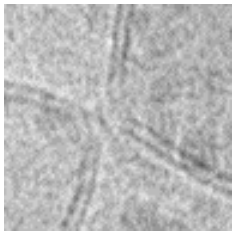
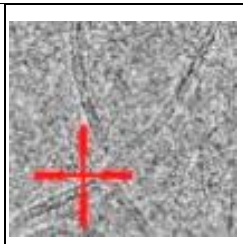
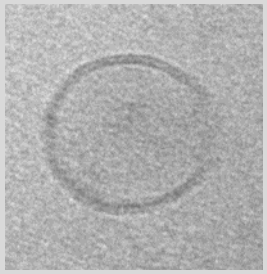
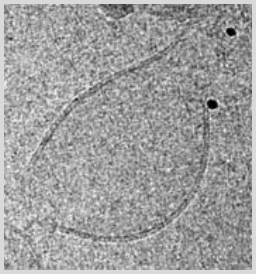
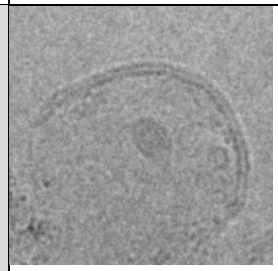
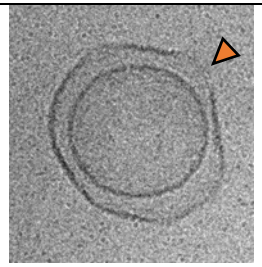
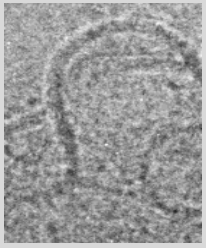
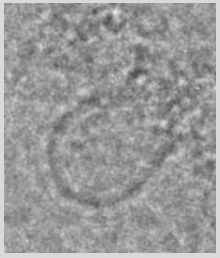
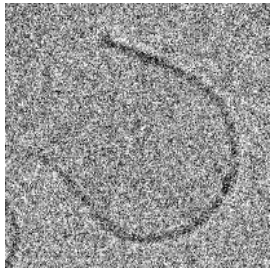
Intact circular					
Distorted – all counted as one					
Interfaces					

Table 6.3 Further examples of liposome features observed in liposomes incubated with pVI-WT.

PC/cholesterol (grey background) and PC/PE/cholesterol liposomes (white background).

Intact circular					
Distorted – squashed					
Distorted – elongated					

Distorted - other	 Invaginations			 Scalloped edges	 Scalloped edges
Pointed					
Interfaces	 Curved				

“hemifusion”					
Open liposomes					
Open liposomes – curled edges					

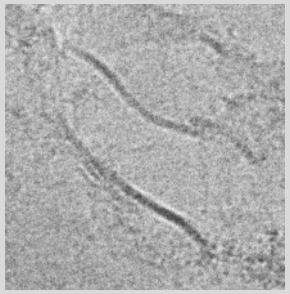
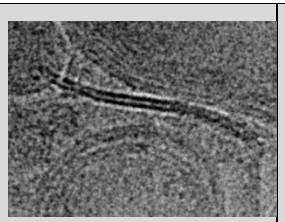
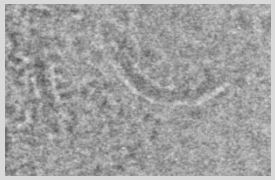
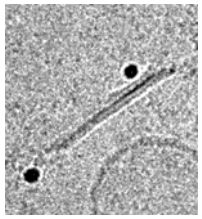
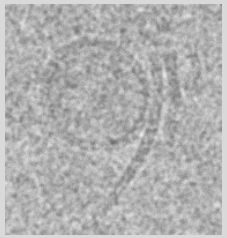
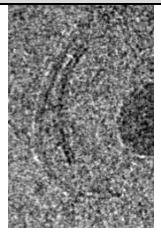
Membrane fragments – Single					
Membrane fragments – Multiple					

Table 6.4 Further examples of liposome features observed in liposomes incubated with pVI-L40Q.

PC/cholesterol (grey background) and PC/PE/cholesterol liposomes (white background).

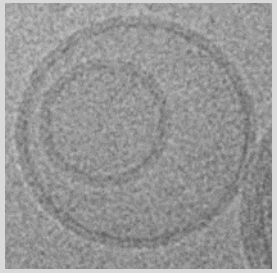
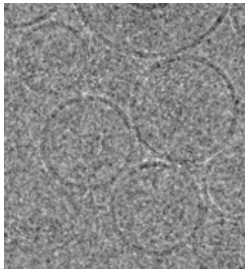
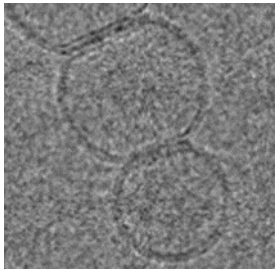
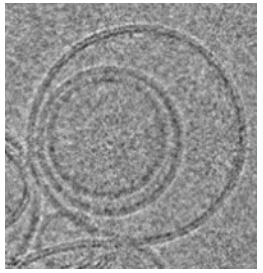
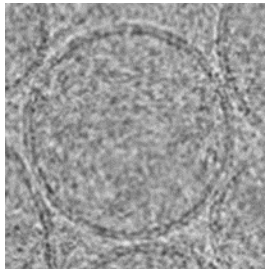
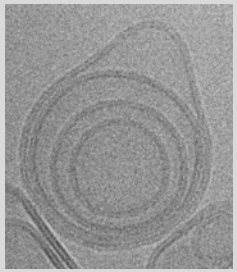
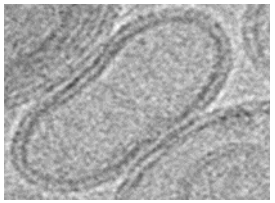
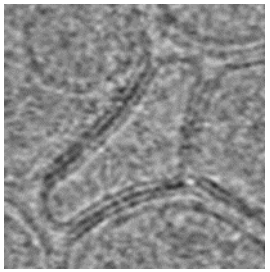
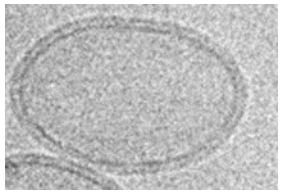
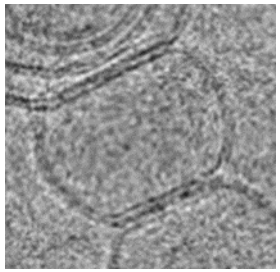
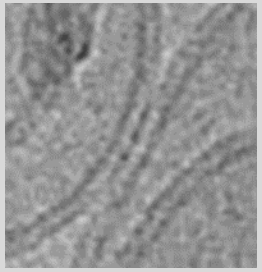
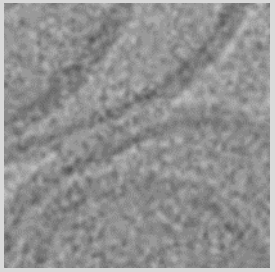
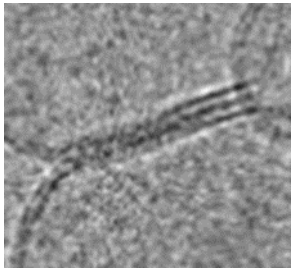
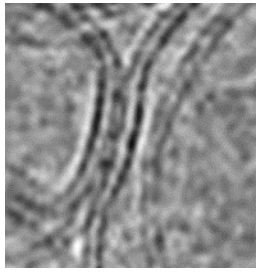
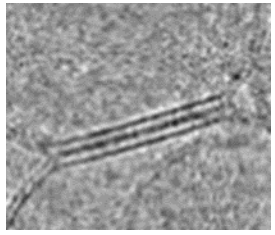
Intact circular					
Distorted					
Interfaces					

Table 6.5 Further examples of liposome features observed in liposomes incubated with pVI-Δ54.

All images are from PC/PE/cholesterol liposomes.

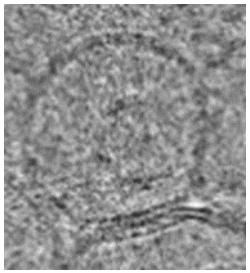
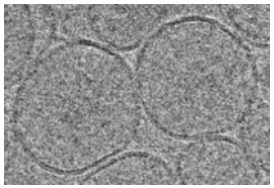
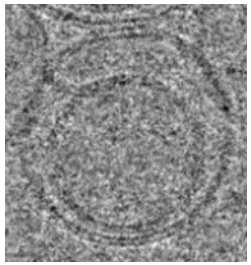
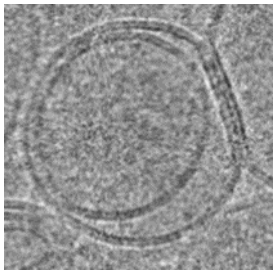
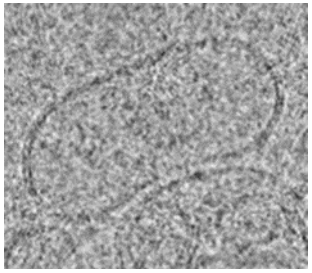
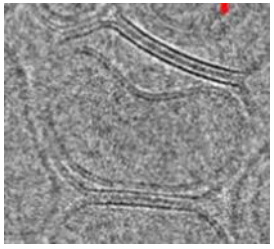
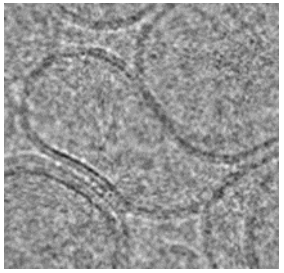
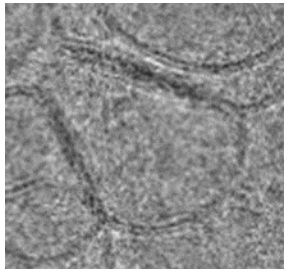
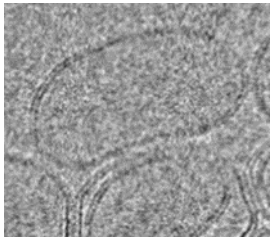
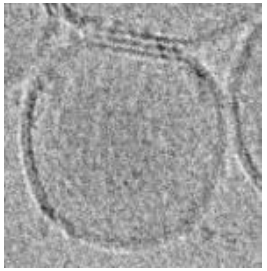
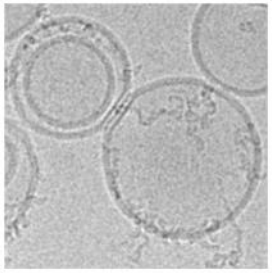
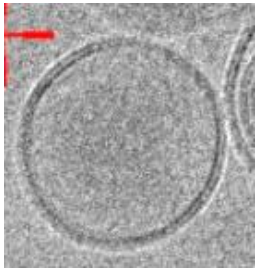
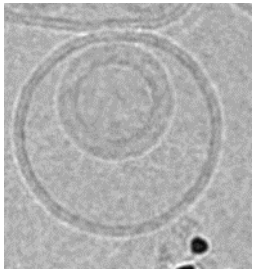
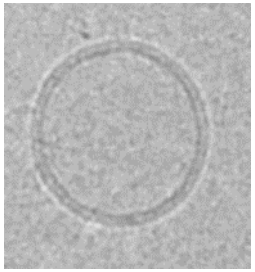
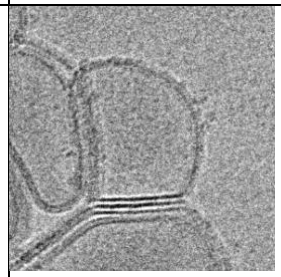
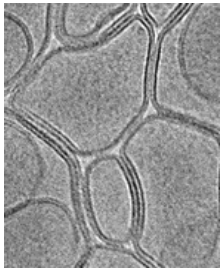
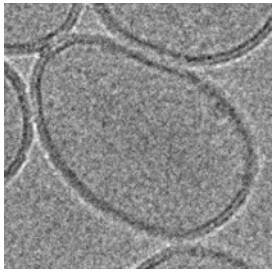
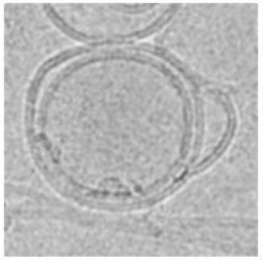
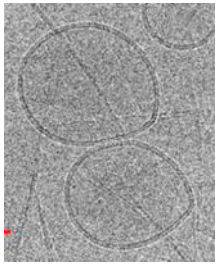
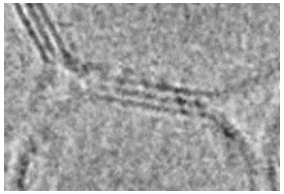
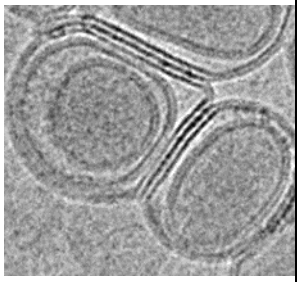
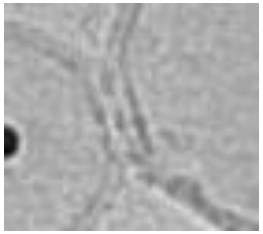
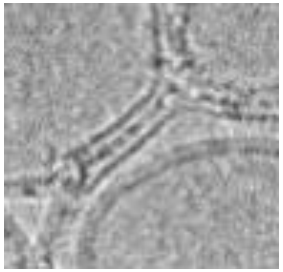
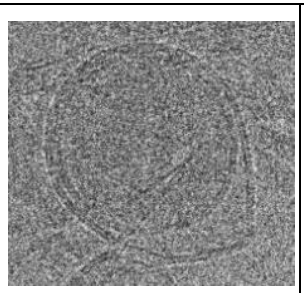
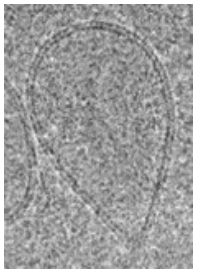
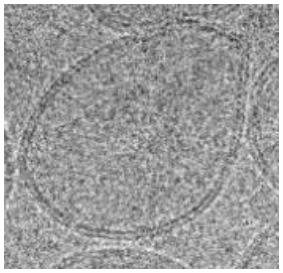
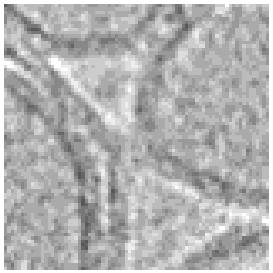
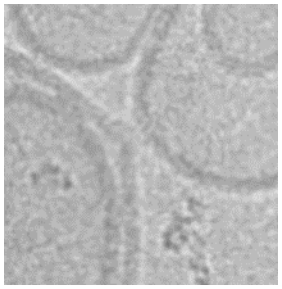
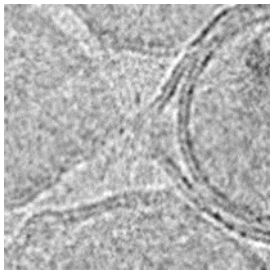
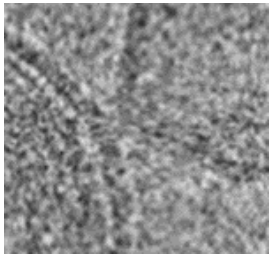
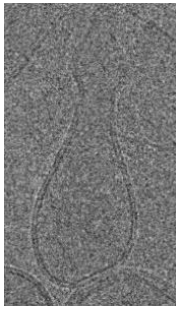
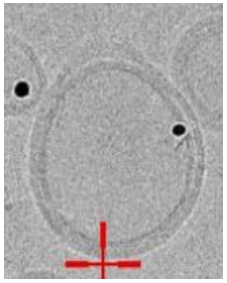
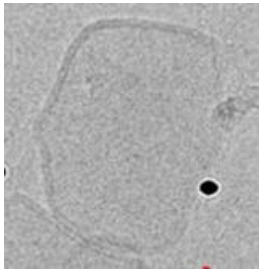
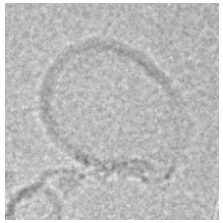
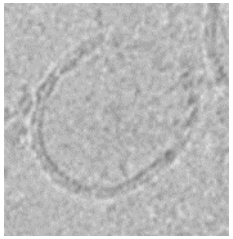
Intact circular					
Distorted					

Table 6.6 Further examples of liposome features observed in liposomes incubated with pVI-34-53.

All images are from PC/PE/cholesterol liposomes.

Intact circular					
Distorted					
Interfaces					

Pointed					
Hemifusion sites					
Open liposomes					

References

1. Cossart, P. and A. Helenius, *Endocytosis of viruses and bacteria.* Cold Spring Harbor perspectives in biology, 2014. **6**(8): p. a016972.
2. Sobhy, H., *A comparative review of viral entry and attachment during large and giant dsDNA virus infections.* Archives of virology, 2017. **162**(12): p. 3567-3585.
3. Marsh, M. and A. Helenius, *Virus Entry: Open Sesame.* Cell, 2006. **124**(4): p. 729-740.
4. Kalia, M. and S. Jameel, *Virus entry paradigms.* Amino Acids, 2011. **41**(5): p. 1147-1157.
5. Sattentau, Q., *Avoiding the void: cell-to-cell spread of human viruses.* Nature Reviews Microbiology, 2008. **6**(11): p. 815-826.
6. Suomalainen, M. and U.F. Greber, *Uncoating of non-enveloped viruses.* Current Opinion in Virology, 2013. **3**(1): p. 27-33.
7. Dimitrov, D.S., *Virus entry: molecular mechanisms and biomedical applications.* Nature Reviews Microbiology, 2004. **2**(2): p. 109-122.
8. von Zastrow, M. and A. Sorkin, *Signaling on the endocytic pathway.* Current opinion in cell biology, 2007. **19**(4): p. 436-445.
9. Conner, S.D. and S.L. Schmid, *Regulated portals of entry into the cell.* Nature, 2003. **422**(6927): p. 37-44.
10. Sorkin, A. and M. von Zastrow, *Endocytosis and signalling: intertwining molecular networks.* Nature reviews. Molecular cell biology, 2009. **10**(9): p. 609-622.
11. Mayor, S. and R.E. Pagano, *Pathways of clathrin-independent endocytosis.* Nature Reviews Molecular Cell Biology, 2007. **8**(8): p. 603-612.
12. Schmid, E.M. and H.T. McMahon, *Integrating molecular and network biology to decode endocytosis.* Nature, 2007. **448**(7156): p. 883-888.
13. Kaksonen, M. and A. Roux, *Mechanisms of clathrin-mediated endocytosis.* Nature Reviews Molecular Cell Biology, 2018. **19**(5): p. 313-326.
14. Stoeber, M., P. Schellenberger, C.A. Siebert, C. Leyrat, A. Helenius, and K. Grünewald, *Model for the architecture of caveolae based on a flexible, net-like assembly of Cavin1 and Caveolin discs.* Proceedings of the National Academy of Sciences, 2016. **113**(50): p. E8069-E8078.

15. Ridley, A.J., *Rho GTPases and actin dynamics in membrane protrusions and vesicle trafficking.* Trends Cell Biol, 2006. **16**(10): p. 522-9.

16. Thorley, J.A., J.A. McKeating, and J.Z. Rappoport, *Mechanisms of viral entry: sneaking in the front door.* Protoplasma, 2010. **244**(1-4): p. 15-24.

17. Snijder, B., R. Sacher, P. Rämö, E.-M. Damm, P. Liberali, and L. Pelkmans, *Population context determines cell-to-cell variability in endocytosis and virus infection.* Nature, 2009. **461**(7263): p. 520-523.

18. Huotari, J. and A. Helenius, *Endosome maturation.* The EMBO journal, 2011. **30**(17): p. 3481-500.

19. Moyer, C.L., C. M. Wiethoff, and G.R. Nemerow, *Functional genetic and biophysical analyses of membrane disruption by human adenovirus.* J Virol, 2011. **85**(6): p. 2631-2641.

20. Geiger, R., D. Andritschke, S. Friebe, F. Herzog, S. Luisoni, T. Heger, and A. Helenius, *BAP31 and BiP are essential for dislocation of SV40 from the endoplasmic reticulum to the cytosol.* Nature Cell Biology, 2011. **13**(11): p. 1305-1314.

21. Kumar, C.S., D. Dey, S. Ghosh, and M. Banerjee, *Breach: Host Membrane Penetration and Entry by Nonenveloped Viruses.* Trends in Microbiology, 2018. **26**(6): p. 525-537.

22. Tosteson, M.T. and M. Chow, *Characterization of the ion channels formed by poliovirus in planar lipid membranes.* J Virol, 1997. **71**(1): p. 507-511.

23. Agosto, M.A., T. Ivanovic, and M.L. Nibert, *Mammalian reovirus, a nonfusogenic nonenveloped virus, forms size-selective pores in a model membrane.* Proceedings of the National Academy of Sciences, 2006. **103**(44): p. 16496.

24. Luzio, J.P., Sally R. Gray, and Nicholas A. Bright, *Endosome–lysosome fusion: Figure 1.* Biochemical Society Transactions, 2010. **38**(6): p. 1413-1416.

25. Nieva, J.L., V. Madan, and L. Carrasco, *Viroporins: structure and biological functions.* Nat Rev Microbiol, 2012. **10**(8): p. 563-74.

26. Bolduan, S., J. Votteler, V. Lodermeyer, T. Greiner, H. Koppensteiner, M. Schindler, G. Thiel, and U. Schubert, *Ion channel activity of HIV-1 Vpu is dispensable for counteraction of CD317.* Virology, 2011. **416**(1-2): p. 75-85.

27. Verdiá-Báguena, C., J.L. Nieto-Torres, A. Alcaraz, M.L. DeDiego, J. Torres, V.M. Aguilella, and L. Enjuanes, *Coronavirus E protein forms ion channels with functionally and structurally-involved membrane lipids.* Virology, 2012. **432**(2): p. 485-94.

28. Denolly, S., C. Mialon, T. Bourlet, F. Amirache, F. Penin, B. Lindenbach, B. Boson, and F.-L. Cosset, *The amino-terminus of the hepatitis C virus (HCV) p7 viroporin and*

its cleavage from glycoprotein E2-p7 precursor determine specific infectivity and secretion levels of HCV particle types. PLOS Pathogens, 2017. **13**(12): p. e1006774.

29. Luik, P., C. Chew, J. Aittoniemi, J. Chang, P. Wentworth, R.A. Dwek, P.C. Biggin, C. Vénien-Bryan, and N. Zitzmann, *The 3-dimensional structure of a hepatitis C virus p7 ion channel by electron microscopy.* Proceedings of the National Academy of Sciences, 2009. **106**(31): p. 12712-12716.

30. Davis, M.P., G. Bottley, L.P. Beales, R.A. Killington, D.J. Rowlands, and T.J. Tuthill, *Recombinant VP4 of Human Rhinovirus Induces Permeability in Model Membranes.* Journal of Virology, 2008. **82**(8): p. 4169-4174.

31. Bong, D.T., C. Steinern, A. Janshoff, J.E. Johnson, and M. Reza Ghadiri, *A highly membrane-active peptide in Flock House virus: implications for the mechanism of nodavirus infection.* Chemistry & Biology, 1999. **6**(7): p. 473-481.

32. Wiethoff, C.M. and G.R. Nemerow, *Adenovirus membrane penetration: Tickling the tail of a sleeping dragon.* Virology, 2015. **479**: p. 591-599.

33. Liu, E.B., D.A. Wadford, J. Seto, M. Vu, N.R. Hudson, L. Thrasher, S. Torres, D.W. Dyer, J. Chodosh, D. Seto, and M.S. Jones, *Computational and serologic analysis of novel and known viruses in species human adenovirus D in which serology and genomics do not correlate.* PLoS One, 2012. **7**(3): p. e33212-e33212.

34. *Human Adenovirus Working Group: National Center for Biotechnology/GenBank*. 2019 [cited 2020 20th October]; Available from: http://hadvwg.gmu.edu/.

35. Lion, T., *Adenovirus Infections in Immunocompetent and Immunocompromised Patients.* 2014.

36. Abbas, K.Z., E. Lombos, V.R. Duvvuri, R. Olsha, R.R. Higgins, and J.B. Gubbay, *Temporal changes in respiratory adenovirus serotypes circulating in the greater Toronto area, Ontario, during December 2008 to April 2010.* Virology Journal, 2013. **10**(1): p. 15-15.

37. Greber, U.F. and J.W. Flatt, *Adenovirus Entry: From Infection to Immunity.* Annual Review of Virology, 2019. **6**(1): p. 177-197.

38. Rowe, W.P., R.J. Huebner, L.K. Gilmore, R.H. Parrott, and T.G. Ward, *Isolation of a Cytopathogenic Agent from Human Adenoids Undergoing Spontaneous Degeneration in Tissue Culture.* Proceedings of the Society for Experimental Biology and Medicine, 1953. **84**(3): p. 570-573.

39. Hllleman, M.R. and J.H. Werner, *Recovery of New Agent from Patients with Acute Respiratory Illness.* Proceedings of the Society for Experimental Biology and Medicine, 1954. **85**(1): p. 183-188.

40. Huebner, R.J., W.P. Rowe, and W.T. Lane, *Oncogenic effects in hamsters of human adenovirus types 12 and 18.* Proceedings of the National Academy of Sciences of the United States of America, 1962. **48**(12): p. 2051-2058.

41. Huebner, R.J., W.P. Rowe, W.E. Schatten, R.R. Smith, and L.B. Thomas, *Studies on the use of viruses in the treatment of carcinoma of the cervix.* Cancer, 1956. **9**(6): p. 1211-8.

42. Mennechet, F.J.D., O. Paris, A.R. Ouoba, S. Salazar Arenas, S.B. Sirima, G.R. Takoudjou Dzomo, A. Diarra, I.T. Traore, D. Kania, K. Eichholz, E.A. Weaver, E. Tuaillon, and E.J. Kremer, *A review of 65 years of human adenovirus seroprevalence.* Expert Review of Vaccines, 2019. **18**(6): p. 597-613.

43. Rhee, E.G. and D.H. Barouch, *145 - Adenoviruses*, in *Mandell, Douglas, and Bennett's Principles and Practice of Infectious Diseases (Eighth Edition)*, J.E. Bennett, R. Dolin, and M.J. Blaser, Editors. 2015, Content Repository Only!: Philadelphia. p. 1787-1793.e2.

44. Trentin, J.J., Y. Yabe, and G. Taylor, *The Quest for Human Cancer Viruses.* A new approach to an old problem reveals cancer induction in hamsters by human adenovirus, 1962. **137**(3533): p. 835-841.

45. Berk, A.J. and P.A. Sharp, *Structure of the adenovirus 2 early mRNAs.* Cell, 1978. **14**(3): p. 695-711.

46. Sarantis, H., G. Johnson, M. Brown, M. Petric, and R. Tellier, *Comprehensive detection and serotyping of human adenoviruses by PCR and sequencing.* J Clin Microbiol, 2004. **42**(9): p. 3963-3969.

47. Uusi-Kerttula, H., S. Hulin-Curtis, J. Davies, and A.L. Parker, *Oncolytic Adenovirus: Strategies and Insights for Vector Design and Immuno-Oncolytic Applications.* Viruses, 2015. **7**(11): p. 6009-6042.

48. Khanal, S., P. Ghimire, and A.S. Dhamoon, *The Repertoire of Adenovirus in Human Disease: The Innocuous to the Deadly.* Biomedicines, 2018. **6**(1): p. 30.

49. Hierholzer, J.C., *Adenoviruses in the immunocompromised host.* Clinical microbiology reviews, 1992. **5**(3): p. 262-274.

50. Wilson, P. and A. Zumla, *Transmission and prevention of acute viral respiratory tract infections in hospitals.* Current Opinion in Pulmonary Medicine, 2019. **25**(3).

51. Kaneko, H., K. Aoki, S. Ishida, S. Ohno, N. Kitaichi, H. Ishiko, T. Fujimoto, Y. Ikeda, M. Nakamura, G. Gonzalez, K.O. Koyanagi, H. Watanabe, and T. Suzutani, *Recombination analysis of intermediate human adenovirus type 53 in Japan by complete genome sequence.* Journal of General Virology, 2011. **92**(6): p. 1251-1259.

52. Meyer-Rüsenberg, B., U. Loderstädt, G. Richard, P.-M. Kaulfers, and C. Gesser, *Epidemic keratoconjunctivitis: the current situation and recommendations for prevention and treatment.* Deutsches Arzteblatt international, 2011. **108**(27): p. 475-480.

53. Lai, C.Y., C.J. Lee, C.Y. Lu, P.I. Lee, P.L. Shao, E.T. Wu, C.C. Wang, B.F. Tan, H.Y. Chang, S.H. Hsia, J.J. Lin, L.Y. Chang, Y.C. Huang, and L.M. Huang, *Adenovirus serotype 3 and 7 infection with acute respiratory failure in children in Taiwan, 2010-2011.* PLoS One, 2013. **8**(1): p. e53614.

54. Aoki, K., H. Ishiko, T. Konno, Y. Shimada, A. Hayashi, H. Kaneko, T. Ohguchi, Y. Tagawa, S. Ohno, and S. Yamazaki, *Epidemic Keratoconjunctivitis Due to the Novel Hexon-Chimeric-Intermediate 22,37/H8 Human Adenovirus.* Journal of Clinical Microbiology, 2008. **46**(10): p. 3259-3269.

55. Jones, M.S., 2nd, B. Harrach, R.D. Ganac, M.M.A. Gozum, W.P. Dela Cruz, B. Riedel, C. Pan, E.L. Delwart, and D.P. Schnurr, *New adenovirus species found in a patient presenting with gastroenteritis.* Journal of virology, 2007. **81**(11): p. 5978-5984.

56. Ghebremedhin, B., *Human adenovirus: Viral pathogen with increasing importance.* European journal of microbiology & immunology, 2014. **4**(1): p. 26-33.

57. Curiel, D., *Adenoviral vectors for gene therapy*.

58. Jelinek, T., D.S. Pereira, and F.L. Graham, *Tumorigenicity of adenovirus-transformed rodent cells is influenced by at least two regions of adenovirus type 12 early region 1A.* J Virol, 1994. **68**(2): p. 888-896.

59. Lee, C.S., E.S. Bishop, R. Zhang, X. Yu, E.M. Farina, S. Yan, C. Zhao, Z. Zeng, Y. Shu, X. Wu, J. Lei, Y. Li, W. Zhang, C. Yang, K. Wu, Y. Wu, S. Ho, A. Athiviraham, M.J. Lee, J.M. Wolf, R.R. Reid, and T.-C. He, *Adenovirus-mediated gene delivery: Potential applications for gene and cell-based therapies in the new era of personalized medicine.* Genes & Diseases, 2017. **4**(2): p. 43-63.

60. Fields, B.N., D.M. Knipe, and P.M. Howley, *Adenoviridae*. 2013, Wolters Kluwer Health/Lippincott Williams & Wilkins Philadelphia p. 1724-1751.

61. Wold, W.S.M. and K. Toth, *Adenovirus vectors for gene therapy, vaccination and cancer gene therapy.* Current gene therapy, 2013. **13**(6): p. 421-433.

62. Zabner, J., L.A. Couture, R.J. Gregory, S.M. Graham, A.E. Smith, and M.J. Welsh, *Adenovirus-mediated gene transfer transiently corrects the chloride transport defect in nasal epithelia of patients with cystic fibrosis.* Cell, 1993. **75**(2): p. 207-216.

63. Wilson, J.M., *Adenoviruses as gene-delivery vehicles.* N Engl J Med, 1996. **334**(18): p. 1185-1187.

64. Hemminki, O., J.M. Dos Santos, and A. Hemminki, *Oncolytic viruses for cancer immunotherapy.* Journal of hematology & oncology, 2020. **13**(1): p. 84-84.

65. Ries, S. and W.M. Korn, *ONYX-015: mechanisms of action and clinical potential of a replication-selective adenovirus.* British journal of cancer, 2002. **86**(1): p. 5-11.

66. Tatsis, N. and H.C.J. Ertl, *Adenoviruses as vaccine vectors.* Molecular Therapy, 2004. **10**(4): p. 616-629.

67. Vemula, S.V. and S.K. Mittal, *Production of adenovirus vectors and their use as a delivery system for influenza vaccines.* Expert opinion on biological therapy, 2010. **10**(10): p. 1469-1487.

68. Fougeroux, C. and P.J. Holst, *Future Prospects for the Development of Cost-Effective Adenovirus Vaccines.* International journal of molecular sciences, 2017. **18**(4): p. 686.

69. Zhu, F.-C., Y.-H. Li, X.-H. Guan, L.-H. Hou, W.-J. Wang, J.-X. Li, S.-P. Wu, B.-S. Wang, Z. Wang, L. Wang, S.-Y. Jia, H.-D. Jiang, L. Wang, T. Jiang, Y. Hu, J.-B. Gou, S.-B. Xu, J.-J. Xu, X.-W. Wang, W. Wang, and W. Chen, *Safety, tolerability, and immunogenicity of a recombinant adenovirus type-5 vectored COVID-19 vaccine: a dose-escalation, open-label, non-randomised, first-in-human trial.* The Lancet, 2020. **395**(10240): p. 1845-1854.

70. Amanat, F. and F. Krammer, *SARS-CoV-2 Vaccines: Status Report.* Immunity, 2020. **52**(4): p. 583-589.

71. van Doremalen, N., T. Lambe, A. Spencer, S. Belij-Rammerstorfer, J.N. Purushotham, J.R. Port, V. Avanzato, T. Bushmaker, A. Flaxman, M. Ulaszewska, F. Feldmann, E.R. Allen, H. Sharpe, J. Schulz, M. Holbrook, A. Okumura, K. Meade-White, L. Pérez-Pérez, C. Bissett, C. Gilbride, B.N. Williamson, R. Rosenke, D. Long, A. Ishwarbhai, R. Kailath, L. Rose, S. Morris, C. Powers, J. Lovaglio, P.W. Hanley, D. Scott, G. Saturday, E. de Wit, S.C. Gilbert, and V.J. Munster, *ChAdOx1 nCoV-19 vaccination prevents SARS-CoV-2 pneumonia in rhesus macaques.* bioRxiv, 2020.

72. Hassan, A.O., N.M. Kafai, I.P. Dmitriev, J.M. Fox, B.K. Smith, I.B. Harvey, R.E. Chen, E.S. Winkler, A.W. Wessel, J.B. Case, E. Kashentseva, B.T. McCune, A.L. Bailey, H. Zhao, L.A. VanBlargan, Y.N. Dai, M. Ma, L.J. Adams, S. Shrihari, J.E. Danis, L.E. Gralinski, Y.J. Hou, A. Schäfer, A.S. Kim, S.P. Keeler, D. Weiskopf, R.S. Baric, M.J. Holtzman, D.H. Fremont, D.T. Curiel, and M.S. Diamond, *A Single-Dose Intranasal ChAd Vaccine Protects Upper and Lower Respiratory Tracts against SARS-CoV-2.* Cell, 2020.

73. Mercado, N.B., R. Zahn, F. Wegmann, C. Loos, A. Chandrashekar, J. Yu, J. Liu, L. Peter, K. McMahan, L.H. Tostanoski, X. He, D.R. Martinez, L. Rutten, R. Bos, D. van Manen, J. Vellinga, J. Custers, J.P. Langedijk, T. Kwaks, M.J.G. Bakkers, D. Zuijdgeest, S.K. Rosendahl Huber, C. Atyeo, S. Fischinger, J.S. Burke, J. Feldman,

B.M. Hauser, T.M. Caradonna, E.A. Bondzie, G. Dagotto, M.S. Gebre, E. Hoffman, C. Jacob-Dolan, M. Kirilova, Z. Li, Z. Lin, S.H. Mahrokhian, L.F. Maxfield, F. Nampanya, R. Nityanandam, J.P. Nkolola, S. Patel, J.D. Ventura, K. Verrington, H. Wan, L. Pessaint, A. Van Ry, K. Blade, A. Strasbaugh, M. Cabus, R. Brown, A. Cook, S. Zouantchangadou, E. Teow, H. Andersen, M.G. Lewis, Y. Cai, B. Chen, A.G. Schmidt, R.K. Reeves, R.S. Baric, D.A. Lauffenburger, G. Alter, P. Stoffels, M. Mammen, J. Van Hoof, H. Schuitemaker, and D.H. Barouch, *Single-shot Ad26 vaccine protects against SARS-CoV-2 in rhesus macaques.* Nature, 2020. **586**(7830): p. 583-588.

74. Horne, R.W., S. Brenner, A.P. Waterson, and P. Wildy, *The icosahedral form of an adenovirus.* Journal of Molecular Biology, 1959. **1**(1): p. 84-86.

75. Zubieta, C., G. Schoehn, J. Chroboczek, and S. Cusack, *The structure of the human adenovirus 2 penton.* Mol Cell, 2005. **17**(1): p. 121-135.

76. Dai, X., L. Wu, R. Sun, and Z.H. Zhou, *Atomic Structures of Minor Proteins VI and VII in Human Adenovirus.* Journal of virology, 2017. **91**(24): p. e00850-17.

77. Yu, X., D. Veesler, M.G. Campbell, M.E. Barry, F.J. Asturias, M.A. Barry, and V.S. Reddy, *Cryo-EM structure of human adenovirus D26 reveals the conservation of structural organization among human adenoviruses.* Science Advances, 2017. **3**(5): p. e1602670.

78. Reddy, V.S. and G.R. Nemerow, *Structures and organization of adenovirus cement proteins provide insights into the role of capsid maturation in virus entry and infection.* Proceedings of the National Academy of Sciences of the United States of America, 2014. **111**(32): p. 11715-11720.

79. Kundhavai Natchiar, S., S. Venkataraman, T.-M. Mullen, G.R. Nemerow, and V.S. Reddy, *Revised Crystal Structure of Human Adenovirus Reveals the Limits on Protein IX Quasi-Equivalence and on Analyzing Large Macromolecular Complexes.* Journal of Molecular Biology, 2018.

80. Prage, L., U. Pettersson, S. Hoglund, K. Lonberg-Holm, and L. Philipson, *Structural proteins of adenoviruses. IV. Sequential degradation of the adenovirus type 2 virion.* Virology, 1970. **42**(2): p. 341-358.

81. Smith, K.O., W.D. Gehle, and M.D. Trousdale, *Architecture of the Adenovirus Capsid.* Journal of Bacteriology, 1965. **90**(1): p. 254-261.

82. Flatt, J.W. and S.J. Butcher, *Adenovirus flow in host cell networks.* Open biology, 2019. **9**(2): p. 190012-190012.

83. Liu, H.R., L. Jin, S.B.S. Koh, I. Atanasov, S. Schein, L. Wu, and Z.H. Zhou, *Atomic Structure of Human Adenovirus by Cryo-EM Reveals Interactions Among Protein Networks.* Science, 2010. **329**(5995): p. 1038-1043.

84. Colby, W.W. and T. Shenk, *Adenovirus type 5 virions can be assembled in vivo in the absence of detectable polypeptide IX.* Journal of virology, 1981. **39**(3): p. 977-980.

85. Flint, S.J., *Viral Moulds and Cement: How interactions among human adenovirus hexons and their protein IX cement may buttress human adenovirus particles*. 2017.

86. San Martín, C., *Latest Insights on Adenovirus Structure and Assembly.* Viruses, 2012. **4**(5): p. 847-877.

87. Vellinga, J., S. Van der Heijdt, and R.C. Hoeben, *The adenovirus capsid: major progress in minor proteins.* J Gen Virol, 2005. **86**(Pt 6): p. 1581-1588.

88. Alba, R., A. Bosch, and M. Chillon, *Gutless adenovirus: last-generation adenovirus for gene therapy.* Gene Ther, 2005. **12 Suppl 1**: p. S18-27.

89. Goncalves, M.A. and A.A. de Vries, *Adenovirus: from foe to friend.* Rev Med Virol, 2006. **16**(3): p. 167-186.

90. Saban, S.D., M. Silvestry, G.R. Nemerow, and P.L. Stewart, *Visualization of alpha-helices in a 6-angstrom resolution cryoelectron microscopy structure of adenovirus allows refinement of capsid protein assignments.* J Virol, 2006. **80**(24): p. 12049-12059.

91. San Martin, C., R.M. Burnett, F. de Haas, R. Heinkel, T. Rutten, S.D. Fuller, S.J. Butcher, and D.H. Bamford, *Combined EM/X-ray imaging yields a quasi-atomic model of the adenovirus-related bacteriophage PRD1 and shows key capsid and membrane interactions.* Structure, 2001. **9**(10): p. 917-930.

92. Harrison, S.C., *Looking Inside Adenovirus.* Science, 2010. **329**(5995): p. 1026-1027.

93. Everitt, E., B. Sundquist, U. Pettersson, and L. Philipson, *Structural proteins of adenoviruses: X. Isolation and topography of low molecular weight antigens from the virion of adenovirus type 2.* Virology, 1973. **52**(1): p. 130-147.

94. Everitt, E., L. Lutter, and L. Philipson, *Structural proteins of adenoviruses: XII. Location and neighbor relationship among proteins of adenovirion type 2 as revealed by enzymatic lodination, immunoprecipitation and chemical cross-linking.* Virology, 1975. **67**(1): p. 197-208.

95. Stewart, P.L., S.D. Fuller, and R.M. Burnett, *Difference Imaging Of Adenovirus - Bridging The Resolution Gap Between X-Ray Crystallography And Electron-Microscopy.* Embo Journal, 1993. **12**(7): p. 2589-2599.

96. Fabry, C.M.S., M. Rosa-Calatrava, J.F. Conway, C. Zubieta, S. Cusack, R.W.H. Ruigrok, and G. Schoehn, *A quasi-atomic model of human adenovirus type 5 capsid.* Embo Journal, 2005. **24**(9): p. 1645-1654.

97. Nemerow, G. and J. Flint, *Lessons learned from adenovirus (1970–2019).* FEBS Letters, 2019. **593**(24): p. 3395-3418.

98. Davison, A.J., M. Benkő, and B. Harrach, *Genetic content and evolution of adenoviruses.* Journal of General Virology, 2003. **84**(11): p. 2895-2908.

99. Mangel, F.W. and C. San Martín, *Structure, Function and Dynamics in Adenovirus Maturation.* Viruses, 2014. **6**(11).

100. Nemerow, G. and J. Flint, *Lessons Learned from Adenovirus (1970-2019).* FEBS Letters, 2019. **n/a**(n/a).

101. Mangel, W.F., W.J. McGrath, K. Xiong, V. Graziano, and P.C. Blainey, *Molecular sled is an eleven-amino acid vehicle facilitating biochemical interactions via sliding components along DNA.* Nature communications, 2016. **7**: p. 10202-10202.

102. Graziano, V., W.J. McGrath, M. Suomalainen, U.F. Greber, P. Freimuth, P.C. Blainey, G. Luo, X.S. Xie, and W.F. Mangel, *Regulation of a viral proteinase by a peptide and DNA in one-dimensional space: I. binding to DNA AND to hexon of the precursor to protein VI, pVI, of human adenovirus.* J Biol Chem, 2013. **288**(3): p. 2059-2067.

103. Mangel, W.F., W.J. McGrath, K. Xiong, V. Graziano, and P.C. Blainey, *Molecular sled is an eleven-amino acid vehicle facilitating biochemical interactions via sliding components along DNA.* Nature Communications, 2016. **7**(1): p. 10202.

104. Xiong, K. and P.C. Blainey, *Molecular sled sequences are common in mammalian proteins.* Nucleic Acids Res, 2016. **44**(5): p. 2266-73.

105. Wodrich, H., A. Cassany, M.A. D'Angelo, T. Guan, G. Nemerow, and L. Gerace, *Adenovirus core protein pVII is translocated into the nucleus by multiple import receptor pathways.* J Virol, 2006. **80**(19): p. 9608-9618.

106. Imelli, Nicola, Ruzsics, Zsolt, Puntener, Daniel, Gastaldelli, Michele, Greber, and U. F, *Genetic reconstitution of the human Adenovirus type 2 temperature-sensitive 1 mutant defective in endosomal escape.* Virology Journal, 2009. **6**(1): p. 1-1.

107. Rancourt, C., H. Keyvani-Amineh, S. Sircar, P. Labrecque, and J.M. Weber, *Proline 137 Is Critical for Adenovirus Protease Encapsidation and Activation but Not Enzyme Activity.* Virology, 1995. **209**(1): p. 167-173.

108. Wiethoff, C.M., H. Wodrich, L. Gerace, and G.R. Nemerow, *Adenovirus Protein VI Mediates Membrane Disruption following Capsid Disassembly.* J Virol, 2005. **79**(4): p. 1992-2000.

109. Silvestry, M., S. Lindert, J.G. Smith, O. Maier, C.M. Wiethoff, G.R. Nemerow, and P.L. Stewart, *Cryo-electron microscopy structure of adenovirus type 2 temperature-sensitive mutant 1 reveals insight into the cell entry defect.* Journal of virology, 2009. **83**(15): p. 7375-7383.

110. Silvestry Ramos, M., *Insight into adenovirus programmed disassembly from cryoEM : the structures of Ad2ts1 and the Ad35f+defensin HD5 complex*. 2009, Vanderbilt University Libraries. p. 170.

111. Cohen, C.J., J.T.C. Shieh, R.J. Pickles, T. Okegawa, J.T. Hsieh, and J.M. Bergelson, *The coxsackievirus and adenovirus receptor is a transmembrane component of the tight junction.* Proceedings of the National Academy of Sciences, 2001. **98**(26): p. 15191-15196.

112. Bergelson, J.M., J.A. Cunningham, G. Droguett, E.A. Kurt-Jones, A. Krithivas, J.S. Hong, M.S. Horwitz, R.L. Crowell, and R.W. Finberg, *Isolation of a common receptor for Coxsackie B viruses and adenoviruses 2 and 5.* Science, 1997. **275**(5304): p. 1320-1323.

113. Gaggar, A., D.M. Shayakhmetov, and A. Lieber, *CD46 is a cellular receptor for group B adenoviruses.* Nature Medicine, 2003. **9**(11): p. 1408-1412.

114. *Nature Reviews Molecular Cell Biology: Endocytosis*. 2011 [cited 2015; Available from: http://www.nature.com/nrm/focus/endocytosis/index.html.

115. Meier, O., K. Boucke, S.V. Hammer, S. Keller, R.P. Stidwill, S. Hemmi, and U.F. Greber, *Adenovirus triggers macropinocytosis and endosomal leakage together with its clathrin-mediated uptake.* The Journal of cell biology, 2002. **158**(6): p. 1119-31.

116. Wickham, T.J., P. Mathias, D.A. Cheresh, and G.R. Nemerow, *Integrins alpha v beta 3 and alpha v beta 5 promote adenovirus internalization but not virus attachment.* Cell, 1993. **73**(2): p. 309-19.

117. Burckhardt, ChristophÂ J., M. Suomalainen, P. Schoenenberger, K. Boucke, S. Hemmi, and UrsÂ F. Greber, *Drifting Motions of the Adenovirus Receptor CAR and Immobile Integrins Initiate Virus Uncoating and Membrane Lytic Protein Exposure.* Cell Host & Microbe, 2011. **10**(2): p. 105-117.

118. Gastaldelli, M., N. Imelli, K. Boucke, B. Amstutz, O. Meier, and U.F. Greber, *Infectious Adenovirus Type 2 Transport Through Early but not Late Endosomes.* Traffic, 2008. **8**: p. 2265-2278.

119. Maier, O., S.A. Marvin, H. Wodrich, E.M. Campbell, and C.M. Wiethoff, *Spatiotemporal dynamics of adenovirus membrane rupture and endosomal escape.* J Virol, 2012. **86**(19): p. 10821-10828.

120. Gruenberg, J. and F.G.v.d. Goot, *Mechanisms of pathogen entry through the endosomal compartments.* Nature Reviews Molecular Cell Biology, 2006. **7**(7): p. 495-504.

121. Nemerow, G.R. and P.L. Stewart, *Role of alpha(v) integrins in adenovirus cell entry and gene delivery.* Microbiology And Molecular Biology Reviews, 1999. **63**(3): p. 725-734.

122. Martinez, R., *Etude du rôle des modifications post-traductionnelles de la protéine VI lors de l'entrée de l'adénovirus dans sa cellule hôte*. 2012.

123. Wodrich, H., D. Henaff, B. Jammart, C. Segura-Morales, S. Seelmeir, O. Coux, Z. Ruzsics, C.M. Wiethoff, and E.J. Kremer, *A Capsid-Encoded PPxY-Motif Facilitates Adenovirus Entry.* PLoS Pathogens, 2010. **6**(3): p. e1000808-e1000808.

124. Maier, O., D.L. Galan, H. Wodrich, and C.M. Wiethoff, *An N-terminal domain of adenovirus protein VI fragments membranes by inducing positive membrane curvature.* Virology, 2010. **402**(1): p. 11-19.

125. Silvestry, M., S. Lindert, J.G. Smith, O. Maier, C.M. Wiethoff, G.R. Nemerow, and P.L. Stewart, *Cryo-electron microscopy structure of adenovirus type 2 temperature-sensitive mutant 1 reveals insight into the cell entry defect.* J Virol, 2009. **83**(15): p. 7375-7383.

126. Meier, O. and U.F. Greber, *Adenovirus endocytosis.* The Journal of Gene Medicine, 2004. **6**(S1): p. S152-S163.

127. Bremner, K.H., J. Scherer, J. Yi, M. Vershinin, S.P. Gross, and R.B. Vallee, *Adenovirus transport via direct interaction of cytoplasmic dynein with the viral capsid hexon subunit.* Cell Host Microbe, 2009. **6**(6): p. 523-535.

128. Miyazawa, N., R.G. Crystal, and P.L. Leopold, *Adenovirus serotype 7 retention in a late endosomal compartment prior to cytosol escape is modulated by fiber protein.* Journal of Virology, 2001. **75**(3): p. 1387-1400.

129. Montespan, C., C.M. Wiethoff, and H. Wodrich, *A Small Viral PPxY Peptide Motif To Control Antiviral Autophagy.* Journal of virology, 2017. **91**(18): p. e00581-17.

130. Greber, U.F., M. Suomalainen, R.P. Stidwill, K. Boucke, M.W. Ebersold, and A. Helenius, *The role of the nuclear pore complex in adenovirus DNA entry.* The EMBO journal, 1997. **16**(19): p. 5998-6007.

131. Webster, A., I.R. Leith, and R.T. Hay, *Activation of adenovirus-coded protease and processing of preterminal protein.* Journal of virology, 1994. **68**(11): p. 7292-7300.

132. Ullman, A.J., N.C. Reich, and P. Hearing, *Adenovirus E4 ORF3 Protein Inhibits the Interferon-Mediated Antiviral Response.* Journal of Virology, 2007. **81**(9): p. 4744.

133. Hoeben, R.C. and T.G. Uil, *Adenovirus DNA replication.* Cold Spring Harbor perspectives in biology, 2013. **5**(3): p. a013003-a013003.

134. Ahi, Y.S. and S.K. Mittal, *Components of Adenovirus Genome Packaging.* Frontiers in Microbiology, 2016. **7**(1503).

135. Condezo, G.N., R. Marabini, S. Ayora, J.M. Carazo, R. Alba, M. Chillon, and C. San Martin, *Structures of Adenovirus Incomplete Particles Clarify Capsid Architecture and Show Maturation Changes of Packaging Protein L1 52/55k.* J Virol, 2015. **89**(18): p. 9653-9664.

136. Condezo, G.N. and C. San Martín, *Localization of adenovirus morphogenesis players, together with visualization of assembly intermediates and failed products,*

favor a model where assembly and packaging occur concurrently at the periphery of the replication center. PLOS Pathogens, 2017. **13**(4): p. e1006320.

137. Jiang, H., E.J. White, C.I. Ríos-Vicil, J. Xu, C. Gomez-Manzano, and J. Fueyo, *Human adenovirus type 5 induces cell lysis through autophagy and autophagy-triggered caspase activity.* Journal of virology, 2011. **85**(10): p. 4720-4729.

138. Montespan, C., S.A. Marvin, S. Austin, A.M. Burrage, B. Roger, F. Rayne, M. Faure, E.M. Campell, C. Schneider, R. Reimer, K. Grünewald, C.M. Wiethoff, and H. Wodrich, *Multi-layered control of Galectin-8 mediated autophagy during adenovirus cell entry through a conserved PPxY motif in the viral capsid.* PLoS pathogens, 2017. **13**(2): p. e1006217-e1006217.

139. Zeng, X. and C.R. Carlin, *Host Cell Autophagy Modulates Early Stages of Adenovirus Infections in Airway Epithelial Cells.* Journal of Virology, 2013. **87**(4): p. 2307-2319.

140. Xie, Z. and D.J. Klionsky, *Autophagosome formation: core machinery and adaptations.* Nat Cell Biol, 2007. **9**(10): p. 1102-9.

141. Baehrecke, E.H., *Autophagy: dual roles in life and death?* Nat Rev Mol Cell Biol, 2005. **6**(6): p. 505-10.

142. Jiang, H., E.J. White, C. Gomez-Manzano, and J. Fueyo, *Adenovirus's last trick: you say lysis, we say autophagy.* Autophagy, 2008. **4**(1): p. 118-20.

143. Maier, O. and C.M. Wiethoff, *N-terminal α-helix-independent membrane interactions facilitate adenovirus protein VI induction of membrane tubule formation.* Virology, 2010. **408**(1): p. 31-38.

144. Moyer, C.L., E.S. Besser, and G.R. Nemerow, *A Single Maturation Cleavage Site in Adenovirus Impacts Cell Entry and Capsid Assembly.* Journal of Virology, 2016. **90**(1): p. 521-532.

145. Matthews, D.A. and W.C. Russell, *Adenovirus protein-protein interactions: molecular parameters governing the binding of protein VI to hexon and the activation of the adenovirus 23K protease.* J Gen Virol, 1995. **76 (Pt 8)**: p. 1959-69.

146. Consortium, T.U., *UniProt: a worldwide hub of protein knowledge.* Nucleic Acids Research, 2018. **47**(D1): p. D506-D515.

147. Sudol, M., *Structure and function of the WW domain.* Prog Biophys Mol Biol, 1996. **65**(1-2): p. 113-132.

148. Martinez, R., P. Schellenberger, D. Vasishtan, C. Aknin, S. Austin, D. Dacheux, F. Rayne, A. Siebert, Z. Ruzsics, K. Grünewald, and H. Wodrich, *The Amphipathic Helix of Adenovirus Capsid Protein VI Contributes to Penton Release and Postentry Sorting.* Journal of Virology, 2015. **89**(4): p. 2121-2135.

149. Seiradake, E., D. Henaff, H. Wodrich, O. Billet, M. Perreau, C. Hippert, F. Mennechet, G. Schoehn, H. Lortat-Jacob, H. Dreja, S. Ibanes, V. Kalatzis, J.P. Wang,

R.W. Finberg, S. Cusack, and E.J. Kremer, *The cell adhesion molecule "CAR" and sialic acid on human erythrocytes influence adenovirus in vivo biodistribution.* PLoS Pathog, 2009. **5**(1): p. e1000277-e1000277.

150. Harty, R.N., J. Paragas, M. Sudol, and P. Palese, *A proline-rich motif within the matrix protein of vesicular stomatitis virus and rabies virus interacts with WW domains of cellular proteins: implications for viral budding.* J Virol, 1999. **73**(4): p. 2921-2929.

151. Jayakar, H.R., K.G. Murti, and M.A. Whitt, *Mutations in the PPPY motif of vesicular stomatitis virus matrix protein reduce virus budding by inhibiting a late step in virion release.* Journal of virology, 2000. **74**(21): p. 9818-9827.

152. Harty, R.N., M.E. Brown, G. Wang, J. Huibregtse, and F.P. Hayes, *A PPxY motif within the VP40 protein of Ebola virus interacts physically and functionally with a ubiquitin ligase: Implications for filovirus budding.* Proc Natl Acad Sci U S A, 2000. **97**(25): p. 13871-13876.

153. Everitt, E. and L. Philipson, *Structural proteins of adenoviruses: XI. Purification of three low molecular weight virion proteins of adenovirus type 2 and their synthesis during productive infection.* Virology, 1974. **62**(1): p. 253-269.

154. Snijder, J., M. Benevento, C.L. Moyer, V. Reddy, G.R. Nemerow, and A.J. Heck, *The cleaved N-terminus of pVI binds peripentonal hexons in mature adenovirus.* J Mol Biol, 2014. **426**(9): p. 1971-1979.

155. Stewart, P.L. and R.M. Burnett, *Adenovirus Structure As Revealed By X-Ray Crystallography, Electron-Microscopy, And Difference Imaging.* Japanese Journal of Applied Physics Part 1-Regular Papers Short Notes & Review Papers, 1993. **32**(3B): p. 1342-1347.

156. Reddy, V.S., S.K. Natchiar, P.L. Stewart, and G.R. Nemerow, *Crystal Structure of Human Adenovirus at 3.5 Å Resolution.* Science, 2010. **329**(5995): p. 1071-1075.

157. Moyer, C.L. and G.R. Nemerow, *Disulfide-bond formation by a single cysteine mutation in adenovirus protein VI impairs capsid release and membrane lysis.* Virology, 2012. **428**(1): p. 41-47.

158. Petersen, M.T., P.H. Jonson, and S.B. Petersen, *Amino acid neighbours and detailed conformational analysis of cysteines in proteins.* Protein Eng, 1999. **12**(7): p. 535-48.

159. van Rosmalen, M.G.M., G.R. Nemerow, G.J.L. Wuite, and W.H. Roos, *A single point mutation in precursor protein VI doubles the mechanical strength of human adenovirus.* Journal of Biological Physics, 2018. **44**(2): p. 119-132.

160. Hernando-Pérez, M., N. Martín-González, M. Pérez-Illana, M. Suomalainen, G.N. Condezo, P. Ostapchuk, J. Gallardo, M. Menéndez, U.F. Greber, P. Hearing, P.J. de

Pablo, and C. San Martín, *Dynamic competition for hexon binding between core protein VII and lytic protein VI promotes adenovirus maturation and entry.* Proceedings of the National Academy of Sciences, 2020. **117**(24): p. 13699-13707.

161. van Oostrum, J. and R.M. Burnett, *Molecular composition of the adenovirus type 2 virion.* Journal of virology, 1985. **56**(2): p. 439-48.

162. Lehmberg, E., J.A. Traina, J.A. Chakel, R.-J. Chang, M. Parkman, M.T. McCaman, P.K. Murakami, V. Lahidji, J.W. Nelson, W.S. Hancock, E. Nestaas, and E. Pungor, *Reversed-phase high-performance liquid chromatographic assay for the adenovirus type 5 proteome.* Journal of Chromatography B: Biomedical Sciences and Applications, 1999. **732**(2): p. 411-423.

163. Benevento, M., S. Di Palma, J. Snijder, C.L. Moyer, V.S. Reddy, G.R. Nemerow, and A.J.R. Heck, *Adenovirus composition, proteolysis, and disassembly studied by in-depth qualitative and quantitative proteomics.* Journal of Biological Chemistry, 2014. **289**(16): p. 11421-11430.

164. Roberts, R.J., K.E. O'Neill, and C.T. Yen, *DNA sequences from the adenovirus 2 genome.* Journal of Biological Chemistry, 1984. **259**(22): p. 13968-13975.

165. Drin, G., J.-F. Casella, R. Gautier, T. Boehmer, T.U. Schwartz, and B. Antonny, *A general amphipathic alpha-helical motif for sensing membrane curvature.* Nature structural & molecular biology, 2007. **14**(2): p. 138-46.

166. Drin, G. and B. Antonny, *Amphipathic helices and membrane curvature.* FEBS Letters, 2010. **584**(9): p. 1840-1847.

167. Seelig, J., *Thermodynamics of lipid–peptide interactions.* Biochimica et Biophysica Acta (BBA) - Biomembranes, 2004. **1666**(1-2): p. 40-50.

168. Murayama, T., S. Pujals, H. Hirose, I. Nakase, and S. Futaki, *Effect of amino acid substitution in the hydrophobic face of amphiphilic peptides on membrane curvature and perturbation: N-terminal helix derived from adenovirus internal protein VI as a model.* Biopolymers, 2016. **106**(4): p. 430-439.

169. Gautier, R., D. Douguet, B. Antonny, and G. Drin, *HELIQUEST: a web server to screen sequences with specific alpha-helical properties.* Bioinformatics, 2008. **24**(18): p. 2101-2.

170. Maier, O., *Mechanisms of Adenovirus Membrane Permeabilization. http://ecommons.luc.edu/luc_diss/283*. 2011, Dissertations. Paper 283.

171. Schreiner, S., P. Wimmer, H. Sirma, R.D. Everett, P. Blanchette, P. Groitl, and T. Dobner, *Proteasome-Dependent Degradation of Daxx by the Viral E1B-55K Protein in Human Adenovirus-Infected Cells.* Journal of Virology, 2010. **84**(14): p. 7029-7038.

172. Schreiner, S., R. Martinez, P. Groitl, F. Rayne, R. Vaillant, P. Wimmer, G. Bossis, T. Sternsdorf, L. Marcinowski, Z. Ruzsics, T. Dobner, and H. Wodrich, *Transcriptional activation of the adenoviral genome is mediated by capsid protein VI.* PLoS Pathog, 2012. **8**(2): p. e1002549-e1002549.

173. Day, P.M., R.B. Roden, D.R. Lowy, and J.T. Schiller, *The papillomavirus minor capsid protein, L2, induces localization of the major capsid protein, L1, and the viral transcription/replication protein, E2, to PML oncogenic domains.* J Virol, 1998. **72**(1): p. 142-50.

174. Korioth, F., G.G. Maul, B. Plachter, T. Stamminger, and J. Frey, *The nuclear domain 10 (ND10) is disrupted by the human cytomegalovirus gene product IE1.* Exp Cell Res, 1996. **229**(1): p. 155-8.

175. Maul, G.G., A.M. Ishov, and R.D. Everett, *Nuclear domain 10 as preexisting potential replication start sites of herpes simplex virus type-1.* Virology, 1996. **217**(1): p. 67-75.

176. Wodrich, H., T. Guan, G. Cingolani, D. Von Seggern, G. Nemerow, and L. Gerace, *Switch from capsid protein import to adenovirus assembly by cleavage of nuclear transport signals.* EMBO J, 2003. **22**(23): p. 6245-6255.

177. Singh, N., A. Joshi, and G. Verma, *Chapter 10 - Engineered nanomaterials for biomedicine: Advancements and hazards*, in *Engineering of Nanobiomaterials*, A.M. Grumezescu, Editor. 2016, William Andrew Publishing. p. 307-328.

178. Patil, Y.P. and s. Jadhav, *Novel methods for liposome preparation.* Chemistry and Physics of Lipids, 2014. **177**: p. 8-18.

179. Tegel, H., S. Tourle, J. Ottosson, and A. Persson, *Increased levels of recombinant human proteins with the Escherichia coli strain Rosetta(DE3).* Protein Expression and Purification, 2010. **69**(2): p. 159-167.

180. Wingfield, P.T., *Use of Protein Folding Reagents*. 1995, John Wiley & Sons, Inc.: Hoboken, NJ, USA. p. A.3A.1-A.3A.4.

181. Kågedal, L., *Immobilized Metal Ion Affinity Chromatography*

in *Protein Purification: Principles, High Resolution Methods, and Applications*, J.-C. Janson, Editor. 2011, Wiley

182. Bornhorst, J.A. and J.J. Falke, *Purification of proteins using polyhistidine affinity tags.* Methods in enzymology, 2000. **326**: p. 245-254.

183. Lim, W.K., J. Rösgen, and S.W. Englander, *Urea, but not guanidinium, destabilizes proteins by forming hydrogen bonds to the peptide group.* Proceedings of the National Academy of Sciences of the United States of America, 2009. **106**(8): p. 2595-600.

184. Auton, M., L.M.F. Holthauzen, and D.W. Bolen, *Anatomy of energetic changes accompanying urea-induced protein denaturation.* Proceedings of the National Academy of Sciences of the United States of America, 2007. **104**(39): p. 15317-15322.

185. Pace, C.N., *Determination and analysis of urea and guanidine hydrochloride denaturation curves.* Methods in enzymology, 1986. **131**: p. 266-80.

186. Huerta-Viga, A. and S. Woutersen, *Protein denaturation with guanidinium: A 2D-IR study.* Journal of Physical Chemistry Letters, 2013. **4**(20): p. 3397-3401.

187. Sambi, I., P. Gatti-Lafranconi, S. Longhi, and M. Lotti, *How disorder influences order and vice versa – mutual effects in fusion proteins containing an intrinsically disordered and a globular protein.* The FEBS Journal, 2010. **277**(21): p. 4438-4451.

188. Lieutaud, P., F. Ferron, A.V. Uversky, L. Kurgan, V.N. Uversky, and S. Longhi, *How disordered is my protein and what is its disorder for? A guide through the "dark side" of the protein universe.* Intrinsically disordered proteins, 2016. **4**(1): p. e1259708-e1259708.

189. Uversky, V.N., J.R. Gillespie, and A.L. Fink, *Why are "natively unfolded" proteins unstructured under physiologic conditions?* Proteins: Structure, Function, and Bioinformatics, 2000. **41**(3): p. 415-427.

190. Graumann, K. and A. Premstaller, *Manufacturing of recombinant therapeutic proteins in microbial systems.* Biotechnol J, 2006. **1**(2): p. 164-86.

191. Giacalone, M.J., A.M. Gentile, B.T. Lovitt, N.L. Berkley, C.W. Gunderson, and M.W. Surber, *Toxic protein expression in Escherichia coli using a rhamnose-based tightly regulated and tunable promoter system.* BioTechniques, 2006. **40**(3): p. 355-364.

192. Siegele, D.A. and J.C. Hu, *Gene expression from plasmids containing the araBAD promoter at subsaturating inducer concentrations represents mixed populations.* Proceedings of the National Academy of Sciences of the United States of America, 1997. **94**(15): p. 8168-8172.

193. Artimo, P., M. Jonnalagedda, K. Arnold, D. Baratin, G. Csardi, E. de Castro, S. Duvaud, V. Flegel, A. Fortier, E. Gasteiger, A. Grosdidier, C. Hernandez, V. Ioannidis, D. Kuznetsov, R. Liechti, S. Moretti, K. Mostaguir, N. Redaschi, G. Rossier, I. Xenarios, and H. Stockinger, *ExPASy: SIB bioinformatics resource portal.* Nucleic Acids Research, 2012. **40**(W1): p. W597-W603.

194. Jones, D.T., *Protein secondary structure prediction based on position-specific scoring matrices.* Journal of Molecular Biology, 1999. **292**(2): p. 195-202.

195. Buchan, D.W.A. and D.T. Jones, *The PSIPRED Protein Analysis Workbench: 20 years on.* Nucleic Acids Research, 2019. **47**(W1): p. W402-W407.

196. Wang, S., W. Li, S. Liu, and J. Xu, *RaptorX-Property: a web server for protein structure property prediction.* Nucleic Acids Research, 2016. **44**(W1): p. W430-W435.

197. Cuff, J.A. and G.J. Barton, *Application of multiple sequence alignment profiles to improve protein secondary structure prediction.* Proteins: Structure, Function, and Bioinformatics, 2000. **40**(3): p. 502-511.

198. Drozdetskiy, A., C. Cole, J. Procter, and G.J. Barton, *JPred4: a protein secondary structure prediction server.* Nucleic Acids Research, 2015. **43**(W1): p. W389-W394.

199. Yachdav, G., E. Kloppmann, L. Kajan, M. Hecht, T. Goldberg, T. Hamp, P. Hönigschmid, A. Schafferhans, M. Roos, M. Bernhofer, L. Richter, H. Ashkenazy, M. Punta, A. Schlessinger, Y. Bromberg, R. Schneider, G. Vriend, C. Sander, N. Ben-Tal, and B. Rost, *PredictProtein--an open resource for online prediction of protein structural and functional features.* Nucleic acids research, 2014. **42**(Web Server issue): p. W337-W343.

200. Kelley, L.A., S. Mezulis, C.M. Yates, M.N. Wass, and M.J.E. Sternberg, *The Phyre2 web portal for protein modeling, prediction and analysis.* Nature Protocols, 2015. **10**(6): p. 845-858.

201. Pollastri, G., D. Przybylski, B. Rost, and P. Baldi, *Improving the prediction of protein secondary structure in three and eight classes using recurrent neural networks and profiles.* Proteins, 2002. **47**(2): p. 228-35.

202. Dunker, A.K., C.J. Brown, and Z. Obradovic, *Identification and functions of usefully disordered proteins*, in *Advances in Protein Chemistry*

G.D. Rose, Editor. 2002. p. 25-49.

203. Dyson, H.J. and P.E. Wright, *Intrinsically unstructured proteins and their functions.* Nature Reviews Molecular Cell Biology, 2005. **6**(3): p. 197-208.

204. Basile, W., M. Salvatore, C. Bassot, and A. Elofsson, *Why do eukaryotic proteins contain more intrinsically disordered regions?* PLoS computational biology, 2019. **15**(7): p. e1007186-e1007186.

205. Suskiewicz, M.J., J.L. Sussman, I. Silman, and Y. Shaul, *Context-dependent resistance to proteolysis of intrinsically disordered proteins.* Protein science : a publication of the Protein Society, 2011. **20**(8): p. 1285-1297.

206. Dunker, A.K., C.J. Brown, J.D. Lawson, L.M. Iakoucheva, and Z. Obradović, *Intrinsic disorder and protein function.* Biochemistry, 2002. **41**(21): p. 6573-6582.

207. Dunker, A.K., C.J. Brown, J.D. Lawson, and L.M. Iakoucheva, *Intrinsic disorder and protein fluctuations.* Biochemistry, 2002. **41**: p. 6573-6582.

208. Johnson, D.E., B. Xue, M.D. Sickmeier, J. Meng, M.S. Cortese, C.J. Oldfield, T. Le Gall, A.K. Dunker, and V.N. Uversky, *High-throughput characterization of intrinsic disorder in proteins from the Protein Structure Initiative.* Journal of structural biology, 2012. **180**(1): p. 201-215.

209. Dosztányi, Z., V. Csizmok, P. Tompa, and I. Simon, *IUPred: web server for the prediction of intrinsically unstructured regions of proteins based on estimated energy content.* Bioinformatics (Oxford, England), 2005. **21**(16): p. 3433-3434.

210. Dosztányi, Z., *Prediction of protein disorder based on IUPred.* Protein science : a publication of the Protein Society, 2018. **27**(1): p. 331-340.

211. Keul, N.D., K. Oruganty, E.T. Schaper Bergman, N.R. Beattie, W.E. McDonald, R. Kadirvelraj, M.L. Gross, R.S. Phillips, S.C. Harvey, and Z.A. Wood, *The entropic force generated by intrinsically disordered segments tunes protein function.* Nature, 2018. **563**(7732): p. 584-588.

212. Forcelloni, S. and A. Giansanti, *New perspectives into the evolutionary pressures acting on the Human intrinsically disordered proteins.* bioRxiv, 2018: p. 484659.

213. Hoffmann, S.V., M. Fano, and M. van de Weert, *Circular Dichroism Spectroscopy for Structural Characterization of Proteins*, in *Analytical Techniques in the Pharmaceutical Sciences*, A. Müllertz, Y. Perrie, and T. Rades, Editors. 2016, Springer New York: New York, NY. p. 223-251.

214. Greenfield, N.J., *Using circular dichroism spectra to estimate protein secondary structure.* Nature protocols, 2006. **1**(6): p. 2876-90.

215. Martin, S.R. and M.J. Schilstra, *Circular dichroism and its application to the study of biomolecules.* Methods in cell biology, 2008. **84**: p. 263-293.

216. Greenfield, N. and G.D. Fasman, *Computed circular dichroism spectra for the evaluation of protein conformation.* Biochemistry, 1969. **8**(10): p. 4108-4116.

217. Holzwarth, G. and P. Doty, *THE ULTRAVIOLET CIRCULAR DICHROISM OF POLYPEPTIDES.* Journal of the American Chemical Society, 1965. **87**: p. 218-228.

218. Venyaminov, S., I.A. Baikalov, Z.M. Shen, C.S. Wu, and J.T. Yang, *Circular dichroic analysis of denatured proteins: inclusion of denatured proteins in the reference set.* Analytical biochemistry, 1993. **214**(1): p. 17-24.

219. Clarke, D.T., *Circular dichroism and its use in protein-folding studies.* Methods in molecular biology (Clifton, N.J.), 2011. **752**: p. 59-72.

220. Ralston, G.B., *Introduction to Analytical Ultracentrifugation*. 1993: Beckman.

221. Cole, J.L., J.W. Lary, T. P. Moody, and T.M. Laue, *Analytical Ultracentrifugation: Sedimentation Velocity and Sedimentation Equilibrium*. 2008. p. 143-179.

222. A. Balbo, P.S., *Analytical Ultracentrifugation in the Study of Protein Selfassociation and Heterogeneous Protein-Protein Interactions* in *Protein-protein interactions. A molecular cloning manual*, P.D.A. E A Golemis, Editor. 2005, Cold Spring Harbor Laboratory Press: New York.

223. Campbell, I., *Biophysical Techniques*. 2012: OUP Oxford.

224. Brown, P.H. and P. Schuck, *A new adaptive grid-size algorithm for the simulation of sedimentation velocity profiles in analytical ultracentrifugation.* Comput Phys Commun, 2008. **178**(2): p. 105-120.

225. Gombotz, W.R., *B.5 - Liposomes*, in *Biomaterials Science (Third Edition)*, B.D. Ratner, et al., Editors. 2013, Academic Press. p. 1039-1041.

226. Pitcher, W.H., 3rd and W.H. Huestis, *Preparation and analysis of small unilamellar phospholipid vesicles of a uniform size.* Biochemical and biophysical research communications, 2002. **296**(5): p. 1352-1355.

227. Yang, P.L., *Chapter 14 - Metabolomics and Lipidomics.*, in *Viral Pathogenesis (Third Edition)*, M.G. Katze, et al., Editors. 2016, Academic Press: Boston. p. 181-198.

228. Dawaliby, R., C. Trubbia, C. Delporte, C. Noyon, J.-M. Ruysschaert, P. Van Antwerpen, and C. Govaerts, *Phosphatidylethanolamine Is a Key Regulator of Membrane Fluidity in Eukaryotic Cells.* The Journal of biological chemistry, 2016. **291**(7): p. 3658-3667.

229. Imelli, N., O. Meier, K. Boucke, S. Hemmi, and U.F. Greber, *Cholesterol is required for endocytosis and endosomal escape of adenovirus type 2.* J Virol, 2004. **78**(6): p. 3089-3098.

230. van Meer, G. and A.I.P.M. de Kroon, *Lipid map of the mammalian cell.* Journal of Cell Science, 2011. **124**(1): p. 5.

231. McMahon, H.T. and E. Boucrot, *Membrane curvature at a glance.* Journal of cell science, 2015. **128**(6): p. 1065-1070.

232. Kaszuba, M., D. McKnight, M.T. Connah, F.K. McNeil-Watson, and U. Nobbmann, *Measuring sub nanometre sizes using dynamic light scattering.* Journal of Nanoparticle Research, 2008. **10**(5): p. 823-829.

233. Stetefeld, J., S.A. McKenna, and T.R. Patel, *Dynamic light scattering: a practical guide and applications in biomedical sciences.* Biophysical Reviews, 2016. **8**(4): p. 409-427.

234. Wishard, A. and B.C. Gibb, *Dynamic light scattering – an all-purpose guide for the supramolecular chemist.* Supramolecular Chemistry, 2019. **31**(9): p. 608-615.

235. Nobbmann, U. *Solvent peaks – how to get rid of the buffer/salt/additive DLS contribution?* 2016 13 Feb 2021]; Available from: https://www.materials-

talks.com/blog/2016/06/15/solvent-peaks-how-to-get-rid-of-the-buffersaltadditive-dls-contribution/.

236. Bae, W. and T.-Y. Yoon, *Properties of Self-Quenching Fluorescence Dye for Vesicle-Vesicle Content Mixing System.* Biophysical Journal, 2013. **104**(2): p. 88a.

237. Zager, R.A., *Plasma membrane cholesterol: A critical determinant of cellular energetics and tubular resistance to attack.* Kidney International, 2000. **58**(1): p. 193-205.

238. Needham, D. and R.S. Nunn, *Elastic deformation and failure of lipid bilayer membranes containing cholesterol.* Biophysical journal, 1990. **58**(4): p. 997-1009.

239. Ivankin, A., I. Kuzmenko, and D. Gidalevitz, *Cholesterol Mediates Membrane Curvature during Fusion Events.* Physical Review Letters, 2012. **108**(23): p. 238103.

240. McIntosh, T.J. and S.A. Simon, *Roles of bilayer material properties in function and distribution of membrane proteins.* Annu Rev Biophys Biomol Struct, 2006. **35**: p. 177-98.

241. Uversky, V.N., *Natively unfolded proteins: a point where biology waits for physics.* Protein Sci, 2002. **11**(4): p. 739-56.

242. Chatterjee, P.K., M.E. Vayda, and S.J. Flint, *Interactions among the three adenovirus core proteins.* J Virol, 1985. **55**(2): p. 379-386.

243. Dyson, H.J., *Coupled Folding and Binding*, in *Encyclopedia of Biophysics*, G.C.K. Roberts, Editor. 2013, Springer Berlin Heidelberg: Berlin, Heidelberg. p. 381-385.

244. Hashimoto, K. and A.R. Panchenko, *Mechanisms of protein oligomerization, the critical role of insertions and deletions in maintaining different oligomeric states.* Proceedings of the National Academy of Sciences, 2010. **107**(47): p. 20352-20357.

245. Pouny, Y., D. Rapaport, A. Mor, P. Nicolas, and Y. Shai, *Interaction of antimicrobial dermaseptin and its fluorescently labeled analogues with phospholipid membranes.* Biochemistry, 1992. **31**(49): p. 12416-23.

246. Dean, R.E., L.M. O'Brien, J.E. Thwaite, M.A. Fox, H. Atkins, and D.O. Ulaeto, *A carpet-based mechanism for direct antimicrobial peptide activity against vaccinia virus membranes.* Peptides, 2010. **31**(11): p. 1966-1972.

247. Oren, Z. and Y. Shai, *Selective lysis of bacteria but not mammalian cells by diastereomers of melittin: structure-function study.* Biochemistry, 1997. **36**(7): p. 1826-35.

248. Sugase, K., H.J. Dyson, and P.E. Wright, *Mechanism of coupled folding and binding of an intrinsically disordered protein.* Nature, 2007. **447**(7147): p. 1021-1025.

249. Krause, M.R. and S.L. Regen, *The Structural Role of Cholesterol in Cell Membranes: From Condensed Bilayers to Lipid Rafts.* Accounts of Chemical Research, 2014. **47**(12): p. 3512-3521.

250. Yeagle, P.L., *Cholesterol and the cell membrane.* Biochim Biophys Acta, 1985. **822**(3-4): p. 267-87.

251. Dosztányi, Z., V. Csizmók, P. Tompa, and I. Simon, *The pairwise energy content estimated from amino acid composition discriminates between folded and intrinsically unstructured proteins.* J Mol Biol, 2005. **347**(4): p. 827-39.

252. Mészáros, B., G. Erdos, and Z. Dosztányi, *IUPred2A: context-dependent prediction of protein disorder as a function of redox state and protein binding.* Nucleic Acids Res, 2018. **46**(W1): p. W329-w337.

253. Erdős, G. and Z. Dosztányi, *Analyzing Protein Disorder with IUPred2A.* Current Protocols in Bioinformatics, 2020. **70**(1): p. e99.

254. Wiedemann, C., P. Bellstedt, and M. Görlach, *CAPITO--a web server-based analysis and plotting tool for circular dichroism data.* Bioinformatics, 2013. **29**(14): p. 1750-7.

255. van Meer, G., D.R. Voelker, and G.W. Feigenson, *Membrane lipids: where they are and how they behave.* Nat Rev Mol Cell Biol, 2008. **9**(2): p. 112-124.

256. Winey, M., J.B. Meehl, E.T. O'Toole, and T.H. Giddings, Jr., *Conventional transmission electron microscopy.* Molecular biology of the cell, 2014. **25**(3): p. 319-323.

257. Mielańczyk, L., N. Matysiak, O. Klymenko, and R. Wojnicz, *The Transmission Electron Microscope - Theory and Applications*, in *Transmission Electron Microscopy of Biological Samples*, K. Maaz, Editor. 2015, ntechOpen.

258. Gordon, R.E., *Electron microscopy: a brief history and review of current clinical application.* Methods Mol Biol, 2014. **1180**: p. 119-35.

259. Cabra, V. and M. Samsó, *Do's and don'ts of cryo-electron microscopy: A primer on sample preparation and high quality data collection for macromolecular 3d reconstruction.* Journal of Visualized Experiments : JoVE, 2015. **95**: p. e52311-e52311.

260. Thompson, R.F., M. Walker, C.A. Siebert, S.P. Muench, and N.A. Ranson, *An introduction to sample preparation and imaging by cryo-electron microscopy for structural biology.* Methods (San Diego, Calif.), 2016. **100**: p. 3-15.

261. Ohi, M., Y. Li, Y. Cheng, and T. Walz, *Negative Staining and Image Classification - Powerful Tools in Modern Electron Microscopy.* Biol Proced Online, 2004. **6**: p. 23-34.

262. Elmlund, D. and H. Elmlund, *Cryogenic Electron Microscopy and Single-Particle Analysis.* Annual Review of Biochemistry, 2015. **84**(1): p. 499-517.

263. Bhella, D., *Cryo-electron microscopy: an introduction to the technique, and considerations when working to establish a national facility.* Biophysical Reviews, 2019. **11**(4): p. 515-519.

264. Wan, W. and J.A.G. Briggs, *Chapter Thirteen - Cryo-Electron Tomography and Subtomogram Averaging*, in *Methods in Enzymology*, R.A. Crowther, Editor. 2016, Academic Press. p. 329-367.

265. Oikonomou, C.M. and G.J. Jensen, *The development of cryo-EM and how it has advanced microbiology.* Nature Microbiology, 2017. **2**(12): p. 1577-1579.

266. Cheng, Y., N. Grigorieff, P.A. Penczek, and T. Walz, *A Primer to Single-Particle Cryo-Electron Microscopy.* Cell, 2015. **161**(3): p. 12-12.

267. Danev, R., H. Yanagisawa, and M. Kikkawa, *Cryo-Electron Microscopy Methodology: Current Aspects and Future Directions.* Trends in Biochemical Sciences, 2019. **44**(10): p. 837-848.

268. Murata, K. and M. Wolf, *Cryo-electron microscopy for structural analysis of dynamic biological macromolecules.* Biochimica et Biophysica Acta (BBA) - General Subjects, 2018. **1862**(2): p. 324-334.

269. Skiniotis, G. and D.R. Southworth, *Single-particle cryo-electron microscopy of macromolecular complexes.* Microscopy, 2015. **65**(1): p. 9-22.

270. Bonetta, L., *Zooming in on electron tomography.* Nature Methods, 2005. **2**(2): p. 139-145.

271. Zhang, P., *Advances in cryo-electron tomography and subtomogram averaging and classification.* Current Opinion in Structural Biology, 2019. **58**: p. 249-258.

272. Baker, L.A., M. Grange, and K. Grünewald, *Electron cryo-tomography captures macromolecular complexes in native environments.* Curr Opin Struct Biol, 2017. **46**: p. 149-156.

273. Noble, A.J., V.P. Dandey, H. Wei, J. Brasch, J. Chase, P. Acharya, Y.Z. Tan, Z. Zhang, L.Y. Kim, G. Scapin, M. Rapp, E.T. Eng, W.J. Rice, A. Cheng, C.J. Negro, L. Shapiro, P.D. Kwong, D. Jeruzalmi, A. des Georges, C.S. Potter, and B. Carragher, *Routine single particle CryoEM sample and grid characterization by tomography.* eLife, 2018. **7**: p. e34257.

274. Dubochet, J., M. Adrian, J.J. Chang, J.C. Homo, J. Lepault, A.W. McDowall, and P. Schultz, *Cryo-Electron Microscopy Of Vitrified Specimens.* Quarterly Reviews of Biophysics, 1988. **21**(2): p. 129-228.

275. Wang, H.W., *Cryo-electron microscopy for structural biology: current status and future perspectives.* Science China-Life Sciences, 2015. **58**(8): p. 750-756.

276. Chernomordik, L.V. and M.M. Kozlov, *Membrane Hemifusion: Crossing a Chasm in Two Leaps.* Cell, 2005. **123**(3): p. 375-382.

277. Bohrer, M.P., W.M. Deen, C.R. Robertson, J.L. Troy, and B.M. Brenner, *Influence of molecular configuration on the passage of macromolecules across the glomerular capillary wall.* J Gen Physiol, 1979. **74**(5): p. 583-93.

278. Shibata, Y., J. Hu, M.M. Kozlov, and T.A. Rapoport, *Mechanisms Shaping the Membranes of Cellular Organelles.* Annual Review of Cell and Developmental Biology, 2009. **25**(1): p. 329-354.

279. Goh, M., A. Hirano-Iwata, M. Niwano, and R. Tero, *Proteoliposome fusion to artificial lipid bilayer promoted by domains of polyunsaturated phosphatidylethanolamine.* Japanese Journal of Applied Physics, 2019. **58**: p. SIIB13.

280. Irie, A., K. Yamamoto, Y. Miki, and M. Murakami, *Phosphatidylethanolamine dynamics are required for osteoclast fusion.* Scientific Reports, 2017. **7**(1): p. 46715.

281. Tivol, W.F., A. Briegel, and G.J. Jensen, *An improved cryogen for plunge freezing.* Microscopy and microanalysis : the official journal of Microscopy Society of America, Microbeam Analysis Society, Microscopical Society of Canada, 2008. **14**(5): p. 375-379.

282. Mastronarde, D.N., *Automated electron microscope tomography using robust prediction of specimen movements.* J Struct Biol, 2005. **152**(1): p. 36-51.

283. Kremer, J.R., D.N. Mastronarde, and J.R. McIntosh, *Computer visualization of three-dimensional image data using IMOD.* J Struct Biol, 1996. **116**(1): p. 71-6.

284. Luisoni, S., M. Suomalainen, K. Boucke, Lukas B. Tanner, Markus R. Wenk, Xue L. Guan, M. Grzybek, Ü. Coskun, and Urs F. Greber, *Co-option of Membrane Wounding Enables Virus Penetration into Cells.* Cell Host & Microbe, 2015. **18**(1): p. 75-85.

285. Mercer, J., M. Schelhaas, and A. Helenius, *Virus entry by endocytosis.* Annu Rev Biochem, 2010. **79**: p. 803-833.

286. Schellenberger, P., R. Kaufmann, C.A. Siebert, C. Hagen, H. Wodrich, and K. Grunewald, *High-precision correlative fluorescence and electron cryo microscopy using two independent alignment markers.* Ultramicroscopy, 2014. **143**: p. 41-51.

287. Rigort, A., F.J.B. Bäuerlein, A. Leis, M. Gruska, C. Hoffmann, T. Laugks, U. Böhm, M. Eibauer, H. Gnaegi, W. Baumeister, and J.M. Plitzko, *Micromachining tools and correlative approaches for cellular cryo-electron tomography.* Journal of Structural Biology, 2010. **172**(2): p. 169-179.

288. Villa, E., M. Schaffer, J.M. Plitzko, and W. Baumeister, *Opening windows into the cell: focused-ion-beam milling for cryo-electron tomography.* Current Opinion in Structural Biology, 2013. **23**(5): p. 771-777.